



university of
 groningen

The origin and dynamics of the cool circumgalactic gas around low-redshift galaxies

PhD thesis

to obtain the degree of PhD of the
 University of Groningen
 on the authority of the
 Rector Magnificus Prof. C. Wijmenga
 and in accordance with
 the decision of the College of Deans.

This thesis will be defended in public on

Friday 10 December 2021 at 14:30 hours

by

Andrea Afruni

born on 14 August 1992
 in Forlì, Italy

Supervisors

Prof. F. Fraternali

Prof. A. Helmi

Dr. G. Pezzulli

Assessment Committee:

Prof. M. A. W. Verheijen

Prof. C. L. Martin

Prof. H. W. Chen

Cover: image created using generative art, by
Marina Papadopoulou
& Andrea Afruni.

Thesis and cover printed by: Gildeprint.

'Look again at that dot. That's here. That's home. That's us. On it everyone you love, everyone you know, everyone you ever heard of, every human being who ever was, lived out their lives. The aggregate of our joy and suffering, thousands of confident religions, ideologies, and economic doctrines, every hunter and forager, every hero and coward, every creator and destroyer of civilization, every king and peasant, every young couple in love, every mother and father, hopeful child, inventor and explorer, every teacher of morals, every corrupt politician, every "superstar," every "supreme leader," every saint and sinner in the history of our species lived there—on a mote of dust suspended in a sunbeam.'

Carl Sagan

Contents

1	Introduction	1
1.1	A brief cosmological overview.	2
1.2	Observations of the CGM	3
1.2.1	Extraplanar gas.	3
1.2.2	Cool ionized CGM	4
1.2.3	Hot and warm CGM	10
1.2.4	The CGM at higher redshifts	12
1.3	Origin of the CGM	13
1.3.1	Gas accretion into the halos	13
1.3.2	The impact of feedback	14
1.3.3	Other origin of the cool CGM.	17
1.4	Interactions between the CGM phases	18
1.5	Open questions	21
1.6	This Thesis	22
2	Cool circumgalactic gas of passive galaxies from cosmological inflow	25
2.1	Introduction.	27
2.2	ETG sample and observational constraints	29
2.3	The model	32
2.3.1	Purely ballistic model	32
2.3.2	Hydrodynamical effects	34
2.3.3	Accretion rate	36
2.4	Comparison with the observations	37
2.5	Results	40
2.5.1	MCMC results.	40
2.5.2	Description of the cloud motion	43
2.6	Discussion.	45
2.6.1	Cloud survival	45
2.6.2	Pressure equilibrium.	48
2.6.3	Comparison with other observations	48
2.6.4	Uncertainties in the accretion rate	51
2.6.5	Origin and fate of the cool absorbers	52
2.7	Summary and conclusions	55
2.A	Geometry of the system	56
2.B	Cloud initial velocity	57

3	Most of the cool CGM of star-forming galaxies is not produced by supernova feedback	59
3.1	Introduction	61
3.2	Galaxy sample and data.	63
3.3	Model.	67
3.3.1	Outflow of cool CGM clouds	68
3.3.2	Outflow rate	74
3.3.3	Comparison with the observations	74
3.4	Results	78
3.4.1	MCMC analysis	78
3.4.2	Physics of the outflows	81
3.5	Discussion.	83
3.5.1	Influence of the hot gas	83
3.5.2	Cool gas distribution.	86
3.5.3	Limitations of the model	88
3.5.4	Origin of the cool CGM	89
3.6	Summary and conclusions	91
3.A	Fitting of the galaxy images.	93
3.B	Tests on mock data.	94
4	Inflow of low-metallicity cool gas in the halo of the Andromeda galaxy	101
4.1	Introduction	103
4.2	Data: the project AMIGA	105
4.3	Model.	107
4.3.1	Creation of the M31 setup	108
4.3.2	Properties of the hot CGM	109
4.3.3	Properties of the cool CGM	111
4.3.4	Comparison with the observations	113
4.4	Results	114
4.4.1	Outflow scenario	115
4.4.2	Inflow scenario	117
4.5	Discussion.	125
4.5.1	Outflow.	125
4.5.2	Inflow.	127
4.5.3	Alternative origins	129
4.6	Summary and conclusions	130
4.A	Properties of the hot gas model	132
5	Hydrodynamical simulations of cool circumgalactic clouds: the case of M31	135
5.1	Introduction	137
5.2	Hydrodynamical simulations	139
5.2.1	Initial conditions of the simulations.	139
5.2.2	Cooling and thermal conduction.	142
5.2.3	Simulation setup	144

5.3	Results	146
5.3.1	2D simulations	146
5.3.2	3D simulations	151
5.4	Comparison with the AMIGA data.	157
5.5	Discussion.	161
5.5.1	Refining semi-analytic models of the drag force. . .	161
5.5.2	Limitations of this study	164
5.5.3	Comparison with previous works	165
5.6	Summary and conclusions	165
5.A	Field length and the role of thermal conduction	168
6	Conclusions and future perspectives	171
6.1	Summary of the Thesis	172
6.2	Main implications for the cool CGM.	174
6.2.1	The predominance of accretion.	174
6.2.2	Fate of the cool CGM.	175
6.3	Future prospects	176
6.3.1	New observational constraints	176
6.3.2	Improving numerical simulations of the CGM. . . .	177
6.3.3	Refining models of the CGM	178
	Bibliography	179
	Summary for non experts	197
	Samenvatting	203
	Sommario	211
	Acknowledgments	219

Chapter 1

Introduction

To understand how galaxies form, how do they acquire their gas during their evolution and how do they gain the specific shapes and properties that we observe today, it is of crucial importance to study the flows of gas in their surrounding environment, which is the central topic of this Thesis. In this Introduction, we describe the current observational and theoretical constraints on this material, known as the *circumgalactic medium*, or CGM.

In Section 1.1, we briefly describe the cosmological context of galaxy evolution; in Section 1.2, we review the current state of the observations of the circumgalactic gas, focusing in particular on low-redshift surveys; in Section 1.3, we outline the possible formation mechanisms of the CGM as predicted by theory, especially by current cosmological hydrodynamical simulations; in Section 1.4, we describe in detail the hydrodynamical interactions between the different phases of the circumgalactic gas; in Section 1.5, we list the main open questions that we will investigate in this work and, finally, in Section 1.6 we give an outline of this Thesis.

1.1 A brief cosmological overview

In the standard cosmological model, Lambda Cold Dark Matter (Λ CDM), the assembly of structures in the Universe starts from the collapse, due to gravitational instability, of overdensity perturbations in the general dark matter density distribution (Mo et al. 2010; Cimatti et al. 2019, and references therein). At the so-called turn-around time, overdense regions decouple from the average density field and collapse, forming, after a so-called virialization time, a virialized structure that we call *dark matter halo*. The size of a halo is given by its *virial radius* r_{vir} , defined as the radius where the enclosed mean matter density is equal to Δ times the critical density of the Universe ρ_{crit} , with Δ being the critical overdensity for virialization. The exact value of this overdensity depends on the adopted cosmology and on the redshift (e.g. Bryan & Norman 1998). The mass of a dark matter halo, also called *virial mass*, is then defined as:

$$M_{\text{vir}} = \frac{4}{3}\pi\Delta\rho_{\text{crit}}r_{\text{vir}}^3 . \quad (1.1)$$

The evolution of the dark matter, which is assumed to be collisionless and interacting with itself and with other matter components only through gravity, is well constrained in the Λ CDM framework. Dark matter halos grow in a *hierarchical* fashion: the smaller structures virialize first and then *merge* together to form more massive ones; hence the most massive dark matter structures in the Universe are also the ones that assembled most recently. The ordinary matter (called *baryons*), follows the evolution of the dark matter and is accreted into the dark matter halos. Galaxies are formed, in particular, by the cold material (at temperatures much lower than the virial temperature, see Section 1.2.3) that accumulates in the centers of the halos and can fuel the formation of stars. However, since baryons, opposite to the dark matter, are a collisional medium, additional physical effects need to be taken into account in order to understand how galaxies form in the Universe (see Section 1.3) and how they acquire their properties.

The baryonic component of each dark matter halo is predicted by cosmology to have a mass equal to a fraction of the total halo mass (equation 1.1), known as the *cosmological baryon fraction* ($f_{\text{bar}} \sim 0.16$, Planck Collaboration et al. 2020). The total mass of stars and interstellar medium (ISM) of galaxies today is, however, found to be much lower than the expected baryonic mass associated to the dark matter halo, around 20% for L^* galaxies and down to only $\sim 5\%$ or less for dwarfs or super- L^* galaxies (e.g. Behroozi et al. 2010; McGaugh et al. 2010). This deficiency leads to what is known as the *missing baryons problem*. Where exactly these baryons reside is still debated. While part of them might be outside of the dark matter halos, in the intergalactic medium (IGM), it has become evident (see Section 1.2) that a significant amount lies within the virial radius, in the circumgalactic medium. The majority of the CGM is likely formed by the inflow of the IGM towards the centers of the dark matter halos (see Section 1.3.1) and/or by outflows of gas from the central galaxies, due to processes known as *supernova* or *AGN feedback* (see Section 1.3.2). These gas

flows eventually determine the properties of the galaxies themselves and have therefore a key role in galaxy formation and evolution. The aim of this Thesis is to understand the dynamics of the CGM that surrounds different types of low-redshift galaxies and to shed light on its formation mechanisms and its fate.

1.2 Observations of the CGM

Based on the considerations of Section 1.1, we expect the halos of galaxies to be filled with gas that accounts for at least part of the missing baryons. Typically, we define the circumgalactic medium as the gas that resides outside a galaxy, but within its virial radius. In the following, we focus in particular on the observations of this gas at redshift $z < 1$, while for a brief overview of the observational evidence at higher redshift see Section 1.2.4.

In the low-redshift Universe, the CGM appears to be multiphase, a mixture of different gaseous components that we can identify based on their physical properties, mainly the temperature, and that can be observed at different wavelengths, from the X-rays to the radio band. We can in particular divide the circumgalactic medium in the following components:

- *extraplanar gas*: at $T \sim 10^4$ K, observed in emission and absorption up to distances of ~ 10 kpc from the disk of the Milky Way (MW) and nearby disk galaxies (see Section 1.2.1);
- *cool ionized gas*: at $10^4 \lesssim T < 10^5$ K, observed mainly in absorption throughout the galactic halo, up to the virial radius (Section 1.2.2);
- *warm gas*: at $10^5 \lesssim T < 10^6$ K, observed throughout the halo through absorption lines of OVI and other ions with high ionization potentials (Section 1.2.3);
- *hot gas*: at $10^6 \lesssim T \lesssim 10^7$ K, characterized by high filling factors and observed in the X-rays (Section 1.2.3).

1.2.1 Extraplanar gas

This medium has been observed in the halo of the MW and of nearby disk galaxies and is located in the inner regions of the halos, within a typical height of about 10 kpc from the disk. It therefore represents the interface between the CGM and the central galaxy. The neutral phase of the extraplanar gas has been extensively studied, through the 21-cm emission from HI, and seems to amount, on average, to about 15% of the HI mass in the disk (Sancisi et al. 2008; Marasco et al. 2019), reaching in some cases up to 30% (Oosterloo et al. 2007). This medium has a peculiar kinematics: it rotates at lower velocities with respect to the disk, showing a vertical velocity gradient of about $\sim 15 - 30 \text{ km s}^{-1} \text{ kpc}^{-1}$ (e.g. Fraternali et al. 2002; Oosterloo et al. 2007), and it also shows the presence of vertical and radial inflow motions (e.g. Marasco et al. 2019). In the Milky Way, the neutral extraplanar gas is seen in the form of clouds, with velocities

that deviate from those predicted for a rotating thin disk (Marasco & Fraternali 2011). These clouds have been historically subdivided in High Velocity Clouds (HVCs, e.g. Wakker 1991; Wakker & van Woerden 1997) and Intermediate Velocity Clouds (IVCs, e.g. Wakker 2001), with velocities that deviate from those expected, respectively, by $> 90 \text{ km s}^{-1}$ and in a range from 40 to 90 km s^{-1} . Even though inferring the distances of these clouds is difficult, the HVCs seem to be typically located within 10 kpc from the disk and the IVCs within a few kpc (Putman et al. 2012).

In nearby star-forming galaxies, the ionized extraplanar gas has been observed primarily in $\text{H}\alpha$ emission up to several kpc above the disk (e.g. Collins & Rand 2001; Rossa & Dettmar 2003), with a similar kinematics as the neutral gas (e.g. Fraternali et al. 2004; Heald et al. 2007). In the MW, this ionized medium has also been detected through $\text{H}\alpha$ emission, either as a diffuse medium within ~ 2 kpc above the disk (Reynolds 1991) or as the ionized counterpart of neutral HVCs (Putman et al. 2012). Moreover, many studies have detected this medium in absorption, using the lines in the spectra of extragalactic sources and halo stars (e.g. Shull et al. 2009; Lehner et al. 2012; Marasco et al. 2013; Bish et al. 2020). Also the ionized gas observed in absorption seems to be often associated to the HI HVCs (Lehner & Howk 2011).

The study of these gas layers is very important to understand how the central galaxies are eventually connected with the CGM and especially how they acquire the cold gas necessary to fuel their star formation (Fraternali & Tomassetti 2012). In this Thesis, however, we are interested in larger scales, from tens up to hundreds of kpc from the central galaxies, with the goal of better understanding the origin and fate of halo gas on large scales, comparable to the virial radius. In the rest of this Chapter and throughout this Thesis, we will then focus on the outer CGM.

1.2.2 Cool ionized CGM

Originally discovered by Boksenberg & Sargent (1978) and Bergeron (1986), the cool extended ionized CGM (which we refer hereafter simply as *cool CGM*) seems to be ubiquitous in galaxy halos. With the advent of instruments like the Cosmic Origin Spectrograph (COS, Froning & Green 2009), the Keck/High Resolution Echelle Spectrograph (HIRES, Vogt et al. 1994) and the MultiUnit Spectroscopic Explorer (MUSE, Bacon et al. 2010), the cool gas in the halos of galaxies has been systemically observed and studied in particular in the last decade. This medium has been found around galaxies of different types, from dwarfs and sub- L^* galaxies (e.g. Bordoloi et al. 2014) to massive luminous red galaxies (e.g. Chen et al. 2018), from starbursts and AGN (e.g. Heckman et al. 2017; Berg et al. 2018) to passive early-type galaxies (ETGs, e.g. Thom et al. 2012).

Given the low emissivity of this medium, there are to date few examples of observations in emission of the cool CGM at $z < 1$. These have been obtained either using resonant lines from the gas surrounding starburst galaxies up to a

few tens of kpc from the galactic disk (Rubin et al. 2011; Burchett et al. 2021), or through stacking analysis techniques (e.g. Zhang et al. 2016, 2018). There are also examples of more extended emission (up to ~ 100 kpc), often associated to galaxy groups and at least partially due to gas stripping from member galaxies (e.g. Epinat et al. 2018; Chen et al. 2019b; Helton et al. 2021). The majority of the current observational evidence of the cool phase of the circumgalactic gas at $z < 1$ and its connection to the host galaxy comes, instead, from absorption lines in the spectra of background sources. This type of studies can be divided into two main categories: transverse absorption-line studies (e.g. Tumlinson et al. 2013; Keeney et al. 2017), where the CGM is observed using the light of external background sources (typically quasi-stellar-objects, QSOs) that lie in projection close to the central galaxy, and ‘down-the-barrel’ observations (e.g. Martin et al. 2012; Rubin et al. 2014), where instead the cool gas is studied using the stellar light of the galaxy itself as a background source. While down-the-barrel observations can be useful in disentangling the outflow (blue-shifted lines) or inflow (red-shifted lines) motions of the gas with respect to the host galaxy (see Rubin et al. 2012, 2014), they provide almost no information on the actual intrinsic position of the absorbers, which could essentially be anywhere along the line of sight, including within the ISM of the galaxy. In this respect, transverse studies have been crucial in demonstrating that cool ionized gas can be found even at hundreds of kpc from the central galaxy (although even in this case the projected distance represents only a lower limit of the actual intrinsic distance of the absorber from the galaxy). The interpretation of this kind of data represents the main focus of this Thesis.

Transverse studies are primarily composed of surveys of multiple QSO-galaxy pairs. These can be obtained through two different approaches: one can (i) start from a sample of QSOs and search for galaxies associated with any detected absorbers (e.g. Stocke et al. 2006; Schroetter et al. 2016, 2019); (ii) select a sample of specific types of galaxies that are close in projection to background QSOs and then look in the QSO spectra for absorption signatures consistent with the redshift of the target galaxy (e.g. Chen et al. 1998, 2010a). The second approach has been extensively used in the last decade to study the properties of the CGM around galaxies of different kinds. Detections of this cool medium are, indeed, very common around low-redshift galaxies (see Tumlinson et al. 2017). Some of the most interesting results are, for example, the presence of cool enriched gas up to at least half the virial radius of dwarf galaxies (Bordoloi et al. 2014), the slightly higher equivalent widths (EW) and velocities of the cool gas around starburst and post-starburst compared to control L^* galaxies (Heckman et al. 2017), the small impact that AGN seem to have on the surrounding cool CGM (Berg et al. 2018), the possible connection between the cool gas and the amount of HI in the disk of star-forming galaxies (Borthakur et al. 2015, 2016). One of the most intriguing findings (see Section 1.5 and Chapter 2) is given by the presence of a large amount of cool gas around quiescent, massive early-type galaxies (e.g. Thom et al. 2012; Huang et al. 2016; Chen et al. 2018; Zahedy et al. 2019), with similar properties to the

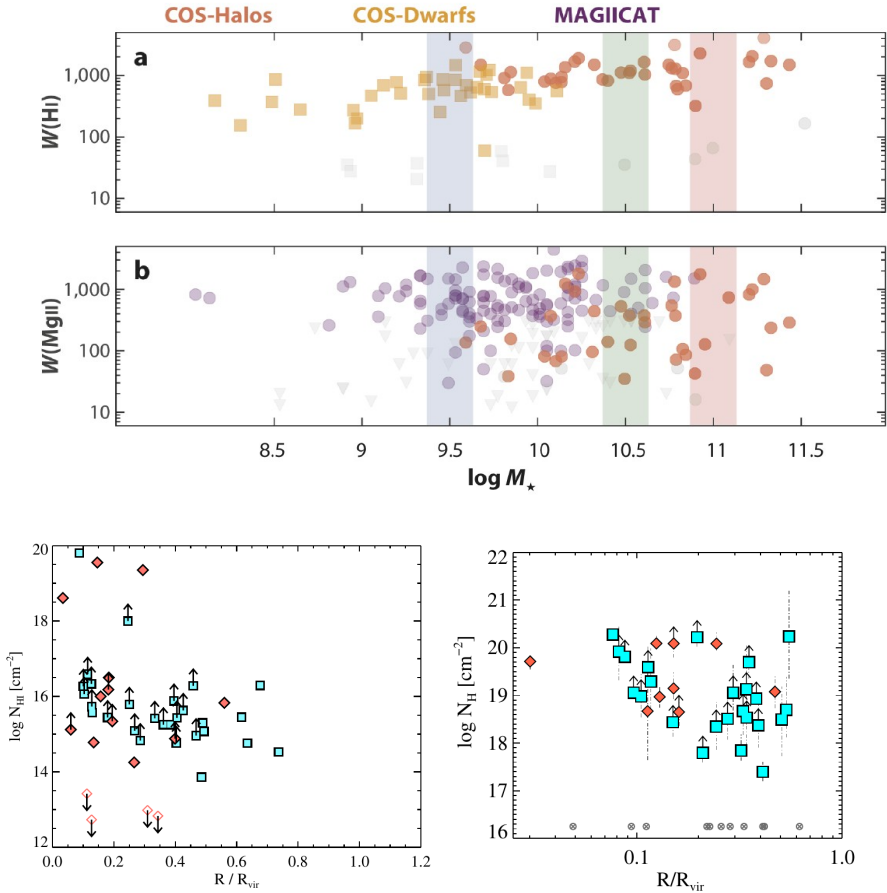


Figure 1.1: Top panels: equivalent width of neutral hydrogen (a) and MgII (b), detected in the cool CGM by the surveys of COS-Halos (Tumlinson et al. 2013, light orange), COS-Dwarfs (Bordoloi et al. 2014, bright orange) and MAGIICAT (Nielsen et al. 2016, purple), as a function of the stellar mass of the central galaxy. The three different vertical bands mark the typical stellar mass of sub- L^* (blue), L^* (green) and super- L^* (red) galaxies. From Tumlinson et al. (2017). Bottom panels: column densities of the cool CGM detected around the star-forming (cyan) and early-type (red) galaxies of the COS-Halos survey, as a function of the projected distance of the QSO sightlines from the central galaxies, normalized by the respective virial radii. Left: neutral hydrogen column densities, from Tumlinson et al. (2013); right: total hydrogen column densities, obtained using the photo-ionization model CLOUDY (Ferland et al. 2013), from Werk et al. (2014).

cool CGM of L^* star-forming galaxies (e.g. Werk et al. 2013).

A limitation of most of these surveys is that each galaxy is typically associated with only one single QSO line of sight. In order to have enough statistics, a necessary and common assumption is therefore to consider that the CGM has similar properties for different galaxies of a given type and to treat different

lines of sight as if they were piercing the CGM of a single galaxy halo. While most of the cool CGM properties (see below) have to date been inferred with this type of surveys, there are a few exceptions, where the position of the galaxy or the adopted techniques made possible to either have extended background sources, like for example galaxies (Rubin et al. 2018), gravitational arcs (Lopez et al. 2018, 2020; Tejos et al. 2021) and multiply-lensed QSOs (Chen et al. 2014), or, alternatively, multiple sightlines on a single halo (e.g. Bowen et al. 2016). This is for example the case for the cool CGM of M31, observed in absorption through more than 40 QSO sightlines (Lehner et al. 2015, 2020), whose analysis will be the focus of Chapter 4.

Properties of the cool CGM

The cool CGM is usually detected through UV absorption lines, produced either by ions with low levels of ionization (called ‘low-ions’, such as Mg II, C II, Si II, Si III), (e.g. Bowen et al. 1995; Gauthier et al. 2009; Huang et al. 2021) or by neutral hydrogen (e.g. Lanzetta et al. 1995; Tumlinson et al. 2013; Borthakur et al. 2015; Chen et al. 2018). The gas properties are derived through the analysis of these UV absorption lines: the neutral hydrogen or ion column densities (N_{HI} and N_{X} , with X being the considered ion) are estimated from the line equivalent widths (e.g. Werk et al. 2013), in the case of non-saturated lines, using the apparent optical depth method (Savage & Sembach 1991); the temperature of the cool medium ($T \sim$ a few 10^4 K) is estimated either from the linewidths, assuming that they are dominated by thermal broadening (e.g. Zahedy et al. 2019), or as a result of photo-ionization modeling (see below); the kinematics, very well determined given the high spectral resolution of instruments like COS ($\approx 15 \text{ km s}^{-1}$) and HIRES ($\approx 5 \text{ km s}^{-1}$), is generally obtained by fitting the absorption lines with Voigt profiles. In the following, we report some of the main results obtained through this analysis.

The equivalent widths and column densities of both HI and ionic species do not strongly depend on the stellar mass of the host galaxy (top panels of Figure 1.1), as the variation in EW is less than one order of magnitude across more than three orders of magnitude in stellar mass, from $\sim 10^8$ to more than $10^{11} M_{\odot}$ (see Tumlinson et al. 2017, and references therein). The cool gas is detected up to hundreds of kpc from the central galaxies (see, for example, Keeney et al. 2017). Typically, the neutral hydrogen column densities and equivalent widths show only a shallow decline with the projected distance up to the galaxy virial radius, with a steeper drop at larger impact parameters (e.g. Liang & Chen 2014; Borthakur et al. 2015). The decline can be instead more prominent for low-ions like Mg II (e.g. Chen et al. 2010b; Huang et al. 2021). Interestingly, both star-forming and passive early-type galaxies seem to host in their surrounding similar amounts of cool gas (see Figure 1.1, bottom panels).

As for the kinematics, the cool CGM appears to be (i) bound to the galaxy, given the low detected line-of-sight velocity offsets (the difference between the line centroid and the galaxy systemic velocity), lower than the escape speed¹

¹Note, however, that the observational data reported in Figure 1.2 are line-of-sight ve-

from the galactic halo; (ii) composed by multiple kinematically distinct absorbers, given that along the same line of sight the same transition is often observed at different velocities (see Figure 1.2). The picture arising from these observations is therefore of a population of clouds with a complex kinematics, that lie in the halos of galaxies, up to distances of hundreds of kpc. Interestingly, different independent studies have shown how these absorbers seem to move at a relatively low speed in the halos of massive ETGs, with a total velocity dispersion that is about half the virial velocity dispersion expected for these massive halos (see Zhu et al. 2014; Huang et al. 2016; Zahedy et al. 2019). This can also be seen in Figure 1.2, where the velocity offsets of the gas around the most massive galaxies in this sample are significantly smaller than the escape speed from their halos (Borthakur et al. 2016). A common explanation for the low velocities of the cool CGM around ETGs is attributed to the slowing effect of the drag force (see Section 1.4) exerted by the hot coronal gas (see Section 1.2.3), but, before the present work, a self-consistent treatment of this effect and in general of the cloud dynamics was lacking. Understanding this peculiar kinematics will be one of the goals of Chapter 2.

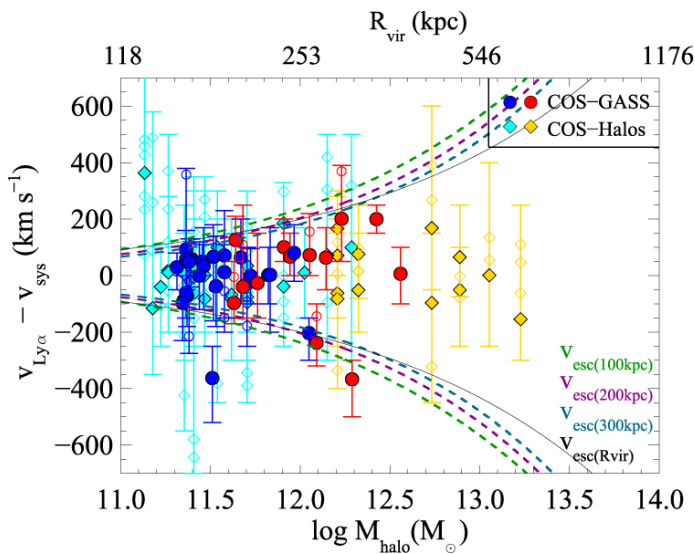


Figure 1.2: Line-of-sight velocities of HI Ly α absorbers with respect to the systemic velocities of the host galaxies, inferred by the COS-Halos and COS-GASS surveys, as a function of the galaxy halo mass and virial radius. Star-forming host galaxies are shown as blue and cyan symbols, while ETGs are depicted in red and orange. Multiple kinematic components are found in each line of sight, with the centroid of the strongest components shown as filled symbols. The curves show, for comparison, the escape speeds necessary for the clouds to leave the halos from a galactocentric distance of 100, 200, 300 kpc and from the virial radius. It is evident how most of the absorbers are bound to their host galaxy. From Borthakur et al. (2016).

locities and are not corrected for projection effects. They are therefore not directly comparable to the theoretical curves.

The cool circumgalactic gas is expected to be photo-ionized: a photon flux (Φ) likely keeps this medium in its ionized state and ensures that it will not cool below its characteristic temperature of $\sim 10^4$ K. What is the ionizing source of the cool CGM is, to some extent, still debated. Generally, it is assumed to be given by the extragalactic UV background (EUVB, e.g. Haardt & Madau 2001, 2012), but also photons coming from the galaxy could play a role (e.g. Cantalupo 2010). Given their photo-ionized state, the total density and the metallicity of the cool CGM absorbers can be inferred using photo-ionization models like CLOUDY (Ferland et al. 2013). Using the observed column densities of neutral hydrogen and metals, and assuming a photo-ionizing source, these models allow to estimate the gas metallicity Z and the ionization parameter U , through which the total (neutral+ionized) hydrogen volume and column densities (n_{H} , N_{H}) can be obtained. Being this gas mostly ionized, between neutral and total hydrogen densities there are differences of typically three orders of magnitude or more, as can be seen by comparing the two bottom panels of Figure 1.1 (see Werk et al. 2014). The total densities are, unfortunately, highly dependent on the photo-ionization models, which are subject to various assumptions and uncertainties. The cool CGM can, for instance, be modelled as a uniform layer of gas (e.g. Werk et al. 2014), or instead considering the individual kinematic components (e.g. Stocke et al. 2013; Keeney et al. 2017; Zahedy et al. 2019). Moreover, both the intensity and the spectral shape of the photo-ionizing sources are still not well constrained (e.g. Acharya & Khaire 2021). As a result, the total hydrogen densities n_{H} of the cool circumgalactic medium remain quite uncertain, with values that can change by orders of magnitudes among different studies.

From a theoretical point of view, one would expect the cool CGM clouds to be pressure confined by a surrounding hot medium in hydrostatic equilibrium

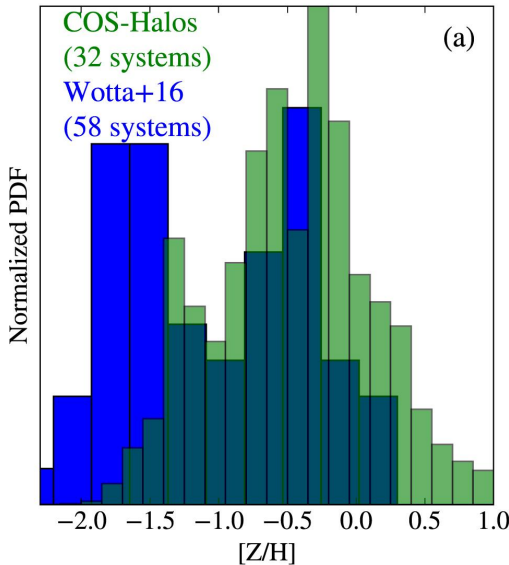


Figure 1.3: Metallicity distribution of the cool CGM inferred from the sample of the COS-Halos survey and from Wotta et al. (2016). Both surveys find large variations in the metallicities of the cool absorbers, varying from very low to almost solar values. The shapes of the two metallicity distributions are, however, very different from each other. From Prochaska et al. (2017).

with the dark matter halo (see Section 1.2.3). However, whether the inferred densities of this gas are consistent with the pressure equilibrium with a hotter gas phase is still unclear (see for example Werk et al. 2014; Zahedy et al. 2019; Voit et al. 2019). The total mass of the cool CGM, estimated from the total densities, varies, both for L^* and super- L^* galaxies, from $10^{10} M_\odot$ to almost $10^{11} M_\odot$ (e.g. Stocke et al. 2013; Werk et al. 2014; Stern et al. 2016; Prochaska et al. 2017; Zahedy et al. 2019). Despite the uncertainties, it seems that the mass of this gas phase is at least comparable to the stellar one, if not higher, therefore a significant amount of the missing baryons probably resides in the cool CGM.

As already mentioned, another fundamental property of this medium that is obtained through photo-ionization models is the gas metallicity. This is important in order to help disentangling the origin of the CGM, given that gas inflows from the IGM occur at low metallicities, while outflows from the central galaxies are expected to have metallicities close to the solar value (see Sections 1.3.1 and 1.3.2). To date, different surveys have found cool gas absorbers spanning a wide range of metallicities, from low to high values, but the exact shape of this distribution (see Figure 1.3) is still debated and is not clear whether it is unimodal (e.g. Prochaska et al. 2017) or more complex, with peaks at different metallicities (e.g. Wotta et al. 2016, 2019). Therefore, also considering the uncertainties related to the photo-ionization modeling described above, the metallicity of the cool CGM is, to date, not well constrained. We will address this problem in Chapter 4.

1.2.3 Hot and warm CGM

The hot phase of the circumgalactic medium has been initially hypothesized by Spitzer (1956) for the Milky Way, as the gas that keeps the HVCs pressure confined. Later, cosmological models (see Section 1.3.1) have predicted that the halos of galaxies of a sufficient mass should be filled with a hot diffuse medium, generally called *corona* (e.g. Fukugita & Peebles 2006), which should account for a significant fraction of the missing baryons. This gas is expected to have a temperature comparable to the galaxy *virial temperature*, defined as:

$$T_{\text{vir}} = \frac{\mu m_{\text{p}} G M_{\text{vir}}}{2 k_{\text{B}} r_{\text{vir}}}, \quad (1.2)$$

where μ is the gas mean molecular weight, m_{p} is the proton mass, G is the gravitational constant and k_{B} is the Boltzmann constant. Given the high temperatures ($T \gtrsim 10^6$ K), this medium is collisionally ionized, differently from the cool clouds described in the previous Section. The hot CGM is believed to originate mainly from IGM accretion and partly from the feedback from the central galaxy (see Sections 1.3.1 and 1.3.2) and for decades has been the most studied phase of the circumgalactic gas, through X-ray observations. Hot coronae have been observed both around elliptical (e.g. Forman et al. 1979; Mathews & Brighenti 2003; O’Sullivan et al. 2007; Bogdán & Gilfanov 2011) and massive spiral galaxies (e.g. Anderson & Bregman 2011; Dai et al. 2012; Li et al.

2018), although with a lower surface brightness than originally expected based on cosmological models (e.g. White & Frenk 1991). This hot medium has also been extensively observed in the Milky Way, mainly through free-free emission, as well as absorption and emission lines of OVII and OVIII (e.g. Gupta et al. 2012; Henley & Shelton 2013; Miller & Bregman 2013, 2015; Li et al. 2017a). In our Galaxy, there are also further constraints on the column density of this hot gas, based the rotation measure of pulsars in the Large Magellanic Cloud (see Anderson & Bregman 2010), as well as indirect evidence based on ram pressure stripping (see Section 1.3.3) from satellite galaxies (e.g. Grcevich & Putman 2009; Gatto et al. 2013; Putman et al. 2021).

Given the low surface brightness, however, the available information is still limited and the properties of galactic coronae are to date uncertain. The X-ray emission is usually detected up to 50-70 kpc from the center of the halo, with inferred densities roughly between 10^{-4} and 10^{-3} cm^{-3} (see Bregman et al. 2018, and references therein) and to infer the mass within the virial radius one necessarily needs to rely on extrapolations. The baryonic mass estimated for the hot CGM using such extrapolations is found to be comparable to the galaxy stellar mass, both for external galaxies and our Milky Way, accounting for about 10% to 50% of the missing baryons² (e.g. Anderson & Bregman 2011; Miller & Bregman 2013; Anderson et al. 2016; Li et al. 2017a; Faerman et al. 2017, 2020). The metallicity is estimated to be subsolar, with values from $0.1 Z_{\odot}$ (e.g. Bogdán et al. 2013; Hodges-Kluck & Bregman 2013) to $0.2 Z_{\odot}$ for external galaxies (Anderson et al. 2016) and up to $0.3 Z_{\odot}$ for the Milky Way (Miller & Bregman 2015), pointing towards an external origin for most of the coronal gas (see Section 1.3).

The hot CGM is usually described as a gas in hydrostatic equilibrium within the gravitational potential of the dark matter halo (e.g. Fukugita & Peebles 2006; Binney et al. 2009; Faerman et al. 2017). From theoretical arguments (e.g. Pezzulli et al. 2017), this medium is also expected to rotate, even though at a lower velocity with respect to the galactic disk (see Chapter 4 for more details). From an observational point of view, however, due to the low spectral resolution of current X-ray observations, little is known about the kinematics of galactic coronae. Evidence of rotation has been obtained for the Milky Way's hot halo by Hodges-Kluck et al. (2016), who found, using Doppler shifts of OVII absorption lines, that the preferred model to reproduce the data is given by an extended hot gaseous halo with a tangential velocity of $\approx 180 \text{ km s}^{-1}$ (with uncertainties of about 40 km s^{-1}). This is consistent with the theoretical expectations, especially in the inner regions of the halo (few tens of kpc), which probably dominate the observational signal studied by Hodges-Kluck et al. (2016).

Intermediate temperature gas, at $T \sim 10^{5-6} \text{ K}$, has also been detected in absorption in the halos of galaxies, traced by ions with ionization potentials $\gtrsim 100 \text{ eV}$, like OVI or NeVIII (see Burchett et al. 2019). In the Milky Way, OVI absorbers have been detected with a covering fraction of about 60% and seem to be related to the HVCs (Sembach et al. 2003), possibly originating at

²These estimates are dependent on the adopted metallicity.

the interface between cold gas and the hot corona (e.g. Fox et al. 2010). As for external galaxies, OVI has been observed up to 200 kpc from the center (Wakker & Savage 2009; Tumlinson et al. 2011; Prochaska et al. 2011) and recently even up to further distances in the halo of M31 (Lehner et al. 2020). Given its intermediate ionization potential, corresponding to energies where both the extragalactic background and galactic radiation fields are poorly constrained, whether the OVI is mainly collisionally ionized or photo-ionized remains an open question and it is unclear what are the exact temperature and the physical processes that may produce it (e.g. Tripp et al. 2008; Stern et al. 2016; Faerman et al. 2017; McQuinn & Werk 2018). As already mentioned, one possibility is that this gas is located at the interface between the cool clouds and the hot corona and is produced by a combination of thermal conduction and mixing (see Section 1.4), as also suggested by hydrodynamical simulations (Armillotta et al. 2017). Despite the exact physical mechanism that produces it, the origin of this possibly warm medium seems to be related to the star formation in galaxies: OVI absorption features are, indeed, more commonly observed around late-type compared to early-type galaxies (Tumlinson et al. 2011). Finally, also the kinematics of the warm CGM seems to be complex (e.g. Marasco et al. 2013; Werk et al. 2016) and is yet not well understood. In this Thesis we will primarily focus on the hot and cool phases of the CGM and we leave a proper analysis of the warm gas for future studies.

1.2.4 The CGM at higher redshifts

This Thesis focuses on the CGM around galaxies at redshift $z < 1$, whose observations have been summarized in some detail above. However, the circumgalactic medium has been extensively observed also at higher redshift, both in absorption around redshift 2-3, using similar techniques to the ones described for the low-redshift cool CGM (e.g. Rudie et al. 2012; Turner et al. 2014; Chen et al. 2020b) and in emission, mainly through the Ly α fluorescence (e.g. Cantalupo et al. 2014). In particular, thanks to the advent in the last decade of new IFU instruments like MUSE and the Palomar and Keck Cosmic Web Imagers (KCWI/PCWI), extended Ly α nebulae have been observed around galaxies and especially quasars from redshift $z \sim 2-3$ (e.g. Borisova et al. 2016; Cai et al. 2018, 2019; Arrigoni Battaia et al. 2018; O’Sullivan et al. 2020), up to $z \lesssim 6$ (see Wisotzki et al. 2016; Farina et al. 2019). From the analysis of Ly α nebulae at $z \sim 3$, Pezzulli & Cantalupo (2019) have found that, at these redshifts, a substantial part of the baryons associated with the dark matter halos ($\gtrsim 70\%$ of the cosmological fraction) are most likely residing in the CGM. These mass measurements are however still subject to uncertainties, partly due to the resonant nature of the Ly α line.

1.3 Origin of the CGM

In Section 1.2, we have seen that the halos of galaxies are filled with multiphase gas, accounting for a significant fraction of the missing baryons. In this Section, we explore the theoretical context for the formation of such a medium, especially from the point of view of cosmological hydrodynamical simulations.

1.3.1 Gas accretion into the halos

We have seen how the Λ CDM model predicts that galaxies form from the accretion of baryons into dark matter halos. The mode of accretion of baryonic matter into the halos of galaxies and the subsequent galaxy formation is highly dependent on three main timescales: the gas cooling time, the dynamical time or free fall time and the Hubble time, which is the age of the Universe. The relation of these three quantities in the context of galaxy formation and evolution has been originally discussed by Rees & Ostriker (1977) and White & Rees (1978) and revised in the last decades both with analytical models and hydrodynamical simulations (e.g. Birnboim & Dekel 2003; Kereš et al. 2009; Nelson et al. 2013; Stern et al. 2020b).

Hot and cold mode accretion

In the classical picture proposed by Rees & Ostriker (1977) and White & Rees (1978), the gas accreted from the IGM into the halo gets heated by shocks to a temperature equal to the virial temperature (see equation 1.2) and the formation of a galaxy at the center of the halo depends on the efficiency of the gas radiative losses, or *cooling*. If the cooling time is longer than the Hubble time, the gas will not cool and a galaxy will not form. Conversely, if the cooling time is short enough, a central galaxy will form as a consequence of the cooling of the hot medium. White & Frenk (1991) have then shown that, in the halo internal regions, the higher densities of the hot gas imply a shorter cooling time and therefore that galaxies might form more easily than what originally proposed by White & Rees (1978). The picture has later been revised by Birnboim & Dekel (2003), who proposed two different modes of accretion: (i) a *hot mode* accretion, with the formation of a hot ambient medium that subsequently cools to form the galaxy and that develops when the cooling time is larger than the dynamical time, but shorter than the Hubble time; (ii) a *cold mode* accretion, where the cooling time is shorter than the dynamical time and the acquired gravitational energy is immediately lost through cooling, with the gas that never gets heated to the virial temperature, accreting directly cold and forming the galaxy at the center of the halo, in line with the picture originally proposed by Binney (1977). The development of hot mode accretion is related to the mass of the dark matter halo: for $M_{\text{halo}} \lesssim 10^{12}$ the gas is not heated to the virial temperature and cold mode accretion develops. At high redshifts, $z \gtrsim 2$, galaxies of all masses are expected to be directly fed by cold accreting

gas, while at low redshift and at sufficiently high masses hot mode accretion is believed to be more common.

The demarcation between hot and cold mode accretion, in terms of halo mass and redshift, is however not necessarily as simple as in the picture outlined above. For example, using 3D idealized spherically symmetric simulations, with the inclusion of galactic feedback, Fielding et al. (2017) have shown how, even though the threshold mass between the two accretion modes does not vary significantly from the estimates of Birnboim & Dekel (2003), for low-mass galaxies the properties of the CGM are largely affected by the outflows from the central galaxy (see also Section 1.3.2). Recently, Stern et al. (2020b) used the same simulations (but without feedback) together with previously derived cooling flow solutions (Stern et al. 2019), finding that the transition between hot and cold mode also depends on the deficiency of baryons in the halos of galaxies and the effect of the central galaxy on the gravitational potential. In this model, the onset of hot-mode accretion can happen, at redshift $z = 0$, also for halos with masses lower than the threshold originally defined by Birnboim & Dekel (2003). Another complication of the classic picture is given by the expected anisotropy of the accretion. Cosmological hydrodynamical simulations have shown that accretion is in general not spherical, but rather occurs along filaments (e.g. Dekel & Birnboim 2006; Kereš et al. 2009), which can coexist with the hot halo. Whether these gas streams can penetrate the halo and directly accrete onto the galaxy (Dekel et al. 2009) or are instead destroyed by interactions with the hot gas, is however unclear and dependent on the adopted numerical scheme (e.g. Kereš et al. 2012; Nelson et al. 2013). The rather low resolution of these simulations does not allow to properly treat the interactions between cold streams and hot halo. Therefore, different authors (e.g. Mandelker et al. 2020) have recently resorted to high-resolution idealized simulations of individual cold streams, as we will discuss in Section 1.4.

Accretion of gas from the IGM into the dark matter halos can therefore give rise to both hot and cool media around galaxies, even though the predictions of the CGM properties and dynamics are uncertain. The relatively low metallicities observed in the corona and in at least part of the cool CGM (see Section 1.2) of low-redshift galaxies indicate that accretion should play an important role in the formation of this gas. This scenario will be extensively explored in Chapters 2 and 4.

1.3.2 The impact of feedback

Accretion of gas from the intergalactic medium is not the only process thought to produce the CGM. Both massive stars in star-forming galaxies exploding as supernovae (SNe) and the release of energy associated to gas accretion onto the central supermassive black holes, through processes that are respectively called *SN (or stellar)* and *AGN feedback*, can create powerful outflows, injecting significant amounts of mass and energy in the surrounding medium and potentially affecting the circumgalactic gas. Outflows have been extensively observed in

external galaxies, at different wavelengths (e.g. Martin 2005; Strickland & Heckman 2007; Rubin et al. 2014; Heckman et al. 2015; Chisholm et al. 2017) and up to at least redshift $z \sim 3$ (e.g. Steidel et al. 2010; Erb et al. 2012; Turner et al. 2015; Chen et al. 2020b). In normal star-forming galaxies, these outflows are expected to fall back onto the disk, forming what is called a *galactic fountain* (Shapiro & Field 1976; Bregman 1980; Fraternali & Binney 2006). In starburst galaxies, instead, the outflows (usually, in this case, called *galactic winds*) are more powerful and, especially at high redshift, might eject gas out of the galaxy's halo and enrich the IGM. In general, however, the spatial extent of these winds and their impact on the surrounding gas are not clear and current inferences from observations, in general, heavily rely on numerous assumptions.

From a theoretical perspective, strong outflows from the central galaxy are often invoked by cosmological models to reproduce at least some of the observed properties of galaxies. The feedback can indeed contribute to (i) reduce the accretion of gas and the subsequent star-formation, which otherwise would reach too high values, leading to galaxies with too large stellar masses; (ii) expel metals from galaxies, where the amount of observed metals has been estimated to be lower than expected (e.g. Peeples et al. 2014); (iii) expel baryons from the galactic halo, possibly solving the missing baryons problem. Recent cosmological simulations (see Somerville & Davé 2015; Naab & Ostriker 2017) have resorted to a very efficient feedback to reproduce the properties explained above. In these simulations, in addition to the cosmological accretion, a substantial part of the circumgalactic medium originates from galactic outflows, that are powered either by supernovae (e.g. Muratov et al. 2015) or by a combination of SN and AGN feedback (e.g. Oppenheimer et al. 2018; Nelson et al. 2019).

Figure 1.4 shows a cartoon representing the picture of the CGM that generally arises from the results of this kind of cosmological simulations. Outflows appear to be collimated along the axis of rotation of the disk (e.g. Nelson et al. 2019; Fielding et al. 2020b), while the direct accretion of IGM happens preferentially along the equatorial plane (Hafen et al. 2019). A substantial part of the cool gas is part of a *recycling* process, hence gas that has previously been ejected in winds and that is not able to escape the galaxy potential well, falling back towards the disk in a few Gyr (e.g. Oppenheimer et al. 2010; Ford et al. 2014; Anglés-Alcázar et al. 2017), similar to the galactic fountain scenario (see above), but on a larger scale. The picture of collimated outflows and equatorial accretion has recently been proposed to explain the observations of the cool CGM around samples of star-forming galaxies (e.g. Martin et al. 2019; Schroetter et al. 2019). In these samples, the cool absorbers seem to be preferentially distributed along the projected minor and/or major axis of the disk for highly inclined galaxies (but see, instead, Borthakur et al. 2015), suggesting a possible connection with the picture explained above. However, there seems to be no correlation between the gas metallicity and the azimuthal position of the observed medium (e.g. Péroux et al. 2016; Kacprzak et al. 2019; Pointon et al. 2019), while the proposed scenario would imply lower metallicities along the

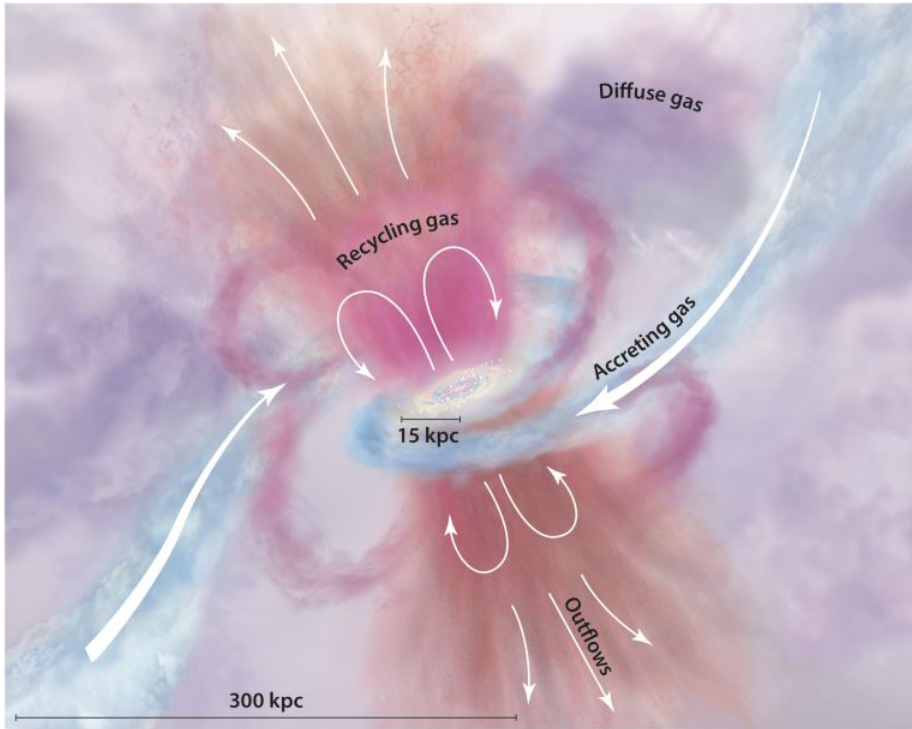


Figure 1.4: Cartoon from Tumlinson et al. (2017), representing a possible view of the CGM dynamics for a typical star-forming galaxy. Filaments of gas from the intergalactic medium are accreting along the disk plane, while feedback from the galaxy ejects material in biconical outflows along the minor axis. This gas can either escape the halo or fall back towards the central galaxy. Whether this view is representative of the real CGM is still debated and will be discussed in this Thesis.

disk's major axis. Moreover, simulations face difficulties in explaining, with outflows, observations of the cool CGM at more than 100 kpc from the galaxy (e.g. Nelson et al. 2019; Stern et al. 2020a, and see Section 1.4). The scenario highlighted in Figure 1.4 is, therefore, still controversial, since a self-consistent dynamical modeling, able to reproduce the observational constraints, is to date missing. This topic will be investigated in Chapters 3 and 4.

As for the gas accretion from the intergalactic medium, the main limitation of cosmological simulations in treating galactic feedback is the resolution. Indeed, resolving the scales of the relevant physical processes associated to star formation and AGN is currently not possible for this type of studies, even in zoom-in simulations (e.g. Hopkins et al. 2014, 2018). In order to perform cosmological simulations, one necessarily have to rely on what are called *sub-grid* models. These are numerical recipes that allow to drive the galactic outflows, circumventing the lack of resolution of the injection scales. In large-box cosmological simulations (e.g. Oppenheimer & Davé 2006; Vogelsberger et al. 2013;

Crain et al. 2015; Pillepich et al. 2018) the winds are normally described by parameters called *loading factors*, which define how much mass, energy and momentum is injected into the winds. These loading factors are calibrated ‘a posteriori’, in order to reproduce current empirical constraints and generally require values that can be orders of magnitude higher than what is found by high-resolution simulations (see Section 1.4). Given all the limitations mentioned above, the predictions of large-scale simulations, especially regarding the circumgalactic gas, are affected by several uncertainties and there is not yet a physical picture that is able to coherently explain from first principles the origin and dynamics of this medium, being at the same time in accordance with all the available observational constraints.

1.3.3 Other origin of the cool CGM

We have seen in this Section how accretion of gas from the IGM and feedback from the central galaxy can give rise to a multiphase circumgalactic medium, with gas that goes from a temperature of $\sim 10^4$ K to temperatures equal to or even higher than the virial temperature of the halo. While these are usually considered the two main mechanisms at play for the formation of the CGM, part of the cool gas can form also via other processes. The two most relevant ones are stripping of gas from satellite galaxies (e.g. Wang 1993) and the development of thermal instabilities that lead to the condensation of the hot medium.

The halos of galaxies are populated with satellite galaxies that, during their motion, might also affect the circumgalactic gas of the main galaxy. If these satellites are gas-rich, part of their interstellar medium can be lost into the surrounding medium, due to either ram pressure (the pressure due to the motion relative to the hot gas) or tidal stripping due to the tidal force from the central galaxy (e.g. Mayer et al. 2007). This gas stripping has been directly observed in the local Universe (e.g. Sancisi et al. 2008; Johnson et al. 2018; Poggianti et al. 2017; Sorgho et al. 2019), with the closest example to us given by the Magellanic Stream, originated by the interaction between the two Magellanic Clouds and the Milky Way (e.g. Brüns et al. 2005; Fox et al. 2010). From a theoretical point of view, different authors have used hydrodynamical simulations, tailored on single dwarf galaxies, to study in detail the stripping of gas from these objects (e.g. Gatto et al. 2013; Tepper-García et al. 2019). Also, in recent cosmological simulations, satellites tend to lose part of their ISM into the CGM of the host galaxy, either because it is stripped or because it is expelled through winds from the satellite galaxies (Marasco et al. 2016; Anglés-Alcázar et al. 2017; Hafen et al. 2019). What is the fraction of cool CGM that originates from this type of interactions is, however, unclear, although it likely represents only a minor fraction of the missing baryons.

Different models and simulations have also predicted that part of the cool CGM can originate from the development of thermal instabilities (e.g. Sharma et al. 2012; Thompson et al. 2016; Voit 2018), which lead the hot corona to condense locally and to create clumps of cool gas. Recently, Nelson et al. (2020)

have found that, in the TNG50 cosmological simulations, structures of cool gas in the halos of massive ETGs can form due to instabilities stimulated by density perturbations in the hot gas, possibly explaining the presence of cool CGM in these passive halos (see Section 1.2.2). However, whether these instabilities can actually develop is still debated (see Binney et al. 2009; Nipoti & Posti 2013, 2014). Compared to accretion and feedback, also this process likely represents only a minor source of the cool gas observed in the halos of galaxies.

1.4 Interactions between the CGM phases

As we have seen in Section 1.2, the CGM is a multiphase gas and to infer its properties it is very important to understand how its different phases interact with each other. To date, both cosmological and idealized halo-scale simulations have insufficient resolution, at best of the order of one kpc, to resolve the cool CGM structures (e.g. van de Voort et al. 2019; Peebles et al. 2019) and to investigate how these interact with the hot surrounding medium. The hot medium can influence the cool gas in different ways. In particular, it can accelerate or decelerate cool material embedded in it, by exerting a *drag force* (e.g. Fraternali & Binney 2008); it can disrupt the cool clumps through hydrodynamical effects like Kelvin-Helmholtz (KH) and Rayleigh-Taylor instabilities or thermal conduction (the transfer of heat between two gas phases with strong temperature gradients, Spitzer 1962); it can condense, increasing the mass of the cool medium. All these effects have been studied extensively in the last decade by utilizing simulations with a pc-scale resolution, whose main results are summarized below.

Regarding the accretion of cool gas from the IGM, useful insight on the survival of the cool streams (see Section 1.3.1) have been obtained by a recent series of high-resolution idealized simulations of filamentary structures of cool gas, embedded in a hot medium (e.g. Mandelker et al. 2016; Padnos et al. 2018; Vossberg et al. 2019; Mandelker et al. 2020). These studies have shown that, without radiative losses, KH instability can be efficient in disrupting the streams before they reach the central galaxy. With the inclusion of cooling, however, the interaction between the stream and the corona might lead to the condensation of the hot gas: indeed, the layer of gas at the interface between the two phases has intermediate temperatures and therefore short cooling times. This implies that this gas will cool rapidly and the stream will increase its mass (see also below), instead of being ablated into the hot environment (see Figure 1.5).

In the context of SN feedback, high-resolution simulations are focused on a local patch of the galactic disk (or on the entire disk in the case of Schneider et al. 2020), up to a few kpc above it. Here, the physics of the ISM and the first stages of the evolution of the SN remnants are resolved (e.g. Gatto et al. 2017; Fielding et al. 2018; Kim & Ostriker 2018; Kim et al. 2020; Armillotta et al. 2019), contrary to large-scale simulations. From the results of this type of high-resolution simulations, it seems that most of the mass of the outflows should reside in the cool gas phase, while most of the energy is transferred to

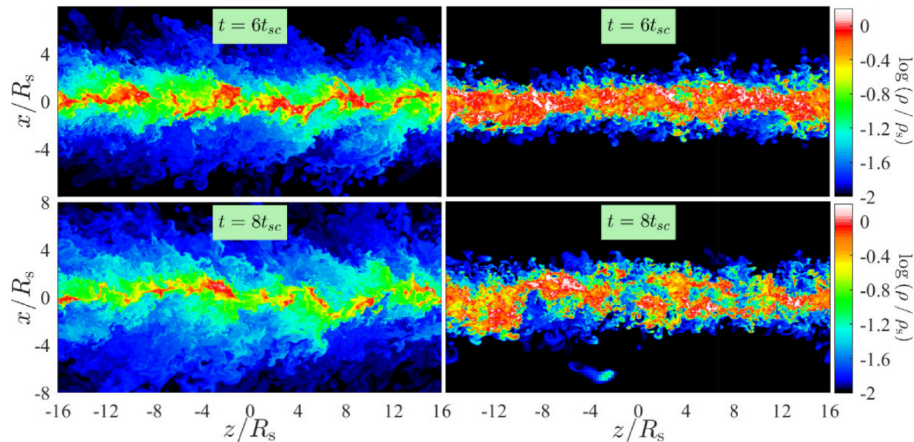


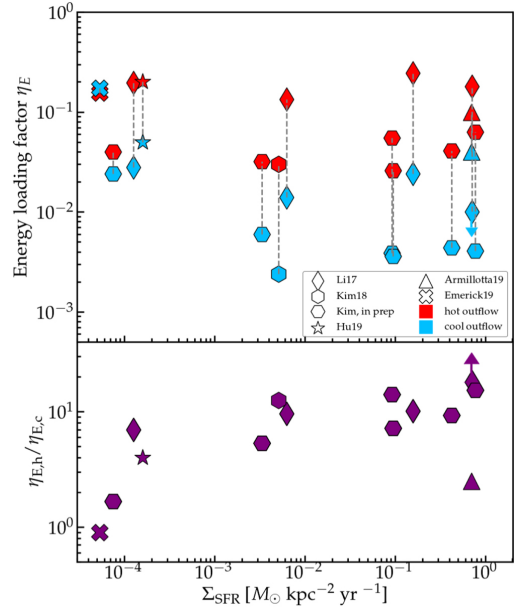
Figure 1.5: Results of the high resolution simulations of a cold gas stream of Mandelker et al. (2020), without (left) and with (right) radiative cooling. The snapshots show the evolution of the density normalized by the initial stream density, at different times (calculated in units of the stream sound crossing time). In the late stages of its evolution, we can see how, with the inclusion of radiative cooling, there is still a substantial amount of cool, high density gas in the stream, due to the condensation of the mixed gas.

the hot winds (see Figure 1.6 and Li & Bryan 2020, with references therein), which presumably can reach larger galactocentric distances. These fast winds tend to accelerate the cool gas, which can be *entrained* and pushed outward by the drag force acted by the hot phase (see Schneider et al. 2020). These simulations also show how the cool gas seems, however, not able to reach large distances and its plausible fate is to fall back to the disk (Kim & Ostriker 2018), as in the galactic fountain scenario (see above).

Another type of high-resolution simulations investigates, instead, the interactions between a single cloud of cool (10^4 K) CGM and the surrounding hot gas. Generally, these studies are focused on the inner regions ($\lesssim 10$ kpc from the galactic disk) of the halo (although see Armillotta et al. 2017) and follow different types of systems: the infall of HVCs towards the disk (e.g. Heitsch & Putman 2009; Grønnow et al. 2018); galactic fountain clouds (Marinacci et al. 2010b; Armillotta et al. 2016); or cool clouds embedded in hot SN outflows (Scannapieco & Brügger 2015; Brügger & Scannapieco 2016; Gronke & Oh 2018).

These simulations have shown that, in addition to the hot gas drag force that slows down the cloud (e.g. Marinacci et al. 2011), the evolution and the survival of the cool gas depend primarily on KH instability, thermal conduction, radiative cooling and magnetic field (and, to a lower extent, self-gravity, see for example Li et al. 2020). The KH instability tends to strip gas from the cloud and to create a region of mixed medium at temperatures lower than the original hot gas. Depending on the initial conditions of the system (like

Figure 1.6: Energy loading factors as a function of the star formation rate density of the disk, for hot (red) and cool (blue) outflows in a series of small-box simulations, all with a resolution of a parsec in length, or $10 M_{\odot}$ in mass, and therefore capable to resolve the evolution of individual SN remnants (Li et al. 2017b; Kim & Ostriker 2018; Kim et al. 2020; Hu 2019; Armillotta et al. 2019; Emerick et al. 2019). Most of the energy of the outflowing gas is in the hot phase, as can be also seen in the bottom panel, which shows the ratio between hot and cool gas energy loading factors, going from 0.9 to 20. From Li & Bryan (2020).



the metallicity of the two gas phases, the initial cloud velocity and size, the temperature and density of the hot environment), the stripping can lead to the complete destruction of the cloud (e.g. Heitsch & Putman 2009; Schneider & Robertson 2017) or to the rapid cooling of the intermediate temperature gas at the interface between the cool and hot gas phases and therefore to the condensation of the hot gas, increasing the mass of the cool cloud (e.g. Marinacci et al. 2010b; Armillotta et al. 2016; Gronke & Oh 2018). Both thermal conduction and magnetic fields tend to suppress the formation of the KH instability and might therefore increase the survival time of the cloud. At the same time, thermal conduction may also lead to a faster evaporation of the cloud (e.g. Brüggén & Scannapieco 2016). Its efficiency is also dependent on the magnetic field, given that the electrons, which are responsible for the transfer of heat, tend to follow the magnetic field lines. Simulations with either thermal conduction (e.g. Armillotta et al. 2016, 2017), magnetic field (e.g. Grønnow et al. 2018) or both (e.g. Kooij et al. 2021), have shown how, even in the presence of these effects, the interactions between cloud and hot gas can lead to the condensation of the corona and therefore to the increase of the cool gas mass, although most of these studies have explored densities typical of small distances (a few kpc) from the galactic disk and the final outcome at larger distances is less well understood (see Armillotta et al. 2017).

The interactions between the different phases of the CGM are, therefore, extremely complex and most of these processes cannot be traced by the large-scale simulations described in Section 1.3. However, at a pc-scale resolution, necessary to resolve these interactions, only small regions of the galactic halos can be studied and a global picture is therefore still missing.

1.5 Open questions

From Sections 1.2, 1.3 and 1.4, we have seen that, both from an observational and a theoretical point of view, the circumgalactic gas is a very complex system. This medium is composed by various gas phases that are observed at different wavelengths and seem to originate from a variety of processes, encompassing scales that go from the size of the entire galaxy halo to sub-pc scales. In this Section, we summarize the main open questions about this medium that this Thesis aims to address, focusing in particular on the cool ionized circumgalactic gas at $T \sim 10^4$ K, around galaxies at redshift $z < 1$.

- 1. What are the physical properties of the cool CGM?** From current observational studies (see Section 1.2.2), especially due to the limitations of photo-ionization models, the total mass and metallicity of the cool CGM are still very uncertain. Moreover, given the nature of the majority of the observational surveys, which are in absorption and with only a QSO line of sight per galaxy, the intrinsic location of the cool CGM and the intrinsic dynamics of the absorbing clouds are not known.
- 2. What is the role of the hot corona on the survival and dynamics of the cool gas?** The cool CGM is likely influenced by the presence of the hot gas (see Section 1.2.3). In Section 1.4 we have seen, in particular, how the survival of the cool clouds is strongly related to the hydrodynamical interactions with the corona. Moreover, the cloud dynamics is also affected by the hot surrounding medium, which tends to slow down the cool gas through the drag force. However, what is the impact of these effects on the global properties and the dynamics of the cool CGM is yet not well understood.
- 3. Is there a connection between the cool CGM and the central galaxy's star-formation?** Cool gas is found around galaxies with very different levels of star formation, from passive ETGs (e.g. Thom et al. 2012) to starburst galaxies (Heckman et al. 2017). Yet, some of the properties of the cool CGM are similar between star-forming and passive galaxies (e.g. Tumlinson et al. 2013; Keeney et al. 2017; Chen et al. 2018, and see Section 1.2.2), with only slight differences in the gas observed around starbursts (Heckman et al. 2017). Is the cool CGM connected to the star-formation? Is it brought to large galactic distances by strong SN-driven outflows? Is it fueling the central galaxy with newly accreting gas?
- 4. What is the origin of the cool gas around galaxies?** In Section 1.3, we have summarized the current possible formation mechanisms proposed for the cool CGM. At the moment, there is no consensus on which process (IGM accretion, feedback, satellite stripping) is the most relevant for the formation of this gas, both around star-forming and early-type galaxies. In particular, the presence of cool (10^4 K) gas in the halos of massive ETGs, along with its peculiar kinematics (see Section 1.2.2), still represents a puzzle.

5. **What is the fate of the cool CGM?** The cool CGM represents a huge reservoir of gas that can fuel the host galaxies and there are hints that this medium might accrete directly onto the galactic disks, potentially feeding the galaxy star-formation (e.g. Borthakur et al. 2015; Ho et al. 2017). Understanding what is the fate of the cool gas is however not trivial, since the survival of this medium depends on many different physical processes (see Section 1.4). If the whole amount of the cool CGM was accreting into the center, galaxies in the local Universe would have much higher star formation rates than we currently observe. Particularly puzzling is the fate of the cool gas in the halos of massive early-type galaxies (see Section 1.2.2), where this medium would be expected to fuel the star-formation of galaxies that are instead passive, or forming stars at a very low rate.

1.6 This Thesis

The goal of this Thesis is to tackle the questions outlined in Section 1.5. In order to do this, we make use, in Chapters 2, 3 and 4, of semi-analytic parametric models, which we compare to different sets of data in order to find, through a Bayesian analysis, the best physical parameters of the CGM that can reproduce the observations. As we have seen in Section 1.3, cosmological simulations, because of the low resolution, cannot accurately reproduce many properties of the cool CGM, including its dynamics. Ideally, one would like to simulate the entire galaxy halo with a pc-scale resolution, in order to trace the interactions between the different gas phases (see Section 1.4), but that is currently not feasible. By using a semi-analytical approach, despite some limitations, we can instead describe the motion and properties of the cool clouds throughout the galaxy halo, considering at the same time the gravitational force and hydrodynamical effects, including pressure confinement, the drag force and the evaporation into the hot corona. Our modeling allows us to estimate previously unknown physical parameters of the CGM, by directly comparing our theoretical predictions with the observational data. In Chapter 5, we finally complement the semi-analytic treatment with high-resolution idealized simulations, which are very useful to properly study the survival and fate of the cool gas.

More specifically, in Chapter 2, we address the puzzle related to the cool CGM observed around massive ETGs. In particular, we investigate whether a model of cosmological gas accretion can consistently explain the observed properties of the cool CGM absorbers around ETGs, with a special focus on their unexpectedly large covering factor and peculiar kinematics.

In Chapter 3, we study the impact of SN feedback on the cool CGM of star forming galaxies and explore whether energetically feasible winds are able to explain the majority of the cool CGM around this type of galaxies.

In Chapter 4, we move to the case of M31, whose cool CGM has been recently characterized in detail by the project AMIGA (Lehner et al. 2015, 2020), and we investigate whether these observational data can be better reproduced by

models of either galactic winds or accretion of gas from the IGM.

In Chapter 5, we analyze, using idealized hydrodynamical simulations, the fate of the cool CGM clouds around M31 (and similar star-forming galaxies), to understand whether the cool gas is able to reach the central galaxy and feed its star formation.

Finally, in Chapter 6, we summarize our results, we draw our main conclusions and we discuss some of the possible future perspectives.

Chapter 2

Cool circumgalactic gas of passive galaxies from cosmological inflow

based on

– A. Afruni, F. Fraternali & G. Pezzulli, 2019 –

Published in *Astronomy and Astrophysics*, A&A 625, A11

Abstract

2

The circumgalactic medium (CGM) of galaxies consists of a multi-phase gas with components at very different temperatures, from 10^4 K to 10^7 K. One of the greatest puzzles about this medium is the presence of a large amount of low-temperature ($T \sim 10^4$ K) gas around quiescent early-type galaxies (ETGs). Using semi-analytical parametric models, we describe the cool CGM around massive, low-redshift ETGs as the cosmological accretion of gas into their dark matter halos, resulting in an inflow of clouds from the external parts of the halos to the central galaxies. We compare our predictions with the observations of the COS-LRG collaboration. We find that inflow models can successfully reproduce the observed kinematics, the number of absorbers and the column densities of the cool gas. Our MCMC fit returns masses of the cool clouds of about $10^5 M_\odot$ and shows that they must evaporate during their journey due to hydrodynamic interactions with the hot gas. We conclude that the cool gas present in the halos of ETGs likely cannot reach the central regions and feed the galaxy star formation, thus explaining why these passive objects are no longer forming stars.

2.1 Introduction

Characterizing the circumgalactic medium (CGM) and understanding its role in galaxy evolution is a key goal of current astrophysical models. Usually defined as the gas between the central galaxy and the surrounding intergalactic medium (IGM), this multi-phase medium has been observed for decades both in emission and absorption from the X-rays (e.g. Anderson et al. 2013; Li et al. 2017a, 2018) to the UV-optical bands (Bordoloi et al. 2011; Keeney et al. 2013; Kacprzak et al. 2014; Borthakur et al. 2015) and seems to flow both inward and outward in the halos of galaxies. However, despite the great observational effort and the significant improvement of large-scale hydrodynamical simulations (van de Voort & Schaye 2012; Ford et al. 2014; Suresh et al. 2015; Nelson et al. 2019), the nature, origin and fate of this elusive medium are still much debated. For a long time the most studied phase has been the hot CGM, also called the galaxy corona, with temperatures of $T \sim 10^{6-7}$ K, predicted decades ago by classical cosmological models (e.g. White & Rees 1978; White & Frenk 1991, but see also Binney 2004) as gas heated by shocks to the galaxy virial temperature. Although the observed luminosities are lower than predicted, hot gas in galaxy halos has been observed through X-ray observations both around early-type (Forman et al. 1979; Jones et al. 2002; Mathews & Brighenti 2003; Bogdán & Gilfanov 2011) and late-type galaxies (e.g. Dai et al. 2012; Li et al. 2017a). The total amount of mass in this hot gas phase is however still uncertain (e.g. Anderson & Bregman 2011; Bogdán et al. 2013; Li et al. 2018).

Recently, a number of investigations (Stocke et al. 2006; Rudie et al. 2012; Werk et al. 2013; Tumlinson et al. 2013) have also focused on the cooler ($T < 10^5$ K), low-density, ionized gas in the galaxy halos, originally discovered by Boksenberg & Sargent (1978) and Bergeron (1986) and observed using UV and optical absorption lines in the spectra of background quasi-stellar objects (QSOs). The presence of this cool gas seems ubiquitous around both external galaxies and the Milky Way, with high covering fractions (e.g. Shull et al. 2009; Lehner & Howk 2011; Werk et al. 2014; Borthakur et al. 2016) and potentially large masses (Werk et al. 2014; Stocke et al. 2013; Stern et al. 2016). Understanding this cool medium is crucial in the study of galaxy evolution and in solving the galaxy missing baryons problem (e.g. McGaugh et al. 2010). So far our knowledge of this medium is largely limited and the general picture is still unclear, especially regarding its origin and dynamics. For star-forming galaxies, both transverse absorption-line studies and down-the-barrel observations of inflows (e.g. Rubin et al. 2012; Lehner et al. 2013; Bouché et al. 2013; Borthakur et al. 2015) and outflows (e.g. Rubin et al. 2014) suggest that the observed CGM dynamics is consistent with the recycling scenario (e.g. Ford et al. 2014) in which the galaxy central enriched outflows are not able to escape from the potential well and then fall down again onto the galaxy. In this picture, the CGM is formed by a continuous cycle throughout the halo similar to the galactic fountain scenario proposed for smaller, galactic scales (Shapiro & Field 1976; Bregman 1980; Fraternali & Binney 2006). We discuss this further in Chapters 3 and 4.

The situation becomes however more complicated for passive early-type galaxies (ETGs). Cool ionized gas is in fact also observed in the CGM of passive massive galaxies, through observations of MgII (Gauthier et al. 2009; Huang et al. 2016), HI and other low-ion absorption lines (Thom et al. 2012; Chen et al. 2018). The presence of cool-enriched gas around quiescent galaxies remains a puzzle. In fact, in the recycling scenario described above, a fundamental role is played by the central galaxy star formation, which causes the outflows thus starting the entire cycle. However, it is not clear how we can explain the presence of cool gas in the halos of galaxies with little or no ongoing star formation. The mechanisms that can produce the cool gas and prevent it from fueling star formation in the central passive galaxy are also unclear. The main goal of this work is to address these questions.

To this purpose, we use the observations of the COS-LRG collaboration (Chen et al. 2018; Zahedy et al. 2019) who, using the Cosmic Origin Spectrograph (COS, Froning & Green 2009) on the Hubble Space Telescope (HST), has detected a large amount of cool CGM in the halos of 16 luminous red galaxies (LRGs), massive elliptical galaxies at $z \sim 0.5$, where in principle cool gas is not expected to exist. These observations confirmed that the cool CGM is not homogeneous, but composed of different absorbing clouds, with different velocities, all bound to the central galaxies, a property of this medium that was already well known from previous absorption-line studies (e.g. COS-Halos survey, see Werk et al. 2013, 2014; Tumlinson et al. 2013). Our purpose is to model the observed cool gas kinematics. Due to the absence of strong outflows in these galaxies, we assume that the cool CGM clouds are infalling toward the central galaxies.

As we will discuss in detail (Section 2.3), the dynamics of the CGM – and in particular the interactions between its different phases – depends on a number of physical processes acting on both very large and very small physical scales. Ideally one would like to model the entire CGM with large-volume high-resolution hydrodynamical simulations. Unfortunately, this is still far out of the current computational capabilities: in fact, even the current ‘zoom-in’ simulations (e.g. Grand et al. 2017; Fattahi et al. 2016), which can trace a single galaxy halo, do not have enough resolution to resolve the small-scale CGM interactions (Armillotta et al. 2017). We therefore adopt a semi-analytical modelling, keeping track of the gravitational force which dominates the dynamics on large scales, as well as taking into account prescriptions on hydrodynamical processes from small-scale high resolution simulations (e.g. Heitsch & Putman 2009; McCourt et al. 2015; Armillotta et al. 2016; Grønnow et al. 2018).

This Chapter is organized as follows: in Section 2.2 we briefly describe the COS-LRG observations, their characteristics and the main observables that we use as a comparison for our models; in Sections 2.3 and 2.4 we describe the construction of the model and the comparison with observations; in Section 2.5 we present our results while in Section 2.6 we discuss the implications of our findings for the properties, origin and fate of the cool CGM around massive ETGs; finally, Section 2.7 contains the summary and the conclusions of the

work.

2.2 ETG sample and observational constraints

2

In this Chapter, we focus on the data of the COS-LRG program. Here we briefly describe the main characteristics of these observations, while we refer, for further information and details, to the COS-LRG papers (Chen et al. 2018; Zahedy et al. 2019). This survey provides high-resolution kinematic data of the cool CGM around 16 massive early-type galaxies and it is therefore the most suitable for the purpose of this work, which aims to reproduce in particular the kinematics of the cool CGM clouds around passive galaxies. We assume that, due to the similarity of the objects in this sample, the CGM has the same behavior and properties in all these galaxy halos, apart from some scaling factors due to the slightly different halo masses and virial radii, which we will account for in our model. The main properties of the galaxies in the sample are reported in Table 2.1.

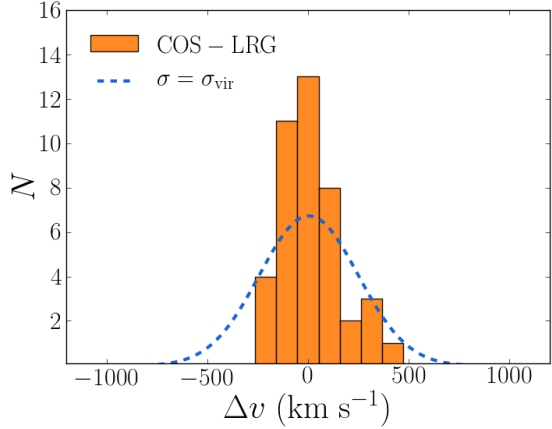
The CGM is characterized using HI and metal absorption lines in the COS and optical echelle spectra of UV-bright QSOs with impact parameters (the projected distances between the QSOs and the galaxies) $R < 160$ kpc. A typical feature of these observations is the presence, for each line of sight, of different velocity components for the same ionic transition, characteristic of a medium that is not uniform, but composed of different clouds with different projected velocities, plausibly different intrinsic positions along the line of sight and possibly different physical properties (e.g. density or ionized fraction). This is studied in Chen et al. (2018) and Zahedy et al. (2019) fitting Voigt profiles and obtaining the velocity offsets Δv of the single components from the galaxy systemic velocity. In this Chapter we use, in particular, the analysis carried out by Zahedy et al. (2019), who fitted the Voigt profiles imposing the same kinematic structure among HI, low-ionization and intermediate-ionization species (including MgII, SiII, SiIII and CIII). This choice is justified by the kinematic agreement found by Chen et al. (2018) in the absorption profiles of these different species. Each velocity component found by Zahedy et al. (2019) represents a single cloud: they find 42 clouds among all the galaxies (including three sight-lines with no detections of absorption lines), with an average of 2.6 clouds per line of sight. In Figure 2.1 we report all the 42 observed cool cloud velocities (Δv , relative to the galaxy systemic velocity) together in one single distribution. The two main observational constraints that we used for the comparison with our model results are then given by:

1. the cloud velocity distribution;
2. the total number of observed clouds.

Due to the high resolution of the COS spectra, these kinematic data are very accurate. Zahedy et al. (2019) also performed a photo-ionization analysis for each kinematic component, using the code CLOUDY v13.03 (Ferland et al.

2013). This analysis allowed them to estimate the values of the total-hydrogen column densities N_{H} for each line of sight (reported in Table 2.1). Differently from the very accurate and reliable kinematic data, these values are however subject to various model-dependent uncertainties and therefore we do not use them as an observational constraint for our model fitting. We will discuss in Section 2.5 the comparison between these data and our final results.

Figure 2.1: In orange, observed velocities of the cool CGM clouds relative to systemic velocities of the galaxies, obtained using the COS-LRG data for a sample of 16 massive passive galaxies (their properties are reported in Table 2.1). The light-blue dashed line is a gaussian with a dispersion equal to the typical 1D (line-of-sight) virial velocity dispersion value in the sample.



For the purpose of this work, we are interested in the virial masses and virial radii of the galaxies in the COS-LRG sample, which allow us to calculate the halo virial temperatures. To calculate these quantities we first obtained M_{200} using the stellar-to-halo mass relation (SHMR) of Kravtsov et al. (2018). We note that at these high stellar masses the slope of the SHMR is uncertain and the galaxy halo masses could be higher using different prescriptions (e.g. Moster et al. 2013). However, the relation from Kravtsov et al. (2018), obtained with a recent stellar mass function based on improved photometry, is in agreement with estimates based on X-ray observations, weak lensing and satellite kinematics for objects with these high masses. Thus we consider this prescription the most reliable for the massive galaxies of our sample. Once we obtained the values of M_{200} , we calculated r_{200} through the formula

$$r_{200} = \left(\frac{M_{200} 2G}{200H^2} \right)^{1/3}, \quad (2.1)$$

where H is the Hubble parameter (we assume $H_0 = 70 \text{ km s}^{-1} \text{ Mpc}^{-1}$) for the standard cosmological model ($\Omega_{\text{m},0} = 0.3$, $\Omega_{\Lambda,0} = 0.7$). Using these values, we calculated the virial masses M_{vir} and radii r_{vir} extrapolating for each halo the dark matter (DM) profile (we assumed a Navarro Frenk White profile, see Section 2.3.1) to the radius corresponding to the virial overdensity, which is Δ times the critical density of the universe, with Δ calculated using the prescription in Bryan & Norman (1998) ($\Delta = 119 - 141$ in our case, depending on the redshift of each galaxy).

(1)	(2)	(3)	(4)	(5)	(6)	(7)	(8)	(9)
Galaxy ID	z	$\log(M_*/M_\odot)$	$\log(M_{\text{vir}}/M_\odot)$	r_{vir} (kpc)	T_{vir} (10^6 K)	R (kpc)	n_{cl}	$\log(N_{\text{H}}/\text{cm}^{-2})$
J094632.40+512335.9	0.41	11.2	13.0	427	3.3	42	5	19.5
J140625.97+250923.2	0.40	11.1	12.9	397	2.8	47	5	19.2
J111132.33+554712.8	0.46	11.4	13.4	564	6.3	77	3	19.2
J080357.74+433309.9	0.25	11.1	12.9	433	2.6	78	4	18.6
J092554.18+400353.4	0.25	11.1	12.9	435	2.6	84	1	19.9
J095000.86+483102.2	0.21	11.0	12.7	381	1.9	94	4	19.7
J112755.83+115438.3	0.42	11.2	12.9	423	3.3	99	2	17.7
J124307.36+353926.3	0.39	11.3	13.2	504	4.4	102	-	-
J155047.70+400122.6	0.31	11.2	13.0	452	3.1	107	4	18.9
J024651.20-005914.1	0.41	11.4	13.4	581	6.1	109	6	19.2
J135727.27+043603.3	0.33	11.3	13.2	522	4.3	126	1	19.0
J091027.70+101357.2	0.26	11.2	13.0	465	3.1	140	4	18.5
J141307.39+091956.7	0.36	11.7	14.1	1028	17.6	149	-	-
J155304.32+354853.9	0.47	11.0	12.6	326	2.1	156	2	17.8
J125859.98+413128.2	0.28	11.6	13.8	855	10.7	159	-	-
J124409.17+172111.9	0.56	11.5	13.5	623	8.9	160	3	18.2

Table 2.1: Properties of the galaxies in our sample. (1) Galaxy name; (2) galaxy redshift; (3) galaxy stellar mass; (4) galaxy virial mass, calculated using the relation of Kravtsov et al. (2018) as explained in Section 2.2; (5) virial radius, see Section 2.2; (6) virial temperature (equation 2.2); (7) projected distance between the line of sight and the galaxy; (8) number of observed clouds; (9) total hydrogen column density. All the data are taken from Chen et al. (2018); Zahedy et al. (2019).

Finally, the virial temperature is given by

$$T_{\text{vir}} = \frac{\mu m_{\text{p}} G M_{\text{vir}}}{2 k_{\text{B}} r_{\text{vir}}}, \quad (2.2)$$

where $\mu = 0.6$ is the mean molecular weight for a hot, totally ionized gas (Sutherland & Dopita 1993), m_{p} is the proton mass, and k_{B} is the Boltzmann constant. Our estimates of these virial quantities for each galaxy are reported in Table 2.1. As explained above, the kinematic distribution in Figure 2.1 is our main constraint and our purpose is to create theoretical models that are able to reproduce a similar distribution, with a comparable shape and a comparable number of clouds. It is interesting to note from Figure 2.1 that the clouds show an unexpected narrow distribution (small Δv). Indeed, the line-of-sight virial velocity dispersion for a galaxy halo with a mass equal to the mean value of the virial masses of our sample ($M_{\text{vir}} = 10^{13.3} M_{\odot}$) is equal to 245 km s^{-1} , while the velocity dispersion of the distribution in Figure 2.1 is equal to only 147 km s^{-1} . If the cloud motion were related only to the dynamical mass of the galaxies we would expect the clouds to have a dispersion comparable to the virial one. The small observed velocity dispersion, instead, suggests that there should be some mechanism that slows down these absorbers during their motion throughout the halos (see also Huang et al. 2016) and this is a fundamental observational feature that our models aim to reproduce.

It is particularly important to compare our model results not only with the cloud velocities, but also with the number of observed clouds, because with this additional constraint we have more information on the total mass accretion rate and cloud masses that are needed to successfully reproduce the observations (see Section 2.3), breaking the degeneracy between different infall models. One limitation of these data is that they only contain observations at relatively small projected radii: we have information only for $R < 160 \text{ kpc}$, which is much smaller than the virial radii of these massive galaxies. The average virial radius of these halos is indeed 526 kpc . We discuss the comparison between our results and other observations at larger distances later in Section 2.6.

2.3 The model

In this Section we describe how we built our dynamical models, starting from the idea that the cool CGM is composed of different clouds (see Sections 2.1 and 2.2), which originate from the cosmological accretion of gas into the galaxy halos and are infalling toward the central galaxies. We first describe, in Sections 2.3.1 and 2.3.2, how we calculated the infall velocities of the clouds for each of the sixteen galaxies of our sample; then in Section 2.3.3 we focus on the total accretion rate of cool gas inside our model halos.

2.3.1 Purely ballistic model

The main force that drives the motion of the cool clouds is the gravitational force of the dark matter halo. Gravity forces the cool medium to accrete toward

the central galaxies. If we considered only this force, the equation of motion would be:

$$\frac{dv}{dr} = \frac{1}{v(r)} \frac{GM(r)}{r^2}, \quad (2.3)$$

where v is the radial velocity, $M(r)$ is the DM mass within the radius r . Throughout this Chapter, we consider the velocity v with a positive sign if it is pointing toward the center of the potential well.

We have assumed in our treatment a Navarro Frenk White (NFW) profile (Navarro et al. 1995), whose mass is described by

$$M(r) = 4\pi\rho_0 r_s^3 \left[\ln(1+r/r_s) - \frac{r/r_s}{1+r/r_s} \right], \quad (2.4)$$

where

$$\rho_0 = \frac{M_{\text{vir}}}{4\pi r_s^3 \left[\ln(1+r_{\text{vir}}/r_s) - \frac{r_{\text{vir}}/r_s}{1+r_{\text{vir}}/r_s} \right]} \quad (2.5)$$

is the central density, M_{vir} and r_{vir} are the virial masses and radii reported in Table 2.1, and $r_s = r_{\text{vir}}/c$ is the scale radius, where c is the concentration calculated for each halo following Dutton & Macciò (2014).

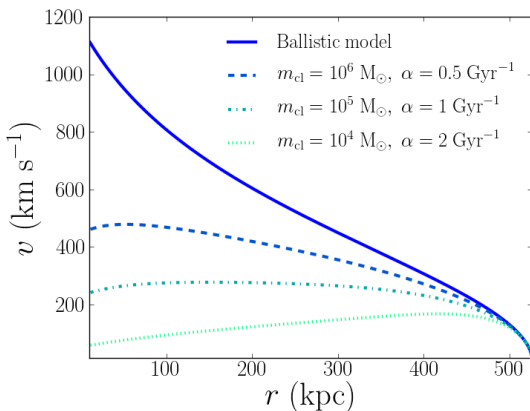


Figure 2.2: Velocity profiles of the cool CGM clouds obtained using the ballistic model (equation 2.3, blue line) and the final model that includes all the hydrodynamical interactions (equation 2.12), with three different choices of $m_{\text{cl,start}}$ and α .

By solving equation (2.3) for a characteristic galaxy of our sample ($M_{\text{vir}} = 10^{13.3} M_{\odot}$ and $r_{\text{vir}} = 526$ kpc, obtained averaging the values of the 16 galaxies in Table 2.1), assuming that the clouds start to fall with $v = 0$ km s⁻¹ from the virial radius, we can obtain the velocity profile shown as a blue line in Figure 2.2. Considering only the gravitational force would lead all the clouds to accrete onto the central galaxies with velocities higher than 1000 km s⁻¹ and this prediction is totally inconsistent with the low velocities observed by COS-LRG (see Figure 2.1). We conclude that a simple ballistic infall is excluded by the observations and we move to more accurate models. As explained in Section 2.1, the CGM is a multi-phase gas and the cool gas clouds must be surrounded by

a hotter medium (corona) that influences their motion. Therefore, to describe the kinematics of the clouds we need, in addition to the gravitational force, to introduce in our model also hydrodynamical effects.

2

2.3.2 Hydrodynamical effects

To simulate the interactions between the cool clouds and the hot coronal gas, we decided to use an analytical parametrization of the hydrodynamical effects that take place in the CGM. Using an analytic treatment has several advantages, including computational speed, flexibility and physical insight.

First, we defined, for each galaxy of the sample, the corona as a gas at the virial temperature (2.2), in hydrostatic equilibrium with the dark matter halo (2.4), which leads to the electron density profile

$$n_{e,\text{cor}}(r) = n_{e,0} \exp \left[-\frac{\mu_{\text{cor}} m_{\text{p}}}{k_{\text{B}} T_{\text{vir}}} (\Phi(r) - \Phi_0) \right], \quad (2.6)$$

where

$$\Phi(r) = 4\pi G \rho_0 r_s^2 \left[\ln \left(1 + \frac{r}{r_s} \right) \frac{r_s}{r} \right] \quad (2.7)$$

is the NFW potential. Here, ρ_0 and r_s are the same as in equation (2.4), k_{B} is the Boltzmann constant, m_{p} is the proton mass, $\mu_{\text{cor}} = 0.6$ is the mean molecular weight, and $n_{e,0}$ is the normalization of the gas profile. We fixed $n_{e,0}$ by requiring that the total coronal mass is equal to 20% of the total baryonic mass within the galaxy halo (assuming $M_{\text{bar}} = 0.158 M_{\text{vir}}$, where 0.158 is the baryon fraction as in Planck Collaboration et al. 2018). The 20% value is justified by observational estimates (e.g. O’Sullivan et al. 2007; Anderson & Bregman 2011; Bogdán et al. 2013; Bregman et al. 2018), although the exact amount of hot gas present in the galaxy halos is still debated.

We assumed then that the cool CGM clouds are pressure confined by the hot gas, using the following formula

$$n_{\text{cl}} T_{\text{cl}} = n_{\text{cor}} T_{\text{vir}}, \quad (2.8)$$

where $T_{\text{cl}} = 2 \times 10^4$ K is the characteristic temperature of the cool absorbers (Zahedy et al. 2019) and $n_{\text{cor}} = 2.1 n_{e,\text{cor}}$ is the total particle number density in the corona. Figure 2.3 shows as an example the density profiles of the hot and cool media for an average galaxy with the same properties as the one used in Section 2.3.1. The coronal density is low at large distances from the central galaxy, while it increases in the central regions of the halo. Due to the pressure equilibrium (2.8), also the densities of the cool clouds, represented by the blue line in Figure 2.3, will increase at lower distances from the central galaxy.

The first effect of the hot gas on the cloud motion is the deceleration due to the drag force, that we can write (e.g. Marinacci et al. 2011)

$$\dot{v}_{\text{drag}} = -\frac{\pi r_{\text{cl}}^2 \rho_{\text{cor}} v^2}{m_{\text{cl}}}, \quad (2.9)$$

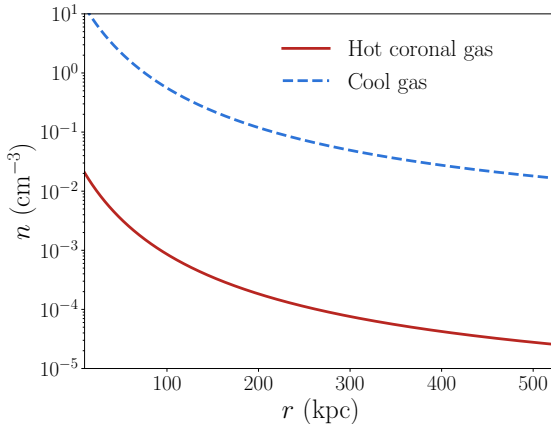


Figure 2.3: In red, profile of the intrinsic density of the hot coronal gas (from equation 2.6) for a galaxy with $M_{\text{vir}} = 10^{13.3} M_{\odot}$, $r_{\text{vir}} = 526$ kpc, $T = T_{\text{vir}} = 6.5 \times 10^6$ K (average of the galaxy halos in our sample), and normalization set as explained in Section 2.3.2. In blue, profile of the intrinsic average density expected for the cool circumgalactic medium if in pressure equilibrium with the corona, obtained through equation (2.8).

where $\rho_{\text{cor}} = \mu_{\text{cor}} m_{\text{p}} n_{\text{cor}}$, v is the cloud velocity, m_{cl} is the cloud mass, and r_{cl} is the cloud radius, given by

$$r_{\text{cl}} = \left(\frac{3m_{\text{cl}}}{4\pi\rho_{\text{cl}}} \right)^{1/3}, \quad (2.10)$$

where $\rho_{\text{cl}} = \mu_{\text{cl}} m_{\text{p}} n_{\text{cl}}$ is the density of the cool medium (assumed constant across the cloud) and $\mu_{\text{cl}} = 0.6$ is the mean molecular weight for a cool gas in photoionization equilibrium. We note that a slightly higher value $\mu_{\text{cl}} = 0.67$ (Sutherland & Dopita 1993) would be appropriate if the cool gas is in collisional ionization equilibrium, which is however uncertain and would have a negligible impact on our results.

Since the density of the cool gas increases with the decrease of the distance from the galaxy, the clouds become smaller during their motion toward the galaxies. Adding the drag force term to equation (2.3) decelerates the clouds during their infall, with a dependence on the cloud mass. Less massive clouds are affected by a stronger drag force and exhibit a higher deceleration. As there are no observational constraints on the mass of the clouds, we let it vary as a free parameter in our model.

With the inclusion of the drag force in the treatment, the results are more accurate and similar to the real behavior of the clouds. However, this simple model still does not take into account the hydrodynamical instabilities that are expected to take place in the system. High-resolution simulations (e.g. Armillotta et al. 2017) show how clouds moving through a hot-gas environment lose mass with time, mostly because of instabilities that strip cool gas from the cloud and mix it with the hotter medium. The likely result of these interactions is the evaporation of the cool cloud in the hot gas. These mass losses obviously affect the cloud velocities and can significantly change the output of the models. For this reason, we introduced in our modeling a mass loss term, described by

$$\frac{dm_{\text{cl}}}{dr} = -\frac{\alpha m_{\text{cl}}}{v}. \quad (2.11)$$

Equation (2.11) approximates the hydrodynamical instabilities, by making the clouds lose mass during their fall at a certain constant evaporation rate α (see Fraternali & Binney 2008; Marinacci et al. 2010a). As for the mass, the exact value of α is unknown and we thus included it in the model as a second free parameter. Since, with the inclusion of equation (2.11), the mass of the clouds is a function of the intrinsic distance, the free parameter that we vary is the mass of the clouds at the starting radius of their infall motion, $m_{\text{cl,start}}$.

The inclusion of all the effects described in equations (2.3) and (2.9) leads to the following final equation of motion:

$$\frac{dv}{dr} = \frac{1}{v(r)} \frac{GM(r)}{r^2} - \frac{\pi r_{\text{cl}}^2(r) \rho_{\text{cor}}(r) v(r)}{m_{\text{cl}}(r)}, \quad (2.12)$$

which is solved together with equation (2.11). In order to solve equation (2.12), the starting velocity v_{start} of the clouds is needed as an initial condition. We adopted $v_{\text{start}} = 0 \text{ km s}^{-1}$, since we have found that to reproduce the observed velocity distribution the clouds must have very low initial velocities (see Appendix 2.B for details). We also fixed the starting radius of the cloud infall motion at the virial radius of the galaxies (Table 2.1). This choice is justified by the observations of the cool circumgalactic medium extending till distances comparable to the virial radii of these galaxies (Zhu et al. 2014; Huang et al. 2016) and from our assumption that these clouds are inflowing from the external parts of the halos toward the center. We have also explored models with different starting radii for the clouds (Section 2.6).

Solving equation (2.12) we can find the velocities of the clouds with respect to their distance r from the galaxy center, taking into account both the gravitational force and the hydrodynamical effects. The different curves in Figure 2.2 show how the velocity profile varies with different choices of the parameters, using the same average galaxy used in Section 2.3.1 for the ballistic motion and the coronal model in Figure 2.3. After being initially accelerated by the gravitational force the clouds will be decelerated by the interactions with the corona. Models with lower cloud masses and higher evaporation rates have, particularly in the central regions, clouds with lower velocities, due to the higher efficiency of the hydrodynamical interactions. It is therefore crucial to explore the parameter space to understand which choice of the parameters leads to a velocity profile consistent with what we observe.

2.3.3 Accretion rate

In the model outlined above the clouds start from the virial radius and then are attracted by the gravitational force toward the center of the halos. The last step in creating the model is to define the total cool gas accretion rate at the virial radius.

To this purpose, we assumed that the CGM cool clouds are coming from the cosmological gas accretion. Cosmological models predict that the DM halos are growing in time by the accretion of external matter. We can estimate the

quantity of matter accreted per unit time by using the prescription in Fakhouri et al. (2010), who proposed a fit for the mass growth rate of the DM halos based on the results of the Millennium simulations (Springel et al. 2005; Boylan-Kolchin et al. 2009). Multiplying this prescription by the baryonic fraction, we obtain the rate of baryonic matter accreting in the halos:

$$\begin{aligned} \dot{M}_{\text{cosm}} = 47.6 h^{-1} M_{\odot} \text{yr}^{-1} & \left(\frac{M_{\text{vir}}}{10^{12} h^{-1} M_{\odot}} \right)^{1.1} (1 + 1.11z) \\ & \times \sqrt{\Omega_{\text{m},0}(1+z)^3 + \Omega_{\Lambda,0}} \times f_{\text{b}} , \end{aligned} \quad (2.13)$$

where $h = 0.7$, $\Omega_{\text{m},0} = 0.3$, $\Omega_{\Lambda,0} = 0.7$, and $f_{\text{b}} = 0.158$ is the baryon fraction by Planck Collaboration et al. (2018).

We related the accretion rate \dot{M}_{accr} to the cosmological accretion, using the formula

$$\dot{M}_{\text{accr}}(r_{\text{vir}}) = f_{\text{accr}} \dot{M}_{\text{cosm}} , \quad (2.14)$$

where f_{accr} is the third and last free parameter that we need in our analysis. If the value of f_{accr} is equal to 1, all the gas predicted by cosmological models to be accreted into the galaxy halo is what we observe as cool circumgalactic medium.

Once we have defined the value of the accretion rate at the virial radius, we can estimate the mass flux rate as a function of the intrinsic radius, using the formula:

$$\dot{M}_{\text{accr}}(r) = 4\pi \rho_{\text{cool}}(r) v(r) r^2 = \dot{M}_{\text{accr}}(r_{\text{vir}}) f_{\text{mass}}(r) , \quad (2.15)$$

where $\rho_{\text{cool}}(r)$ is the volume averaged mass density of the cool gas and $f_{\text{mass}} = m_{\text{cl}}(r)/m_{\text{cl,start}}$ is a term that takes into account the mass losses of the clouds at every radius. In this way, the mass flux decreases at smaller distances from the center, consistently with the evaporation of the clouds in the hot gas. For models with $\alpha = 0$, which means no evaporation of the clouds, the mass flux is constant with radius.

Inverting equation (2.15) we obtained the value of $\rho_{\text{cool}}(r)$, which will be useful in the next Section in order to compare the results with the observations.

2.4 Comparison with the observations

In this Section we explain how we obtained, starting from the intrinsic quantities calculated in Section 2.3, the results that are directly comparable to the observations. To this purpose, we created random distributions of cool clouds over the whole halo, each of them with the properties defined by the model, and we observed them through synthetic observations.

The quantity $\rho_{\text{cool}}(r)$ describes the total mass density of the cool gas per unit of volume. If we divide this density by the mass of the clouds, which is a function of the intrinsic radius, described by equation (2.8), we obtain the number of clouds per unit of volume. The integral of this quantity over the whole volume of the halo is equal to the total number of cool absorbers expected in the

system:

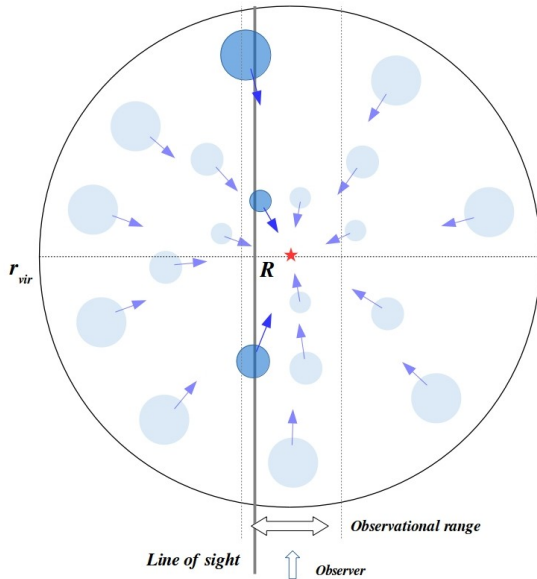
$$N_{\text{cl}} = 4\pi \int_0^{r_{\text{vir}}} \frac{\rho_{\text{cool}}(r)r^2}{m_{\text{cl}}(r)} dr . \quad (2.16)$$

We then created a distribution with a total number of objects given by equation (2.16). The clouds are not distributed uniformly in the galaxy halo, as their probability to be at a certain radius r is predicted by the argument of the integral in equation (2.16). Therefore, we populated the halos using a probability density function (PDF) given by:

$$\frac{4\pi\rho_{\text{cool}}(r)r^2}{m_{\text{cl}}(r)N_{\text{cl}}} . \quad (2.17)$$

This gives us N_{cl} objects, each of them located at a certain radius r and with all the properties given by the results of equations (2.8), (2.10), (2.11), and (2.12). Then, we associated to every cloud two other coordinates θ and ϕ , taken in order to have random distribution of clouds over a sphere (see Appendix 2.A for the detailed 3-D geometry).

Figure 2.4: 2-D representation of the synthetic observations performed in our model. The clouds (blue circles) are distributed throughout the halo (the sphere with radius r_{vir}), all infalling towards the central galaxy (the central red star) with a radial velocity described by equation (2.12). The vertical gray line represents the line of sight, consistent with the projected distance R of the galaxy from the background QSO, while the area included between the two vertical dashed lines represents the range spanned by the COS-LRG observations. The observer is located at the bottom side of the panel.



This setup was created for each one of the galaxies reported in Table 2.1. Figure 2.4 is a cartoon representation of the cloud distribution, flattened in two dimensions: the clouds are randomly distributed throughout the halo, each one of them with the properties explained above. The last step was to create synthetic observations: we selected the observed clouds tracing a line-of-sight through the galaxy halos, as explained in detail in Appendix 2.A and shown in Figure 2.4. We note that at the same projected distance we can intercept clouds at very different intrinsic distances from the central galaxy, potentially

till the virial radius of the halo.

After selecting the clouds, we calculated their velocity projections along the line of sight (Appendix 2.A). Figure 2.4 shows the range of the projected distances between the galaxies and the QSOs in the COS-LRG observations. As already mentioned in Section 2.2, these impact parameters are all much smaller than the typical virial radii of our massive galaxies. Therefore, the observations span only a small central area of the halos. As a result, most of the clouds that we observe have a direction of the motion that is almost parallel to the line-of-sight and the projection corrections of the velocities are relatively small. We repeated this procedure for all the galaxies and finally we put together all the observed velocities in a single line-of-sight velocity distribution.

The modeling described above allowed us to find the choice of parameters for our models that best reproduces the observations. To this purpose, we performed a Markov Chain Monte Carlo (MCMC) analysis over the parameter space defined by $m_{\text{cl,start}}$, α , and f_{accr} . We now describe the likelihood of the models, needed to perform the MCMC. This is obtained using the comparisons between our model results and the two observables outlined in Section 2.2: the line of sight velocity distribution and the number of clouds. The total likelihood is the product of the likelihoods associated to these two observational constraints. In particular, we used the logarithm of the likelihood

$$\ln \mathcal{L}_{\text{tot}} = \ln \mathcal{L}_1 + \ln \mathcal{L}_2 , \quad (2.18)$$

where \mathcal{L}_1 and \mathcal{L}_2 are the two different likelihoods.

To compare the two velocity distributions we have to assume for both of them the same number of velocity bins n_{bin} in which the velocity range is divided. We considered a velocity range spanning from -1000 to 1000 km s^{-1} , to include all the possible velocities predicted by our models, and we divided it in 20 different bins. We verified that slightly different choices of the number of bins do not affect the final results. The comparison between the two velocity distributions is then given by the reduced chi squared:

$$\ln \mathcal{L}_1 = -\frac{1}{2(n_{\text{bin}} - 3)} \sum_{b_i} \frac{|d_i - m_i|^2}{\sigma_i^2} , \quad (2.19)$$

where $n_{\text{bin}} = 20$, $n_{\text{bin}} - 3$ is the number of degrees of freedom, d_i and m_i are respectively the values of the observed and model distributions in the velocity bins b_i , and σ_i are the errors on the observed values, calculated using the bootstrapping method¹.

Finally, the second constraint is given by the comparison between the number of clouds observed in our synthetic models (n_{mod}) and the total number of clouds

¹We created 1000 randomizations of the observed velocity distribution: for each distribution, the number of objects is the same of the original one (42) and its elements are randomly taken from the original distribution with the possibility of replacement. Then we divided all the distributions in the same number of velocity bins and we calculated for each of them the standard deviation σ_i .

observed by COS-LRG ($n_{\text{obs}} = 42$, see Section 2.2), using

$$\ln \mathcal{L}_2 = -\frac{1}{2} \left(\frac{|n_{\text{obs}} - n_{\text{mod}}|}{\sqrt{n_{\text{obs}}}} \right)^2, \quad (2.20)$$

where $\sqrt{n_{\text{obs}}}$ is the standard deviation of the Poisson distribution with a mean value equal to n_{obs} . The priors used in this analysis are flat for all the parameters but f_{accr} , which sets the value of the total mass accretion rate of cool gas at the virial radius. In particular we employed a gaussian prior centered on 1 and with a dispersion of 0.5, in order to have the accretion rate consistent with the total baryonic accretion rate predicted by cosmology (equation 2.13). Negative values of f_{accr} are excluded. Regarding the other two parameters, the logarithm of the cloud mass (in solar masses) is allowed to vary uniformly in the range from 4 to 7, while the evaporation rate α can vary uniformly from 0 to 3.5 Gyr^{-1} . A negative α would in fact mean that the clouds are gaining cool mass and we excluded this scenario, because condensation is highly unlikely at these high temperatures: the cooling time of the hot gas is indeed too long for it to cool down and increase the amount of cool gas in the system. This is also supported by hydrodynamical simulations (Armillotta et al. 2016).

2.5 Results

In this Section we report the results of the MCMC analysis that we used to compare our results to the observations and to find the best models that describe the CGM of massive ETGs. Then we discuss the physical scenario arising from our models.

Parameter	32nd	50th	68th
$\log (m_{\text{cl,start}}/M_{\odot})$	4.62	4.85	5.1
$\alpha \text{ (Gyr}^{-1}\text{)}$	1.54	1.8	2.05
f_{accr}	1.11	1.29	1.5

Table 2.2: Results of the MCMC analysis. Best values (50th percentile), 32nd and 68th percentiles for the three free parameters.

2.5.1 MCMC results

The results of the MCMC study are reported in Figure 2.5 and Table 2.2. Figure 2.5 shows the corner plot where both the one and two dimensional projections of the posterior probabilities of the three parameters are shown, while in Table 2.2 we show the 32nd, 50th (the median value) and 68th percentiles of the parameter one dimensional probabilities. Models with parameters in the ranges reported in Table 2.2 are the best in maximizing the total likelihood \mathcal{L}_{tot}

and therefore the best in reproducing the COS-LRG observations.

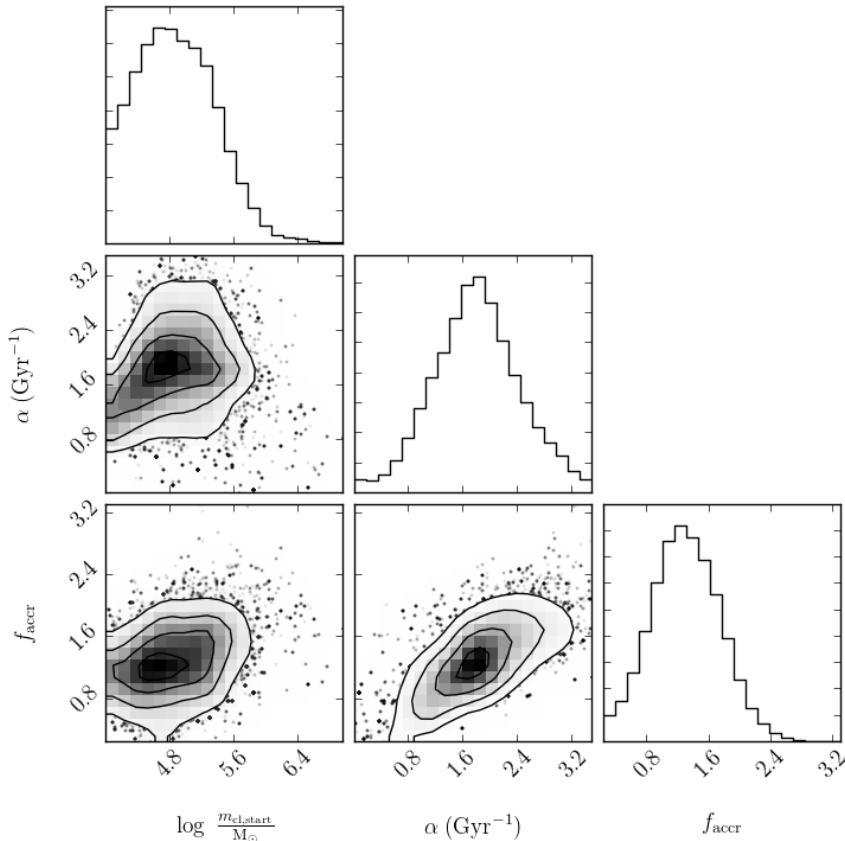


Figure 2.5: Corner plot with the MCMC results, representing the one and two dimensional projections of the posterior probabilities for the three free parameters of our models.

In the left and right panels of Figure 2.6 we show the outputs of these models, respectively the line of sight velocity distribution and the total hydrogen column densities, with their comparison with the observations. The errors in the observed distribution are calculated using the bootstrapping method explained in Section 2.4. The model velocity distribution is dependent on the random populations of clouds, as explained in Section 2.4. Therefore, to have a more robust comparison between our model output and the observations, the model distribution in the left panel of Figure 2.6 is the result of the average of 2000 models with the values of the parameters included within the 32nd and the 68th percentiles reported in Table 2.2, weighted with the value of the posterior probability of each model. The model and observed velocity distributions are both normalized to have a subtended area equal to 1. The kinematics of the

model clouds, fitted by the MCMC analysis, is in good agreement with the observed one. The consistency between the two distributions is also evident from the comparison between the cumulative distribution functions (CDFs) in Figure 2.9. The result of a Kolmogorov-Smirnov test between the two samples confirms that they are likely drawn from the same distribution. The averaged number of clouds of the 2000 randomizations used to create the plot in the left panel of Figure 2.6 is 43 ± 10 (the error is given by the weighted standard deviation), consistent with the observed one of 42.

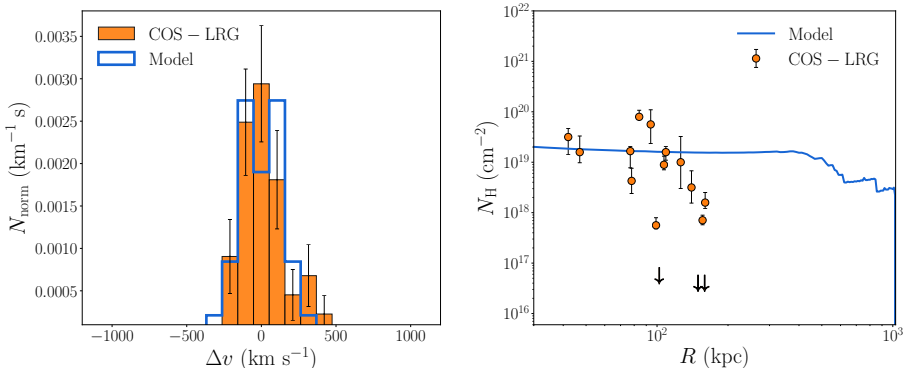


Figure 2.6: Comparison between the observations (orange bars and circles) and our best model results (blue lines). Left panel: normalized line-of-sight velocity distribution, where the errors in the observations are obtained with the bootstrapping method; right panel: total hydrogen column density. The downward arrows represent the upper limits of the non-detections.

The hydrogen column density of our model (blue curve) in the right panel of Figure 2.6 is instead obtained converting the density of clouds ρ_{tot} (see Section 2.3.3) into a numeric hydrogen density and projecting it along the line of sight. More precisely, the model curve in Figure 2.6 is the average of the sixteen column densities calculated for each galaxy. This profile is not dependent on the random populations of clouds and therefore we show here the result of a single model with the parameters given by the median values reported in Table 2.2. The orange circles represent instead the column density observations by Zahedy et al. (2019), also reported in Table 2.1. These values are affected by various uncertainties, depending on the different assumptions made to perform the photo-ionization models. These uncertainties can potentially be very large and are not fully quantified by the error bars shown in Figure 2.6. As an example, the COS-Halos collaboration (Werk et al. 2013, 2014; Tumlinson et al. 2013) analysed with similar photo-ionization models and slightly different assumptions (see Prochaska et al. 2017) five of the galaxies in our sample, finding column densities that, in some cases, are one or two orders of magnitudes different from the COS-LRG estimates. Because of these uncertainties in the data, we have not included the column densities in the MCMC fit. We can note however that our predictions are not inconsistent with the observations.

Interestingly, with our models we can also make predictions about the density profile in the outer part of the halos: we will discuss the implications in Section 2.6.3.

We conclude that, with the correct choice of parameters, models of clouds that are starting from the virial radii of the halos, infalling at a cosmologically motivated rate and then interacting with the hot coronal gas, can successfully reproduce the observed kinematics, number of absorbers and column densities of the cool CGM around early-type galaxies. This is our first and main result. In Section 2.5.2 we analyze the motion and the properties of our model clouds and we discuss the physical scenario that these particular models describe.

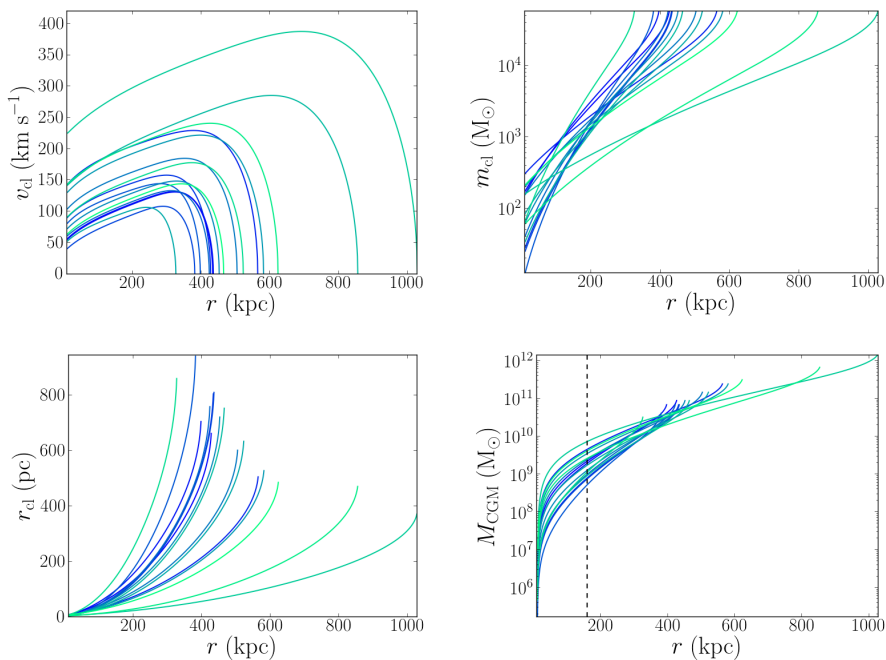


Figure 2.7: Properties of the cool CGM clouds described by our best model. All the profiles are plotted with respect to the intrinsic distance from the central galaxies and the different colored lines represent the result for the sixteen different galaxies of the sample. Top left: velocity profiles of the cool clouds; top right and bottom left: respectively masses and radii of the cool clouds; bottom right: cool CGM cumulative mass profile, with the vertical dashed line representing the distance of 160 kpc.

2.5.2 Description of the cloud motion

Using the median parameters of Table 2.2 we can have an indication on the properties of the best models that reproduce the observations and we can analyze in detail the motion of the infalling clouds. In Figure 2.7 and 2.8 we report our results on the cool CGM properties, all with respect to the intrinsic

distance r from the central galaxies. For the moment we do not discuss the possible origin of the cool clouds (Section 2.6.5), but we just describe their behavior throughout their infall. The different blue-tone lines in Figure 2.7 and 2.8 represent the results obtained for the 16 different galaxies that we are modeling. Since we are describing all the galaxies with the same model, the general trends of the cool CGM properties are similar in all the objects and the arising physical picture is the same for all the galaxies of our sample, with small variations due to the different virial masses and radii.

In the top left panel of Figure 2.7 we show the cloud velocity profiles. The clouds start at the virial radii with very low velocities, they are accelerated by the gravitational force and then, as already explained in Section 2.3, they are decelerated by the drag force and the other hydrodynamical interactions. We stress that it is this hydrodynamical deceleration that allows the resultant line-of-sight velocity distribution to be consistent with the observed one (see left panel of Figure 2.6).

With our analysis we can also estimate, only using our analytical description of these systems, the mass and size of the cool CGM clouds, which were so far largely uncertain (Stocke et al. 2013; Werk et al. 2014). The top right and bottom left panels of Figure 2.7 show the evolution of these two quantities and the direct effects of the evaporation and the pressure equilibrium on the clouds. The profiles in the top panel show that the clouds start at the virial radii of the galaxies with a mass of $\sim 10^5 M_\odot$, then they progressively lose mass due to the interaction with the corona. In the central region they have lost more than 99% of their mass and have masses of about $10^2 M_\odot$. Also the radii of the clouds (bottom panel), obtained from equation (2.10), strongly decrease with time, starting from $r_{\text{cl}} \sim 1$ kpc at the virial radius and reaching sizes of a few pc in the central regions, due to the effects of both the cloud evaporation and the pressure equilibrium (in the central regions the corona and cloud densities are higher). The conclusion is that in the central regions the cool CGM clouds are much smaller and also less massive, because most of their mass is evaporated in the hot corona.

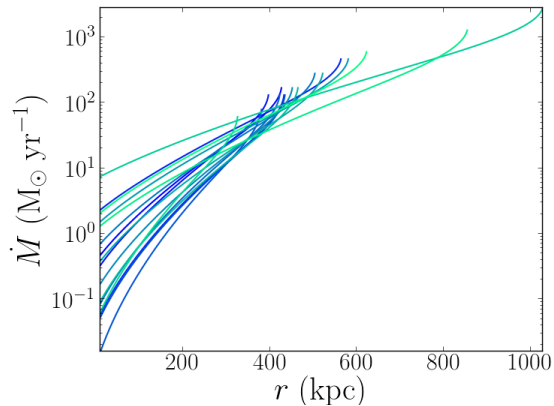


Figure 2.8: Same as Figure 2.7, but for the total mass flux profile of the cool CGM.

From the bottom right panel of Figure 2.7, which shows the cumulative mass profiles of the cool gas, we can infer how the mass loss of the clouds influences the distribution of the cool CGM mass throughout the halo. Most of the cool gas mass is concentrated in the external regions of the halos, since the clouds located in these regions are more massive. Indeed, because of the cloud evaporation, the decline of the mass profiles is much steeper than what expected without evaporation and the inner regions are almost devoid of cool gas. While on average the total mass of the cool medium within the galaxy halo is $2.5 \times 10^{11} M_{\odot}$, the cool gas mass within $r = 160$ kpc (highlighted by the vertical dashed line) is only $\sim 1\%$ of the total. Therefore, we are describing with our models a system where most of the cool CGM gas is not reaching the central regions and is not accreting onto the galaxy. This is also shown by the cool gas accretion rate, reported in Figure 2.8: starting from a cosmological rate at the virial radius, the accretion in the inner parts is reduced to less than 1% of the initial value.

With this result we are therefore in agreement with the observations of a great amount of cool CGM in these halos and we also go in the direction of explaining why this large reservoir of cool gas is not feeding the star formation of these thus passive central early-type galaxies. We discuss this further in 2.6.1.

2.6 Discussion

With our analysis we have found that infall models of cool clouds can successfully describe the COS-LRG observations of the cool CGM around massive ETGs. We presented our findings in Section 2.5. In this Section we discuss all the possible limitations of our analytical models (Sections 2.6.1 and 2.6.4), the comparison with other observations (Section 2.6.3) and the implications of our findings for the cool gas state, origin and fate (Sections 2.6.2 and 2.6.5).

2.6.1 Cloud survival

We have seen in Section 2.5.2 that with our models we describe a scenario where, due to the evaporation of the CGM clouds, only a very small part of the cool gas accreting into the galaxy halos is reaching the inner regions. Nevertheless, we also find that this small amount of cool gas (on average a few $M_{\odot} \text{ yr}^{-1}$) is reaching the central ETGs, possibly feeding the galaxy star formation at a similar rate. In this Section we discuss whether this problem may be alleviated by additional effects that we have not taken into account, focusing in particular on the survival time of the cool clouds.

As already explained, the analytical model of Section 2.3 is only an approximation of all the hydrodynamical interactions taking place in the CGM. As a consequence, the clouds described in our treatment can lose mass, but they cannot completely evaporate in the hot gas or be destroyed by the cloud-corona interactions, which is instead what we expect in reality and what we observe

in high-resolution simulations (e.g. Heitsch & Putman 2009). Therefore, it is important to estimate the time after which the clouds are probably completely evaporated in the surrounding hot medium. We consider as an estimator of the cloud survival time the conduction time, which is the time needed for the thermal conduction to be efficient and therefore for the cloud to be entirely evaporated in the corona. In our massive galaxy halos, where there is a high temperature gradient between the different gas layers (the coronal gas is almost three orders of magnitudes hotter than the cool clouds) we expect the thermal conduction to be particularly efficient and to play a major role in the evaporation of the clouds (Armillotta et al. 2016).

The conduction time is defined as (Spitzer 1962)

$$t_{\text{cond}} = \frac{n_{\text{cool}} k_{\text{B}} r_{\text{cl}}^2}{f k_{\text{sp}}}, \quad (2.21)$$

where f is the suppression factor due to the magnetic field (e.g. Chandran & Cowley 1998) and:

$$k_{\text{sp}} = \frac{1.84 \times 10^{-5} T^{5/2}}{\ln \Psi} \text{ erg s}^{-1} \text{ K}^{-1} \text{ cm}^{-1} \quad (2.22)$$

is the heat conduction coefficient, where $\ln \Psi$ is the Coulomb logarithm (≈ 30) and T is the temperature in K of the hot gas. We estimated the mean value of this time for a cloud at the virial radius with $m_{\text{cl,start}} \sim 10^5 M_{\odot}$ (see Table 2.2) and $f = 0.1$, obtaining $t_{\text{cond}} \sim 200$ Myr. This has to be compared to the mean infall time of a cloud in our best models, calculated using the formula

$$t_{\text{fall}} = \int_{r_{\text{vir}}}^0 \frac{dr}{v(r)}. \quad (2.23)$$

Averaging this time over the seven galaxies of our sample, we obtained that $t_{\text{fall}} \sim 3.7$ Gyr, much longer than the estimated conduction time. This means that the clouds cannot survive their entire journey from the virial radius to the central galaxy and they most likely completely evaporate in the hot gas at relatively large distances from the center of the halos. Therefore, the cool CGM is not feeding the central galaxies, thus explaining the quiescence of these objects. However, the comparison between these two times is not straightforward, since there are uncertainties on both quantities. The derived value of the conduction time is in fact dependent on the magnetic field, whose intensity and orientation is unknown. If the magnetic field suppression is larger than what we have considered in our estimate, the suppression factor f in equation (2.21) would be lower and therefore the conduction time would be longer than what we have found. On the other hand, since the clouds become smaller with time, the conduction is more efficient in the inner regions of the halos and therefore our estimate is an upper limit on the survival time of the clouds. Finally, there are also uncertainties on the infall time obtained through equation (2.23), since we are considering in our analysis only a radial infall. Adding any tangential

component would probably increase the final estimate of the total cloud infall time. Based on these considerations, we consider very likely that the clouds cannot survive for the entire infall time, although it is hard to define precisely the region of the halo where they completely evaporate.

The kinematic distribution of our model is arising from clouds distributed all over the halos, while we have argued with the last estimation that the central regions are probably devoid of cool gas. To prove that this property does not affect our final findings, we have performed again the MCMC analysis, with the same likelihood expressed in Section 2.4 and the same parameter space outlined in Section 2.5.1, but with the central regions of the halos forced to be completely devoid of clouds. To do this, we have defined the destruction radius r_{destr} as the inferior limit of the integral in equation (2.16) in place of 0 and as the smallest intrinsic radius where the clouds are present in our distribution. In this way we can assess how much the cloud destruction influences the final results. We have run a second MCMC, with $r_{\text{destr}} = r_{\text{vir}}/2$, obtaining the results reported in Table 2.3. We can see how the best-fit parameters are consistent within the errors with the ones found with the first MCMC, reported in Table 2.2. The physical scenario is the same described in Section 2.5.2, but with the cool clouds by construction not reaching the central galaxies. Also with this kind of model we are able to successfully reproduce the two observational constraints. In Figure 2.9 we show the comparison between the cumulative distribution functions of the velocity of the models and the observations: the kinematic distribution of the last model is perfectly consistent both with the result of our main model (Section 2.5) and with the observations, with a number of clouds equal to 44 ± 11 . The reason why the results of our model did not change with this last modification is that, even without imposing the cloud destruction, the vast majority the clouds observed by our synthetic observation analysis (see Section 2.4) are residing in the halo external regions. The radii of the external absorbers are in fact up to two orders of magnitudes larger than the internal ones (bottom left panel of Figure 2.7), implying much higher cross sections and therefore higher chances to be observed.

We can finally conclude that our model results, although we cannot directly simulate the complete evaporation of the cool clouds, provide a coherent picture where the pressure-confined cool CGM absorbers are: 1) infalling toward the center, 2) slowed down by the coronal drag force and 3) completely destroyed by the interactions with the hot gas before reaching the galaxy, thus not feeding any central star formation.

A similar scenario was discussed by Huang et al. (2016) to explain the kinematics of cool CGM clouds around massive elliptical galaxies: they argue that the observed low velocities could be reproduced by clouds with $m_{\text{cl}} \sim 5 \times 10^4 M_{\odot}$, slowed down by the effect of the hot gas drag force, though they do not assess this possibility with detailed dynamical models, as we have developed with our work. Also Chen et al. (2018) discuss the same physical scenario for the cool CGM, arguing that most of the clouds with $m_{\text{cl}} < 10^6 M_{\odot}$ cannot reach the center if they originate at large distances from the galaxies, in agreement with our final

findings. Our work is the first attempt to develop a coherent dynamical model to describe the CGM around massive ETGs. Similar semi-analytical models for the cool circumgalactic medium have recently been developed by Lan & Mo (2019), though they focus on $10^{12} M_{\odot}$ halos around star-forming galaxies, for which they find that an outflow model can qualitatively reproduce several CGM observed properties. Our approaches are similar, but we concentrate in this Chapter on more massive, passive galaxies (but see Chapter 3) and we directly compare our results with the full observed velocity distribution of the cool gas clouds.

2.6.2 Pressure equilibrium

A fundamental assumption that we made for the cool CGM physical state is the pressure equilibrium between the cool absorbers and the coronal gas, which determines the densities of the clouds. This assumption is physically justified, since we expect any pressure imbalance with the ambient medium to be erased on a cloud sound crossing time-scale, which is roughly ~ 10 Myr and therefore much smaller than the dynamical time.

It is hard to compare our intrinsic densities with the COS-LRG data, because of the already mentioned uncertainties in the observations, due to photo-ionization modelling and, most importantly, to projection effects. However, Zahedy et al. (2019) find, through their photo-ionization analysis, that the cool gas is likely in pressure equilibrium with the hot halo, in agreement with our assumption of clouds pressure-confined by the corona. We conclude that, in addition to being physically motivated, this assumption is also supported by observations (although earlier studies had been suggesting different results, see Werk et al. 2014). We plan to investigate these aspects further, including explicit photo-ionization modelling, in future works.

Model	$\log(m_{\text{cl,start}}/M_{\odot})$	α	f_{accr}
		(Gyr^{-1})	
$r_{\text{destr}} = r_{\text{vir}}/2$	$4.88^{+0.23}_{-0.22}$	$1.71^{+0.31}_{-0.33}$	$1.29^{+0.20}_{-0.21}$
$r_{\text{start}} = r_{\text{vir}}/2$	$4.91^{+0.25}_{-0.26}$	$2.40^{+0.52}_{-0.55}$	$1.20^{+0.19}_{-0.18}$

Table 2.3: MCMC results of the two additional models. 50th percentiles (with errors given by the 32nd and the 68th percentiles) of the posterior distributions of the three parameters obtained with the MCMC fits performed for models with $r_{\text{destr}} = r_{\text{vir}}/2$ (Section 2.6.1) and $r_{\text{start}} = r_{\text{vir}}/2$ (Section 2.6.3).

2.6.3 Comparison with other observations

The results of this Chapter are obtained from the comparison of our model predictions with the observations of the COS-LRG collaboration, which analyzed

both metal and hydrogen CGM absorption lines with a very high spectral resolution, allowing us to have detailed data on the kinematics of the cool clouds around 16 massive ETGs (Section 2.2). A comparable analysis has been done by the COS-Halos program (Werk et al. 2013, 2014; Tumlinson et al. 2013; Prochaska et al. 2017), a larger survey of the cool CGM around galaxies with a broad stellar mass range. Five of the galaxies analysed by this program are also part of the COS-LRG sample. We have applied our models also to this sub-sample of five objects, using only the kinematic data of the COS-Halos collaboration. The results of the MCMC analysis are totally consistent with the ones showed in this study.

However, the above data sets have also some limitations, mostly due to the lack of observations at projected radii larger than 160 kpc (in both samples the projected distance of the galaxy from the background QSO is always smaller than 160 kpc). It is important therefore to compare our findings with observations at larger projected distances. Zhu et al. (2014) and Huang et al. (2016) have observed MgII absorptions from cool CGM around large samples of ETGs out to very large distances from the central galaxies and they both found that the cool gas has a kinematics consistent with what is found by COS-LRG and COS-Halos. Their data have not been included in our analysis, because the resolution of these observations is not sufficient to disentangle the different clouds along a single line of sight. Also, they have observed only the MgII, which could be not representative of the behavior of the whole gas. However, it is interesting to compare our predictions with their results.

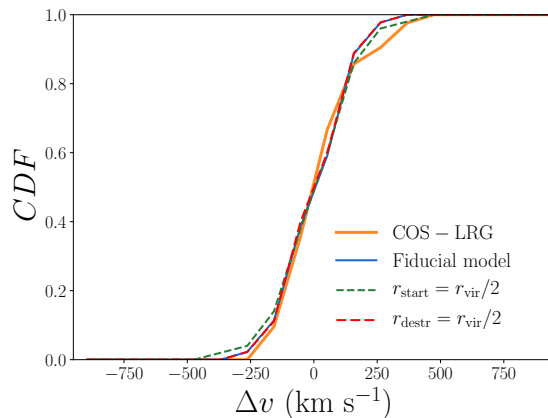
As seen in Section 2.5.1, with our model we can make predictions on the cool CGM behavior at large distances, in particular for the projected profile of the total hydrogen column density. The result of our best model is reported as a blue curve in the right panel of Figure 2.6: the column density is only slightly declining at large distances from the galaxies. This behavior is expected because our model predicts that most of the cool gas is concentrated in the halo external regions, as explained in Section 2.5.2. Therefore, the amount of gas observed by a line of sight at a large impact parameter is almost equal to the one observed at low projected distances from the galaxy and the resulting projected profile is nearly flat. By construction, the column density of each galaxy goes to zero at the virial radius, beyond which, in our modeling, there is no cool gas. The gradual decline of the column density profile is therefore also due to the fact that different galaxies live in different dark matter halos, with the small bumps corresponding to the different virial radii (reported in Table 2.1), where the column density of each galaxy goes to zero.

Huang et al. (2016) show that there are strong MgII absorptions up to 500 kpc from the central galaxies, with the covering fraction declining at projected radii larger than 100 kpc. Zhu et al. (2014), who analyze stacked spectra, observe MgII absorptions till and beyond the galaxy virial radii, finding that the total MgII surface density is decreasing with the projected distance. Both works are therefore consistent with our findings of cool absorbers still present at very large distances from the central galaxies and the decrease in the absorption strength,

which is less than two order of magnitudes from the center to the virial radius, is roughly compatible with the decline of our total hydrogen column density. Recently Berg et al. (2019) have analyzed the HI in the CGM around 21 massive ETGs, with sightlines within ~ 500 kpc from the central object. They find a covering fraction of the cool gas that is decreasing going from the central regions to high impact parameters. Our models also predict a decline in the projected profile of the covering fraction that is consistent with these observations, although it is hard to make a quantitative comparison between observations and model predictions. Since Berg et al. (2019) have not provided kinematic estimations, we have not included these data in our analysis.

There is also the possibility that the cool clouds start infalling from distances smaller than the virial radius (see Section 2.6.5) and in this scenario the steepness of the column density and the covering fraction profiles would be different, with very low values at large distances. With our current dataset we cannot directly constraint the cloud starting radius, since we are using observations till 160 kpc. Therefore, instead of considering the starting radius as an additional free parameter of our models, we have run an MCMC analysis as in Section 2.4, but fixing the starting radius at the value of $r_{\text{start}} = r_{\text{vir}}/2$. We present the results of this fit in Table 2.3: the best parameters are consistent with our previous findings, with a physical scenario similar to the one described in Section 2.5.2. Also, the line-of-sight velocity distribution and the number of clouds (49 ± 13) resulting from this model are consistent with the observations, as shown by the CDFs comparison in Figure 2.9. Therefore, even models with smaller starting radii can successfully describe the cool CGM properties. Future high-resolution observations of cool CGM absorbers at impact parameters comparable to the virial radius will help distinguishing between different scenarios.

Figure 2.9: Cumulative Distribution Functions of the line-of-sight velocity distributions of the observations (orange curve) and of our models. In blue we report the result of our main model (Section 2.5), while the dashed curves represent models with starting radius $r_{\text{start}} = r_{\text{vir}}/2$ (green, dashed) and destruction radius $r_{\text{destr}} = r_{\text{vir}}/2$ (red, small dashed).



2.6.4 Uncertainties in the accretion rate

In Section 2.5.1 we have shown that the best models in reproducing the observations have a mass accretion rate which is slightly (1.2 times) higher than the prediction of cosmological models, while in principle we would not expect the cool mass accretion to be greater than the cosmological rate. The reasons for this unexpected value are probably due to the simplifications of our models. The first reason could be the simplified structure of our model clouds. They are in fact spherical, with their radius becoming smaller as they fall throughout the halos. Although this is probably a good approximation for the head of the clouds, hydrodynamical simulations show that the interactions with the hot gas create a tail of partially mixed gas which can be much more extended than the main head. We cannot model this effect with analytical descriptions, but we argue that it would mainly have an effect on the number of clouds observed by the synthetic observations of our models. The cross section of the clouds will indeed be larger (see also Chapter 5) and we would synthetically observe more clouds than what we are doing with our current models. Therefore, to observe the same number of clouds we would need a lower total accretion of cool gas, in agreement with the prediction of the cosmological models. We note that this effect would likely have also an impact on the shape of the model velocity distribution. With our simplification of the structure of the clouds, we are indeed underestimating mostly the cross section of the slowest clouds, that had more interactions with the corona. Therefore we expect, from a more thorough analysis, to observe more clouds with very low velocities, populating the very central region of the model velocity distribution (see the left panel of Figure 2.6) and alleviating the tension in that bin between the observations and our predictions.

Another reason why we are probably overestimating the accretion rate is instead given by our assumption of isotropic inflow onto the galaxy halos. As explained in Sections 2.3.3 and 2.4, to calculate the mass accretion rate of the cool gas we assumed that the cool gas is inflowing isotropically, starting from the virial radius. However, the accretion could be anisotropic, with the cool medium inflowing through filaments toward the galaxies (cool gas filamentary accretion is common in high-resolution cosmological simulations, e.g. Nelson et al. 2016). In this scenario, the filaments would not fill the entire volume of the halos and the total accretion of gas would be different than what predicted by our model. However, the low number statistics does not allow us to constraint the real geometry of the gas inflow and to understand whether and how much we are overestimating the cool CGM accretion with our simplified, isotropic models. We leave a more detailed analysis about the geometry of the gas accretion for future works.

Finally, we are comparing the accretion of gas predicted by our models with the cosmological gas accretion expected at the exact redshifts of the galaxies in our sample. However, we have seen that the clouds experience an infall that lasts about 4 Gyr and have therefore entered the halo at a time when the expected accretion was higher (Fakhouri et al. 2010). The variation of the cosmological

accretion of gas with time could explain the slight discrepancy that we have found in our results.

2.6.5 Origin and fate of the cool absorbers

2

In the previous Sections we have focused on the physical description of the cool absorbers behavior throughout the halos. In this Section we instead analyze the possible scenarios for the origin of the cool CGM, as well as their consequences on galaxy evolution. The aim of this Section is only to speculate on the different possible pictures that can arise from our models, leaving a detailed analysis of the cool CGM origin and fate for future works.

External origin

Our favourite interpretation for the origin of the cool CGM in ETGs is that it is coming from the accretion of external gas. As explained in Section 2.3, cosmological models predict that galaxy halos acquire gas at a rate described by equation (2.13) and our assumption is that the cool CGM is originated by this accretion of external gas: in our models we set indeed the cool gas accretion rate in order to be consistent with the cosmological one. In this picture, the filaments of low-metallicity intergalactic gas accrete into the galaxy halo and form the cool clouds whose infall motion is described by our modeling. This assumption is motivated by the COS-LRG analysis of the cool CGM metallicities (Zahedy et al. 2019): they find that about half of the galaxies in their sample host metal poor clouds, consistently with our picture of accretion of external gas, which is expected to have low metallicities (see Lehner et al. 2016). Also a recent work by Chen et al. (2019a) states that very low metallicity gas is present in the halos of massive ETGs, probably coming from the accretion of intergalactic medium. The scenario of external origin has more difficulties to explain the observations of absorbers with higher metallicities, that are common in the COS-LRG survey and also in previous surveys like COS-Halos. Prochaska et al. (2017) find indeed that the CGM absorbers in the whole COS-Halos sample span a broad range in metallicities, with a median value around 30% solar. A way to produce these metal-rich absorbers is to invoke internal origins for the clouds, which we will discuss in Section 2.6.5.

Another way to explain the observation of a broad range of metallicities is with the destruction of the cool accreting filaments. It is possible in fact that the clouds are formed by the fragmentation of the filaments and their mixing with the corona, explaining higher metallicities than what expected in the IGM. Also, in this scenario, the filaments are slowed down by these processes and it is reasonable to believe that the resulting clouds will start their infall with low velocities, as indicated by our results² (see Appendix 2.B). Due to these con-

²The fragmentation of the filaments could also happen at radii larger than the virial radius, for example at the virial shock radius ($\approx 1.25 r_{\text{vir}}$, see Nelson et al. 2016). In this scenario, the filaments are fragmented outside the galaxy halo and they enter the virial radius already in the form of slow-moving clouds.

siderations, we consider the external accretion consistent with our results and the most likely picture for the cool CGM absorbers around ETGs.

Alternative origins

A plausible alternative origin for the cool circumgalactic gas in the halos of massive ETGs would be from the stripping of ISM of satellite galaxies by tidal or ram pressure forces. Signatures of cool gas coming from this type of interactions have been obtained directly in emission in different massive halos (e.g. Epinat et al. 2018; Johnson et al. 2018). The cool gas stripped by the satellite could eventually fall down towards the central massive galaxy, in a journey compatible with the motion described by our model. Although the accretion from external gas remains our favourite scenario, we do not reject this last picture as a possibility for the origin of a fraction of the cool CGM.

Another scenario that can give rise to cool clouds falling through the halos is related to the presence of outflows from the central galaxy, which we have not considered so far in our treatment. This neglect is justified by the nature of the galaxies that we are studying, that are by definition in a quiescent state and should therefore not experience strong outflows of gas. However, although they are currently quiescent, there could have been outflows in the past of these objects, due to either star formation bursts or AGN activity. AGNs are indeed known to drive massive multi-phase outflows (e.g. Greene et al. 2012) and cool, high velocity gas is often observed in the CGM of quasars (e.g. Bowen et al. 2006; Prochaska et al. 2013; Johnson et al. 2015). It is possible to think that, as in the recycling scenario (see Section 2.1), the outflows due to recent star formation or AGN episodes have reached the external parts of the halos, cooled and eventually fallen down again toward the center. In this picture we are observing the last part of this cycle, composed by the infalling cool CGM clouds, which in this case have an internal origin. This would mean that we are not observing a continuous accretion but a sporadic event of infall due to a recent outflow episode happened in the central galaxies. Although this picture would explain the high metallicities observed in part of the cool CGM (Prochaska et al. 2017), all our galaxies should have experienced an outflow burst at similar times, with comparable timescales and we consider this scenario unlikely. Thus, the recycling is most probably not the main driver of the cool CGM formation around early-type galaxies.

The last possibility is that the clouds are condensing out of the hot gas due to thermal instabilities, developing a multi-phase halo. Multi-phase gas has indeed been observed in both nearby clusters and elliptical galaxies (Voit & Donahue 2015; Voit et al. 2015) and the same origin scenario has been proposed also for the cool CGM around massive ETGs by different observational work (see Huang et al. 2016; Zahedy et al. 2019). This picture is motivated by various theoretical works (e.g. Sharma et al. 2012; McCourt et al. 2012; Voit 2018) that predict that the instabilities can develop at a cooling radius $r_c < r_{\text{vir}}$, where the cooling time is comparable to the dynamical time of the gas. In this scenario, clouds are created within the galaxy halos with very low velocities, (which may

be of the order of the turbulence of the hot coronal gas, see Voit 2018) and then start to fall down toward the central galaxies, consistently with our main findings. However, it is so far not clear if such instabilities can spontaneously develop in the hot corona (e.g. Binney et al. 2009; Nipoti & Posti 2014) and therefore it is difficult to establish whether this scenario could be an important contributor to the cool CGM.

We conclude then that the bulk of the cool circumgalactic gas is likely coming from the accretion of the external IGM, although the other processes outlined above may originate part of the observed cool clouds, also explaining the broad range in the observed metallicities.

Fate of the cool gas

Many works in the last decades have studied the fate of the accretion of cool gas from the IGM onto galaxy halos, both with analytical prescriptions and cosmological simulations (e.g. Birnboim & Dekel 2003; Ocvirk et al. 2008; Dekel et al. 2009; Nelson et al. 2013, 2016). The general picture is that, in low mass DM halos, filaments can penetrate through the halo reaching the central galaxy, while in the most massive objects the filaments are shock heated to the galaxy virial temperature and are unable to feed the central galaxy. In this scenario, the CGM clouds that we are studying are the products of the fragmentation of the cool gas filaments. In agreement with the general picture outlined above, we predict that these cool gas components are not able to survive their journey and reach the central galaxy (see Section 2.6.1), but they instead evaporate in the hot corona at large distances from the center. We therefore believe that these absorbers cannot be straightforwardly linked with the observations of the High Velocity Clouds (HVCs, see Putman et al. 2012), clouds of cold gas observed mostly in HI around the Milky Way and whose counterparts have been detected also in nearby star-forming galaxies (Sancisi et al. 2008). HVCs reside in fact primarily within 10 kpc from the central galaxy disk and their origin is still debated (Wakker et al. 2007; Fraternali et al. 2015). On the contrary, we expect our CGM clouds around ETGs to be completely destroyed by the interactions with the hot gas at much larger distances. The fate of the cool CGM, by the evaporation of the clouds, is therefore to increase the mass of the hot corona.

From Figure 2.8 we can infer the rate of cool gas accreting onto the galaxy halos: on average, the gas accretion at the virial radius is about $500 M_{\odot} \text{ yr}^{-1}$. If it is coming from the cosmological inflow, this amount of cool gas is continuously injecting baryons in the galaxy halo, by evaporating into the hot coronal gas. At this rate, (which could be slightly lower, due to the considerations of Section 2.6.4) the mass of the corona would be doubled in about 2 Gyr. This may be related to the current and future location of the so-called missing baryons (Bregman & Lloyd-Davies 2007; McGaugh 2008), although a more thorough discussion of these aspects is outside the scope of this work (but see Chapter 4).

2.7 Summary and conclusions

In this Chapter we carried out a detailed dynamical analysis of the cool circumgalactic medium around massive early-type galaxies at low-redshift, in order to explain the presence of a substantial amount of cool gas around quiescent galaxies and the narrowness of the observed velocity distribution of the cool CGM clouds.

In particular we focused on the observations of the COS-LRG collaboration around 16 massive ETGs. We developed semi-analytical models of cool clouds infalling from the external regions of the halos to the central galaxies, approximating the hydrodynamical interactions of the clouds with the hot corona with analytical parametrizations. These models aim to reproduce the two observational constraints given by the kinematic distribution and the number of the cool clouds. Our model has three free parameters that account for the properties of the infalling clouds and for their interaction with the ambient medium. We constrained these free parameters on the available data with an MCMC analysis.

From our results we draw the following conclusions:

1. models of cool CGM clouds infalling through the galaxy halos at a cosmologically motivated rate can successfully reproduce the observations, explaining the number of observed clouds and their line-of-sight velocity distribution. These results are also consistent with the total hydrogen cool CGM column densities reported by COS-LRG;
2. our best models describe clouds with an initial mass $m_{\text{cl}} \sim 10^5 M_{\odot}$ at the virial radius, that during their infall lose more than 99% of their mass due to the hydrodynamical interactions with the hot coronal gas, implying that the internal regions of the halos are almost devoid of cool gas;
3. despite the uncertainties given by our approximation in the hydrodynamical treatment, we can conclude that the cool CGM clouds most probably cannot survive the journey but will completely evaporate into the hot corona as the timescale of thermal conduction is much shorter than the dynamical time. Thus the cool gas will probably not accrete onto the central galaxies, providing an explanation of their quiescence.

The results of this Chapter represent a step forward in solving the puzzle of the existence of large unused reservoirs of cool circumgalactic gas around quiescent galaxies. Future improvement of the observational data and ad-hoc hydrodynamical simulations could reduce the uncertainties in our current description. In Chapters 3 and 4, we apply similar models to larger samples of data and in particular to star forming galaxies, in order to study the impact of the CGM kinematics and dynamics on the evolution of different kinds of galaxies.

2.A Geometry of the system

In Section 2.4 we have described how we compared our results with the data, using synthetic observations of random populations of clouds. Here we report in detail the geometry used to infer the number of observed clouds and their line-of-sight velocities. We created for each galaxy a 3-dimensional distribution of clouds over a sphere with radius r_{vir} (see Table 2.1), representing the virial halo. As already explained in Section 2.4, the total number of clouds for each halo is calculated using equation (2.16), while the intrinsic distance of each cloud from the galaxy is found using the probability density function expressed by (2.17). We then associated to each cloud two other coordinates θ and ϕ . These last two coordinates are chosen to have the clouds uniformly distributed over the sphere: we created a random distribution of the angle ϕ uniformly distributed between 0 and 2π and a random distribution of $\cos\theta$ uniformly distributed between -1 and 1, with $0 < \theta < \pi$. Each cloud has therefore a specific position in the halo, expressed by the coordinates (r, θ, ϕ) .

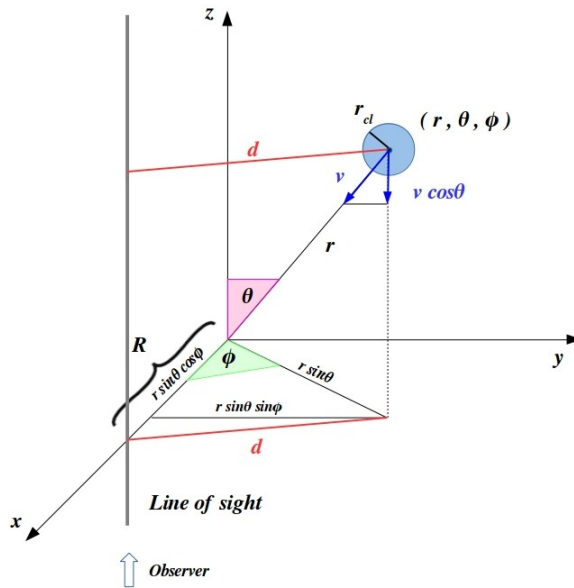


Figure 2.10: 3-dimensional representation of the synthetic observation of a generic cloud, as performed in our model.

Figure 2.10 shows the method used to perform the synthetic observations. Here, the line of sight is given by the line at $x = R$ in the plane $\phi = 0$, where R is the distance of the galaxy from the sightline, reported for each object in Table 2.1. The cloud in (r, θ, ϕ) is observed if the projected distance d of this point from the line of sight is smaller than the cloud radius, expressed by

$$d < r_{\text{cl}} , \quad (2.24)$$

where

$$d = \sqrt{(R - r_1 \sin \theta \cos \phi)^2 + (r_1 \sin \theta \sin \phi)^2} . \quad (2.25)$$

If the cloud is observed, that is if condition (2.24) is true, we calculated its line-of-sight velocity, as shown in Figure 2.10, through

$$v_{\text{los}} = v \cos \theta \quad (2.26)$$

and we added it to the model velocity distribution to be compared with the COS-LRG observations.

2.B Cloud initial velocity

In Section 2.3 we have described the construction of our semi-analytical models and we have argued that the starting velocity of the clouds (v_{start} , the velocity of the clouds at the virial radius of the galaxy) is needed to solve equation (2.12). In this Appendix we assess models where v_{start} is not fixed, but free to vary between different values. In order to do this, we have run an MCMC analysis as in Section 2.4, but adding v_{start} as a fourth free parameter, with a flat prior from 0 to 350 km s⁻¹. Figure 2.11 shows the results of this analysis, the one and two dimensional projections of the posterior probabilities of the four parameters. The distributions of the first three parameters are in strong agreement with the ones in Figure 2.5, meaning that adding the initial velocity as a free parameter does not change the final results.

The four bottom panels of Figure 2.11 represent the posterior distributions regarding v_{start} . We note that models with clouds starting from the virial radius with high velocities are strongly disfavored by the MCMC analysis and that the distributions are instead peaked on very low values. This means that the best models in reproducing the COS-LRG observations have clouds with initial velocities close to zero. This condition is indeed needed by the models to reproduce the central region of the line-of-sight velocity distribution, which shows an excess of clouds with very low velocities (see Figure 2.1 and the left panel of Figure 2.6). For this reason, we have used in our work only three free parameters, fixing the starting velocity of the cool CGM clouds to zero.

2

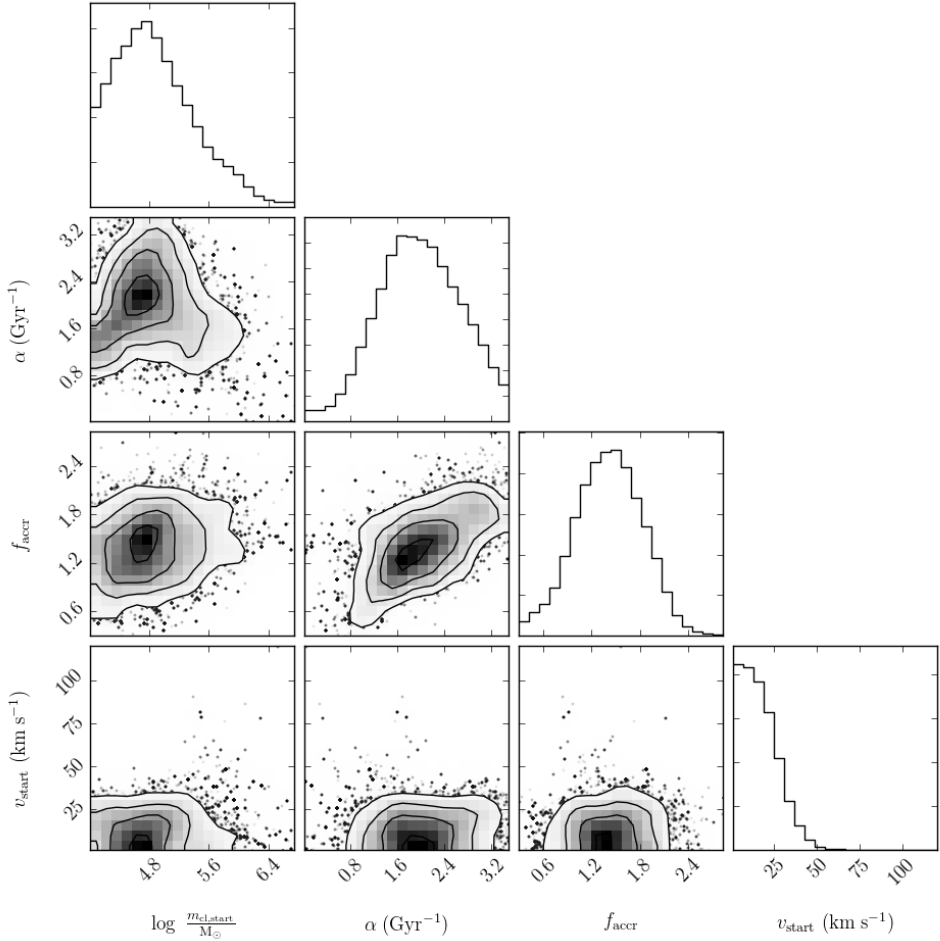


Figure 2.11: Corner plot with the results of the MCMC analysis described in Appendix 2.B, where also the starting velocity of the clouds is added as a fourth free parameter. Both the one and two dimensional projections of the posterior probabilities of the four free parameters are shown.

Chapter 3

Most of the cool CGM of
star-forming galaxies is not
produced by supernova
feedback

based on

– A. Afruni, F. Fraternali & G. Pezzulli, 2021 –

Published in Monthly Notices of the Royal Astronomical Society,
MNRAS 501, 5575

Abstract

The characterization of the large amount of gas residing in the galaxy halos, the so called circumgalactic medium (CGM), is crucial to understand galaxy evolution across cosmic time. In this Chapter, we focus on the the cool ($T \sim 10^4$ K) phase of this medium around star-forming galaxies in the local universe, whose properties and dynamics are poorly understood. We developed semi-analytical parametric models to describe the cool CGM as an outflow of gas clouds from the central galaxy, as a result of supernova explosions in the disk (galactic wind). The cloud motion is driven by the galaxy gravitational pull and by the interactions with the hot ($T \sim 10^6$ K) coronal gas. Through a Bayesian analysis, we compare the predictions of our models with the data of the COS-Halos and COS-GASS surveys, which provide accurate kinematic information of the cool CGM around more than 40 low-redshift star-forming galaxies, probing distances up to the galaxy virial radii. Our findings clearly show that a supernova-driven outflow model is not suitable to describe the dynamics of the cool circumgalactic gas. Indeed, to reproduce the data, we need extreme scenarios, with initial outflow velocities and mass loading factors that would lead to unphysically high energy coupling from the supernovae to the gas and with supernova efficiencies largely exceeding unity. This strongly suggests that, since the outflows cannot reproduce most of the cool gas absorbers, the latter are likely the result of cosmological inflow in the outer galaxy halos, in analogy to what we have found in Chapter 2 for early-type galaxies.

3.1 Introduction

The perfect laboratory to study and understand how galaxies evolve through cosmic time is the ionized gas that resides in the region between them and the intergalactic medium (IGM), the so called circumgalactic medium (CGM). This medium is observed, at very different temperatures, both around our Milky Way and almost ubiquitously around external galaxies (e.g. Anderson & Bregman 2011; Werk et al. 2013; Miller & Bregman 2015; Tumlinson et al. 2017). From a theoretical point of view, the halos of galaxies are expected, depending on their mass (e.g. Birnboim & Dekel 2003), to be filled with hot gas at about the virial temperature (generally called corona, predicted decades ago by cosmological models, see White & Rees 1978), and with colder gas likely distributed along filaments that can either penetrate to the halo central regions (Dekel et al. 2009) or evaporate into the hot corona (Nelson et al. 2013).

Although the halos of galaxies with different masses and morphologies show the presence of very large amounts of cool ($T \sim 10^4$ K) CGM absorbers (e.g. Thom et al. 2012; Stocke et al. 2013; Bordoloi et al. 2014; Heckman et al. 2017; Zahedy et al. 2019) there is still much debate on the general dynamics of these clouds and on their possible origins, which might also depend on the galaxy type. For passive early-type objects, given the absence of activity in the center, the cool clouds probably originate either from the inflow of external intergalactic medium (see Chapter 2) or from the condensation of the hot coronal gas (Voit 2018; Nelson et al. 2020). Also for star-forming galaxies, observations of this cool gas had in some cases been interpreted as clouds falling towards the galaxy, presumably feeding its star formation (e.g. Bouché et al. 2013; Borthakur et al. 2015), as expected from theoretical models. For these star-forming objects however, the central galaxy is also believed to have an active role in the formation and regulation of the cool CGM. Over the years, multiphase outflows have been observed in the central regions of both dwarfs (e.g. McQuinn et al. 2019) and L_* spiral galaxies (e.g. Veilleux et al. 2005; Martin et al. 2012; Rubin et al. 2014; Concas et al. 2019), with claims of these winds being part of large-scale galactic outflows, extending till several tens of kpc from the center (e.g. Schroetter et al. 2019). It is not clear however whether these ionized outflows are powered by star formation and, if so, what is their impact on the surrounding CGM (see Martin & Bouché 2009; Borthakur et al. 2013, who studied the properties of the circumgalactic gas of starburst galaxies).

Generally, at the typical scales of the CGM (~ 100 kpc), it is hard to distinguish whether the cool gas is outflowing from or inflowing to the central object, given the limited information coming from the observations. Despite having now quite some evidence of CGM emission at high redshift (e.g. Cantalupo et al. 2014; Farina et al. 2019, and references therein), observations of the cool gas around galaxies in the local Universe are primarily in absorption and consist of one single line of sight for each galaxy (see Tumlinson et al. 2017, and references therein), with very few examples of observations in emission (e.g. Burchett et al. 2020), sometimes using stacking techniques (see Zhang et al. 2018). There are

therefore very few constraints on the intrinsic location of the cool clouds and on their dynamics.

Different studies, focused on metal UV absorption lines (Kacprzak et al. 2012; Martin et al. 2012; Schroetter et al. 2019; Veilleux et al. 2020) have found a segregation of absorbers along the galaxy minor and major axes, which would hint towards a bi-conical outflow scenario, with accretion along the disk plane. The same feature is however not observed in other samples where the absorptions are more uniformly distributed (see Borthakur et al. 2015; Pointon et al. 2019) and therefore more statistics is needed in order to draw any conclusion on the gas origin or dynamics.

One key ingredient to disentangle between inflow or outflow motion is the gas metallicity: clouds inflowing from the IGM are expected to have very low metallicities (Lehner et al. 2016), while gas originated from the supernova triggered winds will transport a larger amount of metals. Deriving this gas property is, however, not trivial, since it requires photo-ionization modeling with multiple underlying assumptions, especially on the gas ionization factor (Werk et al. 2014; Wotta et al. 2016). Generally, both low and high metallicity absorbers are observed (e.g. Prochaska et al. 2017), without however a clear dependence between the metallicity and the azimuthal position of the absorbers (Péroux et al. 2016; Kacprzak et al. 2019; Pointon et al. 2019), as we would expect instead from the scenario of bi-conical outflows plus planar accretion.

The study of the CGM from a theoretical point of view is mostly based on hydrodynamical simulations that can trace the whole amount of gas inside a single galaxy halo, either with 'zoom-in' simulations of cosmological suites (e.g. Muratov et al. 2017; Pillepich et al. 2018; Oppenheimer et al. 2018; Rahmati & Oppenheimer 2018) or with idealized ad-hoc simulations of a single galaxy (e.g. Fielding et al. 2017). In both approaches, central winds seem to play an important role in defining the CGM properties and, while part of the cool gas is coming from the accretion of pristine gas, a significant fraction is either outflowing from the center or recycling back in the form of metal enriched clouds, after being previously ejected (e.g. Ford et al. 2014, 2016; Anglés-Alcázar et al. 2017; Oppenheimer et al. 2018).

However, these simulations often have to rely on subgrid models to treat the physics of stellar feedback, that make the predictions of the circumgalactic gas properties not completely reliable and in many cases, like the predicted gas metallicity distributions, not in agreement with the observations (see Wotta et al. 2019). Moreover, the main limitation is given by the resolution, that can reach at best a kpc-scale (e.g. van de Voort et al. 2019), which is not high enough to properly trace and resolve the clumpy cool circumgalactic gas in the galaxy halos. The general properties and structure of this gas, as well as its kinematics (Peeples et al. 2019), are indeed dependent on the resolution of the simulations (van de Voort et al. 2019), without clear signs of convergence. Several authors have, thus, resorted to high-resolution hydrodynamical simulations (Armillaotta et al. 2016; Schneider et al. 2018; McCourt et al. 2018; Grønnow et al. 2018; Gronke & Oh 2018; Fielding et al. 2020a) focused on the

small-scale interactions between hot and cool gas. They found that at least a pc-scale resolution is necessary to resolve the instabilities developing at the cloud/corona interface and therefore to properly describe the evolution of the cool clouds. Such a resolution is far from being achievable in simulations of the entire galaxy halo.

To overcome the issues related to hydrodynamic simulations we developed, in this work, semi-analytic parametric models. The analytic approach is rarely used to understand the circumgalactic medium (e.g. Stern et al. 2016; Lan & Mo 2019; Afruni et al. 2019) and the few works done so far have very different characteristics and goals between each other. However, the ability of an analytical study to describe the whole circumgalactic medium distribution within the galaxy halo, with straight-forward assumptions on the gas physics and origin, is key to understanding the observational data and draw conclusions on the CGM properties and dynamics. In Chapter 2, with a comparison of our model predictions with kinematic data from Zahedy et al. (2019), we have shown that the cool circumgalactic gas of early-type galaxies is consistent with an inflow of clouds coming from the cosmological accretion of gas onto the galaxy halos. Here, we will build a new type of semi-analytic models and compare their predictions with the observations of the COS-Halos and COS-GASS surveys (see Section 3.2, Werk et al. 2013; Borthakur et al. 2015), focusing in particular on a sample of star-forming galaxies. We describe the cool circumgalactic gas as an outflow of clouds powered by supernova explosions in the central galaxies, taking into account the combined effect on the cloud orbits of the gravitational pull of the galaxies and of the interactions between the clouds and the hot coronal gas. The comparison of our models with the very accurate kinematics of the COS data will allow us to determine the properties of the CGM of star-forming galaxies and to test whether it can be the product of supernova-driven galactic winds.

This Chapter is organized as follows: in Section 3.2 we show the sample of galaxies and the absorption kinematic data that we will use in this work; in Section 3.3 we describe how we built our semi-analytic models; in Sections 3.4 and 3.5 we report our results and we discuss the implications of our findings, while in Section 3.6 we summarize our work and conclusions.

3.2 Galaxy sample and data

The findings of this work are obtained through the comparison of our model predictions with the observational data of the COS-Halos and COS-GASS surveys (Werk et al. 2013; Borthakur et al. 2015), which are focused on the cool CGM around low-redshift early and late-type galaxies, over a large range of stellar masses. These observations are taken pointing the Cosmic Origin Spectrograph (COS, Froning & Green 2009) aboard the Hubble Space Telescope towards background quasi-stellar objects (QSOs) in the projected vicinity of the galaxies. The gas is then characterized through the analysis of the hydrogen and metal absorption lines (Tumlinson et al. 2013; Werk et al. 2014;

(1)	(2)	(3)	(4)	(5)	(6)	(7)	(8)	(9)
Galaxy ID	z	$\log(M_*/M_\odot)$	SFR ($M_\odot \text{ yr}^{-1}$)	n_{comp}	x_{los} (kpc)	y_{los} (kpc)	R_d (kpc)	i ($^\circ$)
3936	0.0441	10.1	3.98	2	38	99	2.6	65
20042	0.0468	10.0	2.51	1	-130	-146	1.6	49
8634	0.0464	10.1	0.20	1	-97	-34	0.6	25
23457	0.0354	10.1	0.25	1	76	-158	2.8	82
29871	0.0342	10.2	3.16	1	-230	-27	3.0	61
38018	0.0297	10.1	0.40	1	-32	-156	2.9	84
42191	0.0320	10.1	2.00	1	-232	72	0.7	49
41869	0.0414	10.1	3.16	3	83	103	2.0	68
170_9	0.3557	10.0	3.04	2	-33	-33	1.9	20
274_6	0.0252	9.9	0.64	2	13	31	3.2	36
359_16	0.1661	10.2	1.37	1	-13	44	3.0	38
236_14	0.2467	10.0	5.68	2	-25	58	3.7	32
168_7	0.3185	10.2	3.42	3	29	-9	4.5	36
289_28	0.1924	10.1	1.99	2	-43	92	2.1	37
126_21	0.2623	10.1	5.56	2	-74	-65	3.4	44
232_33	0.2176	10.1	2.60	2	-88	96	2.3	48
88_11	0.1893	10.1	4.18	1	27	-31	3.7	44
8096	0.0345	10.3	1.58	1	-83	158	2.1	59
32907	0.0349	10.5	0.63	-	204	-78	2.8	80
23419	0.0400	10.4	2.51	1	-48	132	2.4	70
49433	0.0458	10.5	1.58	2	231	25	1.9	40
50550	0.0350	10.3	1.99	1	158	121	1.8	52
13159	0.0437	10.4	0.40	2	100	-27	1.9	75
51025	0.0450	10.3	0.79	1	-47	214	2.3	74
41743	0.0462	10.5	1.99	2	-57	-218	2.7	69
28365	0.0321	10.4	6.3	1	124	-27	4.3	29
34_36	0.1427	10.4	14.12	2	12	-114	3.7	49
106_34	0.2284	10.5	4.52	1	61	-108	3.7	19
94_38	0.2221	10.5	4.38	4	-204	-13	4.1	59
349_11	0.2142	10.5	0.62	1	32	23	3.7	37
132_30	0.1792	10.3	11.36	1	110	-7	3.1	12
55745	0.0278	10.9	3.98	1	-16	-62	6.6	35
22822	0.0270	10.6	1.58	1	228	-96	1.8	64
55541	0.0429	10.6	3.16	1	-120	194	3.9	81
5701	0.0422	10.7	0.63	1	141	-141	2.1	31
48604	0.0334	10.6	0.40	2	-117	-90	2.2	50
48994	0.0322	10.7	1.99	1	79	-74	6.7	86
13074	0.0486	10.9	3.16	2	176	-98	3.5	71
157_10	0.2270	10.7	6.04	3	33	-12	3.1	25
97_33	0.3218	10.6	7.42	1	23	-197	5.7	61
68_12	0.2024	10.8	18.96	2	-44	-15	6.8	30

Table 3.1: Properties of the galaxies in our sample. (1) galaxy ID; (2) redshift; (3) stellar mass; (4) star formation rate; (5) number of kinematic components identified in the QSO spectrum (from Tumlinson et al. 2013; Borthakur et al. 2015); (6) and (7) x and y coordinates of the line of sight with respect to the galactic disk, see text; (8) stellar disk scalelength; (9) inclination.

Borthakur et al. 2015, 2016) in the QSO spectra. One single galaxy is associated to each QSO and the impact parameters (projected distance between the central galaxy and the QSO line of sight) lie in the range between 10 kpc and 250 kpc from the central object, probing the circumgalactic gas from the center up to the galaxy virial radius. For a detailed description of the two surveys, see the COS-Halos and COS-GASS papers.

The purpose of this work is to derive the properties of the CGM of typical star-forming galaxies and the impact of supernova-driven galactic outflows on the cool gas dynamics and formation. To this end, we selected only a subsample of 41 disk galaxies, that satisfy the two criteria of being star-forming ($\text{sSFR} > 10^{-11} \text{ yr}^{-1}$) and having a stellar mass $10^{10} \lesssim M_*/M_\odot < 10^{11}$. With this selection we therefore excluded dwarf galaxies and massive passive galaxies (but see Chapter 2), where the cool CGM could have different origins or dynamics (see Section 3.5).

As a comparison to the predictions of our models, we will use in this work the kinematic information provided by the two surveys. For both studies, UV absorption lines of both low-ionization metals and neutral hydrogen are identified in the QSO spectra through a Voigt profile fitting analysis (Werk et al. 2013; Tumlinson et al. 2013; Borthakur et al. 2015, 2016) in a spectral window that goes from -600 to $+600 \text{ km s}^{-1}$ from the systemic velocity of the central galaxy, with a velocity resolution of about 18 km s^{-1} . Cool gas is observed in all but one spectra in our sample¹.

For consistency, we decided to focus only on one tracer and therefore to use in this work only the data concerning the hydrogen Ly α lines. This line (similarly to the metal ones) is observed in the same spectrum with different velocities, identifying different kinematic components. The presence in the spectra of multiple-component absorptions implies that the cool CGM is not a homogeneous and uniform layer of gas, but rather a composition of different clouds moving throughout the halos with a complex kinematics, a common feature found by many different studies (e.g. Bordoloi et al. 2014; Werk et al. 2016; Stern et al. 2016; Keeney et al. 2017; Zahedy et al. 2019). This will be a fundamental assumption for our models. The total number of Ly α components found around the 41 galaxies of our sample is 62 and in Table 3.1 we report the number of components for each galaxy-QSO pair. The average number of components per line of sight is 1.5.

All the properties of our sample relevant to our analysis are reported in Table 3.1 and are retrieved directly from Tumlinson et al. (2013) and Borthakur et al. (2015), except for the geometric parameters (coordinates of the sightlines with respect to the galactic disks, disk scale lengths and disk inclinations), which are obtained performing a fit for each galaxy using the software GALFIT (Peng et al. 2010). The details of the fitting procedure are explained in Appendix 3.A. In Figure 3.1 we report the absolute values of the positions of all the lines of sight, together as in one single halo, with the galaxy at the center

¹For the non-detection, Borthakur et al. (2015) report an equivalent width equal to three times the noise in the spectrum in the vicinity of the expected transition.

and the x-axis and y-axis corresponding respectively to the major and minor axis of the projected galaxy disk. The exact position of each line of sight with respect to the central object is reported in Table 3.1 and was inferred through the GALFIT analysis (see Appendix 3.A). The black solid curve depicts the median virial radius (see Section 3.3) of the 41 galaxies in our sample, equal to $r_{\text{vir}} = 272$ kpc. The size of the symbols in Figure 3.1 represents the number of components found for each sightline, which varies from one to four (the cross represents instead the only non-detection), while the different colours represent the average Ly α absorption velocities with respect to the systemic velocity of the central galaxies.

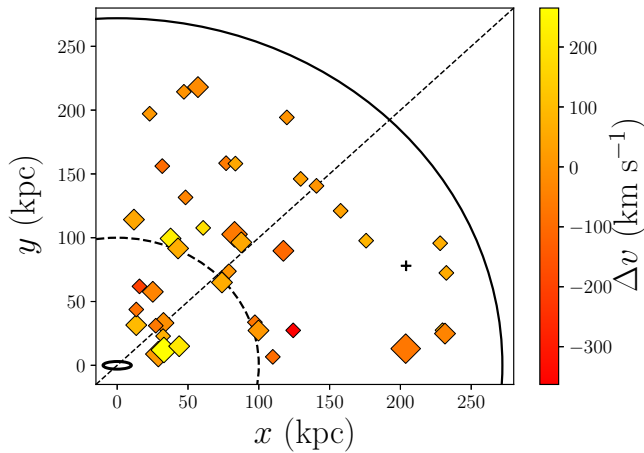


Figure 3.1: Plane of the observations for our subsample of galaxies taken from the COS-Halos and COS-GASS surveys. The ellipse at the bottom left corner represents the central disk galaxy, while the symbols depict the QSO lines of sight, placed at their corresponding distance from the central object, with the black cross representing the non-detection. The colorbar shows the average velocity of the cool CGM found for each sightline, while the size of the symbols is related to the number of components identified in each spectrum. The black solid curve represents the median virial radius of our galaxy sample (272 kpc), while the dashed curve represents a radius of 100 kpc. The dashed straight line depicts instead the bisector of the plane.

From Figure 3.1 it is therefore clear how the observations give us information spanning the entire extension of the galaxy halos, with the limitation, however, that each object has only one sightline associated to it. It is also important to note that, contrary to the claims of other surveys (e.g. Schroetter et al. 2019; Martin et al. 2019), where the cool gas absorbers seem to be found primarily along the galaxy major/minor axis, this dataset does not show any evidence of a preferential orientation for the absorption of the cool CGM, whose detections are uniformly distributed throughout the halo. We will see in Section 3.4 how this feature influences the results of our analysis.

In Figure 3.2 we report in orange the velocity distributions of all the detected components, with values ranging approximately from -400 to 400 km s $^{-1}$. As a

comparison, we also show in purple the velocity distribution of the cool CGM around galaxies selected from the surveys of Keeney et al. (2017) and Martin et al. (2019) using the same two criteria on the stellar mass and star formation rate previously used for our sample. These surveys have features similar to the ones of COS-Halos and COS-GASS, but will not be directly used in this work as a constraint for our models². We can see, however, from Figure 3.2 how the kinematics of the absorbers of our sample is representative of the one found by different studies, which justifies the choice of these two surveys as our fiducial dataset.

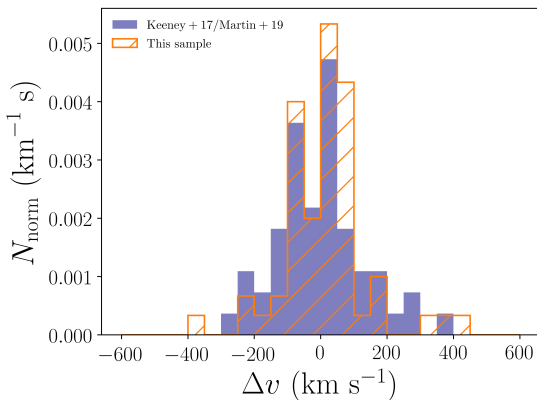


Figure 3.2: Orange-hatched histogram: velocity distribution of all the 62 Ly α components identified in the 41 QSO spectra in our sample. Purple histogram: velocity distribution of the cool CGM for a subsample of star-forming galaxies with stellar masses consistent with our main sample, drawn from (Keeney et al. 2017; Martin et al. 2019). Both distributions are normalized in order to have a subtended area equal to 1.

Figures 3.1 and 3.2 give us an overview of all the information derived from the COS observations. The cool CGM kinematics is derived throughout the whole galaxy halos, combining both the velocity of the absorbers, their number and their projected position with respect to the central galaxy. The aim of this work is to reproduce, through dynamically motivated models, all the observed velocity components at their distance from the galaxy.

3.3 Model

We mentioned in Section 3.2 that the basic assumption that underlines our modeling is that the cool circumgalactic gas is composed of different clouds. We modelled the dynamics of these clouds taking into account the gravitational potential of the galactic disk and the dark matter halo, together with the interactions of these cool absorbers with the pre-existing hot CGM. To this end, we used the publicly available python package GALPY (Bovy 2015), which allows to perform a 2-dimensional orbit integration within an arbitrary potential (we refer for more details on GALPY to the work of Bovy 2015). To develop our

²Martin et al. (2019) observed the cool gas through MgII, while we focus here only on the hydrogen lines. The galaxies from Keeney et al. (2017) have instead less strict conditions for isolation with respect to the COS-Halos and COS-GASS galaxies, therefore their cool CGM is more likely to be contaminated by other objects.

models, we implemented a modification in the code that takes into account the drag force acted by the hot corona, that strongly modifies the cloud motion (see Section 3.3.1). In this Section we describe how we built our parametric dynamical models for the cool CGM clouds ejected by star-forming galaxies and how we compare, through a Bayesian analysis of the parameter space, the predictions of our models with the COS observations of our galaxy sample.

3.3.1 Outflow of cool CGM clouds

3

In this Chapter, we investigate the scenario where the cool clouds are part of gas outflows (galactic winds) coming from the central galaxies, originated by the feedback from supernova explosions in the disk. As already introduced in Section 3.1, we model the outflow motion of the cool gas only, neglecting the effects of the hot wind, that we will discuss in Section 3.5.

Galaxy potential

In order to describe the motion of the cool clouds, we first need to assume a gravitational potential, that will pull the outflowing clouds back towards the central galaxy and, in the absence of hydrodynamical effects, determine the cloud orbits. We used an axisymmetric choice of the total potential, composed of two different components, the potentials of a razor-thin disk for the galaxy and of a dark matter halo described by a Navarro Frenk White profile (NFW, Navarro et al. 1996), whose density distributions are, respectively

$$\rho(R, z) = \Sigma_{d,0} \exp(-R/R_d) \delta(z), \quad (3.1)$$

$$\rho(r) = \frac{\rho_0}{\frac{r}{r_s} \left(1 + \frac{r}{r_s}\right)^2}, \quad (3.2)$$

where $\Sigma_{d,0} = M_*/(2\pi R^2)$ and R_d are the central surface density of the disk and its scale length (the latter obtained from the GALFIT analysis, see Appendix 3.A), $r = \sqrt{R^2 + z^2}$ is the intrinsic galactocentric radius (where R is the cylindrical radius and z is the height), M_* is the stellar mass and ρ_0 and r_s are, respectively, the central density and the scale radius of the dark matter halo. The last two quantities are inferred using the same procedure explained in Chapter 2, starting from the calculation of the virial mass and radius of the halo. To infer the halo mass we have used, given the properties of our galaxy sample, the stellar to halo mass relation of Posti et al. (2019a), obtained through the fit of rotation curves for a sample of low-redshift spiral galaxies with $10^7 \leq M_*/M_\odot < 10^{11}$. We used in particular the linear fit on the same relation performed in Posti et al. (2019b) (equation B.7). The virial mass is then calculated from M_{200} as in Chapter 2.

We acknowledge the simplistic choice of the gravitational potential, which neglects the possible presence of a bulge or other features at the center of our galaxies and employs galaxy disks that are unrealistically thin. This is however

justified by the general absence of bulges or bars in our objects (see Figures 3.11 - 3.13 in Appendix 3.A) and by the negligible influence that a thicker disk would have on the cloud orbits. The implementation of this simple potential, on the other hand, reduces the computational cost of the integration.

Integration initial conditions

Ideally, one would like to model the cloud orbits for each galaxy, each of them with a different potential, given by the different virial masses and disk radii (see Table 3.1 and equations 3.1, 3.2). That would however come at a very high computational cost. We therefore made the choice to divide our objects in three subsamples depending on their stellar masses and to create, for each one of these three samples, only one model with a potential calculated using median properties. The same model will be then applied to all the galaxies in the same subsample. We will refer to the three models as Gal1, Gal2 and Gal3 and we list their properties in Table 3.2.

(1)	(2)	(3)	(4)	(5)	(6)	(7)	(8)	(9)	(10)
	$\log(M_*/M_\odot)$ Range	n_{obj}	$\log(M_*/M_\odot)$ Median	z	SFR ($M_\odot \text{ yr}^{-1}$)	R_d (kpc)	$\log(M_{\text{vir}}/M_\odot)$	r_{vir} (kpc)	T_{vir} (10^6 K)
Gal1	9.9 – 10.3	17	10.1	0.1661	2.60	2.53	11.9	228	0.58
Gal2	10.3 – 10.6	14	10.4	0.0454	1.99	2.65	12.1	286	0.74
Gal3	10.6 – 11.0	10	10.7	0.0425	3.16	3.82	12.3	331	0.98

Table 3.2: Properties of the 3 galaxy models described in Section 3.3.1. (1) Model name; (2) range in stellar mass; (3) number of galaxies per subsample; (4) median stellar mass; (5) median redshift; (6) median star formation rate; (7) median stellar disk length; (8), (9) and (10) median galaxy virial mass, radius and temperature (see text and Chapter 2).

Once we have defined the potential, which is axisymmetric, the cloud orbits are integrated in the (R, z) (we will refer to these coordinates from here on as R_{gal} and z_{gal} , since they represent the intrinsic reference frame of the galaxy) plane and will be then uniformly distributed across azimuthal angles ϕ (see Section 3.3.2). Since the clouds are coming from the supernova explosions in the disk, we assume an initial height $z_{\text{gal}} = 0$, while the initial cylindrical radius R_{gal} is randomly selected in the range between 0 and 6 times the disk scale radius R_d , following a probability distribution corresponding to the star formation rate density (SFRD) of each galaxy model³. This is calculated using the theoretical profile of Pezzulli et al. (2015), which was tested on a sample of 35 nearby spiral galaxies. In particular, we used here for each galaxy $\nu_M = \text{SFR}/M_*$ and $\nu_R = 0.35\nu_M$, where ν_M and ν_R are respectively the specific mass growth rate and the specific radial growth rate of the disk. This is consistent with a disk inside-out growth, as found by Pezzulli et al. (2015). The SFRD profiles of the three galaxy models are shown in Figure 3.3. To perform the orbit integration,

³More in detail, the probability distribution takes into account the geometrical factor and is therefore proportional to $R_{\text{gal}} \text{SFRD}$.

the initial cloud velocity is needed. We do not assume a fixed value for this velocity, but we let it vary as a free parameter that we call v_{kick} . Once this value is defined, the two velocity components along R and z and the tangential velocity are obtained, respectively, through

$$\begin{aligned} v_{\text{kick},R} &= v_{\text{kick}} \sin \theta \cos \phi, \\ v_{\text{kick},z} &= v_{\text{kick}} \cos \theta, \\ v_{\text{kick},t} &= v_{\text{circ}} + v_{\text{kick}} \sin \theta \sin \phi, \end{aligned} \quad (3.3)$$

3

where v_{circ} is the disk circular speed⁴, ϕ is randomly selected between 0 and 2π , and θ is the angle between the direction of the kick and the vertical axis z_{gal} , ranging between 0 and the angle θ_{max} and randomly selected from a uniform distribution in $\cos \theta$. θ_{max} represents the aperture of the outflowing cone of clouds (see Figure 3.6) and is another free parameter of our analysis.

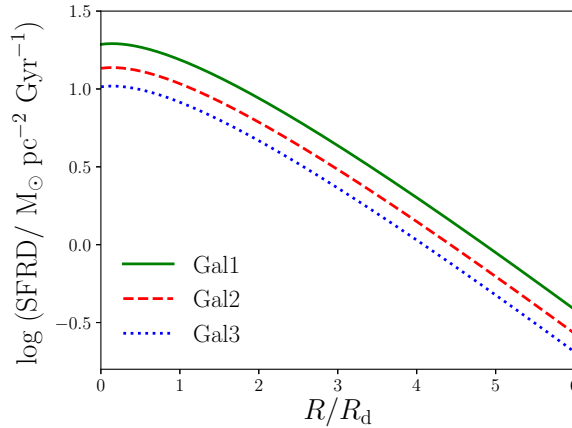


Figure 3.3: Star formation rate density for the three galaxy models described in Section 3.3.1, derived following Pezzulli et al. (2015).

We then created, for each of the three galaxy models that we defined above and for a given choice of v_{kick} and θ_{max} , N different orbits across this range of initial conditions and we integrated them for 10 Gyr. Depending on the initial conditions, the orbits will either be open, meaning that the clouds are escaping the galaxy halos, or closed, with the clouds eventually falling back to the disk. We stop the integration at the moment the clouds reach a distance $r = 1.5r_{\text{vir}}$ from the center or $z_{\text{gal}} = 0$ during their fall.

Interactions with the hot corona

If gravity were the only force driving the motion of the clouds, they would have purely ballistic orbits and the setup described in the previous Section would

⁴In our model, we assumed a positive sense of rotation for all the galaxies, since we do not have information on the direction of the disk rotation. However, using the opposite sign would not change our results.

define completely the orbit integration. However, the halos of galaxies are not devoid of gas, but rather filled with a hot medium, the galaxy corona (e.g. Anderson & Bregman 2011; Li et al. 2017a), at temperatures close to the galaxy virial temperature. In this Section, we describe how we model and introduce the coronal gas in our analysis, in order to make the cool absorber dynamics more realistic than the simple ballistic one.

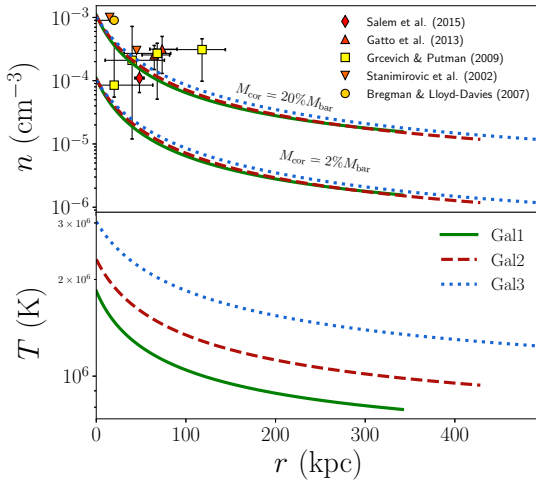


Figure 3.4: Properties of the hot gas medium for the three galaxy models, respectively density profiles on the top panel and temperature profiles on the bottom panel. The profiles are obtained as described in Section 3.3.1. On the top panel we show both the profiles for a corona bearing 20% and 2% of the total baryonic mass expected within the galaxy halo (see main text). The data points represent the observational Local Group constraints of Stanimirović et al. (2002); Bregman & Lloyd-Davies (2007); Grcevich & Putman (2009); Gatto et al. (2013); Salem et al. (2015), all taken from Sormani et al. (2018).

We define the corona as a gas in hydrostatic equilibrium with the dark matter halo described by equation (3.2). More in detail, the hot gas density profile is described by (Binney et al. 2009)

$$\frac{n_e(r)}{n_{e,0}} = \left(\frac{T}{T_0} \right)^{1/(\gamma-1)}, \quad (3.4)$$

where

$$\frac{T(r)}{T_0} = 1 + \frac{\gamma-1}{\gamma} \frac{\mu m_p}{k_B T_0} (\Phi(r) - \Phi_0). \quad (3.5)$$

Here, $\Phi(r)$ is the NFW potential, m_p is the proton mass, $\mu = 0.6$ is the mean molecular weight, γ is the polytropic index and T_0 , $n_{e,0}$ and Φ_0 are respectively the temperature, the density and the potential at the reference radius $r_0 = 10$ kpc. The polytropic index and the two normalization factors are chosen in order to have temperature and density profiles consistent with the (uncertain) observational constraints (see Figure 3.4, where the observational data points are taken from Sormani et al. 2018)⁵. More in detail, we use $\gamma = 1.2$, which allows the

⁵Note that these constraints are all related to the corona of the Milky Way, but we expect the low-redshift star forming galaxies in our sample to have coronae with similar properties.

coronal temperature to vary throughout the halo, without implying too large variations in the density and in the temperature profiles between the internal and the external regions, as shown in the two panels of Figure 3.4. With this choice, the density of the inner regions is consistent with the observational values and it slightly decreases with the galactocentric radius. An isothermal corona ($\gamma = 1$) at a temperature close to the virial one would have central densities too high to be reconciled with the observations (e.g. Salem et al. 2015), while using a higher polytropic index would lead to unrealistically low densities in the external regions of the halos. The density normalization is set in order to have a total mass of the hot gas equal to 20% of the baryonic mass within the galaxy halo, which is a fraction f_{bar} of the galaxy virial mass, where $f_{\text{bar}} = 0.158$ is the cosmological baryon fraction (Planck Collaboration et al. 2018). This choice leads to values of the density that are compatible with the observations, as can be seen in Figure 3.4. We will relax this assumption in Section 3.5.1. Regarding the temperature of the hot gas, we set an inner temperature $T_0 = 2.8T_{\text{vir}}$. The model temperature slightly decreases with the distance from the central galaxy, remaining close to the galaxy virial temperature, as from theoretical expectations (e.g. White & Rees 1978; Fukugita & Peebles 2006).

Once the density and the temperature of the corona are defined, the density of the cool CGM is obtained by imposing pressure equilibrium between the hot gas and the cool clouds (see equation 2.8), assumed to be at a temperature of 2×10^4 K, in agreement with observational estimates (Werk et al. 2013; Keeney et al. 2017; Lehner et al. 2018). The main effect of the hot gas on the clouds is to slow them down by means of the drag force, given by (see Marinacci et al. 2011 and Section 2.3.2)

$$\dot{v}_{\text{drag}} = -\frac{\pi r_{\text{cl}}^2 \rho_{\text{cor}} v^2}{m_{\text{cl}}}, \quad (3.6)$$

where v is the relative velocity between the clouds and the corona, m_{cl} is the cloud mass, r_{cl} is the cloud radius (set by the choice of the mass and the pressure equilibrium, see Section 2.3.2) and $\rho_{\text{cor}} = \mu m_{\text{p}} n_{\text{cor}}$ is the hot gas mass density, with $\mu = 0.6$ and $n_{\text{cor}} = 2.1 n_{\text{e}}$. More massive clouds will be less affected by the interactions with the hot corona, while the motion of less massive clouds will be strongly influenced by the ambient gas. In general, with respect to the ballistic case, the clouds will need higher kick velocities to reach the external parts of the halos. The mass of the clouds m_{cl} is the third free parameter of our models. We implemented in GALPY an additional part of the equation of motion of the cool clouds that takes into account the drag force acted by the hot coronal gas whose properties are described by equations (3.4) and (3.5), to obtain more realistic results from the orbit integration (Fraternali & Binney 2008).

In Figure 3.5 we show the influence of the drag force on the cloud orbits, for the model Gal2. We observe a similar behavior for the other two models. As a reference we chose, to create these orbits, $v_{\text{kick}} = 370 \text{ km s}^{-1}$, $\theta_{\text{max}} = 60^\circ$ and $m_{\text{cl}} = 10^{6.5} M_{\odot}$. The dashed curves represent the ballistic orbits, while the solid curves show the results of the scenario where the corona is also affecting (through the drag) the motion of the clouds. In each of the two scenarios,

the different distances from the central galaxy reached by the orbits are mostly due to the initial cylindrical radius R_{gal} from which the clouds are ejected: orbits starting from larger radii will reach larger distances, due to the lower pull of the gravitational potential. All the orbits end back to the central regions of the disk, with no substantial difference between the drag and ballistic scenarios, as can be seen in the zoom-in panel in the lower right part of Figure 3.5. The main difference between the two models is that in the case including the drag force of the hot gas the clouds reach much smaller distances from the central galaxy. To reach the distances that we see in the observations (up to the galaxy virial radii) we will therefore need kick velocities significantly higher than what we would expect from a purely ballistic model.

3

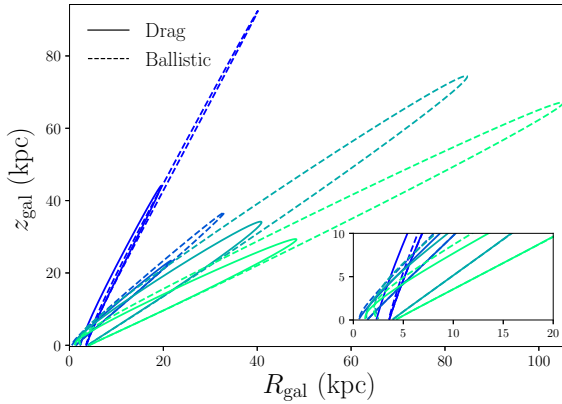


Figure 3.5: Example of cloud orbits for the model Gal2, with the following choice of parameters: $v_{\text{kick}} = 370 \text{ km s}^{-1}$, $\theta_{\text{max}} = 60^\circ$ and $m_{\text{cl}} = 10^{6.5} M_\odot$. The dashed lines represent the prediction of a ballistic model, while the solid ones show the effects of the inclusion of the drag force. The colors represent orbits starting from different positions along the galactic disk and with different angles with respect to the z_{gal} axis, selected in the range from 0 to θ_{max} . Small panel: zoom-in on the central region of the halo.

In reality, the drag force is not the only effect that the corona has on the cloud motion. In fact, our modeling does not take into account all the hydrodynamic instabilities that take place at the interface between the two gas phases (see Armillotta et al. 2017; Grønnow et al. 2018; Gronke & Oh 2018), as well as other effects like the thermal conduction. A full hydrodynamic treatment is outside the scope of this work, given the complications and uncertainties that it would imply. As we will discuss in Section 3.5.3, with a more rigorous treatment of the hydrodynamics the clouds would likely need even higher velocities to be ejected out to the same distances.

3.3.2 Outflow rate

Once the orbits have been calculated, we need to populate them with clouds and this requires the knowledge of the mass outflow rate from the galaxy. We implement a rate of mass ejection from the disk that is constant with time. Since we assume that the cool CGM comes from supernova feedback, we relate the mass outflow rates to the star formation rates of the central galaxies reported in Table 3.2, through the formula

$$\dot{M}_{\text{out}} = \eta \text{ SFR} , \quad (3.7)$$

where η is the mass loading factor and is the fourth and last parameter of our models. Dividing half of the mass outflow rate by the mass of the clouds m_{cl} we obtain the total number of clouds \dot{n}_{out} ejected from one side of the disk per unit of time and we assume that these clouds are uniformly distributed with respect to time along the N orbits that we are modelling. As explained in Section 3.3.1, the integration of each orbit is stopped once the cloud has either fallen back to the galactic disk or reached 1.5 times the galaxy virial radius: the integration time t_{orb} will then be different for every orbit. The number of clouds for each orbit is therefore given by

$$n_{\text{orb}} = \frac{\dot{n}_{\text{out}}}{N} t_{\text{orb}} . \quad (3.8)$$

Each of these clouds is placed in the orbit at a different time, separated by $\Delta t = t_{\text{orb}}/n_{\text{orb}}$, and has the properties (position in the $R_{\text{gal}} - z_{\text{gal}}$ plane, velocity components, density, radius) predicted by our model at that time. To each of the clouds is then assigned a random azimuthal position ϕ ranging from 0 to 2π and the same procedure is performed for both sides of the disk (see Fraternali & Binney 2006, 2008). Throughout this work, we use for the number of orbits $N = 30$, but our results do not depend on the choice of this number.

We show in Figure 3.6 the result in 3D of the procedure explained above, for the same choice of parameters as in Figure 3.5 and with $\eta = 2$: the clouds are distributed in a cone-like structure on both sides of the galactic disk. Note that the intrinsic reference frame of the galaxy can be different from the frame (x, y, z) of the observations, depending on the galaxy inclination (see Table 3.1).

3.3.3 Comparison with the observations

The idea behind our analysis is that our models depend on parameters that define different physical scenarios and that we let free to vary. Through the comparison of our model outputs with the COS observations, we can find the best choice of parameters and therefore the dynamical scenario that better describes the observed kinematics of the cool CGM around star-forming galaxies. In this Section we explain how we perform this comparison.

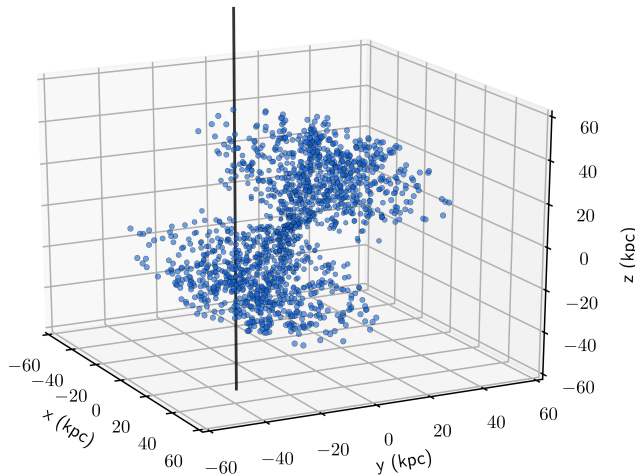


Figure 3.6: Cloud population for the same model used to create Figure 3.5, with $\eta = 2$ and a disk inclination $i = 30^\circ$. The clouds are outflowing from the galaxy in a biconical shape. The black line represents one of the lines of sight that we used to perform our synthetic observations.

Synthetic observations

To compare our results with the data we performed synthetic observations, using the cloud populations created as explained in Section 3.3.2. As already mentioned, these are obtained in the reference frames of the galaxies, which are different from the one of the observations. The lines of sight intersect a plane (x, y) that coincides with the plane $(x_{\text{gal}}, y_{\text{gal}})$, with $x_{\text{gal}} = R_{\text{gal}} \cos \phi$ and $y_{\text{gal}} = R_{\text{gal}} \sin \phi$, only if the galaxy is face on, with $z = z_{\text{gal}}$. This is however not the case for most of our galaxies, as found with the GALFIT analysis (see Appendix 3.A and Table 3.1), and we can see in Figure 3.6 how the direction of the outflowing cones does not match the direction of the line of sight (the inclination of the disk used to create this figure is equal to 30°). The first step to perform the observations of our model halos is to transform the reference frame of the galaxies into the one of the observations, through

$$y = y_{\text{gal}} \cos i + z_{\text{gal}} \sin i , \quad (3.9)$$

while we set $x = x_{\text{gal}}$. This transformation is applied to all the galaxies in Table 3.1. Once we derived the position (x, y) of each cloud, we then traced line of sights at the same positions of the observations and we picked all the clouds intercepted (the distance of the position of the cloud from the position of the line of sight is less than the radius of the cloud) and their line-of-sight velocity, through the formula

$$v_{\text{los}} = -v_{y,\text{gal}} \sin i + v_{z,\text{gal}} \cos i , \quad (3.10)$$

where $v_{y,\text{gal}} = v_R \sin \phi + v_T \cos \phi$ and $v_{z,\text{gal}} = v_z$. With this treatment, we end up having for each line of sight the kinematic prediction of our model, directly comparable with the observations outlined in Section 3.2. The creation of the synthetic observations, along with a visualization of the main parameters and properties of our models, is summarized in the diagram of Figure 3.7.

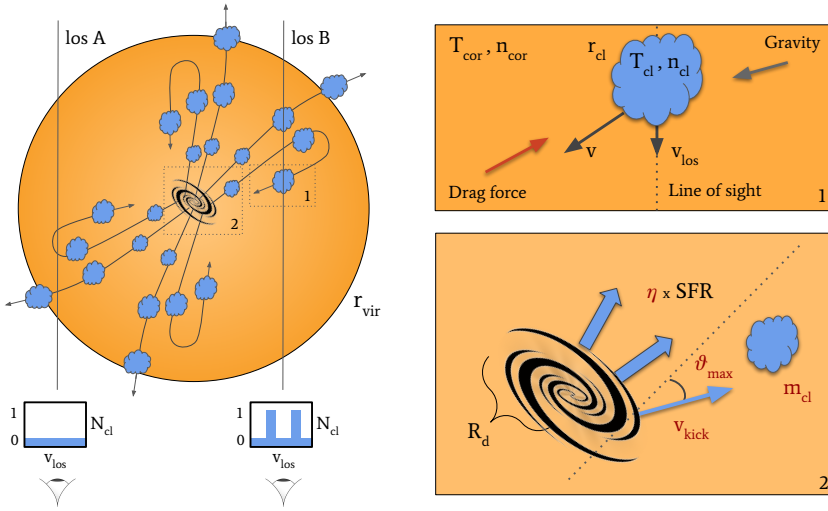


Figure 3.7: Diagram summarizing the modeling used in this work and described in Section 3.3. Left diagram: representation of the biconical outflow of clouds ejected from the central galaxy, with an example of synthetic observations along two different lines of sight. Line of sight (los) A does not intercept any cloud and therefore the resultant velocity distribution is empty, while line of sight (los) B intercepts two clouds, resulting in two different velocity components. Top right panel: zoom-in on a single cool circumgalactic cloud, with temperature $T_{\text{cl}} = 2 \times 10^4$ K and density and radius given by the pressure confinement of the hot coronal gas, whose density and temperature are found respectively through equations (3.4) and (3.5). The cloud is pulled towards the disk by the gravitational force, while the hot gas, through the drag force (equation 3.6), slows it down along its entire orbit. The velocity v_{los} , which will be compared with the real data, is the component along the line of sight of the total cloud velocity v . Bottom right panel: zoom-in on the central galaxy. The four free parameters of our models (m_{cl} , v_{kick} , η , θ_{max}) are depicted in red. The total cool mass outflow rate is proportional to the galaxy star formation rate and the starting points of the orbits are distributed along the disk following the star formation rate density of Pezzulli et al. (2015).

Likelihood

To find the best model that reproduces the observations shown in Section 3.2 we performed a Bayesian Markov Chain Monte Carlo (MCMC) analysis over the 4-dimensional space defined by the four free parameters of our modeling: m_{cl} , v_{kick} , η and θ_{max} . In order to achieve this, we compared the results obtained with the synthetic observations outlined in Section 3.3.3 with the actual COS data. The comparison was done through a likelihood that takes into account the number and velocity distribution of the absorbers observed along each individual line of sight. In particular we developed a technique to compare for each sightline the predictions for the CGM of our modeled galaxies with the observations. We call the likelihood of a single sightline \mathcal{L}_{los} . The total likelihood that we will use for the Bayesian analysis is given by the product of all the 41 single likelihoods, in order to deploy all the kinematic constraints coming from

different projected distances from the central galaxies.

The likelihood \mathcal{L}_{los} can be divided into the products of two different terms, that we call \mathcal{L}_{num} and \mathcal{L}_{kin} , which respectively represent the comparisons between the numbers of components and the kinematic distributions of model and observations. More in detail, for each line of sight we created a velocity distribution over the range from -600 to 600 km s^{-1} , using the line-of-sight velocities calculated as explained above. We divided this range in 24 bins, in order to have a bin width of 50 km s^{-1} , which is consistent with the average line width of the observed absorption lines: 53 km s^{-1} for the COS-GASS sample (from Borthakur et al. 2016) and 30 km s^{-1} for the COS-Halos sample (from Tumlinson et al. 2013). In particular, in order to have statistically significant distributions, for each choice of parameters we averaged the outputs of 50 different realizations of the same model⁶, since one individual model can be affected by fluctuations due to the intrinsic randomness of the cloud positions along the orbits (see Section 3.3.2).

For the first term of the likelihood, we used the Poisson statistics to compare the number of observed (n_{obs} , see Table 3.1) and model components n_{mod} , the latter given by the number of bins of the model velocity distribution with at least one cloud (in particular, n_{mod} is the mean value of the 50 model realizations that we are using for the comparison). This comparison is therefore given by

$$\mathcal{L}_{\text{num}} = n_{\text{mod}}^{n_{\text{obs}}} \frac{e^{-n_{\text{mod}}}}{n_{\text{obs}}!}, \quad (3.11)$$

where $n_{\text{obs}}!$ is the factorial of the observed number of components. Since \mathcal{L}_{num} is not defined for $n_{\text{mod}} = 0$ and $n_{\text{obs}} \neq 0$, in these cases we defined $n_{\text{mod}} = 1/50$, where 50 is the number of realizations. The second term is instead given by the Bayesian probability of the observed velocity components given our model. In particular the probability for each component is given by the value of the normalized model velocity distribution in the bin where that velocity is observed. We can then obtain the value of \mathcal{L}_{kin} through the product of the probabilities predicted by our model for each line of sight.

Once the two terms are defined, the total likelihood of the single line of sight is obtained through

$$\ln \mathcal{L}_{\text{los}} = (\ln \mathcal{L}_{\text{num}} + \ln \mathcal{L}_{\text{kin}}) / (1 + n_{\text{obs}}), \quad (3.12)$$

where the weight in the denominator takes into account for the number of constraints on each line of sight.

It is important to mention that, for each line of sight, the prediction of the model depends on the orientation of the disk with respect to the plane of the sky. From the GALFIT analysis we obtain an inclination angle, but we are not able to disentangle what is the orientation of the disk and therefore the direction of the outflow cones (in Figure 3.6, the direction of the two cones

⁶With 50 realization we are able to take into account the fluctuations of the model, as proven by the successful tests carried out in Appendix 3.B.

would be symmetric to the current one with respect to the z-axis if we chose an opposite disk orientation). For each line of sight, we therefore performed our synthetic observations for both orientations and we kept the one with the highest \mathcal{L}_{los} , i.e. the one more similar to the observations.

We have tested the likelihood explained above on a number of artificial data sets created with our models, in order to verify whether with this analysis we are able to properly constrain the 4 free parameters of our model. We found that the initial set of parameters can be successfully recovered by our MCMC analysis using the likelihood outlined above. The results of these tests are presented in detail in Appendix 3.B. In the next Section we will show instead what we find when we apply this likelihood to the data shown in Section 3.2.

3

3.4 Results

In this Section we report the results of the MCMC analysis on the COS data that we have performed over the parameter space using the likelihood defined in Section 3.3.3 and we discuss the physical meaning of the scenario described by the models that best reproduce the observations.

3.4.1 MCMC analysis

We explored the 4-dimensional parameter space over the following ranges:

- $5 < \log(m_{\text{cl}}/M_{\odot}) < 9$,
- $2 < \log(v_{\text{kick}}/(\text{km s}^{-1})) < 4$,
- $-2 < \log \eta < 2$,
- $\log 20^{\circ} < \log \theta_{\text{max}} < \log 90^{\circ}$,

using flat priors for all the parameters in the logarithmic space. In Figure 3.8 we report the one and two dimensional projections of the posterior distributions for the four parameters, with the values of the 32th, 50th and 68th percentiles (also reported in Table 3.3). Note from Figure 3.8 that there is a very well defined region of the parameter space where the posterior is maximized: the models with this choice of parameters represent the physical scenario that best reproduces the observations.

In Figure 3.9 we show how the results of our best models compare with the observational data that we have used in this work, displaying in particular, on the left, the total velocity distribution of the cool gas absorbers and, on the right, the number of components as a function of the projected distance from the central galaxy. The results are averaged over 100 different models with the 4 free parameters ranging in the area of the parameter space highlighted in Figure 3.8 within the 32nd and 68th percentiles of the posterior distributions. The observed velocity distribution, in orange, is the same as the one shown in Figure 3.2, while the model distribution is obtained combining all the

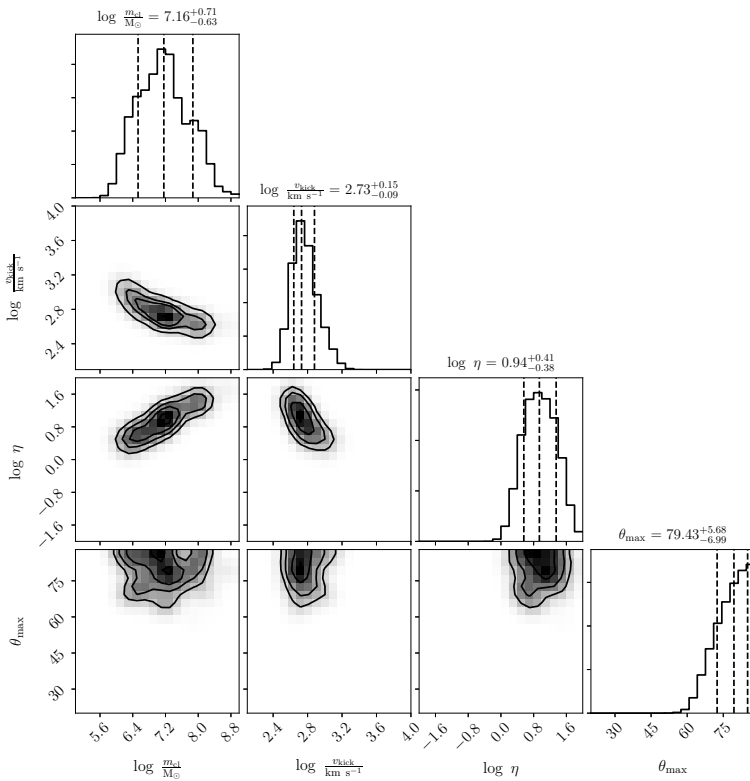


Figure 3.8: Corner plot with the MCMC results, representing the one and two dimensional projections of the posterior probabilities for the four free parameters of our models. The parameter space is explored in the logarithm of the angle θ_{\max} , but the results are transformed here in physical units for clarity.

velocities obtained for each line of sight using the technique explained in Section 3.3.3. We can note how with our analysis we have found models for which the total kinematic distribution of the cool gas clouds is consistent with the observations. A Kolmogorov-Smirnov test confirmed that the two distributions of observations and model are consistent with each other, with a probability value $p = 0.25$. To obtain the plot in the right panel of Figure 3.9 we divided the radial range into uniform bins of 35 kpc, each of them containing a certain number of sightlines. Both for model and observations we calculated the average number of components per line of sight in each bin, with the uncertainties given by the standard deviation of the observations. We can see how, also in this case, the model predictions (blue line connecting the average model values of each bin) are consistent with the observations (orange points), with the number of components decreasing as the distance from the galaxy increases. We therefore conclude that an outflow scenario, using a very particular choice of physical parameters, is overall able to reproduce the observational features of the COS

data of the cool CGM around star-forming galaxies.

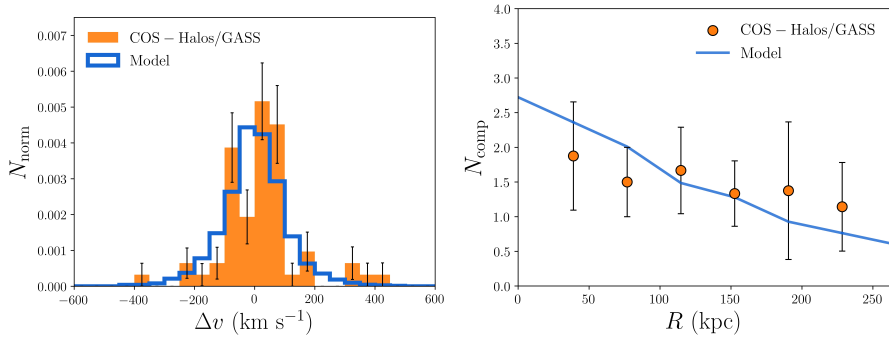


Figure 3.9: Comparison between the outputs of the best models found with the MCMC analysis (blue) and the observations (orange), see Section 3.4.1 for more details. Left: total velocity distributions, with the errors in the observations calculated through bootstrapping. Right: average number of components per line of sight in radial bins of 35 kpc, as a function of the projected distance from the central galaxy (the blue line connects the model values predicted for each bin). The uncertainties are given by the standard deviation of the number of observed components for each bin.

In Figure 3.10 we can look more in detail at the properties of the models outlined above, in particular using the median value of the posterior probabilities of the 4 parameters. One peculiarity of the observations outlined in Section 3.2 is that the cool absorbers are observed till very large distances from the central galaxies (see Figure 3.1). Therefore, to be able to reproduce these data, the orbits derived with our models must reach these large distances: this is visible in the three panels of Figure 3.10, where we show the orbits described by the clouds for the three galaxy models. The higher the mass of the galaxy, hence the virial mass of the halo, the stronger is the gravitational pull and the harder is for the clouds to travel to distances comparable to the virial radius. Moreover, the COS data present only one non-detection, with the cool CGM observed ubiquitously over the (x, y) plane (Figure 3.1). In order to match this feature of the observations, our models require very large apertures for the outflow cones, with $\theta_{\text{max}} \geq 80^\circ$. The outflows are therefore not collimated along the minor axis of the galaxies and they are instead more isotropically distributed. The different length of orbits in the same galaxy model is mainly due to the different initial R_{gal} of each orbit, since the clouds are distributed along the disk in the range going from 0 to 6 times the disk scale radius, as explained in Section 3.3.1. More external orbits will experience a weaker gravitational pull and therefore, at equal ejection velocity, will travel to larger distances.

We can see from Figure 3.10 how some of the orbits are open, with the clouds escaping outside the virial radius (represented by the dashed curve in each panel) and never coming back to the central galaxy, while other orbits describe a cycle in which the clouds are travelling to very large distances and eventually fall back towards the galactic disk. To reach these distances the cloud need to have

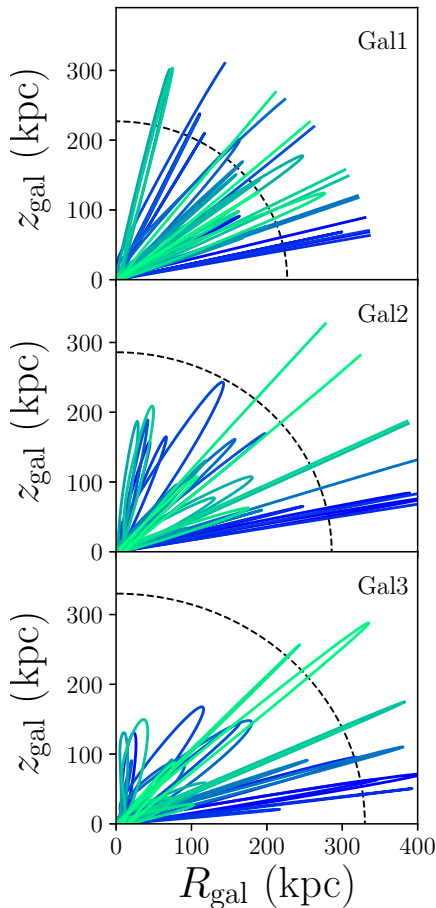


Figure 3.10: Representative orbits of the clouds for the best models, obtained using the median value of the 4 parameters reported in Figure 3.8. The three panels show the results of Gal1, Gal2 and Gal3 and the dashed curves show the value of the virial radius for each of the three galaxies. As in Figure 3.5, different orbits are shown in different colors.

large masses, in order to minimize the drag force (see equation 3.6) acted by the corona, and initial velocities of more than 500 km s^{-1} . We will see in the next Section the physical implications of these values of the parameters.

3.4.2 Physics of the outflows

In Section 3.4.1 we have seen that outflow models of cool clouds can reproduce the COS-Halos and COS-GASS kinematic data. In this Section, we look instead at the implications that this model has for the efficiency of star formation feedback. The value of the 4 parameters has very important implications from an energetic point of view. The kinetic energy produced by supernovae per unit

time and available for the wind is given by (Cimatti et al. 2019)

$$\dot{K} \approx 3 \times 10^{40} \left(\frac{f_{\text{SN}}}{0.1} \right) \left(\frac{E_{\text{SN}}}{10^{51} \text{ erg}} \right) \left(\frac{\text{SFR}}{M_{\odot} \text{ yr}^{-1}} \right) \text{ erg s}^{-1}, \quad (3.13)$$

where f_{SN} is the efficiency of the supernovae in transferring energy to the wind and E_{SN} is the amount of energy released by one supernova explosion. We can estimate the efficiency predicted by our models by calculating the kinetic power of the outflowing wind, which can be expressed as

$$\dot{K}_{\text{out}} = \frac{1}{2} \dot{M}_{\text{out}} v_{\text{kick}}^2, \quad (3.14)$$

where \dot{M}_{out} is the mass outflow rate as defined in equation (3.7). The efficiency necessary to reproduce the cool CGM clouds with our outflow models will then be given by the ratio between equations (3.13) and (3.14). Using as a kick velocity and as a mass loading factor the best values found with the MCMC analysis and the canonical value $E_{\text{SN}} = 10^{51} \text{ erg}$, we obtain $f_{\text{SN}} \sim 2.5$, which corresponds to an efficiency of energy transfer from the supernova explosions to the wind gas of about 250%. Clearly, such a value is not physically justifiable, since it means that the outflows would need more energy than the one available from the supernovae. Moreover, from a theoretical point of view the supernovae are expected to radiate away most of their energy (e.g. McKee & Ostriker 1977) and roughly only 10% of it is expected to be transferred to the gas as kinetic energy (Kim & Ostriker 2015; Martizzi et al. 2016). Recent simulations (Fielding et al. 2018) show that this number could increase to 20-30% if we consider spatial and temporal clustered supernova explosions, but even these enhanced efficiencies are still far lower than the one that would be needed to reproduce the observations in an outflow scenario, as we have found. Other stellar feedback modes, like winds from massive stars, can certainly not account for this discrepancy, since the SNe are by far the dominant source of energy over the other mechanisms (Elmegreen & Scalo 2004). The efficiency would be significantly reduced if the circumgalactic clouds were originated in a period in which the star formation rates of the galaxies were much higher than the current ones. This would reduce the mass loading factors needed to reproduce the observations. However, the typical timescales that our models predict for the clouds to travel from the central galaxy to their current positions are of the order of two Gyr or less and we do not expect all the galaxies in our sample to have had significantly different star formation rates during this period. Even though sporadic fast outbursts of star formation could have happened in the last two Gyr, it is highly unlikely that they can explain the entirety of the cool circumgalactic gas, that is observed almost ubiquitously at any line of sight intersecting the galaxy halos.

We have found therefore that even though the outflow models can reproduce the cool CGM observations, the implications of these models are unfeasible from an energetic point of view. In particular, the velocities and mass loading factors required to reproduce the data lead to unphysical scenarios that need

more energy than the one available from the stellar feedback of the central galaxy. Moreover, the scenario described in Section 3.4.1 is unlikely to be a realistic representation of the CGM also because of other properties of the outflowing clouds. In particular, we have seen that to reach the distances seen in the observations, the clouds need to be extremely massive in order to overcome the deceleration acted by the coronal drag force (see Section 3.3.1). With our fitting analysis we obtain a cloud mass of about $10^7 M_{\odot}$, a value that is much higher than the typical masses (which are however very uncertain) expected for these clouds (see Werk et al. 2014; Keeney et al. 2017). These very high masses lead the clouds to have radii that go from about 2 kpc in the inner regions to 7 kpc in the external parts, where the densities are lower. Even though there is some observational evidence (Rubin et al. 2018) of similar scales for the cool CGM absorbers, it is unlikely that the majority of the clouds have such large radii, in particular the ones just ejected out of the galaxy. Each of these clouds would have a size comparable with the one of the region of the disk from which they were all produced in the first place. The picture described by these models is therefore unrealistic and hardly justifiable.

We conclude that an outflow of clouds driven by star formation in the galactic disk is not a realistic scenario to describe the dynamics of the cool CGM of star forming galaxies in the Local Universe.

3.5 Discussion

We have seen, in the previous Section, that winds of cool clouds powered by the supernova explosions in the central galaxy are not a viable way to successfully describe the circumgalactic medium around star-forming galaxies. This result, in contrast with many claims of cool CGM gas being produced by outflows, both from observations (e.g. Rubin et al. 2014; Chisholm et al. 2015; Schroetter et al. 2019; Martin et al. 2019) and simulations (e.g. Muratov et al. 2015; Ford et al. 2016) may seem controversial, but is motivated by the unphysically high kinetic energy that these outflows would need to reproduce our dataset. In this Section, we discuss the limitations of our models and we try to further verify our results relaxing some of the assumptions that we made in Section 3.3. We will then describe the implications of our findings, especially regarding the origin of the cool CGM.

3.5.1 Influence of the hot gas

One of the main features of our models is the presence of a pre-existing hot circumgalactic corona in the halos of our galaxies, whose interaction with the cool clouds is strongly influencing their motion, as we have seen in Sections 3.3 and 3.4. The drag force (Marinacci et al. 2011) acted by the hot gas decelerates the clouds, forcing them to have high initial velocities in order to reach the large distances where they are observed. Moreover, a fundamental effect of the hot gas is to pressure confine the cool clouds (Pezzulli & Cantalupo 2019). In

Model	$\log (m_{\text{cl,start}}/M_{\odot})$	$\log (v_{\text{kick}}/(\text{km s}^{-1}))$	$\log \eta$	θ (degrees)	f_{SN}
Fiducial	$7.16^{+0.71}_{-0.63}$	$2.73^{+0.15}_{-0.09}$	$0.94^{+0.41}_{-0.38}$	$79.43^{+5.68}_{-6.99}$	2.5
$M_{\text{cor}} = 2\% M_{\text{bar}}$	$7.00^{+0.91}_{-0.87}$	$2.65^{+0.06}_{-0.06}$	$0.42^{+0.42}_{-0.40}$	$77.62^{+7.49}_{-11.56}$	0.6
Minor axis	$6.10^{+1.93}_{-0.59}$	$3.02^{+0.40}_{-0.36}$	$0.35^{+0.92}_{-0.23}$	$53.70^{+20.43}_{-12.02}$	2.6
Inner regions	$5.78^{+1.81}_{-0.39}$	$3.04^{+0.46}_{-0.48}$	$0.42^{+0.66}_{-0.33}$	$47.86^{+19.75}_{-12.38}$	3.3

Table 3.3: 50th percentiles (with errors given by the 32nd and the 68th percentiles) of the posterior distributions of the four parameters obtained with the MCMC fits performed for the 4 models described in this work and consequent efficiencies of the supernova explosions.

fact, without the confinement of an ambient medium, the clouds would tend to expand and would not be in a stable state. We will indeed see later in this Section that the density of the hot gas strongly influences the size of the cool CGM absorbers. As already mentioned in Section 3.1, the presence of hot gas at temperatures similar to the virial one and bearing a significant amount of baryons (e.g. Shull et al. 2012) is well justified by cosmological models (e.g. White & Frenk 1991) and has been confirmed by numerous observations (e.g. Anderson & Bregman 2011; Li et al. 2017a; Bogdán et al. 2017; Faerman et al. 2020).

Our description of this gas phase is physically motivated as a stratified medium in hydrostatic equilibrium with the dark matter halo and is consistent with the current evidence from observations, which are however still limited and mostly reliable only for the inner parts of the halos. We can see from Figure 3.4 how, in particular for the densities, there is a scatter of almost two orders of magnitudes between different observational estimates of the density of the hot gas. Our assumption of a mass of hot gas equal to 20% of the total (cosmological baryon fraction) baryonic mass theoretically associated to the halo (see Section 3.3.1) leads to densities that are well in agreement with the observational range. A slightly smaller mass fraction would however not be inconsistent with the observational estimates, given the large uncertainties. Since the efficiency of the drag force, and therefore the amount of deceleration of the clouds, depends on the density of the hot gas, the conclusion of the previous Section might change using a corona with a mass lower than the one employed in our fiducial model. We tested this possibility lowering the total mass of the hot phase to 2% of the cosmological baryonic one: the density profiles for the three galaxy models of Table 3.2 are showed in the top panel of Figure 3.4. We can see how these profiles are already inconsistent with the majority of the data points, representing then a very extreme model for the hot gas. We exclude the possibility of having a corona with even lower masses.

In Table 3.3 we report the results of the MCMC analysis for a model with

the properties explained above, in particular the median value of the posterior distributions of the 4 parameters, with the 32nd and 68th percentiles. We can see how the different mass of the corona changes the region of the parameter space recovered by the MCMC and therefore the best values of the parameters. As expected, with a more diffuse hot gas the clouds can more easily reach the observed distances from the central galaxies, where they are originated. The ejecting velocities and the mass of the clouds are however only slightly lower than in the previous case. At a fixed mass, the deceleration by drag force is indeed proportional to $\rho_{\text{cor}}^{1/3}$ (see equation 3.6). This dependence is therefore relatively weak and a variation in the normalization of the hot gas density does not dramatically influence the dynamics of the cloud. Moreover, this effect is counteracted by the larger cross section of the absorbers, since a lower gas density leads to larger clouds because of the pressure equilibrium. The main difference in the MCMC findings is in fact given by the mass loading factor, that is less than half what previously found, since the larger clouds can more easily be intercepted by the lines of sight. We therefore need less clouds to reproduce the data, hence a lower mass loading factor.

The efficiency of energy transfer from the supernovae, calculated through equations (3.14) and (3.13) as in Section 3.3 and using the median values of the kick velocity and mass loading factor reported in Table 3.3, is equal. In this case, to 60%. This value means that only a fraction of the energy coming from the supernova explosions is being transferred as kinetic energy to the cool winds and is therefore more realistic than what we previously found with our fiducial model. However, as already mentioned, most of the SN energy is expected to be radiated away (McKee & Ostriker 1977) and typical expectations for the value of the efficiency are of the order of 10% or less (e.g. Kim & Ostriker 2018). The fraction that we find is therefore still far too high to be explained only with the stellar feedback as an energy source. Moreover, in this scenario the clouds have sizes even larger than in our fiducial case, with radii of more than 10 kpc. This feature makes the picture described in this Section even more unrealistic than the one shown in Section 3.4.1. Most importantly, as already mentioned above, the mass of the hot gas used for this test is an extreme scenario, with densities barely consistent with a few and inconsistent with the majority of the observational estimates. We therefore conclude that the choice of the coronal medium does not influence the final result that cool supernova-driven outflows cannot reproduce the entirety of the cool circumgalactic gas.

A final important assumption that we made for the hot medium is about its kinematics. In particular, we assumed the corona to be static and supported only by the hydrostatic equilibrium with the dark matter halo. Theoretical studies (Pezzulli et al. 2017) have shown however how the hot gas is required to rotate in order to satisfy galaxy evolution constraints. From an observational point of view the kinematic information are instead still limited, due to the low spectral resolution of current X-ray telescopes, and related only to the Milky Way (Hodges-Kluck et al. 2016). From both theory and observational estimates we expect the coronal gas to rotate at velocities lower than the rotational ve-

licity of the galactic disk. Considering the very high outflow velocities that we have found for our best models, we do not expect the rotation of the corona to strongly influence the orbits of the cool clouds. We therefore believe that a rotating corona would not significantly influence our results. In Chapter 4, we study the CGM of M31 using a more sophisticated model that also describes the rotation of the hot gas.

A general mechanism that is invoked to bring cool circumgalactic gas to very large distances is the entrainment of cool clouds, pushed by fast-moving hot winds to the external parts of the halos (e.g. Schneider et al. 2020). In this scenario the corona is therefore not static as described by our models, but is flowing out from the central galaxy. The drag force from the outflowing hot gas would work in the opposite direction of the pre-existing hot gas employed in our models, accelerating the clouds and therefore lowering the values of the unphysical efficiencies discussed in Section 3.4. Including this additional push in our models could potentially decrease the initial ejection velocity of the clouds, towards more physically motivated scenarios. However, the gas in the hot phase should have masses comparable to the cool CGM and therefore the mass loading factor should substantially increase, increasing the necessary energy budget of the winds as a direct consequence. Moreover, the hot winds should show velocities of hundreds of km s^{-1} , which are not seen in the (uncertain) observational estimates of the corona kinematics (e.g. Hodges-Kluck et al. 2016), as well as metallicities close to the solar value, which are also in contrast with observational findings (e.g. Bogdán et al. 2017; Bregman et al. 2018). We therefore conclude that a scenario with hot gas outflowing and entraining cool clouds to the external regions is most likely not a viable description of the circumgalactic medium (see also the discussion in Section 4.5.1).

3

3.5.2 Cool gas distribution

In this work we assumed that the cool circumgalactic gas is entirely part of outflows originated by the supernova feedback in the central galactic disk. However, different studies, both from a theoretical and an observational point of view (e.g. Hafen et al. 2019; Martin et al. 2019; Schroetter et al. 2019) have suggested that the cool clouds have two distinct origins and while some of them are part of galactic winds, others are instead accreting along the plane from external gas towards the central galaxy. This picture results in a bimodal angular distribution of the absorbers, segregated along the minor (winds) and major axis (accretion) of the galaxy (e.g. Kacprzak et al. 2012). As mentioned in Section 3.1, this scenario is still debated, in particular since other studies find no correlation between the cool gas metallicity and the azimuthal angle of the absorptions (e.g. Péroux et al. 2016; Pointon et al. 2019). Moreover, in our sample we do not see any evidence of a preferential axis in the detection of the cool CGM.

In the first part of this Section we assume that the picture of the bimodal gas distribution is true and we calculate what would be the efficiency needed by

galactic winds to reproduce only the observations along the galaxy minor axis. In order to do this, we performed our MCMC analysis on a subsample of the observations, selecting only the lines of sight within 45 degrees from the galaxy minor axis (all the absorptions above the bisector in Figure 3.1). In Table 3.3 we report the results of this analysis (minor axis). The models that best reproduce the observations have mass loading factors that are smaller than the ones obtained with our fiducial model (although with large uncertainties). This is expected since in this experiment the outflows need to reproduce a lower number of absorbers. However, the clouds are less massive than what previously predicted, forcing the ejection velocities to be extremely high, of the order of 1000 km s^{-1} . If we calculate the efficiency of the supernovae in transferring energy to the cool winds, we obtain $f_{\text{SN}} \approx 2.6$, very similar to the one obtained through the comparison with all the absorbers. We therefore can conclude that supernova-driven outflows would need to be unphysically powerful in order to reproduce the observed cool gas kinematics along the galaxy minor axis. This could imply that there might be accretion of external gas (see Section 3.5.4) also along this axis, in agreement with what has been found by the studies of the gas metallicity (e.g. Pointon et al. 2019).

A second viable way to reduce the energy budget required by the outflows is to assume that the cool gas does not reach the extremely large distances seen in the observations, comparable with the virial radii, but instead only the internal parts of the halos. The most external absorbers might have a different origin and not be related to the central galaxies (see Section 3.5.4). To investigate further this hypothesis, we have performed a test similar to the one outlined above, but selecting only the lines of sight within a projected radius of 100 kpc (see Figure 3.1). In this way, despite having less information to constrain our models (only 11 lines of sight satisfy the requirement), we can test whether the inner part of the cool CGM can be produced by galactic outflows in a physically motivated scenario. Note however that the distances of the observations are projected and therefore only a lower limit for the intrinsic distances of the clouds in our models. The results of this test might then be influenced by clouds that reach distances larger than 100 kpc.

In Table 3.3 we show the best fit results of this analysis (inner regions). We can see how the main differences with the previous parameter values are the mass of the clouds and the aperture of the outflowing cone. A mass of less than $10^6 M_{\odot}$ is in this case sufficient for the clouds to reach the distances of this subsample of the data and the outflows do not need to be isotropic ($\theta \lesssim 50^{\circ}$), contrary to what we found for our fiducial model⁷. Nevertheless, the ejection velocities and mass loading factors lead to supernova efficiencies that are still extremely high, even higher than the previous ones. This result is then opposite to what we expected (lower efficiencies), but it is motivated by the fact that these models reproduce better than the fiducial model the gas kinematics

⁷This is due to the fact that, in this particular region of the plane of the observations, there is a small number of lines of sight located close to the x -axis, as can be seen in Figure 3.1.

observed in the inner regions (a Kolmogorov-Smirnov test between the model and observed velocity distributions for these 11 lines of sight gives a probability value $p = 0.13$ for the fiducial model and $p = 0.26$ for the model described in this Section). The findings of this experiment demonstrate that most of the observations up to ~ 100 kpc from the central galaxies cannot be explained only with galactic winds, as generally found in hydrodynamical simulations (e.g. Brook et al. 2012; Ford et al. 2014). Indeed, often simulations employ efficiencies of energy transfer that are larger than unity to produce such large-scale outflows, which is consistent with our findings and demonstrates that these galactic outflows are not viable to describe the circumgalactic medium, except for maybe the gas residing in the very central regions (few tens of kpc) of the halos. This result is also in line with the study of Concas et al. (2017), who found that high-velocity galactic winds are rare in the Local Universe and, when present, seem to be driven mainly by AGN activity, rather than pure star formation. We conclude then that most of the cool CGM is not formed by galactic wind outflows, but has instead a different origin, as we will discuss more in detail in Section 3.5.4.

3.5.3 Limitations of the model

The approach of this work is to use semi-analytical models to study the CGM of star-forming galaxies. As we explained in Section 3.1, our method has several advantages with respect to hydrodynamical simulations, both cosmological and idealized high-resolution ones. The former are indeed able to track the whole extent of the circumgalactic gas inside a galaxy halo but are not able to resolve the cool clouds and their interactions with the hot medium; the latter, instead, can trace the hydrodynamic instabilities and thermal conduction that characterize the cloud evolution, but can only focus on a very small part of the halo. Our parametric approach allows us to have a comprehensive view of the CGM and, through a thorough comparison with the observations, to derive some fundamental properties of this medium. This comes however with some limitations, that we will discuss in the following.

Our representation of the cool clouds is simplified, since the real clumps of cool gas are not spherical, but have irregular shapes due to the second-order effects taking place at the interface between hot and cool gas, as clearly shown by hydrodynamical simulations (see Chapter 5). Physical effects like the Kelvin-Helmoltz (KH) instability, that tend to strip gas from the clouds hence destroying them, are neglected in our parametrization, as well as thermal conduction, which on the one hand suppresses the KH instability and on the other makes the clouds evaporate into the hot medium (e.g. Armillotta et al. 2017; Lan & Mo 2019). All these effects influence the survival time of the cool clouds and can lead to their evaporation into the corona, which is a major feature that is not taken into account in our models. Lan & Mo (2019), using semi-analytical models similar to the one developed here, found indeed that more than 50% of the cool clouds ejected from the central galaxy will evaporate into the hot halo.

Nevertheless, the disruption of the clouds goes in the direction of strengthening our result, since the clouds will lose mass and therefore would need even higher velocities than the one predicted by our model in order to overcome the drag force deceleration of the hot gas and reach the external regions of the halo before disruption. We then conclude that the cloud evaporation would not change the findings of this work.

Different studies (e.g. Marinacci et al. 2011; Armillotta et al. 2016; Gronke & Oh 2018) have found how, in the region close to the galaxy disk, the gas at the interface between cool clouds and the hot corona reaches temperatures that allows it to cool very rapidly and therefore to condense, forming more cool gas. This has been proposed as a viable mechanism to accrete new gas and sustain the star formation of the central galaxy (Fraternali & Binney 2008; Marinacci et al. 2010b), or to explain the survival of cool gas clumps embedded in fast hot gas outflows (Schneider et al. 2018). This is however restricted to the very internal regions of the halos, a few kpc above the galactic disk, where the density and temperature of the corona create the condition for the condensation of the mixed gas, while the evaporation of the clouds, whose implications for our findings have already been discussed, seems to be the most relevant effect at larger distances (e.g. Armillotta et al. 2017), which those probed with our study.

Another limitation of our models is to consider that the outflows are powered only by the supernova feedback, neglecting in particular a possible central AGN, which is often invoked in hydrodynamical simulations (e.g. Nelson et al. 2019) as a source of the circumgalactic gas. Although we have no clear evidence in our galaxies of AGN activity (Werk et al. 2013; Borthakur et al. 2015), previous AGN outflows could have influenced the motion of the gas and could have been a potential additional source of energy for the cool winds. This would therefore go in the direction of making the outflow scenarios more realistic from an energetic point of view. We however consider it unlikely for the AGN to be a dominant energy source for the cool outflows along the whole lifetime of all our galaxies and we conclude that this addition would most likely not influence our main result.

3.5.4 Origin of the cool CGM

Throughout this Chapter, we have proved that winds from the galactic disk, powered by the supernova feedback, cannot account for most of the cool circumgalactic gas around star-forming galaxies. In this Section, we will speculate on the possible origin of this gas.

External origin

The main reason for the unphysical efficiencies that we found in this work is the fact that the cool clouds have to travel from the galactic disk out to very large distances in order to reproduce the observations. Zoom-in hydrodynamical simulations (e.g. Oppenheimer et al. 2018; Nelson et al. 2019) show however how

the circumgalactic gas is probably produced by a combination of different processes and while the galactic winds have a crucial role in the gas dynamics and origin (in this type of simulations), a significant part of it is accreted from the intergalactic medium. Cosmological models predict indeed that galaxy halos are acquiring external gas (e.g. Fakhouri et al. 2010) and this accretion might be the origin of the cool absorbers observed by the COS surveys. In particular, we could expect filaments of low-metallicity gas (Lehner et al. 2016) to enter the galactic virial radius and to be disrupted into clouds by the interactions with the hot pre-existent CGM. A similar scenario has also been proposed for the cool gas around early-type galaxies, where outflows from the passive central galaxy likely play a minor role in the origin of the circumgalactic gas (e.g. Huang et al. 2016). In the halos of these galaxies, the drag force acted by the corona on the infalling clouds slows down their motion and leads to cloud velocities that are in agreement with the observations (Zahedy et al. 2019; Chapter 2).

Since we have proven that galactic outflows fail in successfully describing the cool CGM of star-forming galaxies, the accretion of intergalactic gas might be a more plausible scenario for the origin of the cool gas. This picture of inflow of external gas would be consistent with the cold-mode accretion scenario (e.g. Kereš et al. 2009), where cold gas filaments directly enter the galactic virial radius and can eventually reach and feed the central galaxy with new gas (Dekel et al. 2009). As we have seen in Section 3.5.2, our work leads to the conclusion that the outflows can be responsible for the cool CGM only in the very central regions (few tens of kpc) of the halo. We conclude that the most likely origin of the majority of the cool circumgalactic clouds is instead the accretion of external gas, as we have found for early-type galaxies (Chapter 2). As already mentioned, this scenario would also be consistent with the fact that a significant part of the cool gas absorbers observed around low-redshift galaxies have low metallicities (e.g. Wotta et al. 2019).

A second possible external origin for the cool CGM is the stripping of gas from satellite galaxies. Recent simulations (e.g. Anglés-Alcázar et al. 2017; Hafen et al. 2019) have found that winds of cool gas from satellites could produce a significant fraction of the circumgalactic medium of the central object. Moreover, stripping from satellite galaxies has extensively been observed in the Local Universe, with one of the most evident examples being the Magellanic Stream in the halo of the Milky Way (e.g. Brüns et al. 2005). Lately there has been evidence of similarities between the kinematics and positions of dwarf galaxies around M31 and the properties of the cool ionized gas (see Lehner et al. 2020) observed in its halo. Even though we have neglected the stripping from satellite galaxies in our work, this origin can not be ruled out and is likely to be part of the complex picture of the CGM of star-forming galaxies.

Condensation of the hot gas

We have seen that the accretion of external gas is one of the most likely scenarios for the origin of the cool CGM. Another way to form cool gas is through the cooling of the corona residing in the galaxy halo. The direct radiative cooling

of the hot CGM (hot-mode accretion) is not an efficient way to create cool gas, since its very low densities, especially in the outermost regions, imply cooling times of the order of the Hubble time. Thermal instabilities could, however, lead the corona to condense locally, forming cool clumps that eventually fall down towards the galaxies. This type of condensation (still debated, see Binney et al. 2009) has been recently predicted by some theoretical models, where the feedback from the central galaxy regulates the development of the instabilities (e.g. Thompson et al. 2016; Voit 2018). This process, however, generally originate the cool clouds at smaller radii than the typical scales of the CGM analysed in this work. Recent hydrodynamical simulations (Nelson et al. 2020) also show that, at least for massive elliptical galaxies, a non negligible amount of cool gas can originate from thermal instabilities triggered by density perturbations in the hot corona.

Even though we believe that most of the cool gas has an external origin (see Section 3.5.4), the condensation of the hot medium residing in the galaxy halos cannot be excluded and could play a role in the creation of part of the cool CGM.

3.6 Summary and conclusions

In this Chapter, we have developed parametric semi-analytic models in order to describe the kinematics of the cool circumgalactic medium observed in the halos of low-redshift star-forming galaxies.

In particular, we have made the main assumption that the cool gas absorbers are part of galactic wind outflows powered by the supernova explosions in the galaxy disk. We have investigated whether this kind of scenario is able to reproduce the observational dataset of the COS-Halos and COS-GASS surveys, focusing on a subsample of 41 star-forming galaxies. We have compared the outputs of our models with the observations using a Bayesian MCMC analysis, in order to constrain the main properties of the cool gas outflows.

Through this analysis we have obtained the following results:

1. axisymmetric models of cool clouds outflowing from the galactic disk are able to reproduce the line-of-sight velocities and number of components observed by the COS-Halos and COS-GASS surveys. In order for the outputs of our models to be consistent with the observations, the clouds need to have masses of about $10^7 M_{\odot}$ and initial ejection velocities higher than 500 km s^{-1} , while the outflows need to be almost isotropic and with mass loading factors of about 10;
2. given the ejection velocities and mass loading factors necessary to reproduce the data, the energy required by these cool outflows is much larger (250%) than the one available from supernova explosions. The same applies if we compare our models with only the observations along the minor axis or within 100 kpc from the galactic disk. We can therefore conclude that cool outflows from stellar feedback are not producing the cool CGM;

3. since we excluded the outflows as a source for the cool gas, we conclude that most of this medium has different origins, the most promising being accretion from the intergalactic medium, but also potentially condensation of the hot halo gas and gas stripping from satellite galaxies.

With this study we reinforced the idea that most of the cool circumgalactic medium is originated by the accretion of gas from the IGM, similar to what we have previously found for massive early-type galaxies in Chapter 2. Our main conclusion is therefore that supernova-driven outflows from the central galaxies most likely have a much smaller role in the dynamics and origin of the cool CGM than what is generally believed.

3.A Fitting of the galaxy images

Some of the parameters of the galaxies in our samples, reported in Table 3.1, have been retrieved performing a fitting of the data with the software GALFIT, which uses parametric functions to model objects in 2-dimensional images (see for more details Peng et al. 2010). The images of the 41 galaxies in our sample have been retrieved from the Sloan Digital Sky Survey (SDSS, Blanton et al. 2017) for the COS-GASS galaxies (24/41 of our sample) and from the DESI legacy imaging survey (Dey et al. 2019) for the COS-Halos galaxies (17/41 of our sample) and are shown in Figures 3.11, 3.12 and 3.13.

In particular, we used the GALFIT software to fit an exponential disk parametric function on the galaxies, described by

$$\Sigma(r) = \Sigma_0 \exp(-R/R_d), \quad (3.15)$$

where Σ_0 is the central surface brightness and R_d is the disk length. The best models resulting from the fits are shown in Figures 3.11, 3.12 and 3.13, where we can see how the model contours (blue) match very well the observational ones (in orange). The contour levels are placed at 2, 4 and 8 times the noise level in each of the images.

In particular, for our models (see Section 3.3) we are interested in the galaxy inclinations, the positions of the sightlines with respect to the galaxy disk and the galaxy disk scale length. The latter is directly inferred as one of the parameters of the GALFIT fitting⁸, while the other two are calculated starting from the galaxy axis ratio and position angle, which are the direct outputs of GALFIT.

The inclinations in particular are obtained through the formula

$$\cos i = \sqrt{\frac{(b/a)^2 - q_0^2}{1 - q_0^2}}, \quad (3.16)$$

where b and a are, respectively, the minor and major axis of the disk, while b/a and $q_0 = 0.2$ are respectively the apparent and intrinsic disk axis ratio. The position angle is instead used together with the information of the positions of the QSO sightlines and the galaxies (from Tumlinson et al. 2013; Borthakur et al. 2015) to calculate the projected distances of the QSOs from the galaxies, in the reference frame of the galactic disk.

The inclinations, distances of the lines of sight and disk scale lengths of the 41 galaxies in our sample are reported in Table 3.1.

⁸All the distances obtained from GALFIT are transformed from pixel to arcsec using the pixel scales of the SDSS and legacy surveys, respectively 0.396 and 0.06. They are subsequently transformed in kpc using the *cosmology.FlatLambdaCDM* routine of the python *astropy* package.

3.B Tests on mock data

In this appendix, we present tests that we carried out to investigate the validity of the likelihood described in Section 3.3.3. In particular, we applied the MCMC analysis on different sets of mock data, with the purpose of verifying whether with our analysis we can retrieve the true values of the 4 free parameters of our models: m_{cl} , v_{kick} , η and θ_{max} , under the assumption that the cool CGM is outflowing from the central galaxies, powered by the supernova explosions in the disk.

3

We considered specific choices of these four parameters and through the synthetic observations described in Section 3.3.3 we created the mock observations that correspond to a certain number of velocity components for each line of sight. We then performed the MCMC analysis using the likelihood described in Section 3.3.3 and treating the mocks as a set of observations. We present here 3 different tests that we carried out using 3 different choices of the input parameters. In Figures 3.14, 3.15 and 3.16 we show the results of these tests, showing in particular the one and two dimensional posterior distributions of the free parameters, with the blue points representing the values of the parameters from which the mock data have been created. We can see how these values, in all the tests, have been successfully retrieved by our MCMC analysis. From the corner plots we observe some degeneracy, meaning that there is not a single choice of parameters, but an entire region of the parameter space that leads to models that have outputs consistent with the true one. The true value is however always within the 32nd and 68th percentiles of the posterior distributions. From this analysis we conclude that, if the cool clouds are part of galactic outflows, with our likelihood we are able to properly find the choice of parameters, or at least the region of the parameter space, that best reproduces the real observational data.

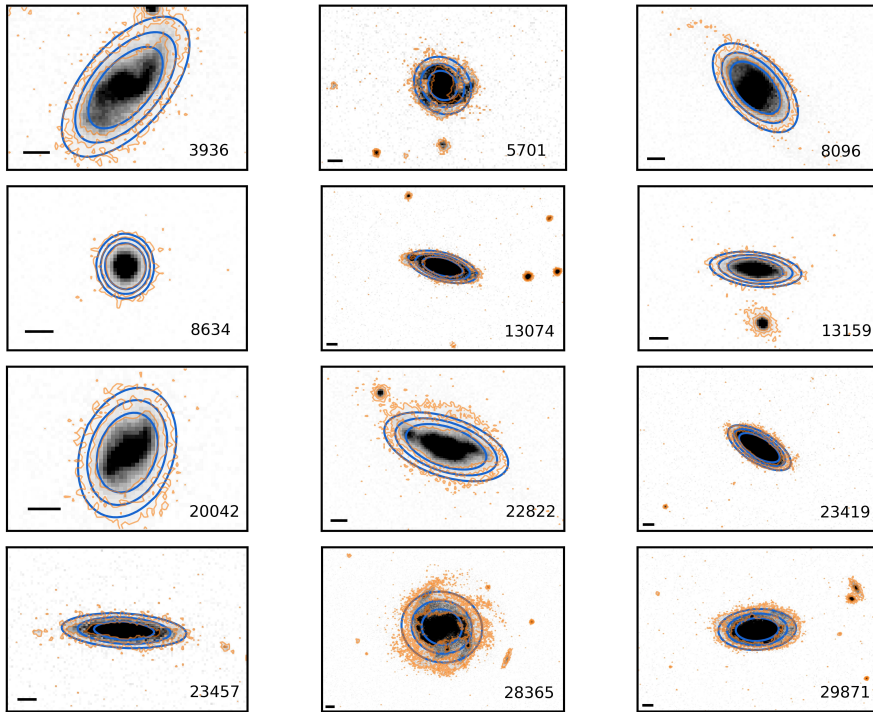


Figure 3.11: SDSS images of 12 out of the 24 galaxies selected from the COS-GASS survey. The contours are placed at 2, 4 and 8 times the noise level in each image. The orange contours represent the data, while the blue ones represent the GALFIT best model. The black bar depicts an angular size of 3 arcseconds.

3

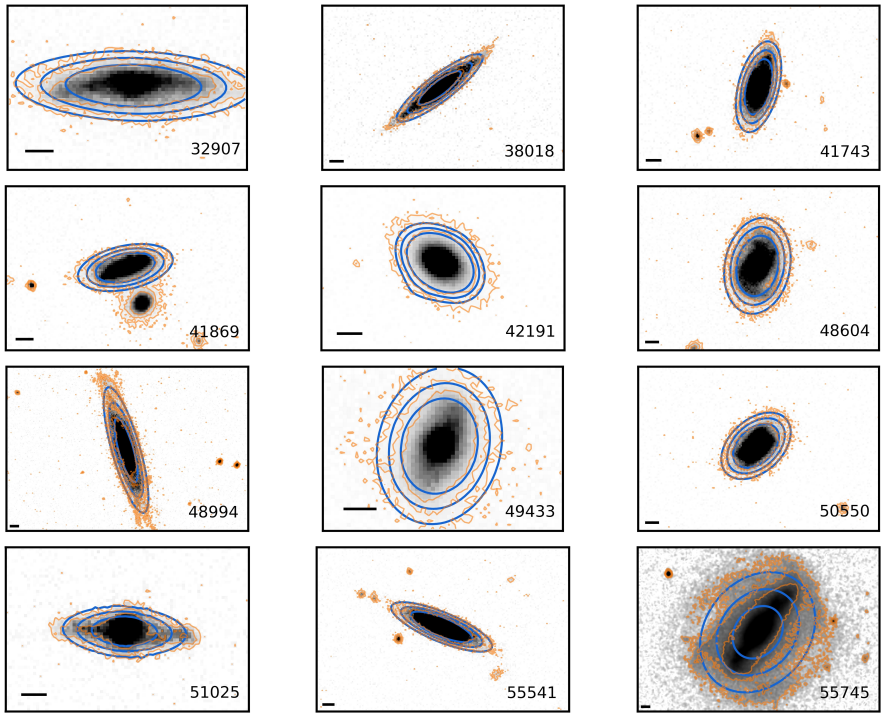


Figure 3.12: Same as Figure 3.11, for the rest of the galaxies in our sample of COS-GASS galaxies.

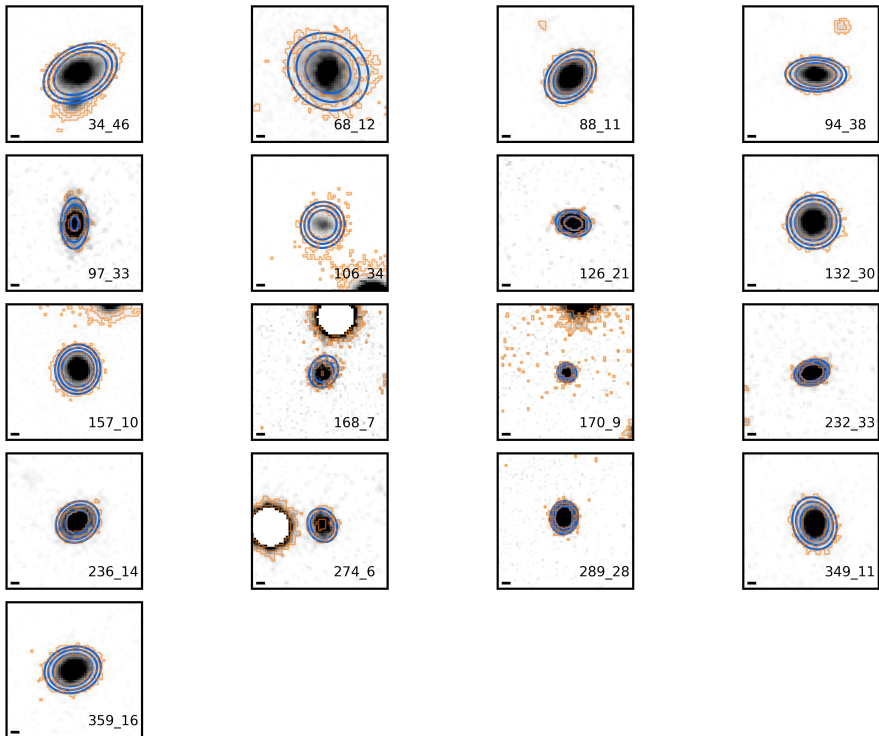


Figure 3.13: DESI legacy images of the 17 galaxies selected from the COS-Halos survey. The contours and the black bar are the same as in Figures 3.11 and 3.12.

Figure 3.14: Corner plot with the MCMC results, representing the one and two dimensional projections of the posterior probabilities for the four free parameters of our model. Test on the mock data obtained with input values of the parameters $\log m_{\text{cl}} = 6$, $\log v_{\text{kick}} = 3.1$, $\log \eta = 0.5$ and $\theta_{\text{max}} = 75^\circ$, represented by a blue dot in the parameter space.

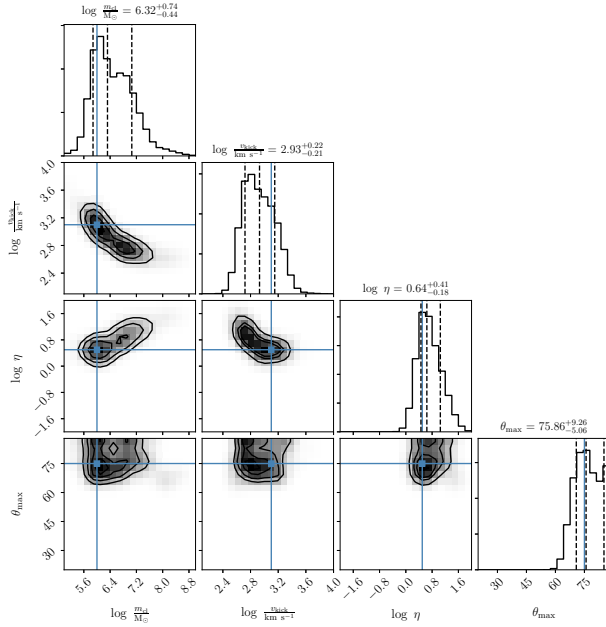
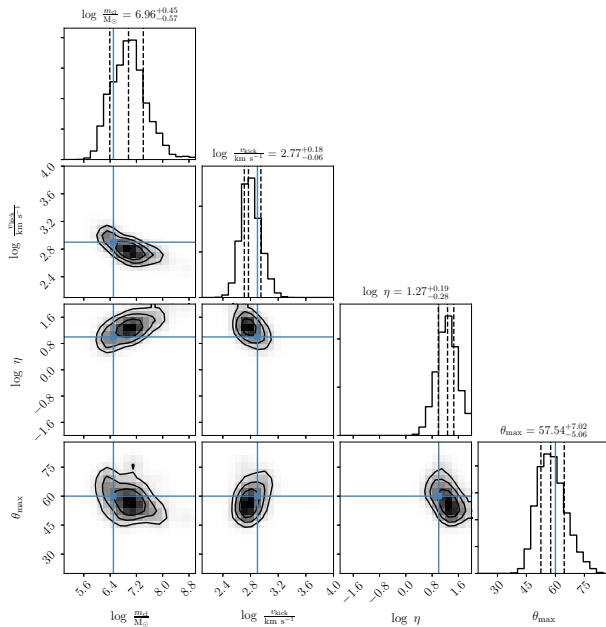


Figure 3.15: Same as Figure 3.14, for the mock data obtained with $\log m_{\text{cl}} = 6.5$, $\log v_{\text{kick}} = 2.9$, $\log \eta = 1$ and $\theta_{\text{max}} = 60^\circ$.



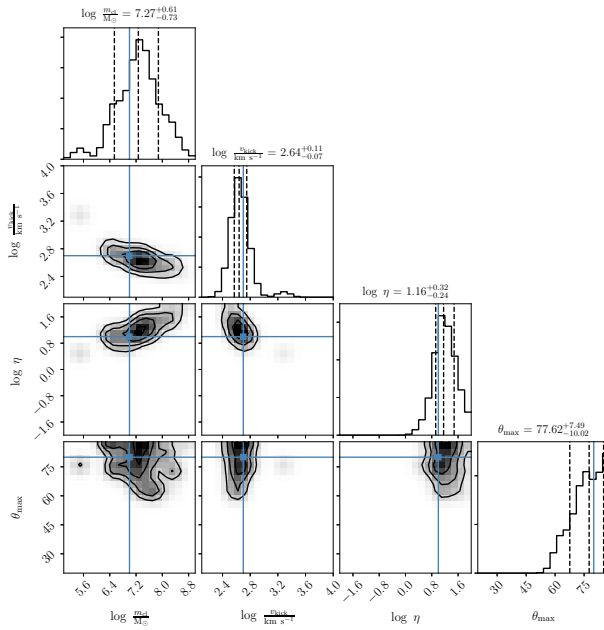


Figure 3.16: Same as Figures 3.14 and 3.15, for the mock data obtained with $\log m_{\text{cl}} = 7$, $\log v_{\text{kick}} = 2.7$, $\log \eta = 1$ and $\theta_{\max} = 80^\circ$.

Chapter 4

Inflow of low-metallicity cool gas in the halo of the Andromeda galaxy

based on

– A. Afruni, G. Pezzulli & F. Fraternali, 2021 –

MNRAS, in press

Abstract

As the closest L^* galaxy to our own Milky Way, the Andromeda galaxy (M31) is an ideal laboratory for studies of galaxy evolution. The AMIGA project has recently provided observations of the cool ($T \sim 10^4$ K) phase of the circumgalactic medium (CGM) of M31, using HST/COS absorption spectra along ~ 40 background QSO sightlines, located up to and beyond the galaxy virial radius. Based on these data, and by the means of semi-analytic models and Bayesian inference, we provide here a physical description of the origin and dynamics of the cool CGM of M31. We investigate two competing scenarios, in which (i) the cool gas is mostly produced by supernova(SN)-driven galactic outflows or (ii) it mostly originates from infall of gas from the intergalactic medium. In both cases, we take into account the effect of gravity and hydrodynamical interactions with a hot corona, which has a cosmologically motivated angular momentum. We compare the outputs of our models to the observed covering factor, silicon column density and velocity distribution of the AMIGA absorbers. We find that, to explain the observations, the outflow scenario requires an unphysically large ($> 100\%$) efficiency for SN feedback. Our infall models, on the other hand, can consistently account for the AMIGA observations and the predicted accretion rate, angular momentum and metallicity are consistent with a cosmological infall from the intergalactic medium. The infalling gas is likely not reaching the disk at the same rate of accretion that we estimate at the virial radius, due to evaporation. A more thorough analysis of the evaporation rate of the cool medium will be carried out in Chapter 5.

4.1 Introduction

The Andromeda galaxy (M31) is our closest external L^* galaxy and therefore represents an ideal laboratory for galaxy evolution studies, in many respects even more than our own Milky Way (MW). The privileged view that we have on this star-forming, disk galaxy, has allowed us to extensively observe and study it for decades, unveiling a large number of its physical properties, including those of its stellar (e.g. Widrow et al. 2003; Waltherbos & Kennicutt 1988; Courteau et al. 2011) and dark matter components (e.g. Corbelli et al. 2010; van der Marel et al. 2012; Zhang et al. 2021), its current and past star-formation rate (e.g. Rahmani et al. 2016; Williams et al. 2017) and the different components of its interstellar medium (e.g. Carignan et al. 2006; Draine et al. 2014; Caldú-Primo & Schruba 2016; Kavanagh et al. 2020).

While the stellar halo of M31 is well known and has been extensively studied in the past (e.g. Ibata et al. 2001; Gilbert et al. 2018; McConnachie et al. 2018; Escala et al. 2020), the current picture of its gaseous halo is however much less complete. The gaseous environment of M31 has been observed in neutral hydrogen (HI) emission, but only clouds within a few tens of kpc from the disk have been detected (in analogy to other nearby star-forming galaxies, e.g. Sancisi et al. 2008; Putman et al. 2012), with the exception of a more extended 'HI bridge' that connects M31 with its companion galaxy M33 (e.g. Braun & Thilker 2004; Thilker et al. 2004; Lockman et al. 2012; Wolfe et al. 2016). There is to date only limited and indirect evidence of the presence of a diffuse hot medium extending up to the galaxy virial radius (Zhang et al. 2021; Putman et al. 2021).

Studies on the MW and on external nearby galaxies have shown how galactic halos typically contain a large amount of ionized gas, the circumgalactic medium (CGM), which represents the interface between the intergalactic medium (IGM) and the central galaxy. A significant amount of baryons seems to reside in the CGM (e.g. Gatto et al. 2013; Werk et al. 2014) and, therefore, the role of this medium is believed to be crucial for the growth and evolution of galaxies. This gas can be used to study both the accretion of gas towards the galaxy (e.g. Kereš et al. 2009) and the effect of supernova/AGN feedback on the galactic environment (e.g. Nelson et al. 2019). Unveiling the properties and dynamics of this medium is therefore key for our understanding of the cycle of baryons in and around galaxies (e.g. Ford et al. 2014).

The CGM is composed of distinct phases with very different temperatures and densities, from the cool ($T \sim 10^4$ K, see for example Borthakur et al. 2015; Keeney et al. 2017; Huang et al. 2021) to the hot ($T \sim 10^{6-7}$ K, see for example Anderson & Bregman 2011; Li et al. 2017a) phase. While the hot medium is primarily observed in X-ray, the cool gas is generally observed in the UV band, using various absorption lines in the spectra of background quasi-stellar objects (QSOs), typically with only one line of sight per galaxy (see Tumlinson et al. 2017, and references therein). To date, the cool phase of the CGM has been associated both with inflow of external gas (e.g. Bouché et al. 2013; Chen et al.

2019a) and outflows from the central galaxy (e.g. Rubin et al. 2014; Schroetter et al. 2019), but what is the relative importance of these two processes and which one is dominant in determining the properties of this gas is still unclear and debated.

While our position inside the galactic disk limits the study of the extended circumgalactic gas in the MW (Marasco & Fraternali 2011; Zheng et al. 2015), M31 represents an ideal candidate for the study of this medium. Recently, a new set of observations from the AMIGA project (Lehner et al. 2015, 2020) has shed light on the cool ($T \sim 10^4$ K) and warm ($T \gtrsim 10^5$ K) phases of the CGM of M31. In particular, they analysed the absorption lines of a number of metal ions, including three different ionization states of Silicon (Si II, Si III and Si VI), in the spectra of more than 40 background QSO sightlines, spanning up to and beyond the galaxy virial radius. These data represent a unique and unprecedented view on the CGM of a single galaxy, showing the distribution of this cool gas across the entire galaxy halo, in contrast with typically one single line of sight available through the halos of more distant galaxies (but see Lopez et al. 2018). However, a clear physical picture able to interpret the AMIGA data is still missing. The aim of this Chapter is to fill this gap and, building on this unique dataset, to provide a physical model for the origin and dynamics of the CGM of M31.

To describe the dynamics and properties of the CGM of M31, we adopted a similar approach as in Chapters 2 (Afruni et al. 2019) and 3 (Afruni et al. 2021), where we made use of semi-analytical parametric models to interpret observations of the CGM of low-redshift galaxies. In particular, we describe the CGM as formed by a population of cool clouds flowing through the galactic halo and embedded in a hot coronal gas. We then compare the predictions of these models with real data through a Bayesian analysis in order to find the best physical parameters that describe the observations. In Chapters 2 and 3, we have coupled our models with observational data from two different samples of respectively early-type (ETGs Chen et al. 2018; Zahedy et al. 2019) and star-forming (see Werk et al. 2013; Borthakur et al. 2015) galaxies. We have found that in the ETGs the cool CGM is well reproduced by an inflow of clouds falling at a rate consistent with the accretion predicted by cosmological models; for star-forming galaxies we investigated instead the impact of galactic feedback on the surrounding CGM, finding that supernova-driven galactic winds cannot reproduce the cool absorbers observed at distances larger than a few tens of kpc from the central galaxy, given the unphysical energy requirements that this scenario would imply.

Our semi-analytic approach allows therefore a physically motivated description of the dynamics of the CGM clouds throughout the galaxy halo, taking into account the effects of gravity, pressure and the drag force acted by the hot medium. These studies are then complementary to cosmological hydrodynamical simulations, which are still limited by insufficient resolution in the circumgalactic medium (e.g. van de Voort et al. 2019; Peebles et al. 2019).

Having only one line-of-sight per galaxy, in our previous studies we have as-

sumed, in both samples of star-forming and early-type galaxies, that the properties of the CGM would be statistically similar for all the galaxies of the same type. The AMIGA data allow us instead to go beyond this statistical approach and to model in detail the CGM of a single galaxy. Moreover, the measures of the total silicon column densities, available from this survey for each line of sight, will allow us to directly estimate the metallicity of the cool CGM, a property that is still very uncertain and debated in the literature (see Prochaska et al. 2017; Wotta et al. 2019; Pointon et al. 2019). This is fundamental to constrain the origin of this medium, given that finding low-metallicity gas would point at IGM accretion, while metallicities close to the solar value would imply gas ejected from the interstellar medium.

Both our previous works hint towards a picture where the accretion of external gas is likely the origin of the vast majority of the cool CGM surrounding galaxies in the local Universe. Here, we explore both scenarios of inflow from the IGM and outflow from a galactic wind as a possible description of the cool CGM of M31, taking into account also the rotation of both the hot and the cool phase.

In Section 4.2 we briefly report the observations of the AMIGA project and the data selected for our work; in Section 4.3 we describe the semi-analytical parametric models and the way we compare our synthetic observations with the AMIGA data; in Section 4.4 we show the results of our analysis and, finally, in Section 4.5 and 4.6 we, respectively, discuss our findings and we report our conclusions.

4.2 Data: the project AMIGA

The AMIGA project (Lehner et al. 2015, 2020) is an HST large program aiming to characterize the properties of the cool/warm phase of the CGM in the halo of M31, using a sample of 43 QSO sightlines at projected distances from 25 to 569 kpc from the center of M31. The target QSOs are observed using the COS spectrograph (Froning & Green 2009) with the G130M and/or G160M gratings. Here we use, in particular, the data reported in Lehner et al. (2020), who analysed the cool and warm (temperatures of about 10^{4-5} K) CGM of M31 through the study of the absorption lines coming from species such as CII, SiII, SiIII, SiIV and OVI. For our analysis, we decided to focus on the absorbers that lie (in projection) within the virial radius of M31 (which we estimate to be 336 kpc, see Section 4.3 and Table 4.1). Absorbers at distances larger than about 350 kpc from the galactic disk have a higher probability of not being directly related to M31 and to possibly be part of a local group medium (see Putman et al. 2021; Qu et al. 2021)¹. This selection leaves us with 23 lines of sight (see Figure 4.1) out of the 43 of the original AMIGA sample (13 out of the 20 excluded sightlines are non-detections).

The spectra were inspected in the velocity range $-700 \leq v_{\text{LSR}} \leq -150 \text{ km s}^{-1}$. The

¹We have verified that applying our models to the whole data sample of the AMIGA Project has a negligible impact on the findings of this work.

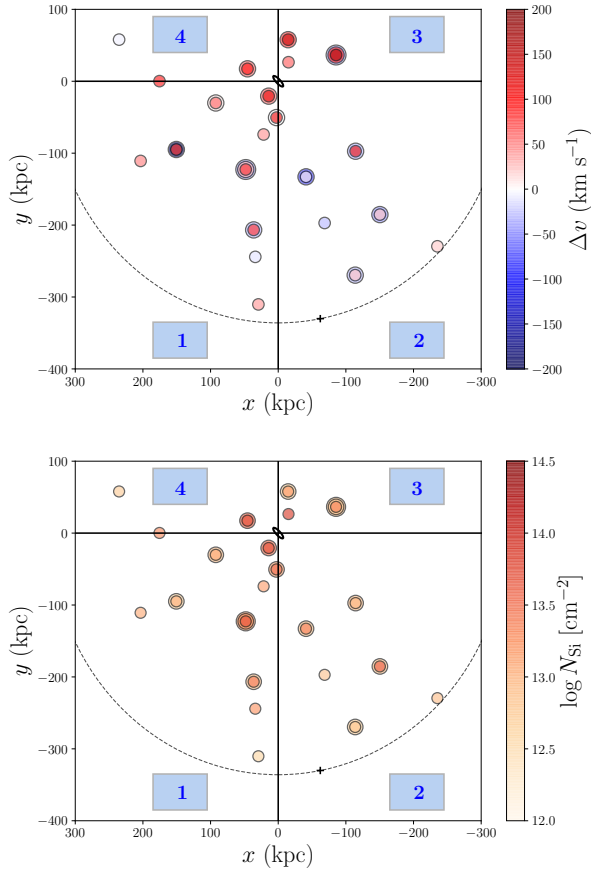


Figure 4.1: Observational data from the AMIGA project (Lehner et al. 2020) used in this work. Top: SiIII velocities with respect to the systemic velocity of M31; bottom: total silicon column densities. In both panels the central ellipse represents the disk of M31, with a position angle in this reference frame of 45° , while the circles represent the 23 QSO sightlines at their projected position. Multiple velocity components are shown by overlapping circles with different colors. The cross depicts the only non-detection of SiIII present in our sample. The dashed circle represents the virial radius of M31, while the vertical and horizontal lines are used to divide the plane in 4 quadrants.

lower limit corresponds to about 100 km s^{-1} less than the most negative velocities associated with the M31 rotation ($\sim -600 \text{ km s}^{-1}$ in the LSR, with the systemic velocity of M31 being -300 km s^{-1} , see Chemin et al. 2009), while the upper limit is set to avoid the absorption of the MW, which dominates at v_{LSR} from -150 to $+50 \text{ km s}^{-1}$. In addition to the Milky Way, another important source of contamination is the Magellanic Stream (MS), since its line-of-sight velocities can overlap with those expected from the CGM of M31. As discussed in detail in Lehner et al. (2015, 2020), this contamination was removed from the

AMIGA data by excluding, for each line of sight, all the kinematic components with velocities that lie within the MS velocity range, inferred by Nidever et al. (2010) using the HI 21 cm emission detected with the Green Bank Telescope. The same cut will be also applied to our models (see Section 4.3.4).

Most of the sightlines host multiple kinematic components and the velocities and column densities for each component were then obtained using the apparent optical depth (AOD, Savage & Sembach 1991) method. For the purpose of this work, we considered the silicon absorption lines as tracers of the cool circumgalactic medium. In particular, following Lehner et al. (2020), we identify the different kinematic components using the SiIII lines, being the SiIII the species with the strongest observable transition. As reported in Lehner et al. (2020), there is a good agreement in the kinematic pattern resulting from low ion absorptions (SiII, CII, SiIII), presumably tracing the same cool gas phase at $T \sim \text{few} \times 10^4$ K. Moreover, detecting the absorption of SiII, SiIII and SiIV, a direct estimate of the total silicon column density² in the cool CGM of M31 is possible, largely insensitive to the details of photo-ionization modelling (see Lehner et al. 2020). The constraint given by the observed total silicon column density will allow us to give an estimate of the gas metallicity directly through the comparison of these densities with the outputs of our models (see Sections 4.3 and 4.4).

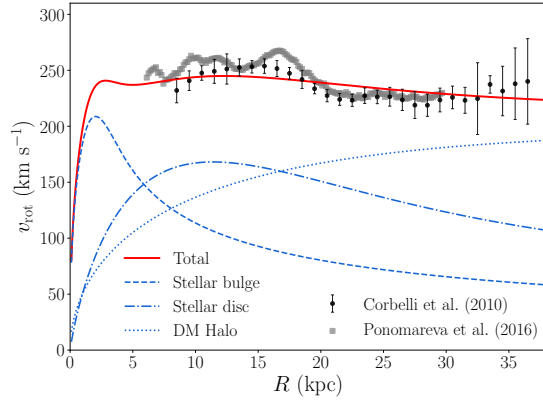
In the two panels of Figure 4.1 we show the velocities (top) and the total silicon column densities (bottom) that we will use as constraints for our models. We show in particular the cool gas kinematics with respect to the systemic velocity of M31, obtained from the observed LSR velocities using the transformation reported in Lehner et al. (2020).

4.3 Model

The model used in this work has many similarities with the models presented in Chapter 2 and Chapter 3. As in our previous works, we describe the cool CGM as a population of clouds in pressure equilibrium with the ambient hot medium (corona), flowing towards the galaxy or outflowing from the central disk. The cool CGM is subject to the gravitational force of the galaxy and the DM halo and to the interaction with the corona. To describe the cloud motion we use the python package GALPY (Bovy 2015), which we modified in order to take into account the drag force acted by the hot coronal gas (see Fraternali & Binney 2008 and Chapter 3). We explore two separate scenarios of outflow and inflow as an origin of the cool clouds, each defined by a different set of 5 free parameters, as we explain in detail in Section 4.3.3.

²In those cases where SiII and/or SiIV were not detected, but SiIII was, we adopted the upper limit for the non-detected lines. This procedure affects the total column densities in about 20% of the sample.

Figure 4.2: Rotation curve decomposition of M31 adopted in this work. The data points are obtained using the HI 21-cm emission and are taken from Corbelli et al. (2010) and Ponomareva et al. (2016). The red curve shows the total circular speed predicted by our model, in good agreement with the observations. The total circular speed is given by the sum of three different components: a stellar bulge (dashed curve), a stellar disc (dotted-dashed curve) and a NFW dark matter halo (dotted curve) (see Section 4.3.1).



4

4.3.1 Creation of the M31 setup

To create the setup for our models, we first need to set up the gravitational potential generated by the central galaxy and the dark matter (DM) halo. For the dark matter component we choose a Navarro Frenk White (NFW, Navarro et al. 1996) profile, while for the stellar component we adopt a thin exponential disk plus a spherical central bulge with a density distribution equal to

$$\rho_{\text{bulge}}(r) = \rho_{\text{bulge},0} \left(\frac{r_0}{r} \right)^\alpha \exp \left[-(r/r_c)^2 \right], \quad (4.1)$$

also used by Bovy (2015) to describe the bulge of the Milky Way, where $\rho_{\text{bulge},0}$ is the bulge mass density at the reference radius r_0 and α and r_c are two parameters representing, respectively, the slope of the inner power law and the cut-off radius (see below). We adopted a disk scale length $R_d = 5.3$ kpc (see Walterbos & Kennicutt 1988; Courteau et al. 2011) and a bulge to total ratio $B/T = 0.25$ (Widrow et al. 2003; Chemin et al. 2009). The mass of both the stellar and the dark matter components are uncertain, with values in the range $1 - 1.5 \times 10^{11} M_\odot$ for the stellar mass (e.g. Corbelli et al. 2010; Sick et al. 2015; Williams et al. 2017) and $0.6 - 2.4 \times 10^{12} M_\odot$ for the dark matter mass (see Zhang et al. 2021, and references therein). In this work, we used intermediate values of $M_* = 1.2 \times 10^{11} M_\odot$ and $M_{\text{vir}} = 2 \times 10^{12} M_\odot$. The choice of these values produces a circular speed that well matches the observed rotation curve of M31 (Corbelli et al. 2010; Ponomareva et al. 2016), as shown in Figure 4.2. We also chose $\alpha = 1.2$ and $r_c = 2$ kpc for the bulge profile (see equation (4.1)) in order to reproduce the observed rotation curve. Note however how the central parts of this curve are not sampled by the observational data, therefore a slightly different choice for α and r_c is possible. This, however, would have minimal effects on our final results. The adopted virial mass implies a concentration

$c = 10.25$ (from Dutton & Macciò 2014) and a virial radius

$$r_{\text{vir}} = \left(\frac{2GM_{\text{vir}}}{\Delta H_0^2} \right)^{1/3} = 336 \text{ kpc} , \quad (4.2)$$

where $H_0 = 67.4 \text{ km s}^{-1} \text{ Mpc}^{-1}$ (Planck Collaboration et al. 2020) and $\Delta = 101$ (calculated using the prescription of Bryan & Norman 1998).

The galactic disk of M31 has an inclination $i = 77^\circ$ (see Walterbos & Kennicutt 1988; Athanassoula & Beaton 2006). The far-side of the galaxy is on the South-East and the near-side on the North-West (see Carignan et al. 2007; Chemin et al. 2009). We set the intrinsic reference frame of all our models in order to have a positive tangential velocity v_t in the same sense of rotation of M31. All the properties of the Andromeda galaxy used in this work are reported in Table 4.1.

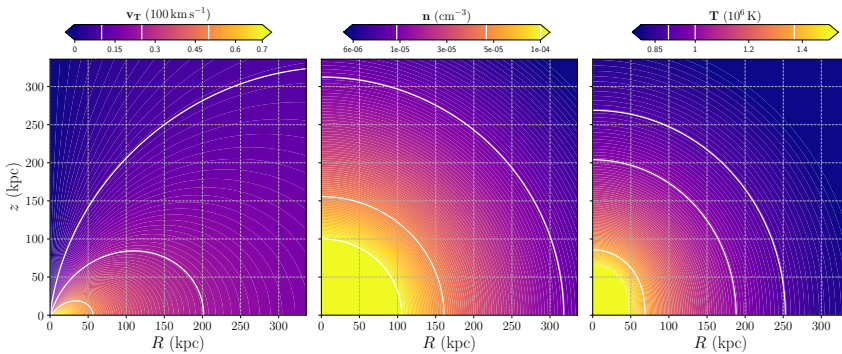
4

M31 property	Value	Reference
M_{vir}	$2 \times 10^{12} M_\odot$	e.g. Zhang et al. (2021)
c	10.25	Dutton & Macciò (2014)
r_{vir}	336 kpc	equation (4.2)
M_*	$1.2 \times 10^{11} M_\odot$	e.g. Sick et al. (2015); Williams et al. (2017)
R_d	5.3 kpc	e.g. Courteau et al. (2011)
B/T	0.25	Widrow et al. (2003); Chemin et al. (2009)
i	77°	e.g. Athanassoula & Beaton (2006)
SFR	$0.35 M_\odot \text{ yr}^{-1}$	Rahmani et al. (2016)

Table 4.1: Main properties of M31 used in this work.

4.3.2 Properties of the hot CGM

As in our previous works, we assume that the halo of M31 is filled with a stratified hot corona that extends up to very large distances from the center. From both observational evidence (Hodges-Kluck et al. 2016) and theoretical arguments (Pezzulli & Fraternali 2016; Pezzulli et al. 2017) we expect the corona of star-forming galaxies to rotate, although less than the local circular speed because of partial pressure support against gravity. For this work we created, using a modified version of the software COROPY from Sormani et al. (2018), an axisymmetric model of a corona rotating in the same direction of the galactic disk, in equilibrium with the dark matter halo and with a physically motivated angular momentum. The details of how this model has been constructed can be found in Appendix 4.A.



4

Figure 4.3: Tangential velocity (left), number density (center), and temperature (right) of the model of the rotating hot corona described in Section 4.3, as a function of height and cylindrical radius. The model is defined to contain 20% of the nominal baryons and an angular momentum comparable to that of the DM halo (see details in Appendix 4.A). In each panel, contours are placed at the values indicated on the corresponding colorbar.

We chose parameters such that the average angular momentum of the hot medium is $l_{\text{cor}} = 3207 \text{ km s}^{-1} \text{ kpc}$. This is comparable to the specific angular momentum expected for the dark matter halo $l_{\text{DM}} = 2619 \text{ km s}^{-1} \text{ kpc}$ (Cimatti et al. 2019). For comparison, the stellar angular momentum³ of M31 (estimated following equation 1 in Mancera Piña et al. 2021) is $l_{\text{M31}} \approx 1900 \text{ km s}^{-1} \text{ kpc}$ and, as expected, is smaller than (but comparable to) that of the rotating corona (see Pezzulli et al. 2017, and references therein). We also checked the stability of our model using the Solberg-Høiland criteria (Tassoul 2000; Sormani et al. 2018) and we checked that the cooling time of the hot medium is significantly higher than 2.5 Gyr (the typical timescale of the cool CGM cloud orbits, see Section 4.4.2) everywhere in the halo, except for the regions close to the disk plane, which are however not relevant for the findings of this work (see Sections 4.4.2 and 4.5.2).

The mass of the corona in our fiducial model is $\sim 6 \times 10^{10} M_{\odot}$ and accounts for 20% of the total baryonic mass associated with the halo of M31. Note that the stellar component of M31 represents almost 40% of the baryonic mass, therefore in our model we have, without considering the cool circumgalactic gas, around 60% of the expected baryons. The rotation velocity, density and temperature of the hot gas are shown in the three panels of Figure 4.3. The corona is rotating significantly in the inner regions, while the rotation velocity declines substantially at large distances from M31. Even though we do not have direct observational estimates of the properties of the corona of M31, our inferred profiles are in broad agreement with current observational estimates of the MW corona (e.g. Salem et al. 2015; Hodges-Kluck et al. 2016) and are consistent with the ones that we used for other low-redshift star-forming galaxies (Chapter 3).

³We neglected the asymmetric drift and we assumed that the bulge is either not rotating ($l_{\text{M31}} = 1885 \text{ km s}^{-1} \text{ kpc}$) or rotating at the same rotational velocity of the disk ($l_{\text{M31}} = 1959 \text{ km s}^{-1} \text{ kpc}$).

Note that in this work we adopt a physically motivated model for the hot CGM, but we have verified that using a simpler, non-rotating model for the corona would not strongly influence our results reported in Section 4.4.

4.3.3 Properties of the cool CGM

Once the corona is defined, we model the cool circumgalactic gas, assuming that this medium is composed by a population of clouds moving through the halo of M31. In particular, these clouds are subject to the gravitational force and to the drag force acted by the hot gas:

$$\dot{v}_{\text{drag}} = -\frac{\pi r_{\text{cl}}^2 \rho_{\text{cor}} v^2}{m_{\text{cl}}}, \quad (4.3)$$

where ρ_{cor} is the coronal mass density, v is the relative velocity between the corona and the cloud, m_{cl} is the cloud mass and r_{cl} is the cloud radius, determined by the pressure balance with the hot medium (see equation 2.8), assuming that the cool gas is at a temperature of 2×10^4 K and that the clouds are spherical. From equation (4.3) we can see how the efficiency of the drag force depends then on the mass of the clouds, which is the first free parameter of our models. We explore models with the cloud mass varying from 10^5 to $10^8 M_{\odot}$ (see Table 4.2). Note that this mass does not vary during the motion of the cloud (this aspect is further discussed in Section 4.5.2).

As already mentioned, a second free parameter in all our models is the metallicity Z of the cool gas, which can be constrained combining the hydrogen column densities predicted by our models with the observational information of the total silicon column densities (see Section 4.2 and 4.3.4). We let the metallicity free to vary from $0.003 Z_{\odot}$ to Z_{\odot} (Table 4.2).

In this work, we explore two different scenarios for the origin and dynamics of the cool CGM: outflow and inflow. These models are both described by three additional free parameters, which differ in the two cases and are explained in detail in Sections 4.3.3 and 4.3.3.

Outflow models

In this scenario, we assume that the cool clouds have originated in the ISM of M31 and have acquired kinetic energy from the supernova explosions in the galactic disk. We follow the same approach as in Chapter 3. In brief, the clouds are ejected from different radii across the disk according to a star formation rate density. As in Section 3.3.1, our fiducial models adopt the profile of Pezzulli et al. (2015) (but see Section 4.5). The initial velocity is the vector composition of (i) the circular velocity of the disk (see Figure 4.2) and (ii) an ejection velocity, defined in a cone around a direction perpendicular to the disk.

In addition to the cloud mass and the gas metallicity, we introduce for the outflow model three other free parameters: the initial ejection velocity v_{kick} , the aperture of the outflowing cone θ_{max} (if $\theta_{\text{max}} = 90^\circ$ the outflows are isotropic) and the mass loading factor η . This last parameter represents the ratio between

the mass outflow rate $\dot{M}_{\text{out}}(t)$ and the star formation rate $\text{SFR}(t)$ of the galaxy, $\eta = \dot{M}_{\text{out}}(t)/\text{SFR}(t)$. Compared to similar star-forming galaxies at low redshift, M31 has currently a rather low star formation rate ($\text{SFR}(0) = 0.35 M_{\odot}\text{yr}^{-1}$, see Rahmani et al. 2016), which is unlikely to power strong outflows to the external regions of the halo. However, there are indications that the SFR was higher in the past. In this work, we adopt as fiducial the star formation history (SFH) derived by Williams et al. (2017), estimated by fitting stellar evolution models to color-magnitude diagrams of the Panchromatic Hubble Andromeda Treasury survey of the disk of M31, and characterized by 2 bursts of star formation around 2 and 8 Gyr ago.

The dynamics (i.e the orbits) of the clouds is uniquely defined by the choice of the three parameters $(m_{\text{cl}}, v_{\text{kick}}, \theta_{\text{max}})$. For each combination of the parameters, we integrate 30 different orbits⁴ for 6 Gyr and, depending on the starting radius and ejection direction, the clouds will either escape the virial radius or fall back onto the disk after a time t_{orb} at which we stop the integration (see for example Figure 3.10). Depending on the time t_{cl} elapsed along the orbits, the number density of clouds at that position is determined by the mass outflow rate at the relevant ejection time and hence proportional to $\text{SFR}(t_{\text{cl}})$, where t_{cl} is the lookback time.

Inflow models

In the second scenario that we explore in this work, the CGM clouds are instead part of the cosmological accretion of gas onto the halo of M31 and are therefore inflowing from the external parts towards the galactic disk. In this case, we assume that the cool absorbers are starting from a spherical shell at the virial radius r_{vir} (see Section 4.2) and are then infalling towards the central parts.

The three additional free parameters in this case are given by the initial radial and tangential velocity of the clouds (v_r and v_t) and by the parameter $f_{\text{accr}} = \dot{M}_{\text{in}}/\dot{M}_{\text{cosm}}$, where \dot{M}_{in} is the total cool gas mass rate of accretion into the halo and \dot{M}_{cosm} is the gas accretion expected from cosmological models. For the latter, we adopted the analytical prescription given in Correa et al. (2015a,b), which gives $\dot{M}_{\text{cosm}} = 11.5 M_{\odot} \text{yr}^{-1}$ at redshift $z = 0$ for a halo with a mass M_{vir} equal to the one of M31 (see Table 4.1) and accounting for the cosmological baryon fraction $f_{\text{bar}} = 0.158$ (see Planck Collaboration et al. 2020). The parameter f_{accr} therefore tells us how much the mass accretion rate of the cool CGM should differ from the cosmological predictions to reproduce the observations. We let this parameter free to vary, imposing however a gaussian prior centered on one (see Table 4.2).

Note that, differently from Chapter 2, in the inflow models of the current study we do not include any mass loss due to the cloud evaporation into the hot corona (see equation 2.11). This choice is due to the higher level of complexity of the current models: given the larger number of free parameters (with respect to Chapter 2), constraining a possible cloud evaporation rate would be hard. We

⁴This number has been chosen in order to sufficiently sample the galactic halo, keeping a reasonably low computational cost.

discuss the implications of the (likely) destruction of the cool CGM clouds on our results in Section 4.5.2 and we will perform a thorough analysis of the cloud survival, using high-resolution hydrodynamical simulations, in Chapter 5.

Also for this scenario we integrate, for each of the combination of the free parameters, 30 different orbits, each of them starting at a different polar angle from r_{vir} , stopping the integration as soon as the clouds reach the central disk.

4.3.4 Comparison with the observations

To compare the predictions of our models with the data of the AMIGA project, we created synthetic observations for both the scenarios described above. In summary, we populate the orbits with a number of clouds given at each time by the cool gas mass outflow/inflow rate divided by the cloud mass. We then trace lines of sight in our model halo, at locations that correspond to the selected QSO sightlines (see Figure 4.1), and we calculate the line-of-sight velocities of the intersected model clouds (see Chapter 3 for more details). In order to be consistent with the observations, we select only clouds with line-of-sight velocities in the same range constrained by the AMIGA data (v_{LSR} ranging from -700 to -150 km s $^{-1}$), excluding all the absorbers whose velocities could overlap with the Milky Way ($v_{\text{LSR}} > -150$ km s $^{-1}$) or the Magellanic stream, as described in Section 4.2.

We also calculate the column density of each 'observed' model cloud, given by the formula

$$N_{\text{cl}} = 2n_{\text{cl}}r_{\text{cl}}\sqrt{1-(d_{\text{cl}}/r_{\text{cl}})^2}, \quad (4.4)$$

where r_{cl} and n_{cl} are respectively the cloud radius and total number density, assumed constant throughout the cloud, and d_{cl} is the projected distance of the center of the cloud from the intercepting sightline.

The last step needed to perform our analysis is the creation of a likelihood based on the comparison of synthetic and real observations. In order to do so we created, for each line of sight, a velocity distribution with the detected line-of-sight velocities (see Section 3.3.3 for more details), dividing the total velocity range in the same intervals used by Lehner et al. (2020) for their AOD analysis (see in particular their Table 2). The likelihood is then composed of three different parts, dealing with respectively the kinematics (\mathcal{L}_{kin}), the number of components (\mathcal{L}_{num}) and the total silicon column densities ($\mathcal{L}_{\text{dens}}$). The first term represents the Bayesian probability of each observed kinematic component given our model, while the second is obtained using the Poisson statistics to compare the number of components found in the observations and in our model for each line of sight. The third term in the likelihood quantifies the comparison, for each component, of the observed total silicon column density with the one predicted by our model. The latter is given by the sum of the column densities ($N_{\text{cl},i}$) of all the model clouds that have line-of-sight velocities in the selected velocity bin (which would appear as one single component in the observations),

converted into a silicon column density by

$$N_{\text{Si}} = \frac{1}{2.3} \left(\frac{Z}{Z_{\odot}} \right) \left(\frac{\text{Si}}{\text{H}} \right)_{\odot} \sum_{i=1}^n N_{\text{cl},i}, \quad (4.5)$$

where n is the number of clouds in the selected velocity bin, $(\text{Si}/\text{H})_{\odot}$ is the silicon solar abundance, determined from $\log(\text{Si}/\text{H})_{\odot} = -4.49$ (Asplund et al. 2009), (Z/Z_{\odot}) is the gas metallicity and the factor 2.3 is used to transform the total numeric density into a hydrogen numeric density, assuming a fully ionized gas and the helium abundance reported in Cox (2000). For each line of sight then we defined $\mathcal{L}_{\text{dens}}$ as:

4

$$\ln \mathcal{L}_{\text{dens}} = -\frac{1}{2(n_{\text{obs}})} \sum \frac{(\log N_{\text{Si}_{\text{obs},i}} - \log N_{\text{Si}_{\text{mod},i}})^2}{\sigma^2}, \quad (4.6)$$

where n_{obs} is the number of observed components and $\sigma = 0.15$ dex is the uncertainty in the logarithm of the silicon column densities. This value represents a conservative choice with respect to the errors reported in Lehner et al. (2020), which have an average value of ≈ 0.07 dex, in order to take into account for SiIII lines close to saturation and for the presence of non-detections in the SiIII and SiIV lines. Note that we perform this comparison only for the components that are classified as detections (in SiIII) by Lehner et al. (2020), as the treatment of non-detections is already included in \mathcal{L}_{num} .

The final likelihood is given by the product of all the likelihoods calculated for each of the 23 lines of sight in our sample. We performed, for both the inflow and outflow scenarios, a Bayesian analysis using this likelihood and flat priors for all the parameters (except for a gaussian prior for f_{accr}), exploring the parameter space in the ranges reported in Table 4.2. In particular, we used the nested sampling method (see Skilling 2004), adopting the python package Dynesty (Speagle 2020). Like the more common Markov Chain Monte Carlo (MCMC) analysis, the nested sampling allows us to estimate the posterior distribution of our model outputs given the data, with the advantage of being more efficient in sampling multimodal distributions. With this analysis we were able to find the best choice of parameters that reproduces the AMIGA data, which we present in the following Section.

4.4 Results

In this Section, we outline the results and implications that we have obtained through the comparison of our models with the data of the AMIGA project, using a Bayesian analysis as described in Section 4.3.4. This allowed us to find for both the outflow and inflow scenarios the best choice of parameters needed to reproduce the observations.

Model	Parameter	Prior (min, max)	Best-fit values
Outflow	$\log m_{\text{cl}}/M_{\odot}$	5, 8	$7.42^{+0.54}_{-0.87}$
	$\log Z/Z_{\odot}$	-2.5, 0	$-1.69^{+0.37}_{-0.24}$
	$\log(\nu_{\text{kick}}/\text{km s}^{-1})$	2, 4	$2.81^{+0.25}_{-0.10}$
	$\log \eta$	-1, 1.5	$1.22^{+0.24}_{-0.46}$
	θ/π	1/6, 1/2	$0.47^{+0.02}_{-0.06}$
Inflow	$\log m_{\text{cl}}/M_{\odot}$	5, 8	$6.69^{+0.70}_{-1.19}$
	$\log Z/Z_{\odot}$	-2.5, 0	$-1.25^{+0.36}_{-0.23}$
	$\nu_{\text{r}} (100 \text{ km s}^{-1})$	0, 5	$0.14^{+0.26}_{-0.12}$
	$\nu_{\text{t}} (100 \text{ km s}^{-1})$	-1, 1	$-0.07^{+0.27}_{-0.35}$
	f_{accr}	0.1, 4	$1.49^{+0.75}_{-0.48}$

Table 4.2: Results of the nested sampling analysis for the two scenarios investigated in this work. All the priors are flat except for f_{accr} , given by a truncated normal profile centered in 1 and with a width of 0.5. The last column shows the values of the 50th percentiles (median) of each parameter distribution, with the 2-sigma errors, which roughly correspond to the percentiles number 2.5 and 97.5.

4.4.1 Outflow scenario

The results for the outflow model are reported in Figure 4.4 and in Table 4.2. In order to reproduce the observations of the cool circumgalactic gas, the outflowing clouds need to be very massive, with $m_{\text{cl}} \geq 10^7 M_{\odot}$. In addition to the high cloud mass, we find that the global galactic wind needs to be nearly isotropic ($\theta_{\text{max}} \sim 90^{\circ}$) and that, most importantly, both the mass loading factor η and the initial ejection velocities ν_{kick} require large values in order to reproduce the observations.

Following the analysis of Section 3.4, we can use these values to calculate the total kinetic power needed by the wind, given by:

$$\dot{K}_{\text{out}} = \frac{1}{2} \dot{M}_{\text{out}} \nu_{\text{kick}}^2, \quad (4.7)$$

where $\dot{M}_{\text{out}} = \eta \text{SFR}(t)$. This can be compared to the kinetic energy available per unit time from the supernova explosions in the disk (equation 3.13), in order to obtain the efficiency f_{SN} of the supernovae in transferring kinetic energy to the wind (see Section 3.4). Through this comparison, we found that to power the wind predicted by our models we need efficiencies of 730%. This is clearly unphysical, since they imply that the outflows would need significantly more energy than the one available from the supernovae⁵. On the contrary, as most

⁵Note that the value of η (and therefore of the efficiency f_{SN}) could be slightly higher than the one we found, since we cut the prior on this parameter at $\log \eta = 1.5$, to avoid

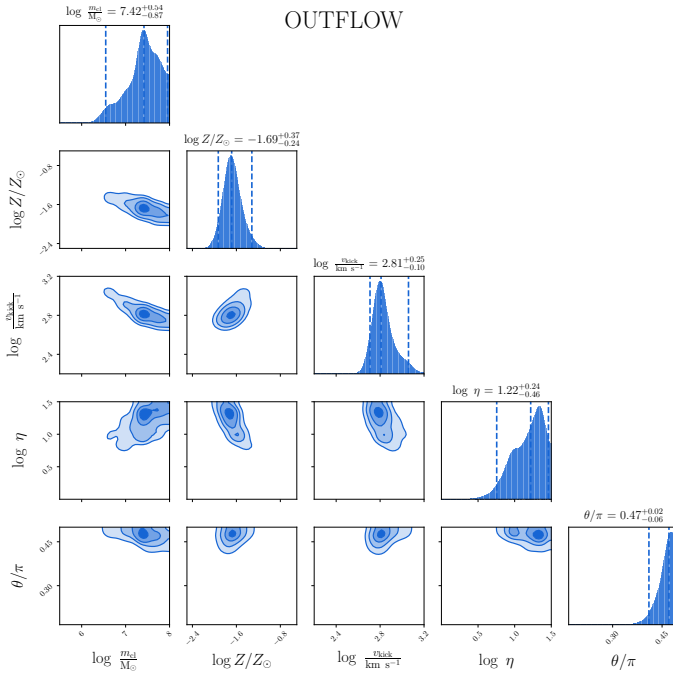


Figure 4.4: Posterior distributions from the Nested Sampling analysis, for the outflow scenario, with reported the median values for each parameter distribution and the 2-sigma errors, which roughly correspond to the percentiles number 2.5 and 97.5.

of the supernova energy is expected to be radiated (e.g. McKee & Ostriker 1977; Kim & Ostriker 2015), the theoretical expectation for f_{SN} is of the order of 10% (e.g. Martizzi et al. 2016), or at most a few tens % in the case of clustered supernova explosions (Fielding et al. 2018). Therefore we conclude that SN driven galactic outflows are not a viable way to reproduce the majority of the cool gas observed in the halo of M31. This is in line with the main result of Chapter 3, where we found that galactic winds cannot reproduce the cool CGM of a sample of about 40 low-redshift star-forming galaxies. Note that in our previous study only one line-of-sight per galaxy was available, while for M31 there are more than 20 QSO sightlines within its virial radius (in projection). Moreover, in our current model we also include the effect of a burst of star formation 2 Gyr ago, observed in the disk of M31 (Williams et al. 2017) as explained in Section 4.3.3. This however does not change our main result that star-formation-driven outflows cannot reproduce the majority of the cool CGM. As a final note, we also find that the metallicity required by this model is extremely low ($Z < 0.05 Z_{\odot}$, as opposed to $Z \sim Z_{\odot}$, expected for gas originated in the ISM), which is pointing to a further inconsistency with what we would expect for gas ejected from the central galaxy. We therefore exclude the outflow

unrealistic values. This would however go in the direction of strengthening our results.

scenario as the main source of the cool CGM of M31 and we conclude that (at least the vast majority of) this medium has a different origin, which we will explore more in detail in the following Section. We do not exclude however the possibility that the outflows might affect the CGM in the internal regions of the halo, close to the galactic disk, as we discuss in Section 4.5.1.

4.4.2 Inflow scenario

In Figure 4.5 and in Table 4.2 we show the results of the nested sampling analysis for the inflow models, whose features are described in Section 4.3.3. We can see that there is a very well defined region of the parameter space that allows us to reproduce the AMIGA observations. In particular, we find that the data are well described by low-metallicity ($Z \approx 0.05 Z_\odot$) clouds with a mass of about $5 \times 10^6 M_\odot$, accreted at a rate only slightly higher than the cosmological gas accretion rate expected at $z = 0$ ($f_{\text{accr}} \approx 1.5$) and with low tangential and radial velocities as they start their infall at the virial radius. Below, we go more in the details of the physical picture arising from this parameter choice.

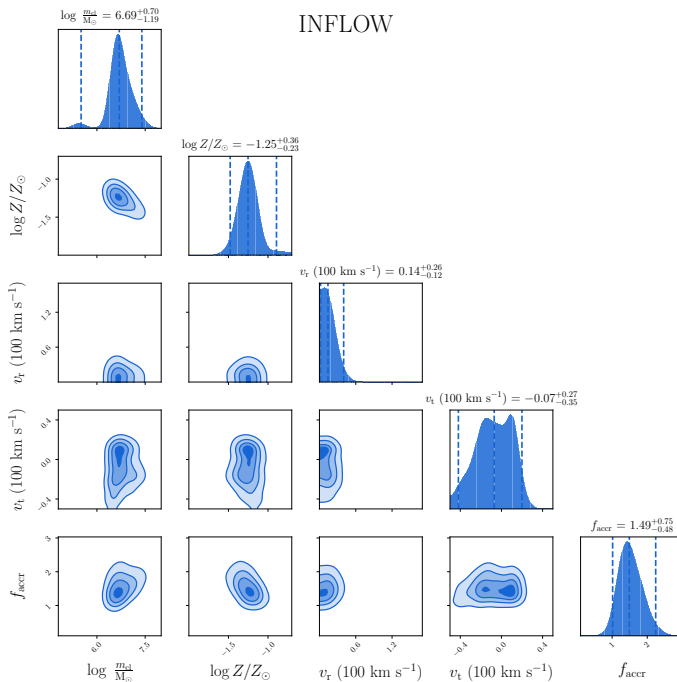
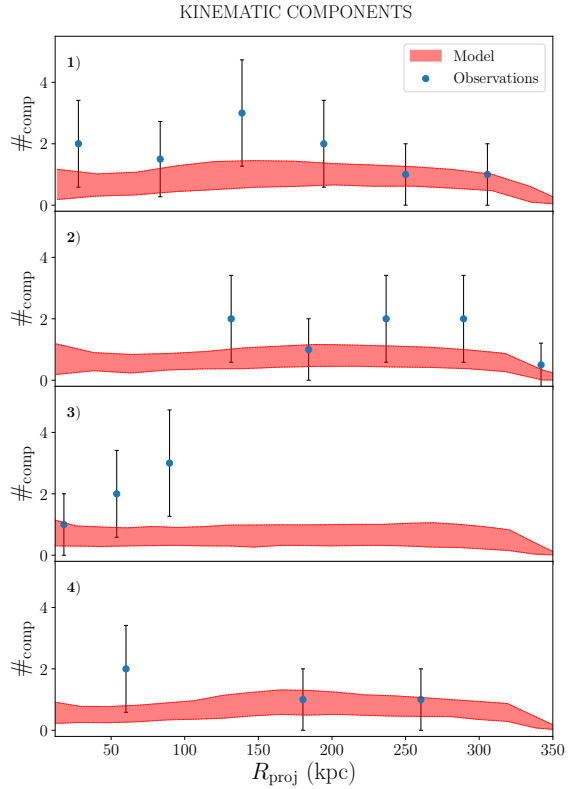


Figure 4.5: Same as Figure 4.4, for the inflow scenario.

Comparison with observations

The comparison between data and model predictions is shown in Figures 4.6, 4.7 and 4.8. Our model of the circumgalactic medium of M31 is not isotropic,

Figure 4.6: Comparison between the predictions of the number of components from the best-fit models described in Section 4.4.2 (red bands) and the observations (blue points), as a function of the projected distance from M31. We show, going from top to bottom, the results for the four quadrants outlined in Figure 4.1, from 1 to 4. The width of the bands represents the standard deviation calculated for the different predictions of the 50 models used for the comparison. The observed number of components is averaged over the projected distance in bins of about 55 kpc, a value chosen in order to have a good enough statistics in the data, with the error bars given by the poissonian error.



since the hot gas is rotating (see Section 4.3.2 and Appendix 4.A) and the cool clouds are not infalling perfectly radially towards the galaxy. We therefore show our results separately for the four quadrants defined in Figure 4.1, in order to investigate any azimuthal dependence in the model and in the comparison of our outputs with the observational data. In Figures 4.6 and 4.7 we show, respectively, the number of kinematic components and the total silicon column density (see Section 4.2), both as a function of the projected distance from M31. The blue points represent the observations, while the red bands represent the predictions of our models. To obtain these predictions, we averaged the results of 50 models with values for the free parameters sampled from the posterior distributions shown in the corner plot of Figure 4.5. We can see how in general the observations are well reproduced by our models for all the four quadrants of the observational plane and there seems not to be any strong azimuthal dependence in the properties of the cool gas, both for model and data. Models with significantly higher accretion rates formally perform better in this respect, but are discarded by our prior on the cosmological accretion. There are a couple of assumptions of our model that can have an impact in the comparison between measured and predicted number of components (see

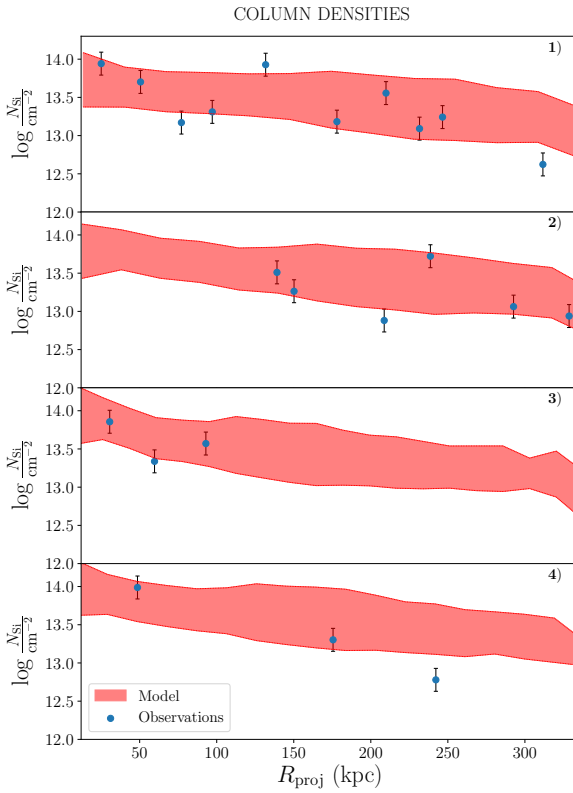


Figure 4.7: Same as Figure 4.6, for the total silicon column densities. The error bars in the data are equal to 0.15 dex.

also Section 4.5.3). First, our clouds are assumed to remain spherical and in pressure equilibrium with the corona throughout their infall. This implies that in the inner regions the clouds are smaller (lower cross section) than in the outer halo. Hydrodynamical simulations (e.g. Armillotta et al. 2017) indicate, instead, that clouds tend to quickly lose their spherical shape and to be significantly more extended than what we assume, being therefore easier to intercept by a line of sight from some viewing directions. The second assumption of our model that is worth mentioning in this context is the isotropy of the accretion. Because we are assuming that the accretion is isotropic, the number of components predicted by our models should be better understood as an average over spherical shells. If the accretion were anisotropic, the number of components in a certain region could be higher than this average value. Unfortunately, it is not easy to directly test this possibility with the available data, as we cannot probe those directions that are not intercepted by a quasar sightline, or which are subject to contamination from the Milky Way (see Figure 4.1).

In the four panels of Figure 4.8 we focus on the comparison of the kinematics (line-of-sight velocity of the cool clouds with respect to the systemic velocity of M31), as a function of the projected radius, predicted by our models

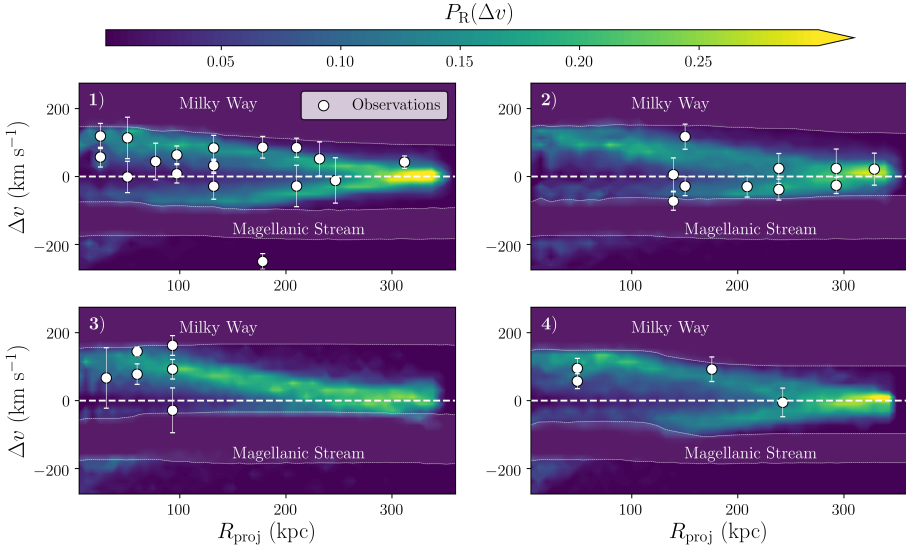


Figure 4.8: Comparison between the kinematics predicted by the best-fit inflow models described in Section 4.4.2 (colormap) and the observed kinematic components (white points), as a function of the projected distance from M31, for the four quadrants outlined in Figure 4.1. The error bars on the data points show the velocity boundaries of each absorption component, as identified by Lehner et al. (2020). The model predictions are calculated as explained in Section 4.4.2 and represent, for each projected radius, the normalized probability distribution $P_R(\Delta v)$ to observe a cloud at a given line-of-sight velocity (with respect to the systemic velocity of M31). We also indicate in each panel the velocity ranges affected by contamination from the Magellanic Stream and the Milky Way, excluded from both observations and models.

and observed in AMIGA. In addition, we show the velocity ranges in these position-velocity plots that are affected by the presence of the Milky Way and the Magellanic Stream. These ranges have been excluded both from the observations and in our models. The observations are shown as white points and correspond to the kinematic components reported in the upper panel of Figure 4.1, with the error bars denoting the velocity ranges associated to each identified absorbing system (see Lehner et al. 2020), also corresponding to the velocity bins that we used to create our likelihood (see Section 4.3.4). In the colormap, we report instead the prediction for the same 50 models used for Figures 4.6 and 4.7, showing, for each line of sight, what is the probability that an intersected cloud has a certain line-of-sight velocity. In particular, the entire velocity range is divided in bins of 20 km s^{-1} and the colormap shows the probability of a component to lie in one of these bins.⁶ The model predictions

⁶Note that all probabilities are normalized in order to have, for each line of sight (i.e. each vertical slice in the diagram), a total probability of 1. The brightest colors in the colormaps are located at large projected radii because at these distances the range of the predicted velocities is smaller, not because in these regions it is more likely to intersect a cloud (see Figure 4.7 for the distribution of components as a function of projected

match remarkably well, except for a few outliers, the velocities observed in the cool circumgalactic gas. In particular, they show the same pattern of the data of having the higher line-of-sight velocities at small projected radii. We note that a few observed components at $R_{\text{proj}} < 150$ kpc tend to have absolute values of the velocities slightly lower than what preferred by our models. This could be due to second-order hydrodynamical effects that, by deforming and possibly disrupting the clouds (see also Section 4.5.2), especially in the last part of their infall, would slow down the cool gas more efficiently than what predicted by our semi-analytical models. We will study more in detail these interactions in Chapter 5.

We have therefore found that there is a class of inflow models that are cosmologically feasible ($f_{\text{accr}} \approx 1.5$) and that can successfully describe the observational data. Interestingly, our models also predict (except for $R_{\text{proj}} \lesssim 100$ kpc) a lack of absorbers at velocities $v_{\text{M31}} \lesssim -200 \text{ km s}^{-1}$, which are not affected by the Magellanic Stream and where also the AMIGA observations show a lack of detections (with only one exception).

Finally, a fundamental property that we are also able to constrain with the comparison between model predictions and observations is the metallicity of the cool gas, which sets the normalization of the silicon column density profile shown in Figure 4.7. The Bayesian analysis returns a metallicity lower than $0.1 Z_{\odot}$, which is consistent with gas poorly enriched by star formation processes, as expected for material that is accreting from the intergalactic medium (see Section 4.5.2). This is consistent with our assumption of cosmological accretion and hence confirms that this is the most likely origin of the majority of the cool CGM around M31. In Section 4.5.2, we compare our estimate with the one obtained by Lehner et al. (2020).

Intrinsic and projected distances of the absorbers

In Figure 4.9 we show the distribution of the intrinsic distances of the intersected clouds as a function of their projected distances from the center. This is, in particular, the prediction of the same 50 best-fit models used to create Figures 4.7 and 4.8 and considering all the azimuthal angles. More in detail, the black curve represents the median of this distribution, with the colours that show instead different percentiles as indicated. Obviously, the projected distance is only a lower limit of the intrinsic one, as depicted by the gray shaded area. More interestingly, from this distribution it is evident how the intrinsic galactocentric distance of a cloud can be much larger than the one that is seen in projection. In particular, note how the vast majority of the clouds that we observe are located beyond 150 kpc from the disk of M31.

This finding is caused by two effects: (i) the cloud size increases with the distance from the center, since in the external regions the clouds are in pressure equilibrium with a lower density hot gas (see Figure 4.3) and it is therefore more likely to intercept these absorbers, given their higher cross-section; (ii) as

distance).

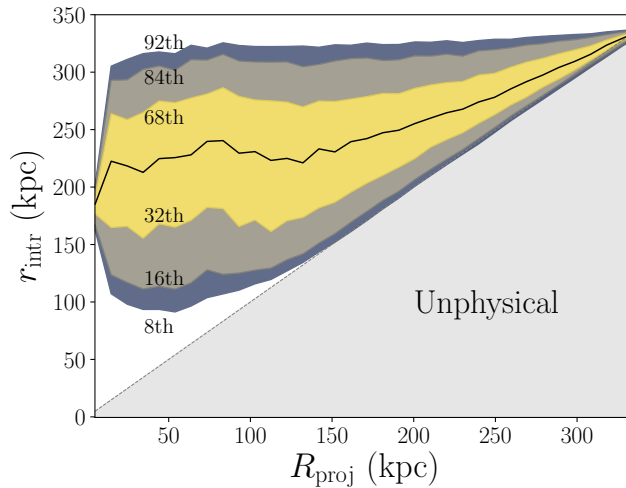


Figure 4.9: Distribution of the intrinsic galactocentric distances (r_{intr}) of the clouds as a function of their projected separation (R_{proj}) from M31, as predicted by our best-fit inflow model. The black curve shows the median values of the distributions of intrinsic distances of the model clouds (‘observed’ as explained in Section 4.3.4) at each projected radius, with the color bands showing different percentiles (8th, 16th, 32nd, 68th, 84th, 92nd). The region where $R_{\text{proj}} > r_{\text{intr}}$ is necessarily empty, as the projected distance is a physical lower limit of the intrinsic one. Note how the majority of the clouds, even at small projected distances, are located at intrinsic distances larger than 150 kpc, suggesting that the cool absorbers are mainly located in the external parts of the halo of M31.

we will see below, the cool CGM is infalling at lower velocities in the external regions of the halo, therefore the orbits are populated with more clouds at these distances.

This result clearly shows how, in absorption studies of the CGM, the projected locations of the lines of sight might be not representative of the real distances of the absorbing gas systems from the central galaxy. We discuss more in details the implications of this finding in Section 4.5.2.

Dynamics and properties of the cool clouds

We now discuss in some greater detail the physical properties and the dynamical behaviour of the cool CGM absorbers, according to the predictions of our best-fit inflow model. The infalling clouds have a mass of about $5 \times 10^6 M_{\odot}$ and an initial radius $r_{\text{cl}} \approx 5.7$ kpc. Under our assumption that they have a constant mass (but see Section 4.5.2) and are pressure confined by the hot corona, these clouds tend to shrink while falling towards the disk, reaching sizes smaller than 1 kpc in the central ($r \lesssim 20$ kpc) regions. We have also performed a test where the cloud masses at the virial radius are extracted from a power-law distribution, whose slope, minimum and maximum cloud mass were left free to vary as free parameters. In this case we find that the slope of the power law is unconstrained and that the range of possible cloud masses is small (0.7 dex) and centered on

the best-fit mass found with our fiducial model. Therefore, allowing the clouds to have a more complex mass distribution does not seem to affect our results. The total mass infall rate of the cool gas is equal to $15.3 M_{\odot} \text{yr}^{-1}$ and the average time needed for the clouds to reach the disk from the virial radius is of about 2.5 Gyr. Since the mass accretion is constant with time in our models, the total amount of cool gas in the halo of M31 is therefore $\approx 4 \times 10^{10} M_{\odot}$. Note that, as we have seen in Section 4.3.2, the sum of the corona and the stellar component of M31 accounts for almost 60% of the total expected baryons. Therefore, since we predict that $\approx 15\%$ of the baryons are in the cool CGM component, in our model the total baryonic mass within the halo of M31 is very close to the expected cosmological fraction.

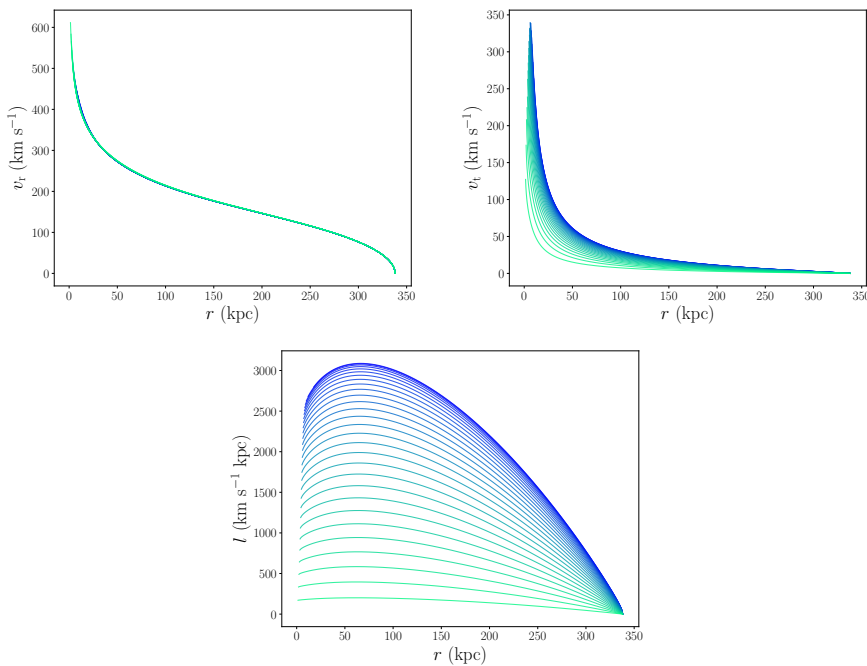


Figure 4.10: Radial velocity (top-left), tangential velocity (top-right) and specific angular momentum (bottom) of the clouds, as a function of the intrinsic distance from the center and as predicted by an inflow model with a choice of parameters representative of the best-fit parameter region reported in Table 4.2. We show different orbits for clouds starting at different polar angles from a shell at the virial radius of M31. The colour of the lines changes with increasing initial cylindrical radius R of each orbit, going from 0 (light green) to r_{vir} (dark blue).

The three panels of Figure 4.10 show the overall intrinsic dynamics of the clouds in our best-fit models, for 30 orbits described by our best-fit parameters, all starting at the virial radius but from different positions across the virial sphere. On the top-left panel, we report the cloud radial velocities as a function of the galactocentric distance: in this case, the profiles for the 30 different orbits

overlap almost perfectly with each other, reflecting that the anisotropies present in our model have only a minor impact on the radial motion of the clouds. At the virial radius the clouds start with a very low (infall) velocity: for this plot we adopted $v_r = 14 \text{ km s}^{-1}$, which is the median value from the posterior distribution obtained with the nested sampling. In order to reproduce the observational data, the initial velocity needs indeed to be lower than a few tens of km s^{-1} (see table 4.2). The clouds then accelerate during their infall, maintaining however a relatively low speed due to the drag force acted by the corona and reaching high velocities only in the central regions, where the gravitational force becomes stronger and the drag force weaker due to the compression of the clouds leading to a smaller cross section.

The clouds described by our best-fit models are not falling only radially towards the galactic disk as their motion has a tangential component. From the nested sampling analysis we found a median value for the initial tangential velocity of -7 km s^{-1} , with uncertainties of about 30 km s^{-1} . Note that, despite the distribution being centered at negative values, this range is consistent with the cool clouds having an initial angular momentum equal to (and oriented in the same way) or even larger than that of the corona, though we cannot determine whether this is the case with the available data. The profiles of the tangential velocities and of the specific angular momentum as a function of the intrinsic distance from the center are shown, respectively, in the top-right and bottom panels of Figure 4.10. These have been obtained assuming an initial $v_t = 0 \text{ km s}^{-1}$ (which is within the uncertainties of our posterior for the initial tangential velocity). The drag force progressively drives the clouds towards co-rotation with the hot CGM (therefore also on the same sense of rotation of the disk, see Section 4.3.1 and 4.3.2) as the two gas phases exchange angular momentum. The cool medium tends to acquire angular momentum from the hot gas, reaching values of a few thousands of $\text{km s}^{-1} \text{ kpc}$, comparable with the angular momentum of the hot corona (see Figure 4.11). After acquiring significant angular momentum from the outer parts of the corona, the cool gas continues its infall motion towards the innermost regions, where the hot gas is relatively poor in angular momentum, and eventually deposits back, at a different location, part of the angular momentum that was previously acquired (see bottom panel of Figure 4.10). We note in passing that in this way cool accreting flows potentially provide a mechanism to transfer angular momentum from the outermost to the innermost regions of the hot halo (though further exploring the possible implications of this mechanism is beyond the scope of this work). After an infall of about 2.5 Gyr, our model predicts that the clouds cross the plane of the disk (defined as $z = 0$) at cylindrical radii between about 1 and 18 kpc. Note however that in reality clouds may not be able to reach such small galactocentric distances (see Section 4.5.2).

4.5 Discussion

In the previous Section, we have seen that our analytic method indicates a clear preference for an inflow, as opposed to an outflow origin, for the cool CGM of M31. It also provides clear predictions for some of the most important properties of the circumgalactic gas of M31. Here, we discuss the implications and limitations for both scenarios of outflow and inflow and we draw conclusions regarding the origin and fate of the cool CGM and its connection with the central galaxy.

4.5.1 Outflow

The first result of this study is the inability of a galactic wind to explain (the majority of) the cool CGM of M31, mainly because of the unphysical energy requirements that are needed in order to reproduce the data. It is important however to remark that the outflows considered in this work are represented by an idealized flow of gas clouds at a constant temperature of 2×10^4 K. Observations (e.g. Strickland & Heckman 2007; Martin et al. 2012) and pc-resolution simulations of supernova-driven winds (e.g. Li et al. 2017a; Kim & Ostriker 2018; Fielding et al. 2018; Kim et al. 2020), focused on a region that goes from the disk up to a few kpc above it, have shown instead how outflows seem to be multiphase, with most of the gas mass residing in the cool phase and most of the energy in the hot phase of the wind (Li & Bryan 2020).

The entrainment and acceleration of the clouds by fast-moving hot winds (see Schneider et al. 2020) could in principle help in bringing the cool gas up to the large galactocentric distances probed in this work. Moreover, this uplifting of the cool medium could happen also because of buoyancy of entropy-driven, slow-moving hot winds (see Keller et al. 2020). We could expect however that in order to be able to do so, the total energy (kinetic plus thermal) injected to the hot wind would need to be comparable to the one that we have found in Section 4.4.1, to overcome the gravitational force and the pressure of the pre-existing corona. Therefore, even though the absence of this effect is a limitation of our models, we consider unlikely that it would strongly affect our main findings and change our conclusions. An accurate modeling of the multiphase winds, as well as a more proper treatment of non-thermal effects such as those associated to cosmic rays (e.g. Pfrommer et al. 2017; Hopkins et al. 2021), is outside the scope of this work and we leave it for future studies.

Another possible source of uncertainty is in the choice of the star formation rate density profile. As in Chapter 3, we adopted the profile predicted by Pezulli et al. (2015) (see also Section 4.3.3), which is however only an approximation of the one observed in the disk of M31. One feature that is not reproduced by this profile is the enhanced star formation rate in a ring roughly between 10 and 12 kpc (e.g. Robles-Valdez et al. 2014). In particular, Lewis et al. (2015) have found that, in the last 400 Myr, the star formation rate density of M31 has been dominated by this ring. Given that the gravitational pull is weaker at $R = 10$ kpc than in the central regions of the disk, it is worth exploring a

scenario in which all the clouds are ejected, at all times, from a ring located between 10 and 12 kpc in the disk of M31. Note that this is an extreme scenario (and therefore a conservative test), as the SFR ring is likely to rather be a relatively recent and short-lived feature, as emphasized by the young ages probed by the studies above. We performed a nested sampling analysis over the same parameter space and using the same likelihood and priors adopted for the fiducial model. The results of this test are reported in the top part of Table 4.3, where we can see how the values of the best-fit parameters are well within the uncertainties of what we found with our previous analysis, leading to a supernova efficiency comparable with the value found with our fiducial model. We therefore conclude that deviations from the star formation density profile adopted in this work do not affect our conclusions.

4

Finally, in addition to the star formation rate, a central AGN could also have an impact on the surrounding CGM. Zhang et al. (2019) found, using X-ray spectroscopy, a possible evidence in M31 for a past AGN event that happened half a million years ago. In this very short timescale, even if the clouds were ejected at 2000 km s^{-1} they would reach a distance of about 1 kpc from the center, much smaller than the distances that we are probing in this study. We cannot exclude that previous events of activity could have also played a role. However, modelling these previous events would require numerous poorly constrained assumptions on the duty cycle, energetics and region of influence of AGN feedback for M31. This is beyond the scope of this work and is left for future studies.

Based on our results of Section 4.4.1 and on the above considerations, we conclude that the majority of the cool CGM of M31 is not produced by a supernova-driven galactic wind. As mentioned in Section 4.4.1, this is also in line with the findings of Chapter 3, where we obtained a similar result for a sample of about 40 nearby star-forming galaxies selected from the COS-Halos and COS-GASS samples (Werk et al. 2012; Borthakur et al. 2015). These results are also consistent with what found by Fielding et al. (2020c) in idealized hydrodynamical simulations, where feedback from the central galaxy is not able to bring cool gas in the outer CGM.

Galactic outflows could however have some role in the production of cool gas in the inner parts of the halo, a few kpc above the disk (e.g. Kim & Ostriker 2018), at distances that are not probed by the AMIGA and the COS-Halos/COS-GASS data. At these heights, the cool/hot gas interface might also lead to condensation of the coronal gas (e.g. Marinacci et al. 2010b; Armillotta et al. 2016; Gronke & Oh 2018; Grønnow et al. 2018; Kooij et al. 2021) and accretion of cool gas onto the galaxy, in a galactic fountain process (Marasco et al. 2013; Fraternali 2017). The study of the inner layers of the CGM is outside the scope of this work.

Model	Parameter	Best-fit values
10 kpc ring	$\log m_{\text{cl}}/M_{\odot}$	$7.24^{+0.63}_{-0.90}$
	$\log Z/Z_{\odot}$	$-1.51^{+0.19}_{-0.37}$
	$\log(\nu_{\text{kick}}/\text{km s}^{-1})$	$2.77^{+0.22}_{-0.07}$
	$\log \eta$	$1.14^{+0.32}_{-0.40}$
	θ/π	$0.44^{+0.05}_{-0.05}$
$M_{\text{cor}} = 0.4M_{\text{bar}}$	$\log m_{\text{cl}}/M_{\odot}$	$6.75^{+0.38}_{-1.09}$
	$\log Z/Z_{\odot}$	$-1.40^{+0.40}_{-0.18}$
	$\nu_{\text{r}} (100 \text{ km s}^{-1})$	$0.11^{+0.24}_{-0.09}$
	$\nu_{\text{t}} (100 \text{ km s}^{-1})$	$0.13^{+0.35}_{-0.37}$
	f_{accr}	$2.01^{+0.56}_{-0.75}$

Table 4.3: Results of the nested sampling analysis for the two additional models presented in Section 4.5.

4.5.2 Inflow

Origin of the cool gas

Our preferred scenario for the origin of the cool CGM of M31 is, instead, direct cold accretion of external gas into its halo. The results outlined in Section 4.4.2 are entirely consistent with a picture where the infalling cool clouds are coming from the cosmological accretion of gas into the halo.

We find an average cool gas mass accretion of $15.3 M_{\odot}\text{yr}^{-1}$. This is slightly higher than the average accretion rate expected for a halo of $M_{\text{vir}} = 2 \times 10^{12} M_{\odot}$ at $z = 0$ ($\dot{M}_{\text{cosm}} = 11.5 M_{\odot} \text{ yr}^{-1}$; Correa et al. 2015b). However, the prediction is only an average value and we can expect variations for a single halo, considering differences in the environment and also taking into account the uncertainties in the virial mass of M31, as we have seen in Section 4.3.1. Moreover, the cloud infall time is approximately 2.5 Gyr and the cosmological accretion of baryons 2.5 Gyr ago is expected to be higher ($\approx 15 M_{\odot} \text{ yr}^{-1}$) than the current value (although this would more significantly affect the internal regions of the halo). In addition to the above considerations, part of the inflowing gas might be coming from the re-accretion of material expelled in the past by M31 or by other galaxies in and around the Local Group (including M31 satellites, see for example Hafen et al. 2019). This could also explain the slightly higher mass accretion rate compared to the estimates of Correa et al. (2015a,b), which are simply based on N-body simulations. For instance, using the EAGLE cosmological hydrodynamical simulations, Wright et al. (2021) found that the total accretion of matter at $z = 0$ (including primordial and ‘pre-processed’ gas, material that has been previously part of a galaxy) into a halo of $2 \times 10^{12} M_{\odot}$ is $\approx 25 M_{\odot} \text{ yr}^{-1}$.

We conclude that our estimate of f_{accr} is in line with the expectations from cosmological gas accretion.

We estimated a metallicity of $Z \approx 0.05 Z_{\odot}$ (see right-hand panel of Figure 4.4 and Table 4.2), which is consistent with the fact that the IGM has been enriched, throughout the evolution of the Universe, by metals expelled from galaxies (e.g. van de Voort & Schaye 2012). Even though the metallicity of the IGM at redshift zero is uncertain, recently Lehner et al. (2019) have found that, at $z < 1$, strong Ly α forest absorbers (SLFs, systems with $15 < \log N_{\text{HI}} < 16.2$), which are thought to be associated with the interface between the outer CGM and the Ly α forest/IGM, have a unimodal metallicity distribution with a median value equal to about $0.06 Z_{\odot}$. This is very consistent with our findings. Our result is, however, in slight disagreement with the estimate of Lehner et al. (2020), who have found a lower limit for the metallicity of the cool CGM of M31 of $0.2 Z_{\odot}$. We recall that this limit was obtained combining detected OI absorption with non-detections of HI in emission (see Howk et al. 2017). As also explained by Lehner et al. (2020), absorption and emission measurements are characterized by inherently different spatial resolutions and it is therefore possible that their estimated metallicity might be affected by the beam dilution effect. Moreover, this ratio is available for only 4 components in the entire AMIGA sample and Lehner et al. (2020) admit that this limit is not stringent. We therefore do not consider our result in tension with previous estimates.

Finding evidence of cool gas accreting onto the halo of a relatively massive star forming galaxy at redshift $z = 0$ is interesting and non-trivial. In the general picture, cool gas is not expected to penetrate directly into galaxy halos with a virial mass $\gtrsim 10^{12} M_{\odot}$ at $z = 0$ (see Dekel & Birnboim 2006; Mandelker et al. 2018). However, the actual mode of gas accretion into the halos of galaxies is still debated and a lack of cool gas predicted by simulations may also be affected by the lack of resolution (see Hummels et al. 2019; van de Voort et al. 2019). It is possible that the cool clouds, whose motion we are describing with our models, are originated from the accreting streams of intergalactic cool gas, fragmented by the interactions with the pre-existing hot CGM in the outer halo. These interactions might also be responsible for the deceleration of the cool clouds, possibly explaining the preference of our models for low initial radial velocities ($v_r \sim 10 \text{ km s}^{-1}$). We therefore consider the cold accretion of gas into the halo a plausible scenario to describe the majority of the cool gas observed in the halo of the Andromeda galaxy. We emphasize however that we are describing only the accretion in the outer halo of M31 and not the direct accretion of 10^4 K gas onto the galactic disk. A more accurate discussion on the fate of this gas is presented in the following Section.

Fate of the cool gas

If the cool CGM of M31 is indeed the result of cosmological gas accretion into the halo, there needs to be a mechanism that prevents $15 M_{\odot}$ of cool gas from accreting every year onto the disk of M31, which has currently a star formation of less than $1 M_{\odot} \text{ yr}^{-1}$ (see Rahmani et al. 2016). One possible explanation could

be the evaporation of the infalling clouds in the hot gas (see also Chapter 2). Since we used an analytical approach to study the dynamics of the cool CGM, our models are limited by the absence of second-order hydrodynamical effects⁷ that could destroy the cool absorbers. High-resolution simulations (e.g. Brüggén & Scannapieco 2016; Armillotta et al. 2017) have shown that cool clouds travelling through a hot corona are prone to destruction primarily due to Kelvin-Helmoltz instability and thermal conduction. The latter becomes particularly important for the evaporation of clouds when the temperature of the hot ambient medium is sufficiently high, as found also through analytical arguments (see Nipoti & Binney 2007). We therefore consider the evaporation a probable fate for the cool gas penetrating the hot halo of M31. In Chapter 5, we investigate the interactions between the different phases of the CGM using high-resolution simulations. Note that even if the clouds are destroyed before reaching the internal parts of the halo, our findings would most likely remain unaffected, since the observational data are reproduced in our model mainly by clouds that are located at large distances from the center, as can be seen in Figure 4.9.

If a substantial part of the cool gas is evaporating into the hot ambient medium, the latter is therefore continuously increasing in mass, a behaviour that our models do not take into account. The mass of the corona that we adopted in our models is about $6 \times 10^{10} M_{\odot}$ and an addition of up to $15 M_{\odot}$ every year would increase the coronal mass by roughly 60% in 2.5 Gyr (the average infall time of the clouds in our model). To investigate what the effect of this increase would be, we performed a fit using a coronal gas with the same properties outlined in Section 4.3, but twice as massive (40% of the total baryons in the halo of M31). The best-fit values of the 5 free parameters, shown in the bottom part of Table 4.3, are well within the range found with our fiducial model. This result implies that the increasing mass of the hot corona is not strongly affecting our findings. Note that a more massive corona would be unphysical, as it would exceed the amount of baryons expected within the halo of M31 (since $\sim 60\%$ of the baryonic mass is given by the sum of the stellar and cool CGM components). We conclude therefore that our results are robust and so is our favoured interpretation that the cool CGM clouds observed in the halo of M31 are part of a large scale inflow of intergalactic gas, which is feeding the halo, but not directly the star formation in the disk of M31.

4.5.3 Alternative origins

As mentioned in Section 4.4.2, the number of components per line of sight observed by the AMIGA Project is slightly larger than what predicted by our models (see Figure 4.7). While we argued that this might be due to some simplified assumptions of our models (spherical clouds in pressure equilibrium and isotropic accretion), alternative sources for the production of the cool gas might also help to explain this small discrepancy. In addition to cosmological accre-

⁷In addition to the first order effects of pressure confinement and drag, which are instead included.

tion, there are, in particular, two other main formation channels for the cool circumgalactic clouds that are not considered in this work. Although exploring in detail the impact of these processes on the CGM is beyond the scope of this work, we briefly describe them in the following.

The first scenario is the stripping of gas from satellite galaxies, which has been extensively observed in the local Universe (e.g. Brüns et al. 2005; Grcevich & Putman 2009; Poggianti et al. 2017; Johnson et al. 2018; Putman et al. 2021) and is one of the channels for the formation of cool CGM in hydrodynamical simulations (for example in galaxy groups in the EAGLE simulations; Marasco et al. 2016). Cold gas could be stripped from satellites and subsequently infall towards the galactic disc, in addition to the cosmological accretion. Moreover, satellites can contribute to the CGM of the main galaxy by expelling gas through winds (Hafen et al. 2019; Di Teodoro et al. 2019).

The above possibility has been explored for the AMIGA data, as some dwarf galaxies surrounding M31 (the vast majority of which are dwarf spheroidals devoid of gas) are found in close proximity of most of the lines of sight of the AMIGA data (Lehner et al. 2020). Even though the overall satellite velocity distribution tends not to follow the one of the CGM absorbers, part of the observed cool gas could have been stripped from a nearby satellite galaxy because of either ram pressure or tidal stripping. This gas would then follow different trajectories with respect to the satellite, possibly explaining the differences in the velocity distribution. Some cool gas has probably been stripped from the disk of M33, as shown by HI observations (Braun & Thilker 2004; Lockman et al. 2012; Wolfe et al. 2016), even though it seems to not affect the CGM detected by AMIGA (see Appendix E of Lehner et al. 2020).

Another possible way to produce cool CGM clouds in the halo of M31 is from the condensation of the hot coronal gas due to thermal instabilities. The cooling time of the hot CGM is too long for spontaneous radiative cooling to happen, especially in the external parts due to the very low densities, therefore some strong perturbation (such as turbulence, see for example Voit 2018) is needed to create dense pockets of gas with short cooling times, which could then perhaps trigger a thermal instability. These perturbations could also be caused by external processes like the cosmological accretion of IGM and/or satellite galaxies (Nelson et al. 2020; Esmerian et al. 2021). However, whether or not these instabilities can develop at all is still under debate (see Binney et al. 2009; McCourt et al. 2012; Sharma et al. 2012; Nipoti & Posti 2013, 2014; Sormani & Sobacchi 2019).

4.6 Summary and conclusions

With this study, we have investigated the properties of the cool CGM residing in the halo of the Andromeda galaxy (M31), using semi-analytic parametric models, where we describe the circumgalactic gas as a flow of cool clouds embedded in a hot ambient medium (corona). Our models take into account the effect of gravity and of the hydrodynamical interactions (drag and pressure

equilibrium) of the clouds with the corona, which also has an angular momentum motivated by cosmological prescriptions. We have compared our model predictions with the observational data of the AMIGA project (Lehner et al. 2020). Our goal was to reproduce the kinematics, the number of components and the total column densities provided by these data, in order to infer the properties of the cool CGM of M31. We investigated two different scenarios for the dynamics and origin of the cool gas: in the first scenario the clouds are part of a supernova-driven galactic wind, while in the second they are part of the cosmological accretion of gas into the galactic halo. We compared our predictions with the observations through a Bayesian analysis, which allowed us to find the best model that can successfully reproduce the data.

The results of our analysis are the following:

1. the cool circumgalactic gas observed in the halo of M31 is not originated by supernova-driven galactic winds. In order to reproduce the observations these outflows would require unphysical supernova efficiencies in transferring kinetic energy to the wind ($\approx 700\%$, while we could expect at most $\sim 10\%$). Moreover, we found that the outflowing gas would need to have low metallicities, in contrast with the expectations for material ejected from the central galaxy's ISM. We therefore discard this scenario as a viable way to describe the observations;
2. the covering factors, kinematics and column densities of the absorbers in the AMIGA sample are well reproduced by our inflow models. In particular, in these models the gas clouds have a mass of about $5 \times 10^6 M_\odot$ and start their infall from the virial radius with low radial and tangential velocities. They then fall towards the center with a spiraling motion, while they exchange angular momentum with a surrounding hot halo. We find a cool gas accretion rate at the virial radius of $\approx 15 M_\odot \text{ yr}^{-1}$, consistent with the infall predicted by cosmological models;
3. to reproduce the observations, the accreted material needs to have metallicities of about $0.05 Z_\odot$, consistent with the low metallicity expected for gas inflowing from the intergalactic medium.

Given our findings and conclusions, we favour a self-consistent scenario where the cool medium observed in the halo of M31 is produced by the accretion of low-metallicity intergalactic gas. We also find that most of the observed clouds, even at small projected distances from the disk, are intrinsically located in the outer parts of the halo, at large galactocentric distances. We argue that, given the second-order hydrodynamical effects that are not accounted for in this analytical analysis, the CGM clouds will likely evaporate in the hot ambient medium and therefore will not reach the disk and directly feed the star formation of M31. We explore in more detail the survival of these cool clouds in Chapter 5.

4.A Properties of the hot gas model

In this Appendix, we describe the properties of the hot CGM presented in Section 4.3.2. We utilized the python package COROPY (Sormani et al. 2018). This package allows to create baroclinic models⁸ of the hot rotating CGM, assuming that the pressure is stratified in ellipsoidal surfaces. The properties of such models are uniquely defined by the choice of the pressure profile along the axis of symmetry ($R = 0$) of the galaxy $P_{\text{axis}}(z)$ and by the axis ratio of the isobaric ellipsoidal surfaces $b/a = q(a)$ as a function of the ellipse semi-major axis. In this work, $P_{\text{axis}}(z)$ is obtained solving the equation of hydrostatic equilibrium along the $R = 0$ axis and assuming a polytropic distribution along this axis: $P_{\text{axis}}(z) = [\rho_{\text{axis}}(z)]^\gamma$, resulting in

4

$$P_{\text{axis}}(z) = P_0 \left[1 + \frac{\gamma - 1}{\gamma} \frac{\mu m_p}{k T_0} (\Phi_{\text{axis}}(z) - \Phi_{\text{axis},0}) \right]^{\gamma/(\gamma-1)}, \quad (4.8)$$

where m_p and k are respectively the proton mass and the Boltzmann constant, γ is the polytropic index, while T_0 and P_0 are temperature and pressure at some reference height z_0 . Here we adopt $\gamma = 1.2$ and $T_0 = 1.3 \times 10^6$ K at $z_0 = 100$ kpc, with $P_0 = P_{\text{axis}}(z_0) = n_0 k T_0$, with the value of n_0 defined below. Finally, $\Phi_{\text{axis}}(z)$ is the potential at the axis of symmetry, with $\Phi_{\text{axis},0} = \Phi_{\text{axis}}(z_0)$. Only to calculate the hot gas properties, we simplified the potential to just the NFW component. This is because, using the full potential, the assumption of Sormani et al. (2018) that the pressure is stratified on ellipses would break the reality condition for the rotation velocity (e.g. Barnabè et al. 2006). However, this effect is limited to only a few kpc above the disk plane and is unimportant for this work. For the axis ratio we use a hyperbolic function:

$$q(r) = \frac{q_{\text{min}} r_{\text{min}} + q_{\text{max}} r}{r_{\text{min}} + r}, \quad (4.9)$$

with $r_{\text{min}} = 5$ kpc, $q_{\text{min}} = 0.6$ and $q_{\text{max}} = 0.9999$.

All the parameters in equations (4.8) and (4.9) ($\gamma, T_0, r_{\text{min}}, q_{\text{min}}, q_{\text{max}}$) have been chosen (by trial and error) in order to have a realistic model for the corona of M31, in particular to reproduce an angular momentum in agreement with the theoretical expectations (for more details see Section 4.3.2). Once all the other parameters are fixed, the normalization factor n_0 is chosen in order to have a total mass in the hot CGM phase equal to 20% of the total baryonic mass expected within the halo, inferred by multiplying the virial mass by the cosmological baryon fraction 0.158 (Planck Collaboration et al. 2020). This corresponds to a mass of the corona of about $6 \times 10^{10} M_\odot$.

With the choice of parameters reported above, we find an average value of the specific angular momentum in our corona model equal to $3207 \text{ km s}^{-1} \text{ kpc}$, which is 20% higher than the DM estimate (see Section 4.3.2). This difference

⁸In these models, the pressure and density are not stratified along the same surfaces and the rotational velocity is not stratified in cylinders.

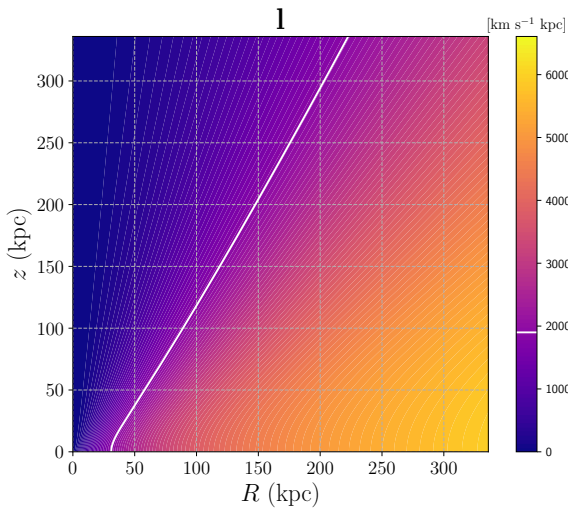


Figure 4.11: Specific angular momentum in our model of the hot CGM of M31 (see also Section 4.3.2), as a function of the cylindrical radius R and height z . The white contour indicates as a reference the angular momentum of the stellar component of M31.

could be attributed to the loss of low angular momentum material ejected by feedback in the past, consistent with the fact that the corona adopted in this work accounts for only 20% of the baryons expected within the dark matter halo (e.g. Pezzulli et al. 2017). The map of the specific angular momentum given by our final model is shown in Figure 4.11, with the white contour showing $l = 1900 \text{ km s}^{-1} \text{ kpc}$, giving an indication of where the angular momentum of the corona equals that of the disk (the lowest portion of this line could be slightly shifted inwards if including the disk contribution to the gravitational potential). Note how the specific angular momentum increases with the cylindrical radius R , as expected for a realistic model where the highest angular momentum material was accreted at later epochs and deposited in the outer regions.

Chapter 5

Hydrodynamical simulations of cool circumgalactic clouds: the case of M31

– A. Afruni, F. Fraternali, G. Pezzulli & A. Grønnow, 2022 –

in preparation

Abstract

The circumgalactic medium (or CGM), contains a large reservoir of potential fuel for star formation and is, therefore, believed to be fundamental in the evolution of star-forming galaxies. In particular, a large amount of cool ($\sim 10^4$ K) ionized CGM has been observed, mainly in absorption, up to the virial radii of low-redshift galaxies. As argued in Chapters 3 and 4, this medium is likely produced by the infall of gas from the surrounding intergalactic medium (IGM). However, whether this gas is accreted by the central galaxies or, instead, it evaporates into the hot phase of the CGM (also called corona, at $T \sim 10^6$ K) is not yet understood. In this Chapter, we study, using 2D and 3D high-resolution hydrodynamical simulations, the evolution of cool CGM clouds falling through the halos of nearby disk galaxies and interacting with the hot coronal gas. We focus in particular on the halo of M31, where this cool medium has been recently observed by the project AMIGA. We use, as initial conditions for our numerical experiments, the results of Chapter 4, where we have found that the observations of the cool CGM of M31 are well reproduced by infalling clouds starting at the virial radius (336 kpc). We setup hydrodynamical simulations, in which the cloud's motion is governed by the gravity of the dark matter halo and the interactions with the surrounding corona; the cool cloud and the hot gas are initially in pressure equilibrium. Apart from the external gravity, we also include the effects of radiative cooling and isotropic thermal conduction. We find that, in all our simulations, the cloud is destroyed by the hydrodynamical interactions with the hot corona and evaporates into the hot gas in about 2 Gyr and at distances from the disk of M31 larger than 150 kpc. This is different from the predictions of the semi-analytical models of Chapter 4, where the cool clouds have a constant mass during their infall. Nonetheless, after incorporating the results from our simulations (in particular the cloud evaporation and the evolution of its velocity, cross section and column density) into the best-fit models of Chapter 4, we find that the model predictions are still consistent with the observational data of the project AMIGA. We conclude, therefore, that the cool CGM of M31 (and likely of low-redshift star-forming galaxies of similar mass) is well described by clouds accreted from the IGM, that do not reach the central galaxy disk, but evaporate, instead, into the corona.

5.1 Introduction

Spiral galaxies continuously grow and form new stars, using the cold gas available in their disks. Typically, the mass of the cold interstellar medium (ISM) is, however, sufficient to feed the galaxy's star formation for only a few Gyr (Kennicutt 1983; Fraternali & Tomassetti 2012). Therefore, in order to sustain the star formation for the entire galaxy lifetime (about 10 Gyr), the ISM must be continuously replenished with accretion from the external gaseous environment (e.g. Sancisi et al. 2008), which is known as the circumgalactic medium, or CGM.

The cool CGM is often associated with inflow (e.g. Ho et al. 2017) and outflow (e.g. Schroetter et al. 2019) motions. In Chapters 3 and 4 we have shown, by comparing the predictions of semi-analytical models with observational data, that outflows from the central galaxies, powered by the supernova explosions in the disk, cannot be the main formation mechanism of the cool gas. Instead, most of the cool CGM is likely originated by accretion of IGM into the galaxy halos. In Chapter 4, in particular, we have demonstrated this for the case of the CGM of M31; specifically, we have considered both inflow and outflow models and we have shown that cosmological inflow, but not supernova-driven outflows, can explain the recent observations of the CGM of M31 by the project AMIGA (Lehner et al. 2015, 2020). More in detail, we have found that an inflow of cool gas clouds from the IGM, at a rate consistent with the predictions of cosmological models (e.g. Correa et al. 2015a), can successfully reproduce the observed kinematics, covering fraction and silicon column densities. We were also able to constrain the cloud properties, finding that they have a mass of $\approx 5 \times 10^6 M_\odot$, initial infall velocities of the order of 10 km s^{-1} and a low metallicity of $\approx 0.05 Z_\odot$. Gas with similar metallicities is generally assumed to be part of accretion from the IGM (e.g. Danforth & Shull 2008; Wotta et al. 2019).

In our semi-analytic model, cool gas clouds interact with the hot phase of the CGM (at $T \gtrsim 10^6 \text{ K}$, also called corona), which influences their motion through the drag force (e.g. Marinacci et al. 2011). However, we were not able to determine whether these clouds would be able to survive to the hydrodynamical interactions with the corona and actually reach the disk, or rather be destroyed during the journey. This is of primary importance, since the accretion of cool gas into the halo, as predicted by our models, is higher than $10 M_\odot \text{ yr}^{-1}$, while the current star formation of M31 is less than $1 M_\odot \text{ yr}^{-1}$ (Rahmani et al. 2016). Describing the cloud evaporation analytically is challenging, since it depends on many second-order effects like the Kelvin-Helmholtz (KH) and Rayleigh-Taylor (RT) hydrodynamical instabilities. In addition to the evaporation, the hydrodynamical effects also modify the cloud shape, while, in our semi-analytical models of Chapter 4, we assumed that the clouds maintain a spherical shape throughout their infall. The aim of this Chapter is to further investigate the cloud/corona interactions, using high-resolution hydrodynamical simulations. To correctly capture KH and RT instabilities, it is essential that simulations have a sufficient spatial resolution. Currently, the resolution of large-box and

'zoom-in' cosmological simulations (e.g. Crain et al. 2015; Pillepich et al. 2018; Hopkins et al. 2018) is at best of the order of one kpc and, therefore, largely insufficient to properly describe the interaction of the cool gas with the corona (e.g. Peebles et al. 2019; van de Voort et al. 2019). To this goal, one approach is to focus on a small region of the galactic halo, following the evolution of a single cloud moving through a hot medium. This kind of high-resolution simulations have been carried out extensively in the last decade (e.g. Heitsch & Putman 2009; Scannapieco & Brüggen 2015; Armillotta et al. 2016; Grønnow et al. 2018). One general result of these studies is that cool gas tends to be stripped from the cloud as a consequence of the KH instability and, in the absence of radiative losses, this effect eventually leads to the destruction of the cloud (e.g. Heitsch & Putman 2009). In the presence of radiative cooling, however, the gas stripping might lead to an opposite result: the gas at the cloud/corona interface has, indeed, intermediate temperatures ($T \sim 10^5$ K, close to the peak of the cooling function) and, depending on the initial conditions of the simulations (in particular the density of the coronal gas), short cooling times. As a result, this medium might cool very rapidly and eventually increase the mass of the cool gas: this effect is called condensation (e.g. Marinacci et al. 2010b; Armillotta et al. 2016; Gronke & Oh 2018).

Another important effect in determining the cloud evolution is thermal conduction, the transfer of heat via free electrons, which takes place in the presence of strong temperature gradients (Spitzer 1962). This diffusive effect tends to hinder the development of the KH instability at the cloud/corona interface and can therefore extend the survival time of the cloud (e.g. Vieser & Hensler 2007; Armillotta et al. 2017). On the other hand, if the temperature difference between the two gas phases is sufficiently large and if the cloud is not massive enough, thermal conduction might also lead to a faster evaporation (e.g. Brüggen & Scannapieco 2016). Magnetic fields also play an important role (e.g. Grønnow et al. 2018; Kooij et al. 2021) and, in particular, they suppress thermal conduction, since electrons follow the magnetic field lines and cannot move in the direction perpendicular to them. However, including magnetic field in simulations is computationally expensive and, in simulations where the magnetic field is not present, the thermal conduction is simply assumed to be isotropically suppressed to a fraction of its efficiency (e.g. Armillotta et al. 2016). Finally, also the self-gravity of the cloud might influence its evolution, but is generally only a minor effect with respect to radiative cooling, thermal conduction, or magnetic fields, because of the presumably low densities of clouds in the CGM (Li et al. 2020). Most of the studies mentioned above are, however, focused on regions up to ~ 10 kpc from the galactic disk, at the interface between the disk and the inner CGM, and there are very few simulations analyzing the evolution of cool clouds at galactocentric distances of $\gtrsim 100$ kpc (e.g. Armillotta et al. 2017). In this Chapter, we aim, instead, to characterize the evolution of the cool CGM detected up to more than 300 kpc away from the galactic disk.

We use high-resolution hydrodynamical simulations with an adaptive grid (see Section 5.2.3), to study the evolution of the cool CGM clouds. We focus in par-

ticular on the halo of M31, using the results of Chapter 4 as initial conditions for our simulations. The results of this work, however, may be applicable to other similar star-forming galaxies in the local Universe, if one assumes that their CGM have similar properties (see Chapters 3 and 4). We consider the effects of radiative cooling, suppressed isotropic thermal conduction and of the gravitational field of the dark matter (DM) halo of M31. Thanks to the adaptive grid, we are able to properly resolve the cool gas and to follow its infall from the virial radius towards the central galaxy. The main goal of this Chapter is to find whether this gas can reach the central regions and feed the star formation, or is instead destroyed by the interactions with the hot corona. Moreover, the results of these hydrodynamical simulations can be used to refine the analytical models presented in Chapter 4, in order to better describe the cool CGM of M31 and of similar star-forming galaxies.

In Section 5.2, we describe in detail the hydrodynamical simulations that we have used in this work; in Section 5.3, we report the results of our 2D and 3D numerical experiments; in Section 5.4, we show the comparison between the findings of our simulations and the AMIGA observations. In Section 5.5, we refine the analytical models based on the results of the simulations, we discuss the limitations of this work and we compare it with previous studies, while, in Section 5.6, we summarize our work and we outline our conclusions.

5.2 Hydrodynamical simulations

In this Section, we describe the setup of the high-resolution hydrodynamical simulations that we ran for this work and that we used to study the motion and properties of the cool CGM clouds in the halo of M31. To carry out our numerical experiments, we used the code PLUTO, version 4.3 (see Mignone et al. 2007, 2012), which is an Eulerian Godunov-type (Godunov 1959) code that solves the system of ideal hydrodynamical equations. We used in particular the HLLC Riemann solver (Toro et al. 1994), which represents a good compromise between accuracy and stability of the simulations (see Grønnow et al. 2018).

5.2.1 Initial conditions of the simulations

We assume that the CGM of M31 is initially composed of two distinct phases: (i) a hot circumgalactic medium, or corona, which represents a volume-filling phase in hydrostatic equilibrium with the halo gravitational potential; (ii) a cool circumgalactic gas phase, composed of multiple clouds pressure-confined by the hot medium and whose initial properties are based on the results of Chapter 4. With our simulations, we study, in particular, the evolution of one of these clouds and its interactions with the hot medium. The domain of our simulations is represented by a cartesian rectangular grid that extends in height from 65 kpc above the galactic disk of M31 (assumed at a height $z = 0$), up to 345 kpc from it (the virial radius of M31 is 336 kpc, see Section 4.3.1). We performed simulations in 2 and 3 dimensions. Both the x and (when present)

the y dimensions have an extension of 80 kpc. The large size of the grid, especially in the z direction, is chosen in order to follow the whole evolution of the cloud throughout the halo. In all our simulations, we assume an ideal gas, so that $P = nk_{\text{B}}T$, where P is the gas pressure, n is the gas volume density, T is the gas temperature and k_{B} is the Boltzmann constant.

We first define the hot corona as a static medium in equilibrium with the DM halo of M31 and we made the assumption that its density and temperature are plane parallel, hence they vary only as a function of the height z . This is justified by the fact that we are studying regions of the halos at large galactocentric distances from the disk. The density and temperature profiles of the corona are then described by

$$n_{\text{cor}}(z) = n_0 \left(\frac{T_{\text{cor}}(z)}{T_{\text{cor},0}} \right)^{1/(\gamma-1)}, \quad (5.1)$$

and

$$\frac{T_{\text{cor}}(z)}{T_{\text{cor},0}} = 1 + \frac{\gamma-1}{\gamma} \frac{\mu m_{\text{p}}}{k_{\text{B}} T_{\text{cor},0}} (\Phi(z) - \Phi_0), \quad (5.2)$$

where $\mu = 0.6$ is the mean molecular weight, valid for a fully-ionized gas, m_{p} is the proton mass, $\gamma = 1.2$ (see Section 4.A) is the polytropic index, $T_{\text{cor},0}$, n_0 and Φ_0 are the temperature, density and gravitational potential at a reference radius $r_0 = 10$ kpc and $\Phi(z)$ is the Navarro Frenk White potential (NFW, Navarro et al. 1996). This is assumed to vary only as a function of the height z and is calculated assuming a virial mass $M_{\text{vir}} = 2 \times 10^{12} M_{\odot}$, a virial radius $r_{\text{vir}} = 336$ kpc and a concentration $c = 10.25$ (see Section 4.3.1). We assume the gravitational potential to be given only by the DM component, neglecting the effects of the stellar disk and bulge of M31 (see Section 4.3.1). At the large distances probed with our simulations, the contribution of the stellar components to the total potential is negligible.

In order to simplify the setup of the simulations, we assume that the corona does not rotate, although it is expected to do so, both from theoretical arguments (e.g. Pezzulli et al. 2017) and observational evidence in the Milky Way (MW Hodges-Kluck et al. 2016). However, as we have seen in Chapter 4, the hot medium should have relatively high rotational velocities only in the inner regions of the halo, while it rotates very slowly at the distances that we are probing with our simulations. This simplification, therefore, does not significantly affect our results. We chose values of γ , $T_{\text{cor},0}$ and n_0 that produce a model of the hot gas whose density and temperature profiles are consistent with the ones of the more sophisticated, rotating hot CGM model presented in Chapter 4. Despite the approximation of a static corona, this choice of parameters ensures that the current model is in agreement with observational estimates for the Milky Way (e.g. Salem et al. 2015) and will allow us to make fair comparisons between the semi-analytical models of Chapter 4 and the results of the simulations. As in the previous Chapters, the total coronal mass is equal to 20% of the total baryonic mass expected within the halo ($M_{\text{vir}} \times f_{\text{bar}}$, where $f_{\text{bar}} = 0.158$ is the cosmological baryon fraction, Planck Collaboration et al. 2020). The

density and temperature profiles of the corona are shown in the two panels of Figure 5.1.

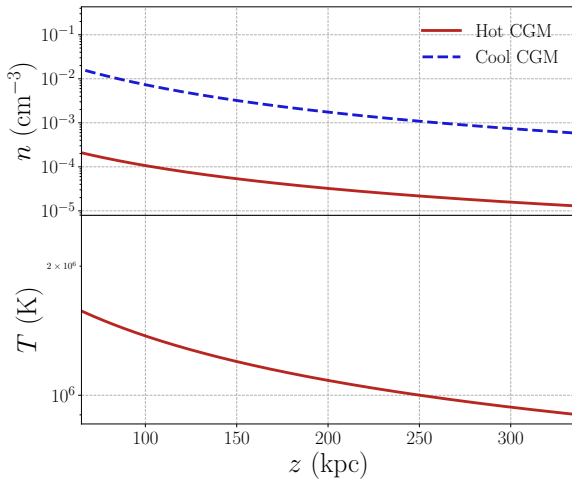


Figure 5.1: Top: density profile of the hot corona (5.1, red solid curve) that we utilize in our simulations, and of cool CGM in pressure equilibrium with the hot gas (5.3, blue dashed curve). The density of the cool CGM at the virial radius is adopted the initial density of the cloud in our simulations. Bottom: temperature profile of the hot corona, described by equation (5.2).

Based on the results of Chapter 4, we simulate here the evolution of a cloud of cool gas, starting at the virial radius of M31, pressure-confined by the hot corona and infalling towards the galaxy due to the gravitational attraction of the halo. The density of cool gas in pressure equilibrium with the hot CGM (see the blue dashed curve in Figure 5.1) is given by:

$$n_{\text{cool}}(z)T_{\text{cool}} = n_{\text{cor}}(z)T_{\text{cor}}(z), \quad (5.3)$$

where $T_{\text{cool}} = 2 \times 10^4$ K is the temperature assumed for the cool CGM (e.g. Keeney et al. 2017; Lehner et al. 2020) and $n_{\text{cor}}(z)$ and $T_{\text{cor}}(z)$ are given, respectively, by equations (5.1) and (5.2). We used equation (5.3) to calculate the initial cloud central density $\rho_{\text{cl}} = \mu m_{\text{p}} n_{\text{cl}}$ (with $\mu = 0.6$), at the virial radius of M31. Once the density is defined, we assume that the cloud is spherical and its initial radius is obtained through

$$r_{\text{cl}} = \left(\frac{3m_{\text{cl}}}{4\pi\rho_{\text{cl}}} \right)^{1/3}, \quad (5.4)$$

where m_{cl} is the initial mass of the cloud, one of the parameters that we vary in our simulations (see below). The cloud density is described by a smooth profile (see Grønnow et al. 2018; Kooij et al. 2021):

$$n(r) = n_{\text{cor}} + 0.5(n_{\text{cl}} - n_{\text{cor}}) \{1 - \tanh[s(r/r_{\text{cl}} - 1)]\}, \quad (5.5)$$

where the parameter s sets the steepness of the profile (we adopted $s = 10$ for all our simulations). This profile produces a smooth transition between the coronal

and the cloud density, with $n(r_{\text{cl}}) \approx n_{\text{cl}}/2$ in the limit where the density of the cloud is significantly higher than the one of the corona, which is the case in all our experiments¹. Note that, as a consequence of the pressure equilibrium, also the temperature of the cloud has a smooth profile that goes from 2×10^4 K to the temperature of the corona. Finally, we impose an initial negative velocity for the cloud along the z -axis $v_z = -10 \text{ km s}^{-1}$, which is within the range found in Chapter 4. All the parameters that remain fixed in all our experiments are listed in Table 5.1. In our simulations, we adopt zero-gradient (or outflow) boundary conditions everywhere, allowing material to freely leave the simulation domain.

(1)	(2)	(3)	(4)	(5)	(6)	(7)
v_z	n_{cl}	$n_{\text{cor}}(r_{\text{vir}})$	T_{cl}	$T_{\text{cor}}(r_{\text{vir}})$	Z_{cool}	Z_{cor}
(km s^{-1})	(cm^{-3})	(cm^{-3})	(K)	(K)	(Z_{\odot})	(Z_{\odot})
-10	5.8×10^{-4}	1.3×10^{-5}	2×10^4	9×10^5	0.05	0.3

Table 5.1: Fixed parameters in our simulations: (1) initial cloud velocity along the vertical direction; (2) initial cloud central density; (3) coronal density at the virial radius; (4) initial central cloud temperature; (5) temperature of the hot corona at the virial radius; (6) metallicity of the cloud; (7) metallicity of the corona.

5

5.2.2 Cooling and thermal conduction

We include, in our simulations, both the effects of radiative cooling and thermal conduction. Cooling is based on the collisional ionization equilibrium tables of Sutherland & Dopita (1993), which provide the cooling rate Λ as a function of temperature and metallicity Z . For simplicity, we are neglecting, in this work, the presence of external ionizing sources, in particular the extragalactic UV background (EUVB, e.g. Haardt & Madau 2012), whose impact on our results will be discussed in Section 5.5.2. The energy loss due to cooling is given by $\Delta E = -n^2 \Lambda(T, Z)$. In all the simulations, the cloud has a metallicity $Z = 0.05 Z_{\odot}$, in agreement with the findings of Chapter 4, while the corona has $Z = 0.3 Z_{\odot}$, consistently with observational evidence for the inner regions of the corona of the Milky Way and nearby massive spiral galaxies (see Miller & Bregman 2015; Anderson et al. 2016). We note that the metallicity of the corona, at distances of hundreds of kpc from the disk, is less well constrained and may be likely lower than the value we adopted. We will discuss the impact of this choice on our results in Section 5.5.2. We keep track of the metallicity using a passive tracer C_Z , initiated at the values stated above and that evolves with the simulation without affecting the gas flow (see Mignone et al. 2012 for the

¹Note that, being the density of the cloud not constant, but described by a smooth profile, the initial mass of the cloud will be slightly ($\sim 5\%$) smaller than the value used in equation (5.4) and that is reported in Table 5.2.

evolution of passive scalars in PLUTO). We assume that the corona is in thermal equilibrium, likely due to the presence of heating sources that balance its cooling and that we do not explicitly include in our simulations. For simplicity, we then assume that the hot gas can not cool. In order to do this, we set an additional tracer C_{cool} , which is used to isolate the coronal material that is not affected by the cloud. This tracer is initially set to 1 for the cloud (for $r < 1.3r_{\text{cool}}$, in order to contain all the cloud material) and 0 elsewhere and evolves with the simulation. At anytime, material where $C_{\text{cool}} < 10^{-8}$ (so not affected by the cloud) is not allowed to cool. We note that likely this choice does not significantly affect our results, since the cooling time of the corona is everywhere in the grid longer than ~ 7 Gyr. Finally, we also impose, in all our simulations, a cooling floor at 2×10^4 K, below which the gas is not allowed to cool. This partially takes into account the effect of the EUVB, which we are otherwise neglecting in this work (see Section 5.5.2), and which does not allow the cool gas to cool below this temperature.

All our simulations also include thermal conduction, which is the transfer of heat via electrons between two gas phases at a different temperature. Given that the hot and cool phases of the CGM are at temperatures that differ by almost two orders of magnitude, thermal conduction is expected to play an important role in the evolution of this system. In the simulations, this effect is introduced by adding an additional divergence term in the energy equation, using the module available in PLUTO (see Mignone et al. 2012). Under the assumption that the mean free path of electrons is much smaller than the temperature scale length, the flux of thermal conduction is in the non-saturated regime and is equal to:

$$\mathbf{q}_{\text{ns}} = -f_{\text{tc}} \kappa_{\text{Sp}}(T) \nabla T, \quad (5.6)$$

where ∇T is the gradient of temperature and $\kappa_{\text{Sp}}(T)$ is the Spitzer conductivity (Spitzer 1962), given by:

$$\kappa_{\text{Sp}}(T) = 1.84 \times 10^{-5} \frac{T^{5/2}}{\ln \Psi} \text{ erg s}^{-1} \text{ K}^{-1} \text{ cm}^{-1}, \quad (5.7)$$

where T is the temperature (in K) of the hot gas and $\ln \Psi$ is the Coulomb logarithm (≈ 30 in our setup). These equations are valid for a fully ionized gas, as appropriate for our conditions. In equation (5.6), we have multiplied the Spitzer standard flux by f_{tc} : a suppression factor lower than 1 that is used to take into account the effect of the magnetic field. Given that, in the presence of such a field, the electrons follow the magnetic field lines, the thermal conduction flux is strongly reduced in the transverse direction. The magnetic suppression is, therefore, anisotropic, but the isotropic approximation works fairly well (e.g. Kooij et al. 2021). In general, the exact value of f_{tc} is largely unconstrained, with different authors finding values that go from 0.001 (e.g. Chandran & Cowley 1998) to 0.2 (Narayan & Medvedev 2001). Recently, this suppression factor has been estimated for a CGM cloud/corona system with

MW-like properties (therefore arguably similar to those of M31), using magnetohydrodynamic (MHD) high-resolution simulations, by Kooij et al. (2021). These authors constrained the value of f_{tc} to be between 0.03 and 0.15.

When the temperature scale length becomes smaller than the mean free path of the electrons, equation (5.6) is not valid anymore. In this case, the thermal conduction flux becomes saturated and is expressed by (Cowie & McKee 1977):

$$\mathbf{q}_{\text{sat}} = 5\phi\rho c_s^3, \quad (5.8)$$

where ρ is the gas density, c_s is the sound speed and ϕ is an efficiency factor less than or of the order of unity (we adopted $\phi = 0.3$). To ensure a smooth transition between the two flux regimes, the flux is described by the formula (Dalton & Balbus 1993):

$$\mathbf{q} = -f_{\text{tc}} \frac{\kappa_{\text{Sp}}(T)}{1 + \sigma} \nabla T, \quad (5.9)$$

where

$$\sigma = \frac{\kappa_{\text{Sp}} \|\nabla T\|}{\mathbf{q}_{\text{sat}}}. \quad (5.10)$$

5

5.2.3 Simulation setup

All the simulations in this study have been performed using the Adaptive Mesh Refinement (AMR) technique, provided by the PLUTO package. This is crucial in order to be able to follow the evolution of the cloud in a reasonable computational time. The cloud occupies only a small fraction (of a size of about 10 kpc) of the grid, but might eventually travel for hundreds of kpc. Hence, the volume is large to capture the whole journey of the cloud, but only some of it (where the cool gas is located) needs to be resolved at any one time. In particular, the cells are refined according to a refinement threshold χ , which is based on the second derivative of the density (see Lohner 1987). We have adopted, in all our simulations, $\chi = 0.8$, which represents a compromise in order to have the required resolution without being too computationally expensive ($\chi = 0$ corresponds to refinement everywhere, while $\chi = 1$ corresponds to no refinement). In order to capture the entire evolution of the cloud, we ran all our simulations (except for one case, the simulation 2D8, see below) for 3 Gyr.

In this Chapter, we present results of runs of both 2-dimensional and 3-dimensional simulations. In the 2D case, the base grid has a resolution of 500 pc and we refine up to 5 levels (6 in simulation 2D8, see Table 5.2), increasing the resolution by a factor 2 for each level, to a maximum resolution, therefore, of ~ 16 pc (~ 8 pc in simulation 2D8). For the 3D simulations, the base grid has instead a resolution of 1 kpc and we refine up to 4 levels, i.e. to a maximum resolution of ~ 62 pc. Based on the results of Chapter 4, the observations of the cool CGM of M31 are best reproduced by clouds with a mass of $5 \times 10^6 M_\odot$, which is therefore the value that we adopt in our fiducial simulation (2DFID) for the

(1)	(2)	(3)	(4)	(5)	(6)
Sim. Id	m_{cl} (M_{\odot})	r_{cl} (kpc)	f_{tc}	Max res. (pc)	Geom.
2DFID	5×10^6	5.2	0.1	16	2D
2DF001	5×10^6	5.2	0.01	16	2D
2DM1E6	10^6	3.0	0.1	16	2D
2D31	5×10^6	5.2	0.1	31	2D
2D62	5×10^6	5.2	0.1	62	2D
2D8	5×10^6	5.2	0.1	8	2D
2D31F001	5×10^6	5.2	0.01	31	2D
2D31F005	5×10^6	5.2	0.05	31	2D
3DFID	5×10^6	5.2	0.1	62	3D
3DF001	5×10^6	5.2	0.01	62	3D

Table 5.2: Varying parameters in our simulations: (1) ID chosen for the simulation; (2) initial cloud mass; (3) initial cloud radius; (4) suppression factor of the thermal conduction; (5) maximum grid resolution; (6) geometry. The naming scheme adopted for the simulation IDs is the following: 2D/3D represents the geometry; FID is used for the fiducial simulations, with $m_{\text{cl}} = 5 \times 10^6 M_{\odot}$, $f_{\text{tc}} = 0.1$ and a maximum resolution of 16 pc in 2D and 62 pc in 3D; the rest of the ID emphasises variations from the fiducial configuration, in terms of resolution, (8, 31, 62), f_{tc} (F001, F005) or m_{cl} (M1E6).

initial mass of the cloud. Given the initial cloud density n_{cl} , this mass implies a cloud radius $r_{\text{cl}} = 5.19$ kpc. The best-fit cloud mass found in Chapter 4 has also uncertainties and therefore it is interesting to investigate how the simulation evolves by adopting a different initial cloud mass. We do this by performing one simulation (2DM1E6) where $m_{\text{cl}} = 10^6 M_{\odot}$, which implies a smaller initial radius of 3 kpc. The sizes of the clouds analyzed in this study are therefore well above the grid resolution of the highest levels. This ensures that the cloud is in all cases well resolved by our simulations, but we discuss more in detail the convergence of our simulations in Section 5.3. Finally, based on the results of Kooij et al. (2021), in our fiducial simulation we use a suppression factor of the thermal conduction, $f_{\text{tc}} = 0.1$. We also ran simulations with lower suppression factors (see also Appendix 5.A), to investigate its effect on the behaviour of the cloud and especially on its survival. All the simulations that we have run for this work are reported in Table 5.2.

5.3 Results

In this Section, we report the results of our numerical experiments. We analyze, in Section 5.3.1 and 5.3.2, the results of, respectively, the 2D and 3D simulations, focusing in particular on the survival of the cool gas. For the 2D simulations (Section 5.3.1), we first investigate the dependence of our results on the grid resolution, then we analyze more in detail the simulations with the highest resolution. In Section 5.3.2, we analyze our two 3D simulations and we present a detailed study on the cross section of the cool gas for our fiducial run.

5.3.1 2D simulations

In Figures 5.2 and 5.3, we show the outputs of our fiducial 2D run (2DFID), with 5 levels of resolution (highest resolution of ~ 16 pc), a cloud with a mass of $5 \times 10^6 M_{\odot}$ and $f_{\text{ic}} = 0.1$. We report, in particular, the evolution of the density (Figure 5.2) and temperature (Figure 5.3) in the entire grid at four different times: $t = 0.7$ Gyr, $t = 1.5$ Gyr, $t = 1.8$ Gyr and $t = 2.2$ Gyr. Note how the density (and, to some extent, the temperature) of the hot medium increases at lower heights, as described by the profile given by equation (5.1) (equation 5.2) and shown in the top (bottom) panel of Figure 5.1. From the density and temperature maps we can clearly see the evolution of the cool gas cloud, which is initially at a distance of 336 kpc, corresponding to the virial radius of M31 (shown by the black crosses), and starts then to fall towards the disk, attracted by the gravitational force.

Given the low initial velocity of the cloud, the low gravitational pull at these large distances and the deceleration caused by the hot corona, the initial motion of the cloud is relatively slow and after almost 1 Gyr the cloud is still located at about 300 kpc from the center. At this point, due to the ram pressure (or drag force) of the hot corona, the cool gas is already starting to lose its spherical shape and is flattened along the z -direction. After 1.5 Gyr, the cool gas has travelled almost 100 kpc from its initial position. Due to the interaction with the hot gas (in particular, Kelvin-Helmoltz and Rayleigh-Taylor instabilities) the cool medium has completely lost its initial shape, having been shredded into filamentary structures. This is even more evident at 1.8 Gyr. Finally, at 2.2 Gyr the cool gas has reached a distance of about 150 kpc from the disk, but at this point most of its mass has evaporated into the hot surrounding medium. Figures 5.2 and 5.3, therefore, already show how the typical CGM cool clouds that we are studying, under the specific assumptions of our fiducial simulation, seem not to be able to reach the galactic disk. Instead, they evaporate into the hot corona at large galactocentric distances.

In order to investigate more quantitatively the cloud survival, we define as cloud mass, at each time, the sum of the mass of all the simulation cells² with a tem-

²Given that these simulations are 2-dimensional, we are effectively simulating a grid with an arbitrary thickness, where the gas properties do not vary along the third dimension. Therefore, the cloud is cylindrical, with an initial circular cross-section of radius r_{cl} . To relate the 2D cool gas mass with the mass of an initially spherical cloud, we multiply

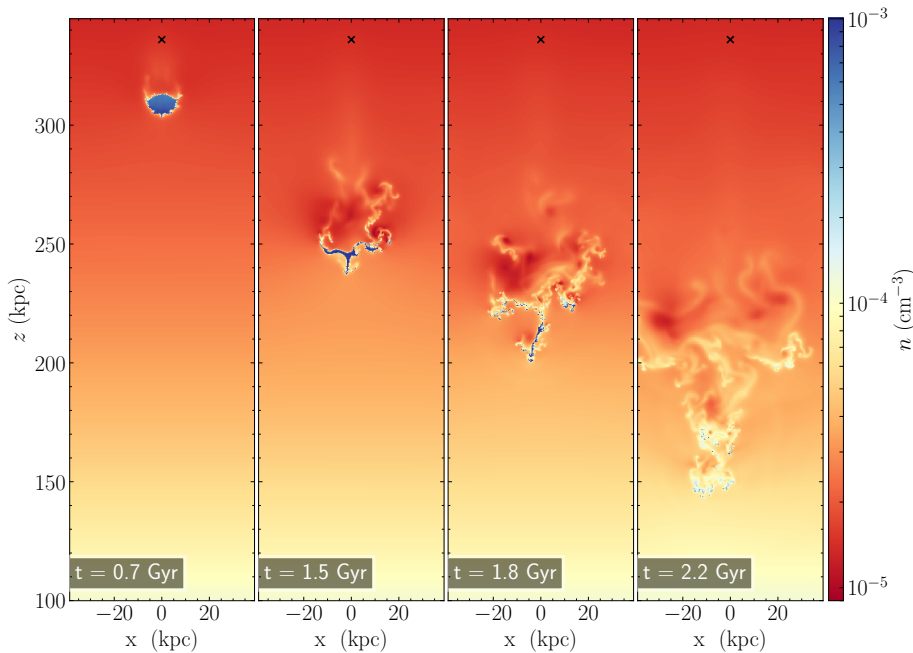


Figure 5.2: Density maps of our fiducial 2D hydrodynamical simulation (2DFID, $m_{\text{cl}} = 5 \times 10^6 M_{\odot}$, $f_{\text{IC}} = 0.1$, maximum resolution ~ 16 pc) at four different times. From left to right, $t = 0.7$ Gyr, $t = 1.5$ Gyr, $t = 1.8$ Gyr, $t = 2.2$ Gyr. The black crosses show the initial position of the cloud, at $z = 336$ kpc.

perature $T < 3 \times 10^4$. This is, in fact, slightly higher than the initial temperature of the cloud (2×10^4 K) and ensures that we are selecting all the cool gas in the simulation³.

In Figure 5.4, we use the evolution of the cool gas mass to investigate the convergence of our simulations, i.e. to explore whether our results are dependent on the grid resolution. We show the mass of the cool gas as a function of time for 4 different simulations at different (maximum) resolutions: ~ 62 pc (2D62), ~ 31 pc (2D31), ~ 16 pc (2DFID) and 8 pc (2D8)⁴. In all the simulations, the cool gas retains most of its mass for the majority of its evolution: indeed, the time in which it has lost 10% of its initial mass goes from 1.38 Gyr for the simulation 2D8 to 1.56 Gyr for 2D62. The cool gas undergoes then a rapid destruction and,

this value by the factor $4/3r_{\text{cl}}$ (see Marinacci et al. 2010b), hence implicitly assuming that $4/3r_{\text{cl}}$ is the thickness of the grid.

³Note that this threshold in temperature is relatively arbitrary and one could choose a different value. We have verified that using $T = 5 \times 10^4$ K and $T = 10^5$ K does not significantly change our results, with the evaporation time (see below) changing by, respectively, only 1% and 3%.

⁴For computational reasons, we were not able to run this simulation for more than ~ 1.5 Gyr. Therefore, in the rest of this Chapter, we consider 16 pc as the highest resolution that we were able to probe.

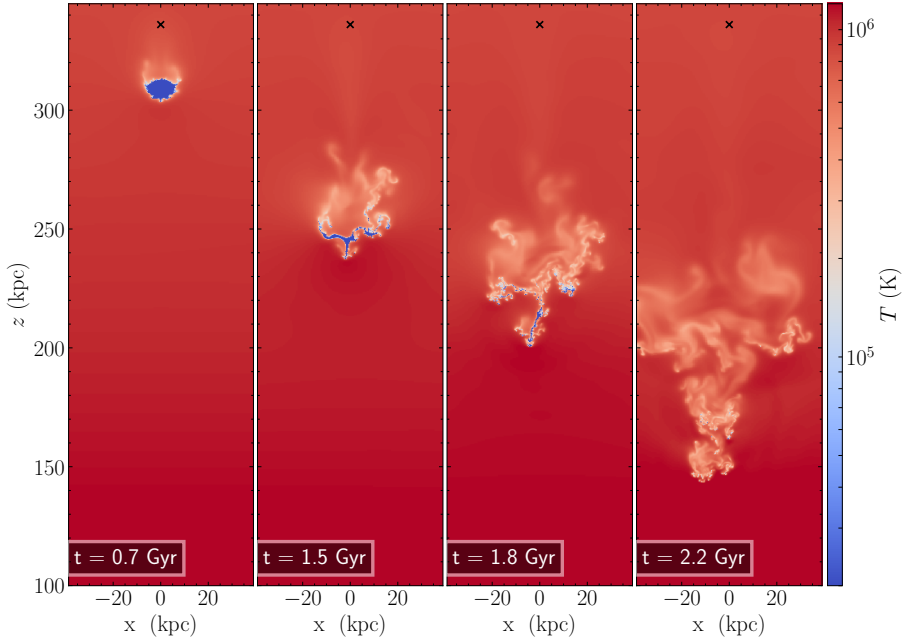


Figure 5.3: Temperature maps of the simulation 2DFID, at the same times of Figure 5.2. The black crosses show the initial position of the cloud, at $z = 336$ kpc.

at 3 Gyr, its initial mass has dropped by at least three orders of magnitude (and in the 2DFID and 2D31 simulations it has completely disappeared at around 2.5 Gyr). More quantitatively, we can define the time t_{ev} in which the cool gas has lost 90% of its initial mass. At this moment, we can indeed consider the cloud as effectively already evaporated into the surrounding medium. Indeed, only 10% of the initial mass is left and the cool gas generally looks fragmented into small clumps that are unlikely to survive. The value of t_{ev} goes from 2.10 Gyr for our fiducial simulation 2DFID to 2.31 Gyr for 2D62 and is shown in Figure 5.4, by denoting with a higher level of transparency the evolution at $t > t_{\text{ev}}$. These times, therefore, are consistent with each other and the cool gas mass evolution at $t < t_{\text{ev}}$ is similar for all the analyzed resolutions, indicating that we are close to convergence. The profiles diverge more significantly after t_{ev} and there seems to be a systematic trend, where the cloud evaporation is faster with increasing the resolution. However, the variation between the different profiles is relatively small and seems to decrease at higher resolutions. We conclude then that, even though simulations at higher resolution would be desirable, our experiments are probably reliable and arguably close to convergence. Thermal conduction has also implications on the resolution needed for convergence, as we discuss in Appendix 5.A. Finally, one may note that all the profiles show an initial small increase of mass. This is due to the density smoothing between cloud and corona (equation 5.5), which implies the presence of a shell of gas

around the cloud at intermediate densities (and therefore temperature). This shell, at temperatures of about 10^5 K (close to the peak of the cooling function) rapidly cools and joins the cool cloud, leading to the initial mass increase. This effect is present in all our simulations and has, however, a negligible impact on our results.

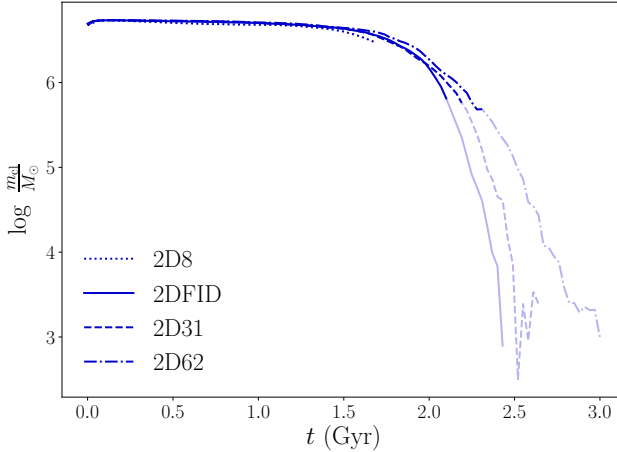


Figure 5.4: Evolution with time of the mass of the cool gas in 4 different simulations with an initial cloud mass of $5 \times 10^6 M_\odot$ and $f_{\text{tc}} = 0.1$, at different resolutions: 2D8 (8 pc), 2DFID (16 pc), 2D31 (31 pc) and 2D62 (62 pc).

In the following, we analyze more in detail the results for the three 2D simulations with the highest resolution that we managed to achieve (16 pc). In Figure 5.5, we present the evolution of the cool gas mass as a function of time (left-hand panel) and height (right-hand panel) for the simulations 2DFID, 2DF001 and 2DM1E6. In particular, we obtained the profile as a function of the height by calculating the height, at each time t , of the center of mass of the cool gas. As for the evaporation time t_{ev} , we calculate an evaporation height z_{ev} , at which the cool gas has lost 90% of its initial mass. For the fiducial simulation (2DFID, solid line), we obtained $z_{\text{ev}} = 174$ kpc.

In the two other simulations reported in Figure 5.5, we investigate the effects on the survival of the cloud, at fixed resolution, of using a suppression factor $f_{\text{tc}} = 0.01$ for the thermal conduction (simulation 2DF001, dashed line) or an initial cloud mass $m_{\text{cl}} = 10^6 M_\odot$ (simulation 2DM1E6). We can see that varying the suppression factor does not significantly change the mass evolution, in particular until t_{ev} (or z_{ev}) and the evaporation time and height are similar to our fiducial case. Therefore, even considering an extremely low efficiency of thermal conduction, the cool gas does not survive in our simulation. Based on these results, we can speculate that the CGM clouds observed in the halo of M31 by Lehner et al. (2020), are likely not able to survive their journey from the virial radius to the center and directly accrete onto the disk. In the low-mass case (dotted curves) the trends of the mass profiles are very similar to the evolution of the higher mass cloud. The main difference is, however, a significantly faster evaporation for the low-mass cloud. This is expected, since the timescales of growth of the KH and Rayleigh-Taylor instabilities are shorter for clouds with

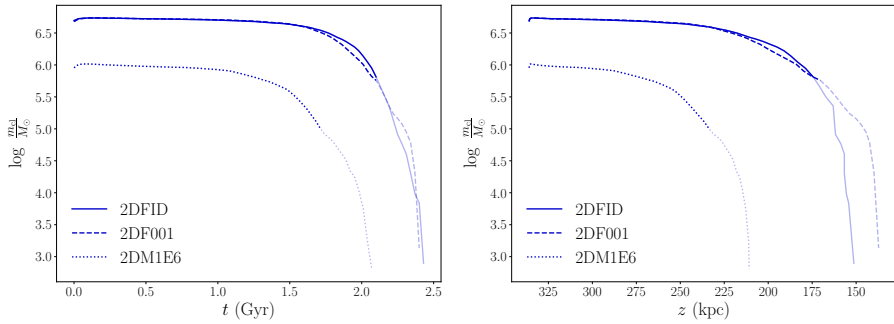


Figure 5.5: Evolution of the cool gas mass with time (left-hand) and height (right-hand) for the simulations 2DFID (solid curve), 2DF001 (dashed curve) and 2DM1E6 (dotted curve). All the curves have a higher level of transparency for $t > t_{ev}$ or $z < z_{ev}$ (see main text for more details).

5

smaller sizes and, therefore, the cloud gets more easily disrupted. Indeed, we find an evaporation time $t_{ev} = 1.7$ Gyr and an evaporation height $z_{ev} = 234$ kpc.

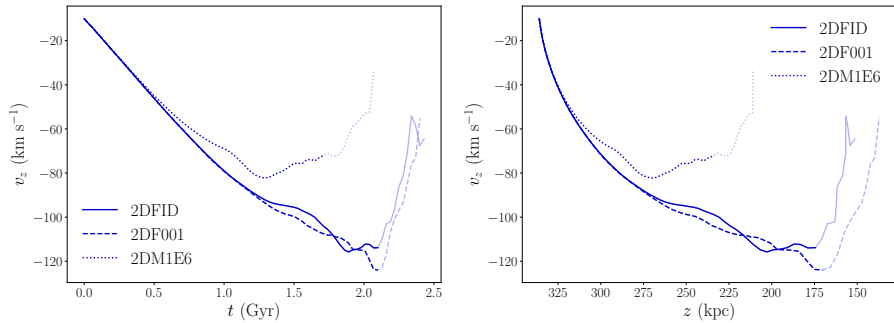


Figure 5.6: Evolution of the cool gas velocity along z , as a function of time (left-hand panel) and height (right-hand panel) for the same simulations shown in Figure 5.5. The level of transparency of the different curves is defined as in Figure 5.5.

To conclude the analysis of the 2D simulations, we show in the two panels of Figure 5.6 the evolution with time (left-hand side) and height (right-hand side) of the velocity of the cool gas (selected with the same criterion explained above) along the z -direction, averaged across all the cells with cool gas, using the cell mass as a weight. We report in particular the results for the same 3 simulations analyzed above (2DFID, 2DF001, 2DM1E6), using the same line and transparency styles as in Figure 5.5. We can see how, for the high-mass cloud, the evolution of the cool gas velocity is very similar for the two simulations, reaching velocities of around -120 km s^{-1} at t_{ev} (or z_{ev}). After this point, the (absolute value of the) velocities start to decrease. At this point of its evolution, the cloud is completely broken up into small cloudlets and most

of its mass is already evaporated into the corona. The $10^6 M_\odot$ cloud shows a similar behaviour, reaching however velocities of only -80 km s^{-1} , reflecting a larger impact of the drag force on low mass clouds, as expected.

5.3.2 3D simulations

We now move to the analysis of the results of the 3D simulations that we performed in this work. In Figures 5.7 and 5.8 we report, respectively, the

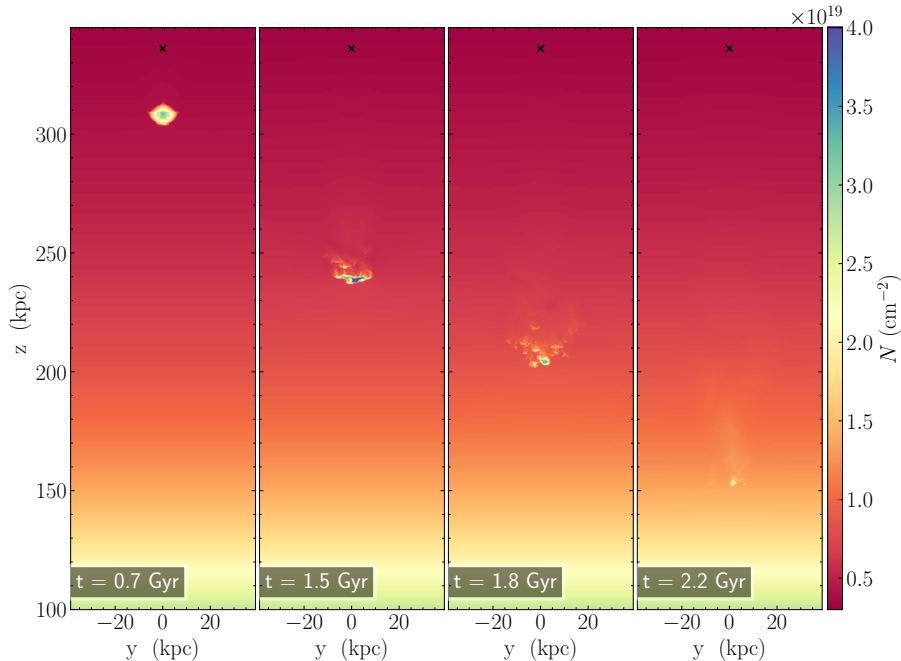


Figure 5.7: Map of the projected density along x for our fiducial 3D hydrodynamical simulation (3DFID, $m_{\text{cl}} = 5 \times 10^6 M_\odot$, $f_{\text{tc}} = 0.1$, maximum resolution ~ 62 pc) at the same times analyzed in Figure 5.2. The black crosses show the initial position of the cloud, at $z = 336$ kpc.

projection of the density distribution and the temperature on a slice along $x = 0$ of the fiducial 3D simulation (3DFID, $m_{\text{cl}} = 5 \times 10^6 M_\odot$, $f_{\text{tc}} = 0.1$, maximum resolution of 62 pc), at the same four different times as for Figure 5.2. We can see how the general evolution is comparable to the 2-dimensional case (see Figures 5.2 and 5.3), with the cool gas that has almost completely disappeared in the last snapshot at 2.2 Gyr. The main difference is in the shape of the cool gas between the 2D and the 3D case. This is most evident in the second and third snapshots at 1.5 and 1.8 Gyr: in the 3D simulation, instead of forming long filamentary structures, the cloud seems more prone to break into smaller cloudlets. Note however how the 2D and 3D simulations discussed above might be not directly comparable. This is due to the difference in resolution, that in

the 3D simulation, due to its computational cost, is necessarily lower than in the 2-dimensional case (however, the filamentary structures are visible also in the simulation 2D62, which has the same resolution of the 3D case. See also the top-left panel of Figure 5.9 for a quantitative comparison of these two simulations). The temperature and density maps along the y direction are similar to those shown in Figures 5.7 and 5.8. This is expected, given the symmetry of the initial conditions along x and y . Below we will, instead, show more thoroughly the evolution of the column density projected along the z -axis (see Figure 5.10).

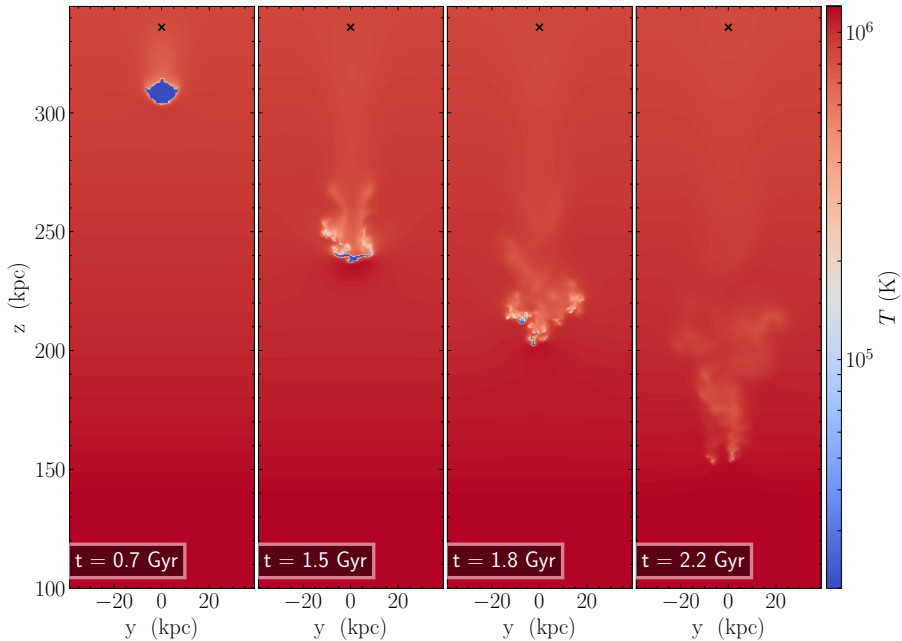


Figure 5.8: Map of the temperature of the simulation 3DFID, on a slice along $x = 0$, at the same times analyzed in Figure 5.2. The black crosses show the initial position of the cloud, at $z = 336$ kpc.

As for the 2D simulations, we selected the cool CGM as the gas contained in the grid cells with $T < 3 \times 10^4$ K and in the four panels of Figure 5.9 we show the evolution of the main properties of the cool gas: mass⁵ (top panels) and velocity along the z -direction (bottom panels), both as a function of time (left column) and height (right column). All the curves shown in Figure 5.9 have a higher level of transparency for $t > t_{ev}$ or $z < z_{ev}$, where t_{ev} and z_{ev} have the same definitions (90% of the initial mass has been lost) as for the 2D simulations. In particular, in the top-left panel we also show, as a comparison, the evolution

⁵In the 3D case, this value can be obtained directly by summing the mass of the simulation cells, without multiplying by the factor used for the cool gas mass in the 2D simulations.

of the cool gas mass for the simulation 2D62 (dotted curve), which, except for the number of dimensions, has the same properties as our fiducial 3D simulation 3DFID. We can see that increasing the number of dimensions changes

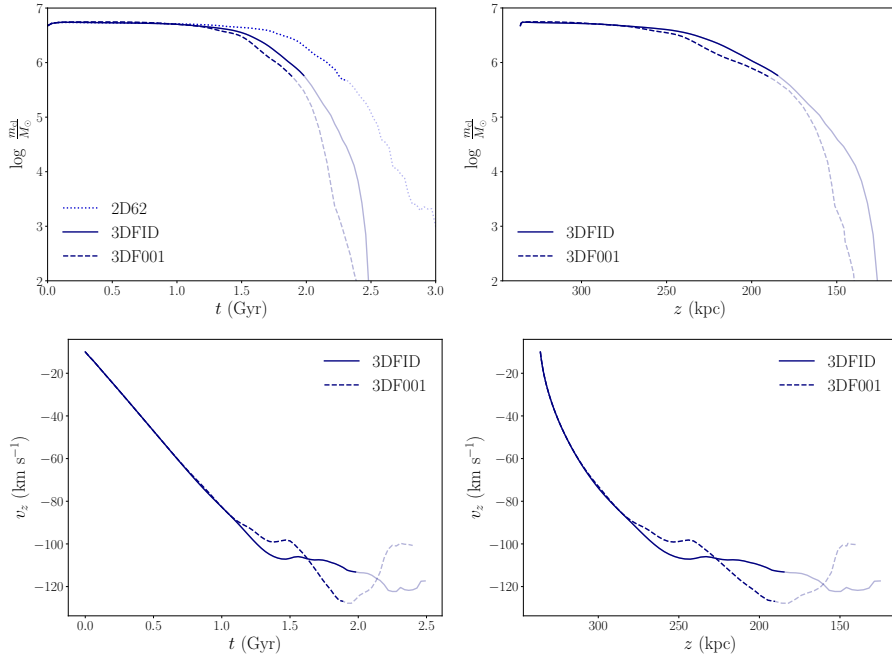


Figure 5.9: Evolution with time (left column) and height (right column) of the cool gas mass (top row) and the velocity along z (bottom row), for the simulations 3DFID (solid curves) and 3DF001 (dashed curves). In the top-left panel we also show, as a comparison, the cool gas mass evolution of simulation 2D62 (dotted curve). The level of transparency of the different curves is defined as in Figure 5.5.

the results, with a much faster evaporation in the 3D simulation compared to the 2D case, consistently with the results from previous works (Grønnow et al. 2018). This is likely due to the contact surface, larger in 3D, between the cloud and the corona, which leads to a more efficient development of hydrodynamical instabilities, which more easily break up the cloud and make it evaporate into the hot gas. As for the two-dimensional study, a more accurate convergence analysis in 3D would be desirable and we plan to investigate it in future studies. In all the panels of Figure 5.9, we also report the results obtained for the simulation 3DF001, where all the initial parameters are as in the fiducial case, except for the thermal conduction suppression, which is set at $f_{tc} = 0.01$. The behaviour of the cool gas is very similar in the two cases, although we can see how, with a more efficient thermal conduction, the cloud survives slightly longer ($t_{ev} = 2$ Gyr for the 3DFID simulation and 1.9 Gyr for the 3DF001 simulation). This might be due to the role that this process has in damping the instabilities that form at the interface between the cool gas and the corona. With a more efficient

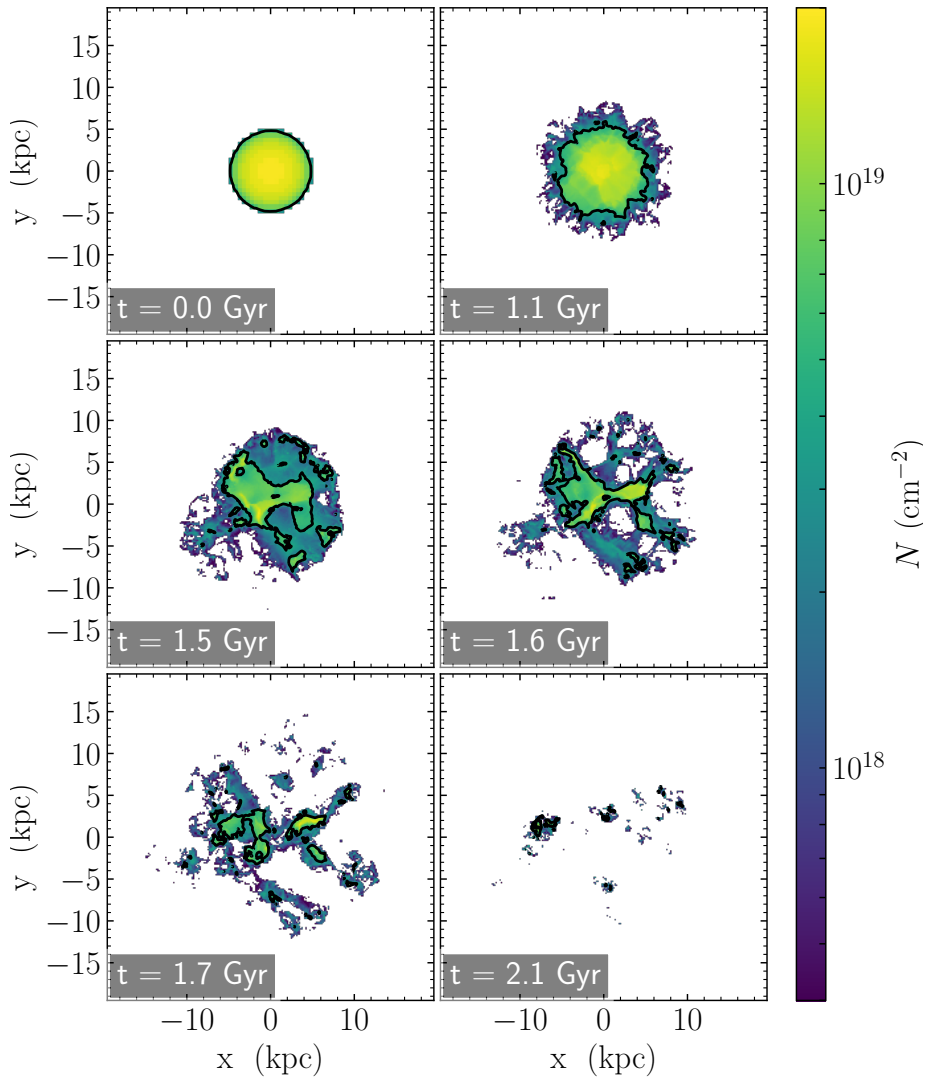
thermal conduction, the cloud stays more compact (see for example Armillotta et al. 2017, and Section 5.1) and therefore its evaporation into the hot gas is delayed. Despite this (small) difference, in both cases the cool gas evaporates into the hot corona way before reaching the disk of M31, confirming the results of the 2D experiments. This can be seen from the top-right panel of Figure 5.9, where we can see how in both simulations the cloud has completely disappeared at a distance just below 150 kpc and has lost 90% of its initial mass at either 185 kpc (3DFID) or 190 kpc (3DF001). Finally, the cool gas velocities, shown in the two bottom panels, are also similar in both simulations and reach a maximum (negative) value of about -120 km s^{-1} , consistently with the findings of the 2D simulations.

Analysis of the cool gas cross section

Differently from the 2D simulations, the 3D experiments allow us to study in a greater detail the evolution of the shape of the cool gas. This will be important especially to properly compare our results with the observations (see Section 5.4) and with the predictions of the analytical models (see Section 5.5.1) of Chapter 4, where the clouds are assumed to be spheres. Of particular interest is the area, or cross section, of the cool gas as seen from different directions. The cloud cross section is important for two main reasons: (i) it affects the dynamics of the cloud, in particular the cross section along z , the direction of infall, which determines the efficiency of the coronal drag force, as we will see more in detail in 5.5.1; (ii) it impacts the covering fraction of the cool gas, affecting the probability of observing the clouds as absorption features (see Section 5.4). The cool gas cross section can be inferred in different ways. The most straightforward is to calculate the total area (in projection) of the whole amount of cool gas present in the simulation. However, we can also define a cross section that is more relevant to infer the cloud dynamics, as we will see in Section 5.5.1, or one that is more appropriate to compare our results with the observations, as we explain in the following. In order to do this, we select only the region of cool gas that satisfies the criterion $N > N_{\text{obs}}$, where N_{obs} is the observational detection limit. A cloud cannot be detected if the cool gas column density is lower than this threshold. We set this limit based on the AMIGA observations (see Section 5.4). In these data, the SiII, SiIII and SiIV lines are on average not detected for $N \lesssim 10^{12} \text{ cm}^{-2}$. The threshold on the total particle density can be obtained, therefore, through (see Lehner et al. 2020; Section 4.3.4)

$$N_{\text{obs}} = 2.3 \left[\left(\frac{Z}{Z_{\odot}} \right) \left(\frac{\text{Si}}{\text{H}} \right)_{\odot} \right]^{-1} N_{\text{Si,obs}}, \quad (5.11)$$

where $N_{\text{Si,obs}} = 3 \times 10^{12} \text{ cm}^{-2}$ (given that the total silicon column density $N_{\text{Si}} = N_{\text{SiII}} + N_{\text{SiIII}} + N_{\text{SiIV}}$), $(\text{Si}/\text{H})_{\odot} = 10^{-4.49}$ is the silicon solar abundance (as in Section 4.3.4), the factor 2.3 is used to transform the total numeric density into a hydrogen numeric density and (Z/Z_{\odot}) is the gas metallicity in solar units. For the metallicity, we used the best-fit value of Chapter 4, equal to $0.05 Z_{\odot}$. We



5

Figure 5.10: Maps of the projected density along z of the cool ($T < 3 \times 10^4$ K) gas in the simulation 3DFID, at 8 different times (specified in the panels). The black contour is placed at the observational detection limit (see main text) and corresponds to $N = 4.3 \times 10^{18} \text{ cm}^{-2}$.

obtained $N_{\text{obs}} = 4.3 \times 10^{18} \text{ cm}^{-2}$.

Figure 5.10 shows the projection along the z -axis of the cool ($T < 3 \times 10^4$ K) gas in the simulation 3DFID at different times in its evolution. We can see how the cloud starts spherical and its cross section progressively increases during its infall, due to the pressure exerted by the hot corona. After reaching a maxi-

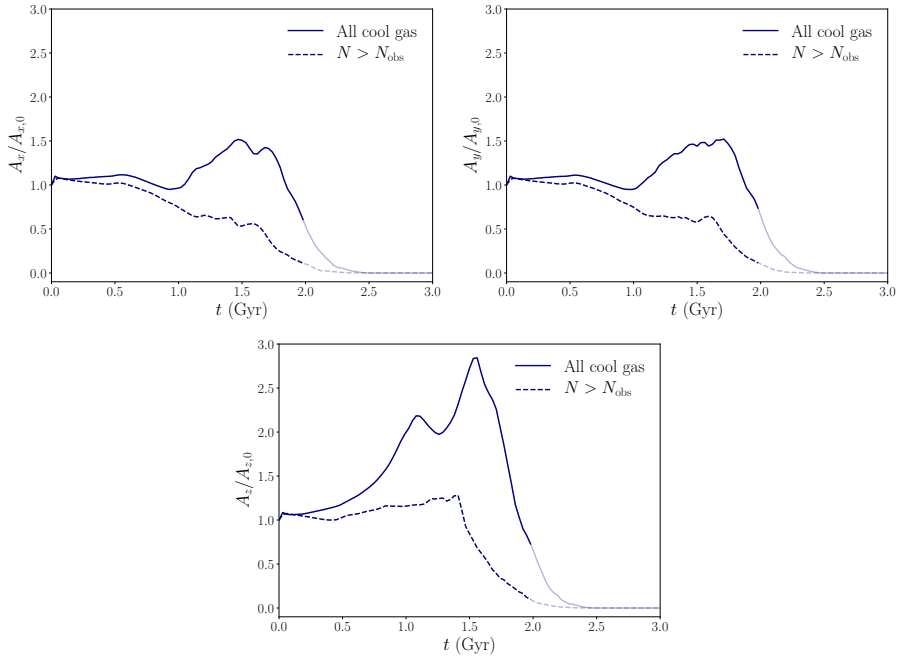


Figure 5.11: Evolution with time of the cool gas cross section, obtained projecting the simulation 3DFID along x (top-left), y (top-right) and z (bottom). The solid curves represent all the cool gas, while the dashed curves represent the cool gas with $N > N_{\text{obs}}$ (see main text). All the curves have a higher level of transparency for $t > t_{\text{ev}}$.

imum area around 1.6 Gyr, the cloud is then broken into multiple pieces and its area starts to decrease. The contour shows the observational detection limit of the cool gas, N_{obs} . It is evident how, considering the observational threshold in column density, the cross section can be significantly smaller than it would be by considering the whole amount of cool gas.

In the three panels of Figure 5.11 we show the evolution of the cool gas cross section with time in the projections along x (top left), y (top right) and z (bottom). We show, for each projection, the cross section of the entire cool gas and the observational one, calculated as explained above. In all the directions, the total area of the cool gas tends to increase up to a certain time where the cloud starts being destroyed by the hydrodynamical interactions with the corona. However, the increase of the cross section along z is significantly more pronounced than for the other two directions. This is because the cloud is infalling along z and therefore the ram pressure of the corona tends to flatten the cloud primarily perpendicularly to this direction. If we consider only the gas with $N > N_{\text{obs}}$, we see that the evolution is significantly different, with the cross section decreasing in the x and y projections and slightly increasing initially in the projection along z (at a much slower rate than in the previous case), with a subsequent fast decrease.

5.4 Comparison with the AMIGA data

In the semi-analytic models of Chapter 4 we assumed, for simplicity, that the cool CGM clouds have a spherical shape and that they have a constant mass throughout their infall towards the disk. In this Chapter, instead, with the use of high-resolution simulations we have more thoroughly studied the hydrodynamical interactions between the cool gas and the hot corona. In particular, we have found that the clouds evaporate into the hot CGM and that their shape, during their evolution, strongly deviates from the spherical one. In this Section, we aim to investigate whether the predictions of the simulations are still in accordance with the AMIGA observations (Lehner et al. 2020), which we used to calibrate the parameters of the analytical models. In the following, we use the results of our fiducial 3D simulation 3DFID (despite the lower resolution than the 2-dimensional case), in order to have a better description of the cloud shape and column density (that cannot be determined in 2D).

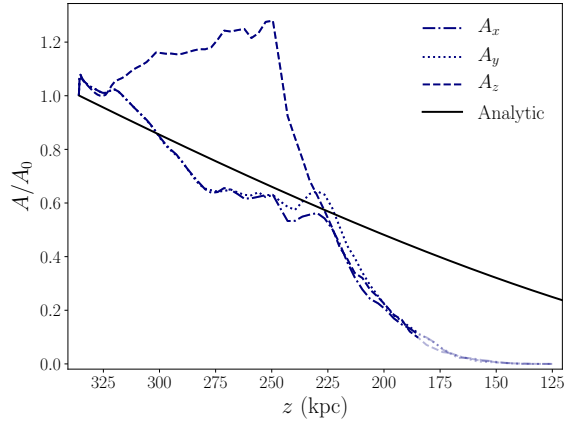
In order to perform the comparison with the observations, we first populated the halo of M31 with clouds, by using the same method used in Chapter 4 (see Section 4.3.4). We assumed a gas accretion rate as found in Chapter 4 and in particular equal to 1.5 times the present-day dark matter accretion rate (Correa et al. 2015a,b), multiplied by the cosmological baryon fraction (see Section 4.4.2 for more details). For simplicity and for consistency with the idealized set-up of our simulations, we assume here purely radial motion, neglecting any tangential motion of the clouds and hot gas, which are in any case expected to be small (see Chapter 4 for details). Depending on its galactocentric distance r , we assumed that the mass, radial velocity, cross section and silicon column density of a cloud are given by the results of the 3DFID simulation, as we will explain more in detail below. Once these properties have been defined, we performed synthetic observations, by ‘observing’ the model clouds using artificial lines of sight, in the same way as described in Section 4.3.4.

The first result of the simulation 3DFID that we incorporated in our current model is the evolution of the cool gas mass and in particular the quick evaporation of the cool CGM clouds at a finite time $t = t_{\text{ev}}$ (see Section 5.3). In practice, we did not populate the halo with clouds at distances lower than $z_{\text{ev}} = 185$ kpc, since at these distances we have found (Section 5.3.2) that the clouds have lost 90% of their mass and therefore are effectively evaporated into the hot corona. Note that, also in Chapter 4, the majority of the clouds detected at small projected distances were, in fact, located at large intrinsic distances, generally larger than ~ 150 kpc (see Figure 4.9). This effect was due to the larger sizes of the clouds in the external regions and to their lower infall velocities (see Section 4.4.2 for more details). Therefore, we do not expect the evaporation of the clouds to greatly impact the findings of Chapter 4, as more quantitatively shown below.

As a second improvement with respect to our semi-analytic model, the cloud velocity, instead of being calculated, as in Chapter 4, by considering only the gravitational attraction and the drag force of the corona, is now given by the

results of our 3D simulation, shown in Figure 5.9. We assumed that the velocity along z corresponds to a radial velocity of the cloud.

Figure 5.12: Variation with the height of the cool gas cross section predicted by the analytical model (black solid line) and of the cross sections along the x , y and z directions obtained from the 3D fiducial simulation 3DFID, calculated by selecting all the cool gas with $N > N_{\text{obs}}$. All the curves from the simulation have a higher level of transparency for $z > z_{\text{ev}}$.



Furthermore, the cloud cross section is important to know whether the cool gas will be intercepted or not by our artificial lines of sight (see Appendix 2.A and equation 2.24). In particular, we are interested in the cross section obtained by selecting the cool gas with a column density greater than the observational limit (N_{obs} , see previous Section). In Figure 5.12, we show the comparison between the cross section predicted analytically for a spherical cloud of $5 \times 10^6 M_{\odot}$ and the observational cross sections along the x, y and z directions calculated from our fiducial hydrodynamical simulation, all as a function of the height with respect to the disk of M31. The analytical cross section is given by πr_{cl}^2 , where r_{cl} is calculated through equation (5.4), assuming that the cloud is spherical at all times. The analytical prediction is initially similar to the evolution of the cross sections along x and y , while the area of the simulated cloud along z is significantly larger than the analytical one. At heights lower than ~ 220 kpc, on the other hand, the analytical profile overestimates the cross sections found with the simulation, due to the fact that at this height the cloud starts to lose a significant amount of mass. The analytical and simulated profiles are, therefore, quite different from one another. To perform the comparison with the observations, we adopted the simulation cross section given by the projection along z . This is a simplification, given that for each cloud we should use a projection that is based on its orientation with respect to the line of sight. We have, however, verified that using the profiles of the cross section (and of the column density, see below) along x or y does not change significantly our results and therefore that taking into account the cloud orientation would not impact the general findings of this Section.

Finally, the total silicon column densities for each of the three projections along x , y and z , are reported in Figure 5.13. These are obtained averaging the column density of the cool gas with $N > N_{\text{obs}}$ and by converting it into a silicon column

density by inverting equation (5.11). As expected, given that the cloud is more extended along x and y (hence the higher cross section in the z -projection), the two corresponding column density profiles exhibit higher values than the one along z . To be consistent with the choice of the cross section, we adopted the column density along z .

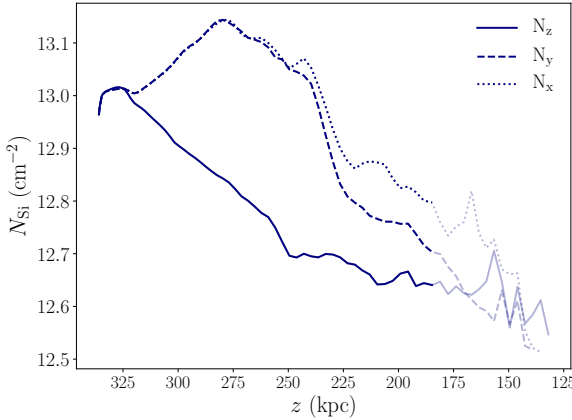


Figure 5.13: Variation with the height of the average silicon column density of the cool gas with $N > N_{\text{obs}}$, along the three different directions (x , dotted; y , dashed; z , solid). The level of transparency of the different curves is defined as in Figure 5.12.

The three panels of Figure 5.14 correspond to the comparison between model and observations for the number of components (top panel), silicon column density (center) and line-of-sight velocities (bottom), all as a function of the projected distance from M31. The bands and the colormap represent the model predictions, while the points represent the observations. From top to bottom, the three plots are obtained in the same way as, respectively, Figures 4.6, 4.7 and 4.8 and we refer to Section 4.4.2 for more details. Here, instead of dividing the observational plane in four quadrants (see Figure 4.1 and Section 4.4.2), we show the whole data sample and the azimuthally averaged results of our present models, given that, because of the absence of rotation, these are isotropic and there are no variations with the azimuthal angle.

From Figure 5.14, we can see how models with the same best-fit values of Chapter 4 and with a more realistic description of the cloud properties, based on high-resolution hydrodynamical simulations, are still able to reproduce the observations of the AMIGA project. In particular, the line-of-sight velocities are in general slightly lower than what we found in Chapter 4 (see Figure 4.8). This is consistent with the fact that the infall velocities predicted by the simulations are lower than the ones predicted by the analytical model. This is a physical effect related to the fact that the clouds are not spherical solid bodies and will be investigated in greater detail in Section 5.5.1. The line-of-sight velocities found with the current model can still explain most of the observational data, except for a few outliers at higher velocities. The number of components is very similar to the results of the semi-analytical model (Figure 4.6) and, as previ-

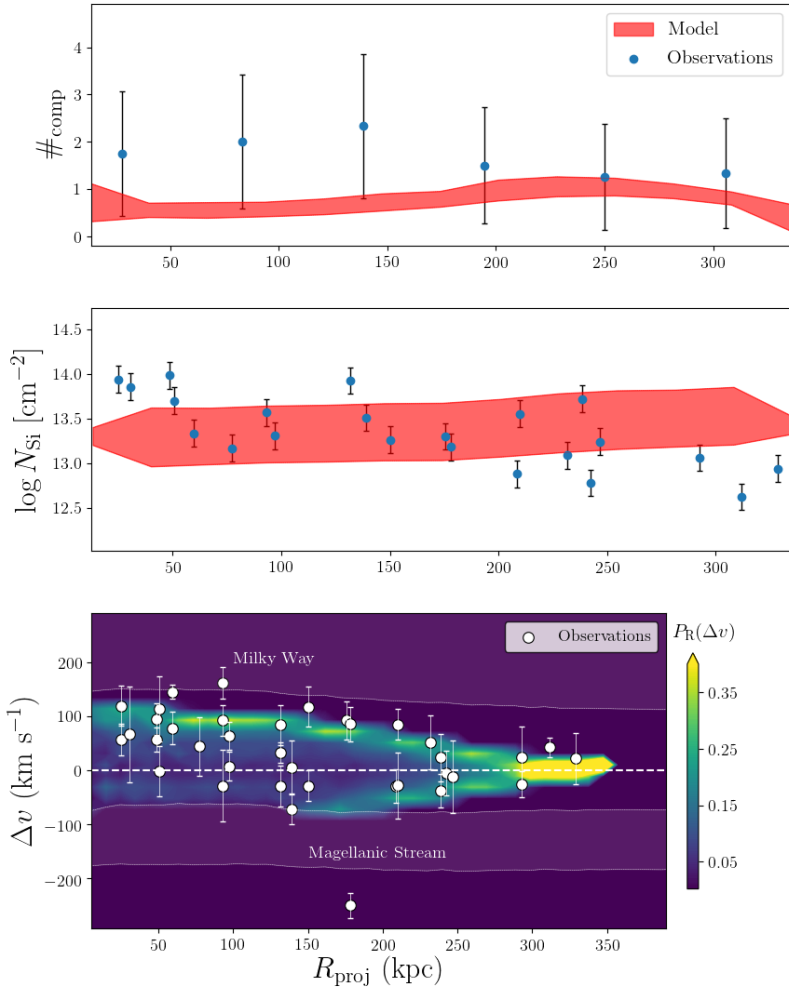


Figure 5.14: Comparison between the predictions of our 3D fiducial simulation (3DFID) and the AMIGA data, as a function of the projected distance from M31, for the number of kinematic components (top), the total silicon column densities (center) and the line-of-sight velocities (bottom). The observational data are given by the points, while the light red bands and the colormap represent the predictions of the model. For more details, see Figures 4.6, 4.7 and 4.8.

ously found, slightly underpredicts the observations. This could mean that, in addition to the cosmological accretion, the cool gas might also be contributed by other processes, as already discussed in Section 4.5.3. Finally, the column density profile has similar values to the observations, but does not show a gradient with the projected distance, which is instead visible in the real data and

that was also present in the semi-analytical models (Figure 4.7). We speculate that this may change using slightly different values of the initial parameters, but further investigation would be required and is left for future work.

Although still preliminary, our hydrodynamical simulations, together with their comparison with the AMIGA data, strengthen the scenario in which the cool CGM of M31 is formed by infalling clouds with parameters similar to those found with our analytic models of Chapter 4. These clouds are accreted from the surrounding IGM, but evaporate into the hot corona before reaching the central galactic disk, in agreement with the relatively low level of star formation therein.

5.5 Discussion

In Section 5.3, we have found, using high-resolution hydrodynamical simulations, that the cool CGM clouds in the halo of M31 are most likely evaporating in the hot coronal gas at large distances from the galactic disk. We have then seen, in Section 5.4, that, after implementing the findings of the numerical experiments, which account for hydrodynamical instabilities, radiative cooling and thermal conduction, the inflow models of Chapter 4 are still able to reproduce the observational data. These findings imply that the cool CGM clouds are therefore not able to reach the disk of M31 and to feed its star-formation, as already argued in Chapter 4. Assuming that their CGM has similar properties to the ones adopted in this work, this result is probably valid in general for L^* star forming galaxies in the local Universe. In this Section, we discuss how we can refine the analytical description of the cool CGM cloud velocity, using insights from the hydrodynamical simulations (Section 5.5.1), then we focus on the limitations of our numerical experiments (Section 5.5.2) and on the comparison with previous works (Section 5.5.3).

5.5.1 Refining semi-analytic models of the drag force

In Section 5.4, we have shown that the results of hydrodynamical simulations can be directly compared to observational data. However, this comparison is based on the best-fit parameters obtained in Chapter 4, while, ideally, one would like to perform again a Bayesian analysis on refined models that take into account the inputs of the simulations. In order to achieve this, it is necessary to understand how we can describe, analytically, the evolution of the cool gas seen in the hydrodynamical simulations. Although a full treatment of this problem is left for future work, we present here a preliminary analysis. We focus, in particular, on the infall velocity of the cloud, which is one of the main properties of the cool CGM that can be directly compared with observational data.

In the models of Chapter 4, the interaction of the clouds with the hot corona is parametrized by the drag force, which is described by (see, for example,

Marinacci et al. 2011 and equation 4.3)

$$\dot{v}_{\text{drag}} = -\frac{Am_{\text{cl}}}{\rho_{\text{cor}}v^2}, \quad (5.12)$$

where ρ_{cor} is the coronal mass density, v is the relative velocity between the corona and the cloud, m_{cl} is the cloud mass and A is the cloud cross section. In this modeling, the clouds are assumed to be spherical and the cross section is described by the analytical profile (black solid curve) shown in Figure 5.12.

The velocity profile predicted by such model, which takes into account the NFW gravitational potential of the DM halo of M31 (see Section 5.2) and the drag force (see equation 2.12 for the full equation of motion), is shown as a dotted line in Figure 5.15. To obtain this curve, we utilize the same cloud properties used for the initial conditions of the fiducial simulation. We show in the same Figure the velocity profile (blue) predicted by the simulation 3DFID: it is evident how the analytical model overestimates the infall velocities of the clouds, especially after ~ 1 Gyr. We argue that the main reason for this discrepancy is given by the two assumptions that the analytical clouds are not losing mass and that their cross section is that of a spherical cloud embedded in the hot corona.

5

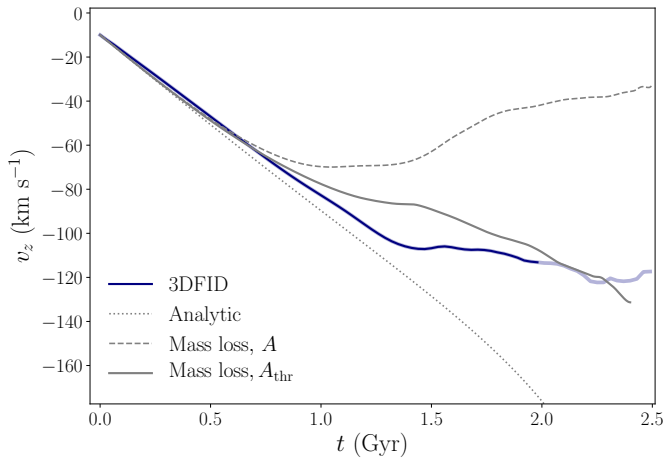


Figure 5.15: Comparison between the evolution in time of the velocity along z of the cool gas in the simulation 3DFID (blue) and three different theoretical predictions: a model with a constant cloud mass and with a cloud radius given by equation (5.4), as in Chapter 4 (dotted line); a model with the cool cloud losing mass with time and with the cross section of the whole amount of cool gas, from the simulation 3DFID (dashed line); as above, but imposing a further threshold with $N > 0.25N_0$ (solid line). The profile from the simulation has a higher level of transparency for $t > t_{\text{ev}}$.

The dashed curve in Figure 5.15 is obtained by numerically solving the same equation of motion mentioned above, but assuming that the mass and cross

section of the cloud vary according to the results of the simulation 3DFID, using the profiles shown by the solid lines in the top left panel of Figure 5.9 and the bottom panel of Figure 5.11. We adopted the cross section of the whole amount of cool gas present in the simulation (see Section 5.3.2) and, given that the cloud is falling vertically towards the disk, we used the cross section calculated from the z -projection, the one along the direction of motion. We can see how the evolution of the cloud velocity is now completely different from the analytical profile, especially after ~ 0.7 Gyr, where the cloud cross section starts to increase significantly, opposite to the simple analytical prediction. However, in this case the cloud slows down much more than what we see in the simulation (blue profile). This implies that the cross section of the whole amount of cool gas is not a good description of the dynamical cross section. It is indeed reasonable to expect that gas with very low column density will easily be stripped from the main cloud and that it will therefore not influence its dynamics. A smaller cross section would lead to higher velocities (see equation 5.12) and therefore to a velocity profile possibly more in agreement with the simulations. In Figure 5.16, we show how the evolution of the cross section varies by choosing different column density thresholds, defined as different fractions of the central column density of the cloud at the initial time of the simulation. The smaller the fraction, the more cool gas is included in the calculation and therefore the larger is the cross section. For the purpose of this analysis, we selected all the cool gas with a column density higher than 25% of the initial central column density of the cloud, since we found, by trial and error, that this value leads to a very good agreement between model and simulation. Indeed, with this choice, we obtained the grey solid curve in Figure 5.15 for the cloud velocity evolution, which we can see is similar to the simulation findings.

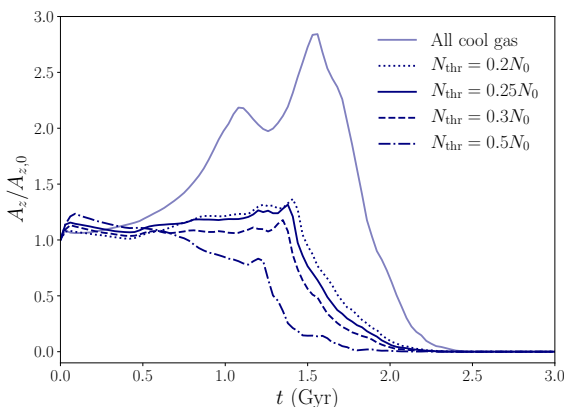


Figure 5.16: Evolution with time of the cross section along z of the cool gas in the simulation 3DFID, calculated selecting only the cool gas with $N > N_{\text{thr}}$, where N_{thr} is an arbitrary threshold. The different curves show the results for different choices of N_{thr} , chosen to be a fraction of the central initial column density of the cloud N_0 .

We have found that, taking into account a more realistic evolution of the cool gas mass and cross section, the drag force caused by the hot corona provides a good description of the deceleration of the cloud. This represents only a

first step that shows how it is possible to refine analytical models based on the results of hydrodynamical simulations. With the use of several simulations, spanning a wide range of different initial conditions, it can be possible to find physically motivated analytical prescriptions that properly describe the cloud deceleration, the mass loss and the evolution of the cloud cross section. These models would naturally produce improved velocity profiles for the cool CGM clouds and could be directly compared with observational data. Coupling hydrodynamical simulations and analytical prescriptions represents, therefore, a promising tool to better understand the CGM of galaxies.

5.5.2 Limitations of this study

All the results of this work are based on our numerical simulations, which are affected by various limitations, some of which have already been discussed throughout this Chapter. In addition to the dependence of our results on the grid resolution (see Section 5.3), we have also made several physical assumptions. For example, we have neglected the rotation of the corona and the self-gravity of the cool cloud, although, as already mentioned, these two effects should have a negligible impact on our results. However, some of the other assumptions of this work might have affected our findings, as we discuss below.

An important limitation is the assumption of collisional ionization equilibrium in the calculation of the cooling function. We know, in fact, that the cool gas is photo-ionized by the EUVB (e.g. Haardt & Madau 2012), which accounts for the UV radiation emitted by all the extragalactic stars and AGN. This effect goes in the direction of reducing the cooling rate of the gas, increasing its cooling time. Given that in all our simulations we have found that the cool gas eventually evaporates into the surrounding hot medium, the presence of the EUVB would most likely facilitate this process, therefore confirming our main result. We also assumed a metallicity $Z = 0.3 Z_{\odot}$ for the hot corona, which is in agreement with observational estimates (e.g. Miller & Bregman 2015), but is unconstrained for galactocentric distances larger than 150 kpc. Current X-ray observations generally probe, indeed, only the corona at distances $\lesssim 50$ kpc from the disk (e.g. Bregman et al. 2018) and the metallicity of the more external gas is, to date, unknown. Here, we expect the hot gas to not be significantly enriched with metals by the feedback from the central galaxy and therefore its metallicity to be lower than the value we adopted. A lower metallicity in the outer regions would result in a lower cooling rate and therefore (as for the EUVB) go in the direction of strengthen our main result. Finally, we neglected the effects of the magnetic field, both because its presence would increase the computational cost of our experiments and because we have, to date, no observational constraints on the magnetic field in the external regions of the halo of M31 (and of galactic halos in general). Including a coronal magnetic field would tend to lower the stripping and the mixing of hot and cool gas (e.g. Grønnow et al. 2018). However, this effect would presumably be small in the outskirts of the corona, where the field is expected to be weak (e.g. Marinacci et al. 2018). In this work, we

indirectly included one important effect of the magnetic field, by assuming an isotropic suppression of the thermal conduction due to the magnetic field, using, for our fiducial simulations, a suppression factor consistent with the findings of recent magneto-hydrodynamical studies of cool CGM clouds in the halos of MW-like galaxies (Kooij et al. 2021).

5.5.3 Comparison with previous works

As explained in Section 5.1, most of the high-resolution simulations that study the evolution of a cool CGM cloud embedded in a hot medium, are focused on the internal regions of the halo, where the density of the corona is significantly higher than in the outer regions probed in this Chapter, and are therefore not directly comparable to our results. At these distances, many authors (e.g. Marinacci et al. 2010b; Armillotta et al. 2016; Grønnow et al. 2018; Kooij et al. 2021), considering a number of effects, including radiative cooling and heating, thermal conduction and magnetic field, have found that the mixing between the cool and the hot gas (which has a temperature and a metallicity consistent with the values used in this Chapter) leads to the condensation of the corona, with the cool gas mass increasing with time. This is due to the fact that the layer of mixed gas has a short cooling time and therefore condenses rapidly. However, the densities of the corona at distances larger than 150 kpc are at least an order of magnitude lower than the densities of the hot gas in the inner regions, implying long cooling times for the mixed gas. Therefore, our finding of the evaporation of the cloud is not in disagreement with these previous works. A study that probes the more external regions of the halo is Armillotta et al. (2017). These authors carried out high-resolution (2 pc) 2D simulations, with the inclusion of radiative cooling, photo-ionization from the EUVB and thermal conduction, of cool clouds travelling through the hot corona of MW-like galaxies, at galactocentric distances of $\sim 50 - 150$ kpc. Despite many differences (e.g. presence of EUVB, higher resolution, absence of the gravitational field, initial cloud velocities that go from 100 to 300 km s⁻¹), these are the simulations that are most similar to the ones performed in this Chapter. They found, for a large range of different initial cloud masses and velocities, that the cool gas mass decreases with time, in agreement with our findings. However, these simulations follow the evolution of the cloud for only 250 Myr (compared to the 3 Gyr of our simulations). Therefore, for clouds more massive than $\sim 10^4 M_{\odot}$, they do not observe the complete destruction of the cloud. We argue that this is not inconsistent with our results, since we found that the clouds need at least 1.5–2 Gyr to completely evaporate in the hot corona.

5.6 Summary and conclusions

In this Chapter, we have analyzed the evolution of cool CGM clouds in the halo of star-forming galaxies. We have used high-resolution hydrodynamical simu-

lations, in order to investigate what is the fate of the cool clouds and whether they are able to reach the galactic disk and feed its star formation. More in detail, we have utilized as initial conditions the findings of Chapter 4, which we think are a good representation of the CGM of M31. In this picture, the cool clouds infall towards the galaxy, starting at the virial radius, with a mass of $\approx 5 \times 10^6 M_{\odot}$, low initial velocities and low metallicities ($Z \approx 0.05Z_{\odot}$).

We have studied the evolution of individual clouds, using the hydrodynamical code PLUTO (Mignone et al. 2012) and adopting an adaptive mesh refinement technique to be able to follow the cool gas for its entire journey from the virial radius towards the central galaxy. We have run 2D and 3D simulations, considering the effect of radiative cooling, thermal conduction and the dark matter gravitational field and we explored different initial conditions for the cloud mass and the thermal conduction suppression factor. Finally, we have compared, through artificial observations, the results of our numerical experiments directly with the AMIGA data.

The main findings of this Chapter are the following:

5

1. In all our 2D and 3D simulations, the cool CGM clouds evaporate into the hot coronal gas, due to hydrodynamical instabilities and thermal conduction, at distances larger than 150 kpc from the center and after an infall of approximately 2 Gyr;
2. in the 3D simulations, we estimated the cloud cross section, finding that, contrary to the semi-analytical models of Chapter 4, it tends to increase with time, until a point in which the cloud gets broken up by the interactions with the corona and rapidly evaporates;
3. with our simulations, we are able to overcome the main assumptions for the clouds made in Chapter 4, in particular constant mass, spherical shape and velocity described by the simple drag formula. We have incorporated the results of the simulations in the semi-analytical model and, through synthetic observations, we have found that the best-fit models of Chapter 4 can still reproduce the observational data of the project AMIGA.
4. we have investigated the possibility of a refined drag formula for a non-spherical cloud, using the results from our simulations. This represents only a first step in using the findings of high-resolution hydrodynamical simulations to refine semi-analytical models.

This work supports the findings of Chapter 4 and strengthens the idea that the cool CGM observed in the halo of M31 (and of similar star-forming galaxies in general) is formed by accretion of IGM and does not feed the central disk, but instead joins the hot coronal gas. A future step will be to expand the work presented in this Chapter, with the implementation of other physical effects, like the presence of an external ionizing source or of the magnetic field. Moreover, we plan to investigate simulations spanning a wider range of initial conditions, with the final aim of improving the accuracy of our semi-analytical models. We

believe that coupling information from these simulations with semi-analytical modeling can, indeed, be a very useful tool to improve our understanding of the dynamics and origin of the circumgalactic gas and its connection with the central galaxies.

5.A Field length and the role of thermal conduction

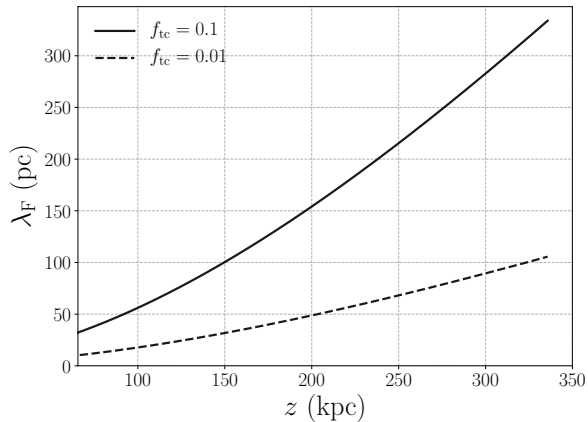
An interesting quantity for our simulations is the Field length (Field 1965):

$$\lambda_{\text{Field}} = \sqrt{\frac{f_{\text{tc}} \kappa_{\text{Sp}} T_{\text{cor}}}{n_{\text{cool}}^2 \Lambda(T_{\text{cool}})}}, \quad (5.13)$$

where $\Lambda(T_{\text{cool}}) = 10^{-22} \text{ erg cm}^3 \text{ s}^{-1}$ is the cooling rate of the cool gas, while T_{cor} and n_{cool} can be obtained, respectively, from equations (5.2) and (5.3). According to the work of Begelman & McKee (1990), radiative processes dominate over thermal conduction if the scale of the considered gas structure is larger than the Field length, while on smaller scales thermal instability is suppressed and thermal conduction dominates. In Figure 5.17 we show the Field length calculated for the CGM system described by our simulations, adopting two different choices of f_{tc} (see equation 5.6). Given that the temperature of the hot gas and the cool gas density change with the distance from the center (see Figure 5.1), the Field length of the system also depends on the galactocentric distance (and in our simulation box on the height above the galactic disk). We can see from Figure 5.17 how this quantity decreases with decreasing distance from M31, going from values of more than a hundred pc at the virial radius to less than 50 pc in the inner regions. Moreover, Figure 5.17 shows how the Field length depends on the suppression factor: with lower values of f_{tc} , the scales at which thermal conduction dominates are also smaller, in proportion to $\sqrt{f_{\text{tc}}}$.

5

Figure 5.17: Field length (equation 5.13) as a function of the height from the galactic disk, for two different values of the suppression factor of the thermal conduction, $f_{\text{tc}} = 0.1$ (solid curve) and $f_{\text{tc}} = 0.01$ (dashed curve).



We could expect simulations that are able to resolve the Field length to also converge in terms of total amount of cool gas mass in the simulation domain. Indeed, thermal conduction being a diffusive process, it should destroy (in a conduction time) all the clumps of gas that are stripped from the main cloud

and are smaller than the Field length. If the grid cells are significantly smaller than this scale, the behaviour should be similar in all the simulations (see, for example, Armillotta et al. 2016). In order to test this, we have run 2D simulations at different resolutions and using different suppression factors (2DFID, 2DF001, 2D31, 2D31F001, 2D31F005). In Figure 5.18, we compare the variation, as a function of the height, of the mass of the cool gas (see Section 5.3) in all these simulations. As we have already seen in Section 5.3.1, using a maximum resolution of 16 pc, the two simulations with $f_{\text{tc}} = 0.1$ and $f_{\text{tc}} = 0.01$ lead to similar results. This is consistent with the fact that, at this resolution, the Field length seems to be resolved in both cases (see Figure 5.17), especially at distances larger than 150 kpc, below which the cool gas is completely evaporated into the hot corona. In Figure 5.18, we show also the evaporation height z_{ev} , by depicting, for each simulation, the mass variation at $z < z_{\text{ev}}$ with a higher level of transparency. The value of z_{ev} is similar for all the simulations, even at lower resolution (31 pc), except for the case of 2D31F001. Therefore, for $z < z_{\text{ev}}$, all the simulations seem close to convergence, except for 2D31F001, which is indeed the case where the Field length is less resolved. Below z_{ev} , the mass profiles start to diverge and we can see a dependence with the resolution and/or suppression factor, even in the simulations where the Field length should be resolved. Note that, however, equation (5.13) is not to be considered as a sharp threshold, since the density and temperature of the gas stripped from the cloud can change significantly as it mixes with the corona. This is particularly relevant for the regions where $z < z_{\text{ev}}$, where the cool gas is fragmented into small cloudlets and cannot be considered anymore as a single cloud. To study in detail these regions, a higher resolution is needed, while in this work we focus primarily on $z > z_{\text{ev}}$.

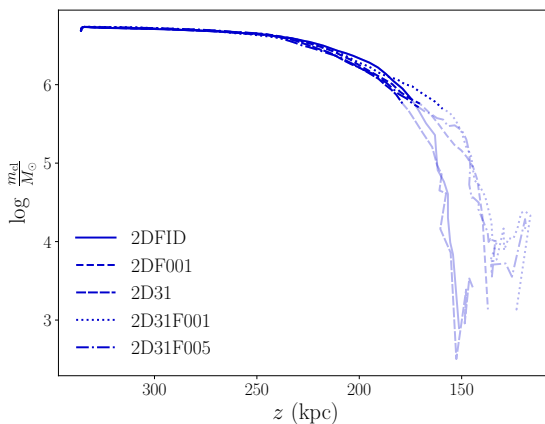


Figure 5.18: Variation of the cool gas mass as a function of the height in the simulations 2DFID, 2DF001, 2D31, 2D31F001 and 2D31F005. The level of transparency of the different curves is defined as in Figure 5.5.

Chapter 6

Conclusions and future perspectives

In this Ph.D. Thesis, we have investigated the properties and dynamics of the cool circumgalactic medium (CGM) of low-redshift galaxies. This is a gas at $T \sim 10^4$ K, which has been extensively observed, mainly through absorption studies, in the halos of galaxies at $z < 1$, up to their virial radius (see Section 1.2.2). The aim of this work has been to address some of the open questions regarding this medium, outlined in the Introduction (see Section 1.5). To date, there are, indeed, several uncertainties related to the physical properties (like its density or metallicity) of the cool CGM and, most importantly, to its formation mechanisms. Whether this cool medium originates primarily from accretion of the intergalactic medium (IGM) into the galaxy halos, from feedback from the central galaxy, or from a combination of the two, is still unclear. Moreover, it is unknown how much the interaction with the hot phase of the CGM (also called corona) influences the properties and dynamics of the cool gas and whether the latter is able to feed the central galaxy's star formation or, instead, evaporates into the surrounding environment. With this Thesis, using state-of-the-art observational constraints, coupled with original semi-analytical modeling and insight from high-resolution hydrodynamical simulations, we have investigated

these problems and we have been able to draw clear conclusions about the origin and fate of the cool CGM.

Below, we explain the main methods utilized in this Thesis and we summarize the results of the previous Chapters (Section 6.1), we list the implications that the findings of this work entail (Section 6.2) and, finally, we outline some of the possible future developments (Section 6.3).

6.1 Summary of the Thesis

Throughout this work, we have described the circumgalactic medium as composed of two distinct phases, with cool gas at $T \sim 10^4$ K in pressure equilibrium with a volume-filling hot ($T \sim 10^{6-7}$ K) medium, or corona. The hot gas is in hydrostatic equilibrium with the dark matter (DM) gravitational potential and generally accounts for 20% of the total amount of baryons associated with the halo¹. This representation of the CGM is justified by several observational constraints, both for the cool (see Tumlinson et al. 2017, and references therein) and the hot (e.g. O’Sullivan et al. 2007; Miller & Bregman 2015; Bregman et al. 2018; Li et al. 2018) phase of this medium. The interactions with the hot corona, including pressure confinement, ram pressure (also called drag), hydrodynamical (e.g. Kelvin-Helmholtz and Rayleigh-Taylor) instabilities and thermal conduction, are crucial in determining the dynamics and most of the properties of the cool clouds. In Chapters 2, 3 and 4, we have developed and used semi-analytic parametric models to describe the CGM system, while in Chapter 5 we have made use of high-resolution hydrodynamical simulations. All the results of this study are based on the comparison of our theoretical predictions with state-of-the-art observations of the cool CGM around both early- and late-type galaxies in the local Universe.

In Chapter 2, we have described the cool CGM around massive early-type galaxies (ETGs) as a radial infall of clouds accreted from the IGM, at a rate comparable to the one predicted by cosmological models (Fakhouri et al. 2010). We have compared our model predictions with the kinematics inferred by the COS-LRG survey (Chen et al. 2018; Zahedy et al. 2019) and, through a Bayesian analysis, we have found that our models can successfully reproduce the data, with the drag force of the hot corona being fundamental in slowing down the cool clouds, bringing them to velocities similar to the observed ones. We also found that, in order to reproduce the observations, the clouds need to evaporate into the hot gas and are therefore not feeding the central galaxy’s star-formation, in agreement with the quiescent nature of ETGs.

In Chapter 3, we have moved our focus on star-forming galaxies. In this case, we have tested a popular model in which the cool CGM clouds are part of biconical outflows, powered by the supernova (SN) explosions in the disk. Similar to Chapter 2, we used a Bayesian analysis to compare our model pre-

¹In Chapters 3 and 4, we also explored models with a corona with a mass equal to, respectively, 2% and 40% of the total baryonic mass, finding similar results to the ones reported below.

dictions with real data, in this case given by the detections of the cool CGM around a sample of ~ 40 star-forming galaxies, from the surveys of COS-Halos (Werk et al. 2013) and COS-GASS (Borthakur et al. 2015). Given that the cool CGM is detected up to the virial radii of these galaxies, in order to overcome the gravitational attraction and the drag force of the hot gas, the outflows need very high velocities and mass loading factors. As a consequence, we have found that, to power such outflows, the efficiency with which the energy of supernova explosions is transferred to the kinetic energy of the outflowing gas needs to be of the order of 250%, which is unphysical. Such efficiencies are also in strong disagreement with theoretical expectations, where most of the energy is radiated away and the efficiency is of the order of 10% (e.g. McKee & Ostriker 1977; Kim & Ostriker 2015). We concluded that SN feedback alone cannot be the origin of most of the cool CGM around star-forming nearby galaxies.

In Chapter 4, we have adopted a similar approach to the one used in the previous Chapters, in order to explain the properties of the cool CGM of M31, which has been recently characterized in detail by the project AMIGA (Lehner et al. 2020), piercing the halo of M31 with more than 40 sightlines. Mapping the cool CGM of one single galaxy across its entire halo, this survey provides then an unprecedented amount of information. In this case, we compared models of both inflow and outflow for the cool clouds. We assumed, in accordance with theoretical arguments (e.g. Pezzulli et al. 2017) and observational constraints (Hodges-Kluck et al. 2016), that the hot corona is rotating, with a total angular momentum that is consistent with the cosmological expectations (see Cimatti et al. 2019) for the halo of M31. We calibrated our models on the AMIGA data. We have found that, similar to the other star-forming galaxies, SN feedback is not a viable way to reproduce the cool CGM around M31, given that the outflows require SN efficiencies of the order of 700%. On the other hand, we found that the inflow of low-metallicity ($Z \approx 0.05 Z_{\odot}$) gas, consistent with the accretion from the IGM, can nicely reproduce the observations. The total mass accretion of the cool medium is similar to the predictions from cosmological models (Correa et al. 2015a,b) and its angular momentum, due to the drag force of the hot gas, is consistent with the one of the corona.

Finally, in Chapter 5, we have utilized high-resolution hydrodynamical simulations, using the software PLUTO (Mignone et al. 2007, 2012), to better describe the interactions between the cool and hot phases of the CGM, focusing in particular on the gas populating the halo of M31. This allowed us to study the fate of the cool CGM clouds, which could not be determined with the semi-analytical models of Chapter 4. We have followed the infall of a single cloud, starting from the virial radius, including the effects of radiative cooling, thermal conduction and the DM halo gravitational potential. We have used the results of Chapter 4 as initial conditions for our numerical experiments. We have found that, in our simulations, the cool clouds are not able to survive their journey and to reach the galactic disk, evaporating instead into the hot corona, at distances larger than 150 kpc from the central galaxy.

6.2 Main implications for the cool CGM

6.2.1 The predominance of accretion

The main conclusion of this work is that the cool CGM is part of the accretion of gas into the halos of galaxies from the intergalactic medium (IGM). This is evident from the results of Chapters 2 and 4, where we have shown that models of gas accretion can successfully reproduce the observational data of COS-LRG (e.g. Chen et al. 2018) and AMIGA (Lehner et al. 2020). Moreover, it is also a natural implication of Chapter 3, where the accretion from the IGM represents the most likely origin of the cool gas, given that we exclude the scenario of SN feedback as a possible formation mechanism (see also below).

We found an accretion rate that is consistent with (although slightly higher than) the estimates of cosmological models based on dark-matter-only simulations (Fakhouri et al. 2010; Correa et al. 2015a,b). Moreover, from Chapter 4, we have found that this medium has low metallicity, with values that are not far from the typical estimates for the IGM (e.g. Danforth & Shull 2008). Therefore, the accretion from the IGM, in addition to successfully reproduce the observed cool CGM properties, represents also a physically motivated and self-consistent scenario. We conclude that this constitutes the main formation mechanism of the cool gas in the halos of both early- and late-type galaxies in the local Universe.

Based on the results from cosmological hydrodynamical models and simulations, the presence of cool accreting gas in the halos of galaxies at least as massive as our Milky Way is not obvious. In the cold/hot mode accretion scenario (e.g. Birnboim & Dekel 2003; Kereš et al. 2009, see Chapter 1), galaxies of this mass, at redshifts close to zero, are expected to be surrounded mainly by a hot gas atmosphere, while cool gas filaments should be able to penetrate in less massive halos (e.g. Dekel et al. 2009). The value of the mass threshold between these two types of accretion is, however, still debated. Moreover, when present, in cosmological simulations the cold accretion is composed by filaments that penetrate into the halos with large infall velocities (e.g. Nelson et al. 2016), while we found that, in our models, the cool clouds start at the virial radius with velocities of about 10 km s^{-1} . We argued that these clouds are originated by the fragmentation of the streams entering the halo and interacting with the hot pre-existing CGM. The absence of cool gas clouds in large-scale hydrodynamical simulations might, instead, be due to the lack of resolution (see van de Voort et al. 2019). With this Thesis, we have demonstrated that the presence of cool gas clouds, accreted from the IGM and that account for a total amount of baryons comparable to the mass of the stellar component, is a common feature of low-redshift galaxies.

Finally, we note that, both in Chapter 2 and 4, we found an accretion rate that is slightly (1.5 times) higher than the theoretical expectations at the present time. This may be due to the fact that the gas accretion was larger in the past (3-4 Gyr ago, consistent with the cloud infall time in our models). However,

this result may also suggest that part of the cool CGM might form from different processes, among which we proposed satellite stripping (e.g. Grcevich & Putman 2009; Marasco et al. 2016; Johnson et al. 2018) or thermal instabilities of the hot gas (e.g. Sharma et al. 2012; Sormani & Sobacchi 2019). Analyzing the details of these processes and their relation with the cool circumgalactic gas is however left for future work.

The (minor) role of SN feedback

One of the goals of this Thesis has been to investigate whether or not there is a connection between the star formation of the host galaxy and its circumgalactic medium. In particular, we explored whether the feedback from supernova explosions in the disk can be one of the main formation mechanisms of the cool CGM. We have seen indeed, in Chapter 1, that a large amount of cool ionized gas is observed both around passive and star-forming galaxies (e.g. Thom et al. 2012; Tumlinson et al. 2013; Huang et al. 2021) and the relation between the star-formation in the galaxy and the cool CGM is, to date, not clear.

While we do not expect strong galactic outflows in quiescent ETGs, many authors have proposed, both from a theoretical and an observational point of view, that, in star-forming galaxies, a crucial role in the formation of the cool CGM is played by the SN feedback (e.g. Ford et al. 2014; Schroetter et al. 2019). We have explored this scenario in Chapters 3 and 4, where we have clearly shown, instead, that SN feedback is not able to impact the cool gas at a distance ≥ 50 kpc from the galactic disk, since the energy requirements to bring these cool clouds up to these very large distances are too high. We conclude, therefore, that SN outflows may be important to determine the properties of the extraplanar gas (see Section 1.2.1), the inner region of the CGM, at the interface with the central galaxy, while the vast majority of the outer cool CGM can be, instead, explained with the accretion from the IGM.

6.2.2 Fate of the cool CGM

Understanding the fate of the cool CGM is crucial to infer the role of this medium in galaxy evolution. If some of this cool gas accretes on the central galaxy, it would join the galaxy's reservoir of HI, which can fuel the formation of new stars at a rate that depends on the star formation efficiency. Observed properties of galaxies can be used to put limits of the amount of cold gas accretion that reaches the disk. If excessive accretion onto the disk takes place, galaxies would have either a gas fraction or a star formation rate (SFR) much higher than what we observe. As an example, in our study of the CGM of M31 (Chapter 4) we have inferred a rate of gas accretion, from the IGM into the CGM, of $15 M_{\odot} \text{ yr}^{-1}$. If all of this gas reached the central galaxy, it would either double the mass of HI in less than 1 Gyr, or result in a star formation rate more than one order of magnitude larger than observed ($\sim 1 M_{\odot} \text{ yr}^{-1}$; Rahmani et al. 2016). The situation is even more puzzling for ETGs, which currently have a star formation rate close to zero and very small fractions of neutral hydrogen,

despite a gas accretion rate at the virial radius of hundreds of $M_{\odot} \text{ yr}^{-1}$ (see Chapter 2). Therefore, in Chapter 1 we argued that some mechanism must halt the flow of cool CGM from reaching the central galaxies. With the work presented in this Thesis, especially in Chapters 2 and 5, we have found that this mechanism is the evaporation of the cool clouds into the hot corona.

In Chapter 2, we attributed the evaporation of the clouds to the development of hydrodynamical instabilities and to thermal conduction, which is likely very efficient in the very hot gaseous halos of massive ellipticals ($T \lesssim 10^7 \text{ K}$), approximating the cloud destruction with a constant evaporation rate. We have seen, in particular, that the cloud destruction is necessary to reproduce the observational data. In Chapter 5, we have found a similar result (the evaporation of the clouds) for star-forming galaxies (M31 in particular), where the temperature of the hot gas is lower ($T \sim 10^6 \text{ K}$) with respect to the coronae of massive ETGs. In this case, we directly solved the system of ideal hydrodynamical equations, with the use of high-resolution numerical simulations. Our semi-analytical models and hydrodynamical simulations, therefore, suggest that, both in massive ETGs and in star-forming L^* galaxies, the fate of the vast majority of the infalling cool CGM is to evaporate into the hot coronal gas (see also Section 6.3.3) and not to feed the central galaxy star formation, which is instead likely regulated by the processes happening in the inner gas layers of the halo (e.g. Marasco et al. 2012; Pezzulli & Fraternali 2016; Fraternali 2017), a problem whose investigation is outside the scope of this Thesis.

Furthermore, we have found that the majority of this cool gas is likely segregated in the external regions (intrinsic galactocentric distances $> 100 \text{ kpc}$) of the halos and that the detections of this gas at impact parameters of a few tens of kpc are mainly due to projection effects.

6.3 Future prospects

6.3.1 New observational constraints

All the findings of this Thesis are based on observational data, that we have used to calibrate our theoretical models. While the total sample used throughout this work is still limited, with a collection of only about 60 galaxies, recent and future surveys can provide numerous observational constraints that can potentially be interpreted by similar models. Combining surveys like MEGAFLOW (Schroetter et al. 2016), CGM² (Wilde et al. 2020) and CUBS (Chen et al. 2020a) can lead to a sample of up to several hundreds of objects, providing a more complete statistical view on the cool CGM of galaxies at redshift $\lesssim 1$ (and potentially also at higher redshift). Moreover, explaining the data of the cool gas around specific types of galaxies, going from dwarfs to galaxies with active galactic nuclei (AGN) and starburst galaxies, is also one of the future directions of this investigation and it can be achieved with the data currently available in the literature (e.g. Bordoloi et al. 2014; Heckman et al. 2017; Berg et al. 2018).

While building large statistical samples is very important, we have seen,

in Chapter 4, how studying the CGM of a single galaxy halo can also be extremely useful in order to draw conclusions about the origin and dynamics of this medium. Extended maps of the cool CGM of single galaxies (like those available from the tomography of gravitational arcs, see for example Lopez et al. 2018; Tejos et al. 2021) can be crucial to improve our understanding of this gas and our models have the potential to interpret also this kind of data. Finally, by directly implementing in our models a self-consistent photo-ionization mechanism (using for example softwares like CLOUDY, Ferland et al. 2013), we could self-consistently reproduce, at the same time, the observed column densities of different ions. This might allow us to separate the properties of ions with low (e.g. Mg II) and high (e.g. O VI) ionization potentials and to, therefore, investigate separately the cool ($T \sim 10^4$ K) and warm ($T \gtrsim 10^5$ K) phases of the CGM.

In addition to the observations of the cool CGM, the launch within the next 15 years of several X-ray missions like ATHENA, Lynx, AXIS or XRISM (see for example Nandra et al. 2013; The Lynx Team 2018; Mushotzky et al. 2019; XRISM Science Team 2020; Simionescu et al. 2021), with a great improvement of both the spatial and spectral resolution of X-ray observations, will open a new window on the properties of the hot coronae surrounding low-redshift galaxies. Given the importance that the hot CGM has on the dynamics and fate of the cool circumgalactic clouds (see Section 6.2.2), a better characterization of this gas will be very useful in improving the accuracy of any model of the CGM.

6.3.2 Improving numerical simulations of the CGM

Hydrodynamical simulations are key to our understanding of the interactions between the different phases of the CGM. While large-scale, cosmological simulations have still an insufficient resolution (e.g. van de Voort et al. 2019), idealized, high-resolution simulations have extensively been used to study the properties of the cool gas and its survival in a hot ambient medium (e.g. Marinacci et al. 2010b; Armillotta et al. 2016; Schneider et al. 2018; Grønnow et al. 2018). However, the external regions of the halos, where we believe most of the cool CGM resides, have rarely been explored with this type of simulations (e.g. Armillotta et al. 2017).

In Chapter 5, we have shown a variety of results focused on the cool gas in the halo of M31. The analysis of these high-resolution hydrodynamical simulations has provided insight on the evolution of the mass, velocity and shape of the cool clouds, results that can be used to improve our semi-analytical models, as we also discuss in the next Section. Before doing so, however, a more thorough analysis is necessary. We plan, indeed, to implement additional physical effects, like the presence of an ionizing extragalactic UV background (e.g. Haardt & Madau 2012) or of the magnetic field (e.g. Kooij et al. 2021, although at these large galactocentric distances the magnetic field has likely only a secondary role in the cool gas evolution) and to further improve the study on the convergence of these simulations with the resolution. Finally, it is crucial to

investigate different initial conditions, in order to have a more complete view of the CGM of galaxies with different properties and to take into account the various uncertainties on the values of parameters including the hot gas temperature, the cloud masses and sizes and the metallicity of both phases of the circumgalactic gas.

6.3.3 Refining models of the CGM

Refining and generalizing the semi-analytic models of Chapters 2, 3 and 4 represents the main goal of this investigation in the near future. This can be done in different ways, some of which have already been discussed throughout this Thesis. As mentioned in Section 6.3.2, a fundamental step will be to incorporate the results of high-resolution simulations into our models, possibly describing the mass loss and size evolution of the clouds with physically motivated analytical prescriptions, which can be directly fit to the observational constraints. We have made a first attempt in this direction in Chapter 5, showing the potential of this approach in explaining the physics and the properties of the CGM.

Another possible improvement of our models is to include the variation of the cosmological accretion rate with time (e.g. Correa et al. 2015b). Furthermore, it would be important to model the mass increase of the hot gas: indeed, we have found that the fate of the cool gas is to evaporate into the hot corona, and given that the masses of the two phases are comparable with each other, the mass of the hot CGM should significantly increase with time. This problem has been briefly discussed throughout this Thesis, but we plan in the future to self-consistently implement this effect in our models. Finally, alternative scenarios to those investigated in this Thesis might also be relevant for the formation of the cool CGM. In particular, future possible studies include the modeling, as an origin of the cool gas, of gas stripping from satellite galaxies, condensation of the hot corona due to thermal instabilities (this scenario has partially been explored in Chapter 2), or of outflows due to AGN. The implementation of these effects will allow us to build a more complete description of the cool gas around galaxies.

Through the interplay between new observational data, results from hydrodynamical simulations and analytical modeling, the investigation started with this Thesis has the aim of improving our knowledge of the circumgalactic medium of galaxies. By understanding the dynamics, origin and fate of this gas, we can indeed take a fundamental step in our comprehension of how galaxies form and evolve in the Universe.

Bibliography

- Acharya A., Khaire V., 2021, arXiv e-prints, p. arXiv:2104.01182
- Afruni A., Fraternali F., Pezzulli G., 2019, *A&A*, 625, A11
- Afruni A., Fraternali F., Pezzulli G., 2021, *MNRAS*, 501, 5575
- Anderson M. E., Bregman J. N., 2010, *ApJ*, 714, 320
- Anderson M. E., Bregman J. N., 2011, *ApJ*, 737, 22
- Anderson M. E., Bregman J. N., Dai X., 2013, *ApJ*, 762, 106
- Anderson M. E., Churazov E., Bregman J. N., 2016, *MNRAS*, 455, 227
- Anglés-Alcázar D., Faucher-Giguère C.-A., Kereš D., Hopkins P. F., Quataert E., Murray N., 2017, *MNRAS*, 470, 4698
- Armillotta L., Fraternali F., Marinacci F., 2016, *MNRAS*, 462, 4157
- Armillotta L., Fraternali F., Werk J. K., Prochaska J. X., Marinacci F., 2017, *MNRAS*, 470, 114
- Armillotta L., Krumholz M. R., Di Teodoro E. M., McClure-Griffiths N. M., 2019, *MNRAS*, 490, 4401
- Arrigoni Battaia F., Prochaska J. X., Hennawi J. F., Obreja A., Buck T., Cantalupo S., Dutton A. A., Macciò A. V., 2018, *MNRAS*, 473, 3907
- Asplund M., Grevesse N., Sauval A. J., Scott P., 2009, *ARA&A*, 47, 481
- Athanassoula E., Beaton R. L., 2006, *MNRAS*, 370, 1499
- Bacon R., et al., 2010, in McLean I. S., Ramsay S. K., Takami H., eds, *Society of Photo-Optical Instrumentation Engineers (SPIE) Conference Series Vol. 7735, Ground-based and Airborne Instrumentation for Astronomy III*. p. 773508, doi:10.1117/12.856027
- Barnabè M., Ciotti L., Fraternali F., Sancisi R., 2006, *A&A*, 446, 61
- Begelman M. C., McKee C. F., 1990, *ApJ*, 358, 375
- Behroozi P. S., Conroy C., Wechsler R. H., 2010, *ApJ*, 717, 379

- Berg T. A. M., Ellison S. L., Tumlinson J., Oppenheimer B. D., Horton R., Bordoloi R., Schaye J., 2018, MNRAS, 478, 3890
- Berg M. A., et al., 2019, ApJ, 883, 5
- Bergeron J., 1986, A&A, 155, L8
- Binney J., 1977, ApJ, 215, 483
- Binney J., 2004, MNRAS, 347, 1093
- Binney J., et al., 2009, MNRAS, 397, 1804
- Birnboim Y., Dekel A., 2003, MNRAS, 345, 349
- Bish H. V., Werk J. K., Peek J., Zheng Y., Putman M., 2020, arXiv e-prints, p. arXiv:2010.03610
- Blanton M. R., et al., 2017, , 154, 28
- Bogdán Á., Gilfanov M., 2011, MNRAS, 418, 1901
- Bogdán Á., et al., 2013, ApJ, 772, 97
- Bogdán Á., Bourdin H., Forman W. R., Kraft R. P., Vogelsberger M., Hernquist L., Springel V., 2017, ApJ, 850, 98
- Boksenberg A., Sargent W. L. W., 1978, ApJ, 220, 42
- Bordoloi R., et al., 2011, ApJ, 743, 10
- Bordoloi R., et al., 2014, ApJ, 796, 136
- Borisova E., et al., 2016, ApJ, 831, 39
- Borthakur S., Heckman T., Strickland D., Wild V., Schiminovich D., 2013, ApJ, 768, 18
- Borthakur S., et al., 2015, ApJ, 813, 46
- Borthakur S., et al., 2016, ApJ, 833, 259
- Bouché N., Murphy M. T., Kacprzak G. G., Péroux C., Contini T., Martin C. L., Dessauges-Zavadsky M., 2013, Science, 341, 50
- Bovy J., 2015, ApJS, 216, 29
- Bowen D. V., Blades J. C., Pettini M., 1995, ApJ, 448, 634
- Bowen D. V., et al., 2006, ApJ, 645, L105
- Bowen D. V., Chelouche D., Jenkins E. B., Tripp T. M., Pettini M., York D. G., Frye B. L., 2016, ApJ, 826, 50

-
- Boylan-Kolchin M., Springel V., White S. D. M., Jenkins A., Lemson G., 2009, MNRAS, 398, 1150
- Braun R., Thilker D. A., 2004, A&A, 417, 421
- Bregman J. N., 1980, ApJ, 236, 577
- Bregman J. N., Lloyd-Davies E. J., 2007, ApJ, 669, 990
- Bregman J. N., Anderson M. E., Miller M. J., Hodges-Kluck E., Dai X., Li J.-T., Li Y., Qu Z., 2018, ApJ, 862, 3
- Brook C. B., Stinson G., Gibson B. K., Roškar R., Wadsley J., Quinn T., 2012, MNRAS, 419, 771
- Brüggen M., Scannapieco E., 2016, ApJ, 822, 31
- Brüns C., et al., 2005, A&A, 432, 45
- Bryan G. L., Norman M. L., 1998, ApJ, 495, 80
- Burchett J. N., et al., 2019, ApJ, 877, L20
- Burchett J. N., Rubin K. H. R., Prochaska J. X., Coil A. L., Rickards Vaught R., Hennawi J. F., 2020, arXiv e-prints, p. arXiv:2005.03017
- Burchett J. N., Rubin K. H. R., Prochaska J. X., Coil A. L., Vaught R. R., Hennawi J. F., 2021, ApJ, 909, 151
- Cai Z., et al., 2018, ApJ, 861, L3
- Cai Z., et al., 2019, ApJS, 245, 23
- Caldú-Primo A., Schrubba A., 2016, , 151, 34
- Cantalupo S., 2010, MNRAS, 403, L16
- Cantalupo S., Arrigoni-Battaia F., Prochaska J. X., Hennawi J. F., Madau P., 2014, Nature, 506, 63
- Carignan C., Chemin L., Huchtmeier W. K., Lockman F. J., 2006, ApJ, 641, L109
- Carignan C., Chemin L., Foster T., 2007, in Combes F., Palouš J., eds, Vol. 235, Galaxy Evolution across the Hubble Time. pp 193–193 (arXiv:astro-ph/0702609), doi:10.1017/S1743921306005990
- Chandran B. D. G., Cowley S. C., 1998, , 80, 3077
- Chemin L., Carignan C., Foster T., 2009, ApJ, 705, 1395
- Chen H.-W., Lanzetta K. M., Webb J. K., Barcons X., 1998, ApJ, 498, 77

- Chen H.-W., Helsby J. E., Gauthier J.-R., Shectman S. A., Thompson I. B., Tinker J. L., 2010a, *ApJ*, 714, 1521
- Chen H.-W., Wild V., Tinker J. L., Gauthier J.-R., Helsby J. E., Shectman S. A., Thompson I. B., 2010b, *ApJ*, 724, L176
- Chen H.-W., Gauthier J.-R., Sharon K., Johnson S. D., Nair P., Liang C. J., 2014, *MNRAS*, 438, 1435
- Chen H.-W., Zahedy F. S., Johnson S. D., Pierce R. M., Huang Y.-H., Weiner B. J., Gauthier J.-R., 2018, *MNRAS*, 479, 2547
- Chen H.-W., et al., 2019a, *MNRAS*, 484, 431
- Chen H.-W., Boettcher E., Johnson S. D., Zahedy F. S., Rudie G. C., Cooksey K. L., Rauch M., Mulchaey J. S., 2019b, *ApJ*, 878, L33
- Chen H.-W., et al., 2020a, *MNRAS*, 497, 498
- Chen Y., et al., 2020b, *MNRAS*, 499, 1721
- Chisholm J., Tremonti C. A., Leitherer C., Chen Y., Wofford A., Lundgren B., 2015, *ApJ*, 811, 149
- Chisholm J., Tremonti C. A., Leitherer C., Chen Y., 2017, *MNRAS*, 469, 4831
- Cimatti A., Fraternali F., Nipoti C., 2019, *Introduction to Galaxy Formation and Evolution: From Primordial Gas to Present-Day Galaxies*
- Collins J. A., Rand R. J., 2001, *ApJ*, 551, 57
- Concas A., Popesso P., Brusa M., Mainieri V., Erfanianfar G., Morselli L., 2017, *A&A*, 606, A36
- Concas A., Popesso P., Brusa M., Mainieri V., Thomas D., 2019, *A&A*, 622, A188
- Corbelli E., Lorenzoni S., Walterbos R., Braun R., Thilker D., 2010, *A&A*, 511, A89
- Correa C. A., Wyithe J. S. B., Schaye J., Duffy A. R., 2015a, *MNRAS*, 450, 1514
- Correa C. A., Wyithe J. S. B., Schaye J., Duffy A. R., 2015b, *MNRAS*, 450, 1521
- Courteau S., Widrow L. M., McDonald M., Guhathakurta P., Gilbert K. M., Zhu Y., Beaton R. L., Majewski S. R., 2011, *ApJ*, 739, 20
- Cowie L. L., McKee C. F., 1977, *ApJ*, 211, 135
- Cox A. N., 2000, *Allen's astrophysical quantities*

-
- Crain R. A., et al., 2015, MNRAS, 450, 1937
- Dai X., Anderson M. E., Bregman J. N., Miller J. M., 2012, ApJ, 755, 107
- Dalton W. W., Balbus S. A., 1993, ApJ, 404, 625
- Danforth C. W., Shull J. M., 2008, ApJ, 679, 194
- Dekel A., Birnboim Y., 2006, MNRAS, 368, 2
- Dekel A., Sari R., Ceverino D., 2009, ApJ, 703, 785
- Dey A., et al., 2019, , 157, 168
- Di Teodoro E. M., et al., 2019, ApJ, 885, L32
- Draine B. T., et al., 2014, ApJ, 780, 172
- Dutton A. A., Macciò A. V., 2014, MNRAS, 441, 3359
- Elmegreen B. G., Scalo J., 2004, ARA&A, 42, 211
- Emerick A., Bryan G. L., Mac Low M.-M., 2019, MNRAS, 482, 1304
- Epinat B., et al., 2018, A&A, 609, A40
- Erb D. K., Quider A. M., Henry A. L., Martin C. L., 2012, ApJ, 759, 26
- Escala I., Gilbert K. M., Kirby E. N., Wojno J., Cunningham E. C., Guhathakurta P., 2020, ApJ, 889, 177
- Esmerian C. J., Kravtsov A. V., Hafen Z., Faucher-Giguère C.-A., Quataert E., Stern J., Kereš D., Wetzel A., 2021, MNRAS, 505, 1841
- Faerman Y., Sternberg A., McKee C. F., 2017, ApJ, 835, 52
- Faerman Y., Sternberg A., McKee C. F., 2020, ApJ, 893, 82
- Fakhouri O., Ma C.-P., Boylan-Kolchin M., 2010, MNRAS, 406, 2267
- Farina E. P., et al., 2019, ApJ, 887, 196
- Fattahi A., et al., 2016, MNRAS, 457, 844
- Ferland G. J., et al., 2013, , 49, 137
- Field G. B., 1965, ApJ, 142, 531
- Fielding D., Quataert E., Martizzi D., Faucher-Giguère C.-A., 2017, MNRAS, 470, L39
- Fielding D., Quataert E., Martizzi D., 2018, MNRAS, 481, 3325
- Fielding D. B., Ostriker E. C., Bryan G. L., Jermyn A. S., 2020a, ApJ, 894, L24

- Fielding D. B., et al., 2020b, *ApJ*, 903, 32
- Fielding D. B., et al., 2020c, *ApJ*, 903, 32
- Ford A. B., Davé R., Oppenheimer B. D., Katz N., Kollmeier J. A., Thompson R., Weinberg D. H., 2014, *MNRAS*, 444, 1260
- Ford A. B., et al., 2016, *MNRAS*, 459, 1745
- Forman W., Schwarz J., Jones C., Liller W., Fabian A. C., 1979, *ApJ*, 234, L27
- Fox A. J., Wakker B. P., Smoker J. V., Richter P., Savage B. D., Sembach K. R., 2010, *ApJ*, 718, 1046
- Fraternali F., 2017, *Gas Accretion via Condensation and Fountains*. p. 323, doi:10.1007/978-3-319-52512-9_14
- Fraternali F., Binney J. J., 2006, *MNRAS*, 366, 449
- Fraternali F., Binney J. J., 2008, *MNRAS*, 386, 935
- Fraternali F., Tomassetti M., 2012, *MNRAS*, 426, 2166
- Fraternali F., van Moorsel G., Sancisi R., Oosterloo T., 2002, , 123, 3124
- Fraternali F., Oosterloo T., Sancisi R., 2004, *A&A*, 424, 485
- Fraternali F., Marasco A., Armillotta L., Marinacci F., 2015, *MNRAS*, 447, L70
- Froning C. S., Green J. C., 2009, *Ap&SS*, 320, 181
- Fukugita M., Peebles P. J. E., 2006, *ApJ*, 639, 590
- Gatto A., Fraternali F., Read J. I., Marinacci F., Lux H., Walch S., 2013, *MNRAS*, 433, 2749
- Gatto A., et al., 2017, *MNRAS*, 466, 1903
- Gauthier J.-R., Chen H.-W., Tinker J. L., 2009, *ApJ*, 702, 50
- Gilbert K. M., et al., 2018, *ApJ*, 852, 128
- Godunov S., 1959, *Matematicheskii Sbornik*, 47(89), 271
- Grand R. J. J., et al., 2017, *MNRAS*, 467, 179
- Grcevich J., Putman M. E., 2009, *ApJ*, 696, 385
- Greene J. E., Zakamska N. L., Smith P. S., 2012, *ApJ*, 746, 86
- Gronke M., Oh S. P., 2018, *MNRAS*, 480, L111
- Grønnow A., Tepper-García T., Bland-Hawthorn J., 2018, *ApJ*, 865, 64

-
- Gupta A., Mathur S., Krongold Y., Nicastro F., Galeazzi M., 2012, *ApJ*, 756, L8
- Haardt F., Madau P., 2001, in Neumann D. M., Tran J. T. V., eds, *Clusters of Galaxies and the High Redshift Universe Observed in X-rays*. ([arXiv:astro-ph/0106018](https://arxiv.org/abs/astro-ph/0106018))
- Haardt F., Madau P., 2012, *ApJ*, 746, 125
- Hafen Z., et al., 2019, *MNRAS*, 488, 1248
- Heald G. H., Rand R. J., Benjamin R. A., Bershady M. A., 2007, *ApJ*, 663, 933
- Heckman T. M., Alexandroff R. M., Borthakur S., Overzier R., Leitherer C., 2015, *ApJ*, 809, 147
- Heckman T., Borthakur S., Wild V., Schiminovich D., Bordoloi R., 2017, *ApJ*, 846, 151
- Heitsch F., Putman M. E., 2009, *ApJ*, 698, 1485
- Helton J. M., Johnson S. D., Greene J. E., Chen H.-W., 2021, *MNRAS*, 505, 5497
- Henley D. B., Shelton R. L., 2013, *ApJ*, 773, 92
- Ho S. H., Martin C. L., Kacprzak G. G., Churchill C. W., 2017, *ApJ*, 835, 267
- Hodges-Kluck E. J., Bregman J. N., 2013, *ApJ*, 762, 12
- Hodges-Kluck E. J., Miller M. J., Bregman J. N., 2016, *ApJ*, 822, 21
- Hopkins P. F., Kereš D., Oñorbe J., Faucher-Giguère C.-A., Quataert E., Murray N., Bullock J. S., 2014, *MNRAS*, 445, 581
- Hopkins P. F., et al., 2018, *MNRAS*, 480, 800
- Hopkins P. F., Chan T. K., Ji S., Hummels C. B., Kereš D., Quataert E., Faucher-Giguère C.-A., 2021, *MNRAS*, 501, 3640
- Howk J. C., et al., 2017, *ApJ*, 846, 141
- Hu C.-Y., 2019, *MNRAS*, 483, 3363
- Huang Y.-H., Chen H.-W., Johnson S. D., Weiner B. J., 2016, *MNRAS*, 455, 1713
- Huang Y.-H., Chen H.-W., Shectman S. A., Johnson S. D., Zahedy F. S., Helsby J. E., Gauthier J.-R., Thompson I. B., 2021, *MNRAS*, 502, 4743
- Hummels C. B., et al., 2019, *ApJ*, 882, 156

- Ibata R., Irwin M., Lewis G., Ferguson A. M. N., Tanvir N., 2001, *Nature*, 412, 49
- Johnson S. D., Chen H.-W., Mulchaey J. S., 2015, *MNRAS*, 452, 2553
- Johnson S. D., et al., 2018, *ApJ*, 869, L1
- Jones C., Forman W., Vikhlinin A., Markevitch M., David L., Warmflash A., Murray S., Nulsen P. E. J., 2002, *ApJ*, 567, L115
- Kacprzak G. G., Churchill C. W., Nielsen N. M., 2012, *ApJ*, 760, L7
- Kacprzak G. G., et al., 2014, *ApJ*, 792, L12
- Kacprzak G. G., Pointon S. K., Nielsen N. M., Churchill C. W., Muzahid S., Charlton J. C., 2019, *ApJ*, 886, 91
- Kavanagh P. J., et al., 2020, *A&A*, 637, A12
- Keeney B. A., Stocke J. T., Rosenberg J. L., Danforth C. W., Ryan-Weber E. V., Shull J. M., Savage B. D., Green J. C., 2013, *ApJ*, 765, 27
- Keeney B. A., et al., 2017, *ApJS*, 230, 6
- Keller B. W., Kruijssen J. M. D., Wadsley J. W., 2020, *MNRAS*, 493, 2149
- Kennicutt R. C. J., 1983, *ApJ*, 272, 54
- Kereš D., Katz N., Fardal M., Davé R., Weinberg D. H., 2009, *MNRAS*, 395, 160
- Kereš D., Vogelsberger M., Sijacki D., Springel V., Hernquist L., 2012, *MNRAS*, 425, 2027
- Kim C.-G., Ostriker E. C., 2015, *ApJ*, 802, 99
- Kim C.-G., Ostriker E. C., 2018, *ApJ*, 853, 173
- Kim C.-G., et al., 2020, *ApJ*, 900, 61
- Kooij R., Grønnow A., Fraternali F., 2021, *MNRAS*, 502, 1263
- Kravtsov A. V., Vikhlinin A. A., Meshcheryakov A. V., 2018, *Astronomy Letters*, 44, 8
- Lan T.-W., Mo H., 2019, *MNRAS*, 486, 608
- Lanzetta K. M., Bowen D. V., Tytler D., Webb J. K., 1995, *ApJ*, 442, 538
- Lehner N., Howk J. C., 2011, *Science*, 334, 955
- Lehner N., Howk J. C., Thom C., Fox A. J., Tumlinson J., Tripp T. M., Meiring J. D., 2012, *MNRAS*, 424, 2896

-
- Lehner N., et al., 2013, *ApJ*, 770, 138
- Lehner N., Howk J. C., Wakker B. P., 2015, *ApJ*, 804, 79
- Lehner N., O'Meara J. M., Howk J. C., Prochaska J. X., Fumagalli M., 2016, *ApJ*, 833, 283
- Lehner N., Wotta C. B., Howk J. C., O'Meara J. M., Oppenheimer B. D., Cooksey K. L., 2018, *ApJ*, 866, 33
- Lehner N., Wotta C. B., Howk J. C., O'Meara J. M., Oppenheimer B. D., Cooksey K. L., 2019, *ApJ*, 887, 5
- Lehner N., et al., 2020, *ApJ*, 900, 9
- Lewis A. R., et al., 2015, *ApJ*, 805, 183
- Li M., Bryan G. L., 2020, *ApJ*, 890, L30
- Li J.-T., Bregman J. N., Wang Q. D., Crain R. A., Anderson M. E., Zhang S., 2017a, *ApJS*, 233, 20
- Li M., Bryan G. L., Ostriker J. P., 2017b, *ApJ*, 841, 101
- Li J.-T., Bregman J. N., Wang Q. D., Crain R. A., Anderson M. E., 2018, *ApJ*, 855, L24
- Li Z., Hopkins P. F., Squire J., Hummels C., 2020, *MNRAS*, 492, 1841
- Liang C. J., Chen H.-W., 2014, *MNRAS*, 445, 2061
- Lockman F. J., Free N. L., Shields J. C., 2012, , 144, 52
- Lohner R., 1987, *Computer Methods in Applied Mechanics and Engineering*, 61, 323
- Lopez S., et al., 2018, *Nature*, 554, 493
- Lopez S., et al., 2020, *MNRAS*, 491, 4442
- Mancera Piña P. E., Posti L., Fraternali F., Adams E. A. K., Oosterloo T., 2021, *A&A*, 647, A76
- Mandelker N., Padnos D., Dekel A., Birnboim Y., Burkert A., Krumholz M. R., Steinberg E., 2016, *MNRAS*, 463, 3921
- Mandelker N., van Dokkum P. G., Brodie J. P., van den Bosch F. C., Ceverino D., 2018, *ApJ*, 861, 148
- Mandelker N., Nagai D., Aung H., Dekel A., Birnboim Y., van den Bosch F. C., 2020, *MNRAS*, 494, 2641
- Marasco A., Fraternali F., 2011, *A&A*, 525, A134

- Marasco A., Fraternali F., Binney J. J., 2012, MNRAS, 419, 1107
- Marasco A., Marinacci F., Fraternali F., 2013, MNRAS, 433, 1634
- Marasco A., Crain R. A., Schaye J., Bahé Y. M., van der Hulst T., Theuns T., Bower R. G., 2016, MNRAS, 461, 2630
- Marasco A., et al., 2019, A&A, 631, A50
- Marinacci F., Binney J., Fraternali F., Nipoti C., Ciotti L., Londrillo P., 2010a, MNRAS, 404, 1464
- Marinacci F., Binney J., Fraternali F., Nipoti C., Ciotti L., Londrillo P., 2010b, MNRAS, 404, 1464
- Marinacci F., Fraternali F., Nipoti C., Binney J., Ciotti L., Londrillo P., 2011, MNRAS, 415, 1534
- Marinacci F., et al., 2018, MNRAS, 480, 5113
- Martin C. L., 2005, ApJ, 621, 227
- Martin C. L., Bouché N., 2009, ApJ, 703, 1394
- Martin C. L., Shapley A. E., Coil A. L., Kornei K. A., Bundy K., Weiner B. J., Noeske K. G., Schiminovich D., 2012, ApJ, 760, 127
- Martin C. L., Ho S. H., Kacprzak G. G., Churchill C. W., 2019, ApJ, 878, 84
- Martizzi D., Fielding D., Faucher-Giguère C.-A., Quataert E., 2016, MNRAS, 459, 2311
- Mathews W. G., Brighenti F., 2003, ARA&A, 41, 191
- Mayer L., Kazantzidis S., Mastropietro C., Wadsley J., 2007, Nature, 445, 738
- McConnachie A. W., et al., 2018, ApJ, 868, 55
- McCourt M., Sharma P., Quataert E., Parrish I. J., 2012, MNRAS, 419, 3319
- McCourt M., O’Leary R. M., Madigan A.-M., Quataert E., 2015, MNRAS, 449, 2
- McCourt M., Oh S. P., O’Leary R., Madigan A.-M., 2018, MNRAS, 473, 5407
- McGaugh S. S., 2008, in Davies J. I., Disney M. J., eds, IAU Symposium Vol. 244, Dark Galaxies and Lost Baryons. pp 136–145 ([arXiv:0707.3795](https://arxiv.org/abs/0707.3795)), doi:10.1017/S1743921307013920
- McGaugh S. S., Schombert J. M., de Blok W. J. G., Zagursky M. J., 2010, ApJ, 708, L14
- McKee C. F., Ostriker J. P., 1977, ApJ, 218, 148

-
- McQuinn M., Werk J. K., 2018, *ApJ*, 852, 33
- McQuinn K. B. W., van Zee L., Skillman E. D., 2019, *ApJ*, 886, 74
- Mignone A., Bodo G., Massaglia S., Matsakos T., Tesileanu O., Zanni C., Ferrari A., 2007, *ApJS*, 170, 228
- Mignone A., Zanni C., Tzeferacos P., van Straalen B., Colella P., Bodo G., 2012, *ApJS*, 198, 7
- Miller M. J., Bregman J. N., 2013, *ApJ*, 770, 118
- Miller M. J., Bregman J. N., 2015, *ApJ*, 800, 14
- Mo H., van den Bosch F. C., White S., 2010, *Galaxy Formation and Evolution*
- Moster B. P., Naab T., White S. D. M., 2013, *MNRAS*, 428, 3121
- Muratov A. L., Kereš D., Faucher-Giguère C.-A., Hopkins P. F., Quataert E., Murray N., 2015, *MNRAS*, 454, 2691
- Muratov A. L., et al., 2017, *MNRAS*, 468, 4170
- Mushotzky R., et al., 2019, in *Bulletin of the American Astronomical Society*. p. 107 ([arXiv:1903.04083](https://arxiv.org/abs/1903.04083))
- Naab T., Ostriker J. P., 2017, *ARA&A*, 55, 59
- Nandra K., et al., 2013, *arXiv e-prints*, p. [arXiv:1306.2307](https://arxiv.org/abs/1306.2307)
- Narayan R., Medvedev M. V., 2001, *ApJ*, 562, L129
- Navarro J. F., Frenk C. S., White S. D. M., 1995, *MNRAS*, 275, 720
- Navarro J. F., Frenk C. S., White S. D. M., 1996, *ApJ*, 462, 563
- Nelson D., Vogelsberger M., Genel S., Sijacki D., Kereš D., Springel V., Hernquist L., 2013, *MNRAS*, 429, 3353
- Nelson D., Genel S., Pillepich A., Vogelsberger M., Springel V., Hernquist L., 2016, *MNRAS*, 460, 2881
- Nelson D., et al., 2019, *MNRAS*, 490, 3234
- Nelson D., et al., 2020, *arXiv e-prints*, p. [arXiv:2005.09654](https://arxiv.org/abs/2005.09654)
- Nidever D. L., Majewski S. R., Butler Burton W., Nigra L., 2010, *ApJ*, 723, 1618
- Nielsen N. M., Churchill C. W., Kacprzak G. G., Murphy M. T., Evans J. L., 2016, *ApJ*, 818, 171
- Nipoti C., Binney J., 2007, *MNRAS*, 382, 1481

- Nipoti C., Posti L., 2013, *MNRAS*, 428, 815
- Nipoti C., Posti L., 2014, *ApJ*, 792, 21
- O’Sullivan E., Sanderson A. J. R., Ponman T. J., 2007, *MNRAS*, 380, 1409
- O’Sullivan D. B., Martin C., Matuszewski M., Hoadley K., Hamden E., Neill J. D., Lin Z., Parihar P., 2020, *ApJ*, 894, 3
- Ocvirk P., Pichon C., Teyssier R., 2008, *MNRAS*, 390, 1326
- Oosterloo T., Fraternali F., Sancisi R., 2007, , 134, 1019
- Oppenheimer B. D., Davé R., 2006, *MNRAS*, 373, 1265
- Oppenheimer B. D., Davé R., Kereš D., Fardal M., Katz N., Kollmeier J. A., Weinberg D. H., 2010, *MNRAS*, 406, 2325
- Oppenheimer B. D., Schaye J., Crain R. A., Werk J. K., Richings A. J., 2018, *MNRAS*, 481, 835
- Padnos D., Mandelker N., Birnboim Y., Dekel A., Krumholz M. R., Steinberg E., 2018, *MNRAS*, 477, 3293
- Peeples M. S., Werk J. K., Tumlinson J., Oppenheimer B. D., Prochaska J. X., Katz N., Weinberg D. H., 2014, *ApJ*, 786, 54
- Peeples M. S., et al., 2019, *ApJ*, 873, 129
- Peng C. Y., Ho L. C., Impey C. D., Rix H.-W., 2010, , 139, 2097
- Péroux C., et al., 2016, *MNRAS*, 457, 903
- Pezzulli G., Cantalupo S., 2019, *MNRAS*, 486, 1489
- Pezzulli G., Fraternali F., 2016, *MNRAS*, 455, 2308
- Pezzulli G., Fraternali F., Boissier S., Muñoz-Mateos J. C., 2015, *MNRAS*, 451, 2324
- Pezzulli G., Fraternali F., Binney J., 2017, *MNRAS*, 467, 311
- Pfrommer C., Pakmor R., Schaal K., Simpson C. M., Springel V., 2017, *MNRAS*, 465, 4500
- Pillepich A., et al., 2018, *MNRAS*, 473, 4077
- Planck Collaboration et al., 2018, preprint, ([arXiv:1807.06209](https://arxiv.org/abs/1807.06209))
- Planck Collaboration et al., 2020, *A&A*, 641, A1
- Poggianti B. M., et al., 2017, *ApJ*, 844, 48

-
- Pointon S. K., Kacprzak G. G., Nielsen N. M., Muzahid S., Murphy M. T., Churchill C. W., Charlton J. C., 2019, *ApJ*, 883, 78
- Ponomareva A. A., Verheijen M. A. W., Bosma A., 2016, *MNRAS*, 463, 4052
- Posti L., Fraternali F., Marasco A., 2019a, *A&A*, 626, A56
- Posti L., Marasco A., Fraternali F., Famaey B., 2019b, *A&A*, 629, A59
- Prochaska J. X., Weiner B., Chen H. W., Mulchaey J., Cooksey K., 2011, *ApJ*, 740, 91
- Prochaska J. X., et al., 2013, *ApJ*, 776, 136
- Prochaska J. X., et al., 2017, *ApJ*, 837, 169
- Putman M. E., Peek J. E. G., Joungh M. R., 2012, *ARA&A*, 50, 491
- Putman M. E., Zheng Y., Price-Whelan A. M., Greевич J., Johnson A. C., Tollerud E., Peek J. E. G., 2021, arXiv e-prints, p. arXiv:2101.07809
- Qu Z., Huang R., Bregman J. N., Li J.-T., 2021, *ApJ*, 907, 14
- Rahmani S., Lianou S., Barmby P., 2016, *MNRAS*, 456, 4128
- Rahmati A., Oppenheimer B. D., 2018, *MNRAS*, 476, 4865
- Rees M. J., Ostriker J. P., 1977, *MNRAS*, 179, 541
- Reynolds R. J., 1991, in Bloemen H., ed., Vol. 144, *The Interstellar Disk-Halo Connection in Galaxies*. p. 67
- Robles-Valdez F., Carigi L., Peimbert M., 2014, , 50, 271
- Rossa J., Dettmar R. J., 2003, *A&A*, 406, 493
- Rubin K. H. R., Prochaska J. X., Ménard B., Murray N., Kasen D., Koo D. C., Phillips A. C., 2011, *ApJ*, 728, 55
- Rubin K. H. R., Prochaska J. X., Koo D. C., Phillips A. C., 2012, *ApJ*, 747, L26
- Rubin K. H. R., Prochaska J. X., Koo D. C., Phillips A. C., Martin C. L., Winstrom L. O., 2014, *ApJ*, 794, 156
- Rubin K. H. R., Diamond-Stanic A. M., Coil A. L., Crighton N. H. M., Stewart K. R., 2018, *ApJ*, 868, 142
- Rudie G. C., et al., 2012, *ApJ*, 750, 67
- Salem M., Besla G., Bryan G., Putman M., van der Marel R. P., Tonnesen S., 2015, *ApJ*, 815, 77

- Sancisi R., Fraternali F., Oosterloo T., van der Hulst T., 2008, , 15, 189
- Savage B. D., Sembach K. R., 1991, *ApJ*, 379, 245
- Scannapieco E., Brügger M., 2015, *ApJ*, 805, 158
- Schneider E. E., Robertson B. E., 2017, *ApJ*, 834, 144
- Schneider E. E., Robertson B. E., Thompson T. A., 2018, *ApJ*, 862, 56
- Schneider E. E., Ostriker E. C., Robertson B. E., Thompson T. A., 2020, *ApJ*, 895, 43
- Schroetter I., et al., 2016, *ApJ*, 833, 39
- Schroetter I., et al., 2019, *MNRAS*, 490, 4368
- Sembach K. R., et al., 2003, *ApJS*, 146, 165
- Shapiro P. R., Field G. B., 1976, *ApJ*, 205, 762
- Sharma P., McCourt M., Quataert E., Parrish I. J., 2012, *MNRAS*, 420, 3174
- Shull J. M., Jones J. R., Danforth C. W., Collins J. A., 2009, *ApJ*, 699, 754
- Shull J. M., Smith B. D., Danforth C. W., 2012, *ApJ*, 759, 23
- Sick J., Courteau S., Cuillandre J.-C., Dalcanton J., de Jong R., McDonald M., Simard D., Tully R. B., 2015, in Cappellari M., Courteau S., eds, Vol. 311, *Galaxy Masses as Constraints of Formation Models*. pp 82–85 ([arXiv:1410.0017](https://arxiv.org/abs/1410.0017)), doi:10.1017/S1743921315003440
- Simionescu A., et al., 2021, *Experimental Astronomy*,
- Skilling J., 2004, in Fischer R., Preuss R., Toussaint U. V., eds, *American Institute of Physics Conference Series Vol. 735, Bayesian Inference and Maximum Entropy Methods in Science and Engineering: 24th International Workshop on Bayesian Inference and Maximum Entropy Methods in Science and Engineering*. pp 395–405, doi:10.1063/1.1835238
- Somerville R. S., Davé R., 2015, *ARA&A*, 53, 51
- Sorgho A., Foster T., Carignan C., Chemin L., 2019, *MNRAS*, 486, 504
- Sormani M. C., Sobacchi E., 2019, *MNRAS*, 486, 215
- Sormani M. C., Sobacchi E., Pezzulli G., Binney J., Klessen R. S., 2018, *MNRAS*, 481, 3370
- Speagle J. S., 2020, *MNRAS*, 493, 3132
- Spitzer Jr. L., 1956, *ApJ*, 124, 20

-
- Spitzer L., 1962. p. 98
- Springel V., et al., 2005, *Nature*, 435, 629
- Stanimirović S., Dickey J. M., Krčo M., Brooks A. M., 2002, *ApJ*, 576, 773
- Steidel C. C., Erb D. K., Shapley A. E., Pettini M., Reddy N., Bogosavljević M., Rudie G. C., Rakic O., 2010, *ApJ*, 717, 289
- Stern J., Hennawi J. F., Prochaska J. X., Werk J. K., 2016, *ApJ*, 830, 87
- Stern J., Fielding D., Faucher-Giguère C.-A., Quataert E., 2019, *MNRAS*, 488, 2549
- Stern J., et al., 2020a, arXiv e-prints, p. arXiv:2006.13976
- Stern J., Fielding D., Faucher-Giguère C.-A., Quataert E., 2020b, *MNRAS*, 492, 6042
- Stoche J. T., Penton S. V., Danforth C. W., Shull J. M., Tumlinson J., McLin K. M., 2006, *ApJ*, 641, 217
- Stoche J. T., Keeney B. A., Danforth C. W., Shull J. M., Froning C. S., Green J. C., Penton S. V., Savage B. D., 2013, *ApJ*, 763, 148
- Strickland D. K., Heckman T. M., 2007, *ApJ*, 658, 258
- Suresh J., Bird S., Vogelsberger M., Genel S., Torrey P., Sijacki D., Springel V., Hernquist L., 2015, *MNRAS*, 448, 895
- Sutherland R. S., Dopita M. A., 1993, *ApJS*, 88, 253
- Tassoul J.-L., 2000, *Stellar Rotation*
- Tejos N., et al., 2021, arXiv e-prints, p. arXiv:2105.01673
- Tepper-García T., Bland-Hawthorn J., Pawlowski M. S., Fritz T. K., 2019, *MNRAS*, 488, 918
- The Lynx Team 2018, arXiv e-prints, p. arXiv:1809.09642
- Thilker D. A., Braun R., Walterbos R. A. M., Corbelli E., Lockman F. J., Murphy E., Maddalena R., 2004, *ApJ*, 601, L39
- Thom C., et al., 2012, *ApJ*, 758, L41
- Thompson T. A., Quataert E., Zhang D., Weinberg D. H., 2016, *MNRAS*, 455, 1830
- Toro E. F., Spruce M., Speares W., 1994, *Shock Waves*, 4, 25
- Tripp T. M., Sembach K. R., Bowen D. V., Savage B. D., Jenkins E. B., Lehner N., Richter P., 2008, *ApJS*, 177, 39

- Tumlinson J., et al., 2011, *Science*, 334, 948
- Tumlinson J., et al., 2013, *ApJ*, 777, 59
- Tumlinson J., Peebles M. S., Werk J. K., 2017, *ARA&A*, 55, 389
- Turner M. L., Schaye J., Steidel C. C., Rudie G. C., Strom A. L., 2014, *MNRAS*, 445, 794
- Turner M. L., Schaye J., Steidel C. C., Rudie G. C., Strom A. L., 2015, *MNRAS*, 450, 2067
- Veilleux S., Cecil G., Bland-Hawthorn J., 2005, *ARA&A*, 43, 769
- Veilleux S., Maiolino R., Bolatto A. D., Aalto S., 2020, , 28, 2
- Vieser W., Hensler G., 2007, *A&A*, 472, 141
- Vogelsberger M., Genel S., Sijacki D., Torrey P., Springel V., Hernquist L., 2013, *MNRAS*, 436, 3031
- Vogt S. S., et al., 1994, in Crawford D. L., Craine E. R., eds, *Society of Photo-Optical Instrumentation Engineers (SPIE) Conference Series Vol. 2198, Instrumentation in Astronomy VIII*. p. 362, doi:10.1117/12.176725
- Voit G. M., 2018, *ApJ*, 868, 102
- Voit G. M., Donahue M., 2015, *ApJ*, 799, L1
- Voit G. M., Donahue M., Bryan G. L., McDonald M., 2015, *Nature*, 519, 203
- Voit G. M., Donahue M., Zahedy F., Chen H.-W., Werk J., Bryan G. L., O'Shea B. W., 2019, *ApJ*, 879, L1
- Vossberg A.-C. E., Cantalupo S., Pezzulli G., 2019, *MNRAS*, 489, 2130
- Wakker B. P., 1991, in Bloemen H., ed., *IAU Symposium Vol. 144, The Interstellar Disk-Halo Connection in Galaxies*.
- Wakker B. P., 2001, *ApJS*, 136, 463
- Wakker B. P., Savage B. D., 2009, *ApJS*, 182, 378
- Wakker B. P., van Woerden H., 1997, *ARA&A*, 35, 217
- Wakker B. P., et al., 2007, *ApJ*, 670, L113
- Walterbos R. A. M., Kennicutt R. C. J., 1988, *A&A*, 198, 61
- Wang B., 1993, *ApJ*, 415, 174
- Werk J. K., Prochaska J. X., Thom C., Tumlinson J., Tripp T. M., O'Meara J. M., Meiring J. D., 2012, *ApJS*, 198, 3

-
- Werk J. K., Prochaska J. X., Thom C., Tumlinson J., Tripp T. M., O'Meara J. M., Peeples M. S., 2013, *ApJS*, 204, 17
- Werk J. K., et al., 2014, *ApJ*, 792, 8
- Werk J. K., et al., 2016, *ApJ*, 833, 54
- White S. D. M., Frenk C. S., 1991, *ApJ*, 379, 52
- White S. D. M., Rees M. J., 1978, *MNRAS*, 183, 341
- Widrow L. M., Perrett K. M., Suyu S. H., 2003, *ApJ*, 588, 311
- Wilde M. C., et al., 2020, arXiv e-prints, p. arXiv:2008.08092
- Williams B. F., et al., 2017, *ApJ*, 846, 145
- Wisotzki L., et al., 2016, *A&A*, 587, A98
- Wolfe S. A., Lockman F. J., Pisano D. J., 2016, *ApJ*, 816, 81
- Wotta C. B., Lehner N., Howk J. C., O'Meara J. M., Prochaska J. X., 2016, *ApJ*, 831, 95
- Wotta C. B., Lehner N., Howk J. C., O'Meara J. M., Oppenheimer B. D., Cooksey K. L., 2019, *ApJ*, 872, 81
- Wright R. J., Lagos C. d. P., Power C., Correa C. A., 2021, *MNRAS*, 504, 5702
- XRISM Science Team 2020, arXiv e-prints, p. arXiv:2003.04962
- Zahedy F. S., Chen H.-W., Johnson S. D., Pierce R. M., Rauch M., Huang Y.-H., Weiner B. J., Gauthier J.-R., 2019, *MNRAS*, 484, 2257
- Zhang H., Zaritsky D., Zhu G., Ménard B., Hogg D. W., 2016, *ApJ*, 833, 276
- Zhang H., Zaritsky D., Behroozi P., 2018, *ApJ*, 861, 34
- Zhang S., Wang Q. D., Foster A. R., Sun W., Li Z., Ji L., 2019, *ApJ*, 885, 157
- Zhang Y., Liu R.-Y., Li H., Shao S., Yan H., Wang X.-Y., 2021, *ApJ*, 911, 58
- Zheng Y., Putman M. E., Peek J. E. G., Jounge M. R., 2015, *ApJ*, 807, 103
- Zhu G., et al., 2014, *MNRAS*, 439, 3139
- van de Voort F., Schaye J., 2012, *MNRAS*, 423, 2991
- van de Voort F., Springel V., Mandelker N., van den Bosch F. C., Pakmor R., 2019, *MNRAS*, 482, L85
- van der Marel R. P., Fardal M., Besla G., Beaton R. L., Sohn S. T., Anderson J., Brown T., Guhathakurta P., 2012, *ApJ*, 753, 8

Summary

- for non experts -

Galaxies in the Universe: not only stars

To observe and study the Universe, we mainly rely on the emission and absorption of radiation, which, using current telescopes, we are able to detect in many different bands of the *electromagnetic spectrum*. Yet, the vast majority of the matter permeating the cosmic space is invisible to us and interacts with its surroundings only through the gravitational attraction: this is known as *dark matter*. On a large scale, the dark matter is distributed along filaments that intersect each other in knots: the general pattern that this distribution creates is called *cosmic web* and is shown in Figure I. The bright spots in this image, located along the thickest filaments and knots of the cosmic web, show the regions of the Universe with the highest concentration of matter: they represent accumulations of dark matter and are generally called *dark matter halos*. These halos act as gravitational wells and attract inside them the ordinary, or *baryonic*, matter, which eventually forms the *galaxies* in their centers.

In the Universe there are about a thousand billion galaxies, which can be defined as agglomerates of stars and gas, bound together by gravity. In particular, the diffuse gas that is located in between the stars is called *interstellar medium*, or *ISM*. Part of this medium is composed of clouds of very cold gas, whose collapse leads to the creation of new stars with their planetary systems. Galaxies have different shapes and properties, like their mass, their gas content, or the rate at which they form new stars. While some of the galaxies have irregular shapes, the majority of them have stars that are either segregated along a disk (which can exhibit features like spiral arms and a central bulge or bar), or distributed in a more spherical or ellipsoidal shape. As a broad classification, disks are generally star-forming (or *late-type*) galaxies and elliptical (*early-type*) galaxies are more passive and not forming stars. In this context, our own Galaxy, the Milky Way, is a disk, star-forming galaxy with a central bar, it forms a few new stars every year and our Sun is located close to one of its spiral arms.

Thanks to the advent of new observational facilities, it has become clear that also the regions around galaxies are not devoid of matter, but are instead filled with elusive material called *circumgalactic medium*, or *CGM*. The CGM is defined as the medium that resides outside galaxies, but within the dark matter halos that host them. It is therefore distinguished from the *intergalactic medium*, or *IGM*, which is instead the material that populates the space in between galaxies, outside of their halos. The circumgalactic gas is, therefore, directly connected with the central galaxies and at the same time represents the interface between them and the external IGM. This makes it very important to understand how galaxies evolve through time. The formation of stars consumes the (cold) interstellar medium in the galaxy, which gets then replenished by the accretion of CGM, maintaining the star formation active. Moreover, stars have a finite lifetime and, if they are massive enough, at the end of their life they die through powerful explosions that are called *supernovae*, creating gas flows that move throughout the halo, as we will see more in detail below. Studying the CGM we can learn how galaxies affect their environment and viceversa, improving our knowledge on galaxy evolution. The study of this gas represents the main focus of this Thesis.

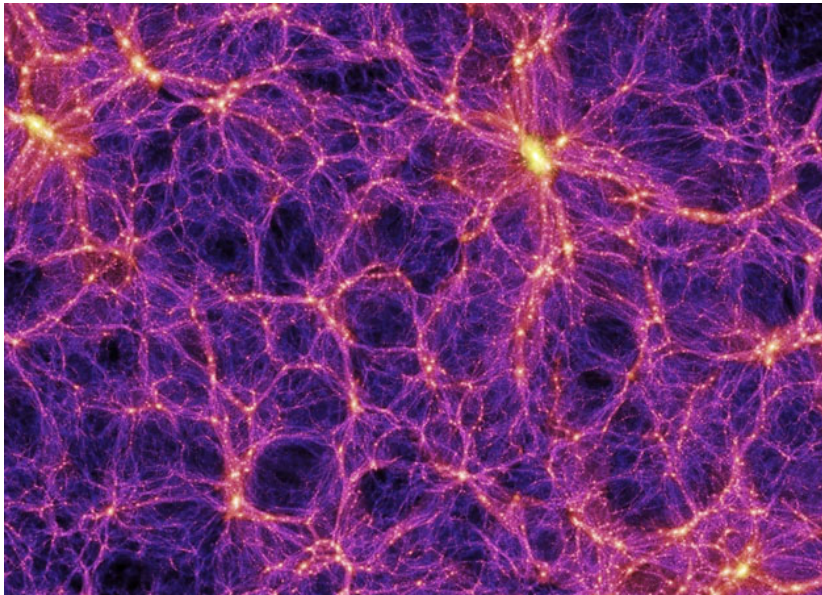


Figure I: Large-scale distribution of the dark matter, resulting from the dark-matter-only *Millennium simulations*: the brighter the color, the higher the concentration of matter in that region. The dark matter is distributed in filaments intersecting each other in knots, forming a distribution that resembles a web. The brightest spots show the regions where the halos are formed. From Springel et al. (2005).

The circumgalactic medium

The CGM is a complex system, formed of different phases that coexist with each other. In this Thesis, we have focused in particular on the two main components of the CGM: the hot and the cool phase. The hot CGM, also called *corona*, has a temperature of 10^{6-7} K (between one and 10 million degrees) and is believed to fill the entire volume of the dark matter halo, in equilibrium with its gravitational potential. Originally hypothesized in the '50s for our Milky Way, the presence of this medium around massive late-type and early-type galaxies has been later confirmed mainly by observations in the X-ray band of the electromagnetic spectrum.

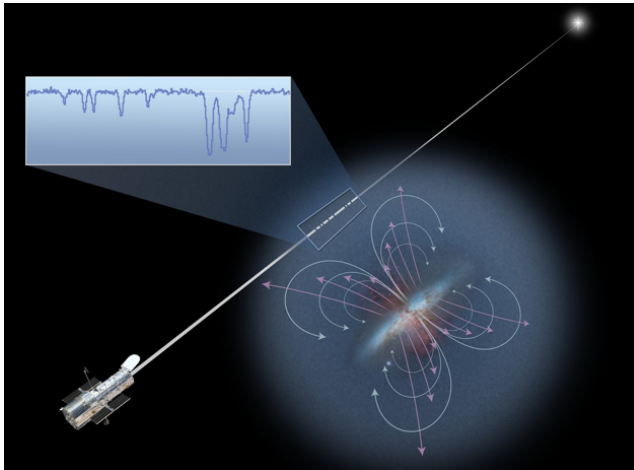


Figure II: Cartoon showing the observational technique generally used to detect the cool circumgalactic medium. We observe the emission coming from a bright source in the background. The gas around the galaxy absorbs part of the incoming radiation and creates the absorption lines visible in the electromagnetic spectrum (shown in the top-left corner). These lines are later used to analyze and characterize the cool CGM. Credit: NASA/STScI/Ann Feild.

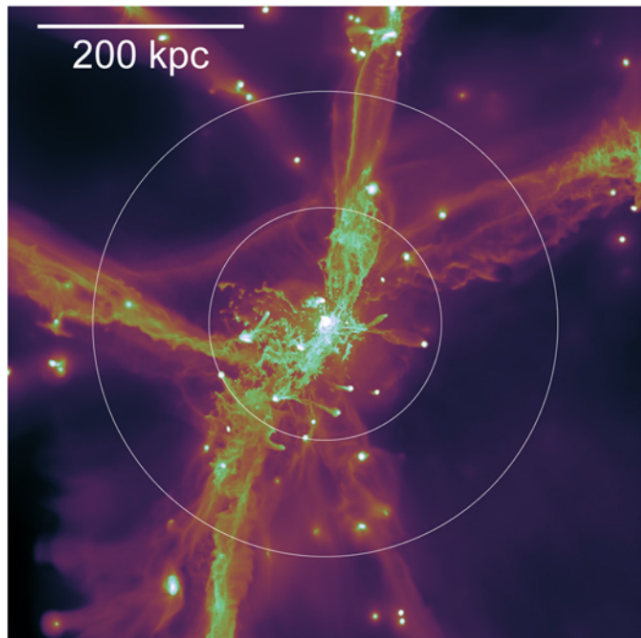
The cool CGM has, instead, temperatures of about 10^4 K (ten thousand degrees) and is likely composed of a variety of clouds, embedded in the hot corona. First discovered in the late '70s, this medium is observable in the ultra-violet (UV) band of the electromagnetic spectrum. Given that the emission of radiation from this cool gas is very faint, it is usually observed in absorption: a bright source in the background acts a big lamp, whose light can be partly blocked by a CGM cloud that is located in front of it. This results in *absorption lines* in the spectrum of the source, which then can be used to analyze the galaxy's CGM properties. This technique is illustrated in Figure II. Through this type of observations, this medium has been detected around different kinds of galaxies, from *dwarfs* (low-mass galaxies) to massive ellipticals. The cool CGM appears to be present up to very large distances from the central galaxy, up and beyond the edge of the dark matter halo. Its properties and especially its origin and its dynamics are debated: having typically one line of sight per galaxy,

reconstructing the overall intrinsic motion of these clouds is, indeed, challenging. The goal of this Thesis has been to understand what is the dynamics of these clouds in the halos of nearby galaxies and, in this way, to also infer their origin.

Inflows and outflows: the baryon cycle

What is the origin of the circumgalactic medium? As we have discussed, baryonic matter flows into the dark matter halo, attracted by its gravitational field. Therefore, at least a fraction of the CGM is expected to originate from the accretion of external IGM. This process creates *shock waves*, that heat up the incoming gas; this is believed to be the main formation mechanism for the hot CGM. However, depending on the properties of the halo, the IGM can also remain cool and flow directly towards the central galaxy. This is believed to be the case for low-mass galaxies and for galaxies at earlier stages of the Universe (about 10 billions years ago, see Figure III). Whether these 'cold flows' are still taking place at the present day, around galaxies at least as massive as our own Milky-Way, is still debated. Hot and cold gas accretion can coexist with each other, with filaments of cold gas penetrating the hot atmosphere and possibly reaching the central galaxy.

Figure III: Snapshot of the gas accretion taking place in the halo of a simulated galaxy halo, as it was about 10 billion years ago, with the galaxy at the center. The extent of the dark matter halo is shown by the inner white circle, while the bright filaments represent the cool gas, which, in this particular model, is directly accreting from the intergalactic medium into the central galaxy. From Nelson et al. (2016).



The accretion of external gas, however, is not necessarily the only process that determines the flows of gas in galaxy halos. As we have seen, the accretion

of cool gas onto the galaxy can trigger star formation and hence the formation of supernovae. If many stars explode at similar times, these explosions might generate powerful flows of gas that can escape the galaxy and travel throughout its halo. The combination of processes related to these outflows is known as *stellar feedback*. This can be either positive, hence it can trigger the accretion of more cold gas from the CGM, enhancing star formation; or negative, by preventing part or the entirety of the gas from accreting into the central regions, halting the formation of stars. In addition, powerful outflows can be triggered by the *super massive black hole* at the galaxy's center, but studying the impact of this process on the surrounding CGM has been outside the scope of this Thesis.

The evolution of a galaxy is then dependent on the balance among these flows going inward and outward, whose combination is generally called *baryon cycle*. Since the CGM is the region of the halo where all these flows are taking place, studying this medium is therefore of key importance. Despite this, there are to date various open questions regarding this gas, which this Thesis had the aim of addressing. What is the main formation channel of the CGM? What is the contribution of accretion and feedback in the baryon cycle? Is the cool gas accreting onto the central galaxies, fueling their star formation? Is there a coherent physical picture that can explain all the observational data?

This Thesis

The main aim of this Thesis has been to answer the questions outlined above and, in this way, better understand how the circumgalactic medium impacts galaxy evolution. We have seen, indeed, that the CGM, through its flows, can regulate the evolution of galaxies in the Universe. Our approach has been to develop theoretical models of this gas (composed of a hot corona and cool clouds) and to compare their predictions with real observational data. Through this comparison, we calibrated the physical parameters of our models in order to reproduce the observations. These models are therefore physically motivated and, at the same time, in agreement with the available data. With this technique, we explored the CGM dynamics and origin in the halos of galaxies of different kinds, in order to investigate how the galaxy properties depend on the characteristics of this gas.

In particular, in Chapter 2, we have analyzed the cool gas around massive elliptical galaxies. These are early-type galaxies and are currently forming stars at extremely low rates. This means that we do not expect cool gas to accrete onto them, since it would replenish the cold ISM and therefore feed the formation of new stars. However, a large amount of cool CGM has recently been observed in the halos of such galaxies. What is the fate of this gas? Why is it not fueling the central star formation? With our models, we have found that we can reproduce the data with cool clouds accreted from the IGM and infalling towards the internal regions of the halo. Instead of accreting onto the central galaxy (and fueling the formation of stars), however, these clouds tend

to be destroyed by the interactions with the hot gas, evaporating into it: this therefore explains why the galaxies at the center are currently passive.

In Chapter 3, we have focused on the CGM residing in the halos of star-forming galaxies. These objects are forming stars at a relatively high rate and the subsequent supernova explosions might create powerful outflows that we would be able to observe in the circumgalactic medium. The cool gas observed in the halos of such galaxies is, therefore, often associated with gas outflows originated in the central galaxies. With our work, we have instead proven that the majority of this cool medium cannot be produced by such outflows, since there is not enough energy available from the supernova explosions: the outflows are not powerful enough to be able to reproduce the observational data. We speculated that the cool medium is likely formed, instead, by the accretion from intergalactic medium

In Chapter 4, we have applied our models to the case of our closest massive neighbouring galaxy, the Andromeda galaxy, or M31. This is a disk, star-forming galaxy, with a mass similar to the Milky Way. Being it close to us, we have a privileged view on this object, including its CGM, which has recently been observed with an unprecedented detail. Comparing our models with the observational data, we were able to discard an outflow scenario as an origin for this medium, finding instead that an accretion of clouds, coming from the IGM and falling through the hot corona, can successfully and self-consistently reproduce all the available data.

Finally, in Chapter 5, we investigated whether the cool clouds observed in the halo of Andromeda, accreting from the IGM, can actually reach the central disk and fuel its star formation. We have found, using state-of-the-art simulations of this gas, that these clouds disappear relatively quickly in the halo of M31, due to the interactions with the hot gas, at very large distances from the central galaxy.

The main result of this Thesis is therefore to have shown how, in the nearby Universe, the vast majority of the cool circumgalactic gas can be explained with the accretion of material from outside the halo of the central galaxy. In this scenario, the outflows originated from the supernovae are, instead, much less important than what generally believed. We have also found that these inflowing cool clouds, both in passive and star-forming galaxies, are most likely evaporating in the hot gas and are not reaching the central regions. The formation of new stars in galaxies is therefore not fueled by the direct accretion of cool gas from the intergalactic medium, but it is most likely linked to other processes.

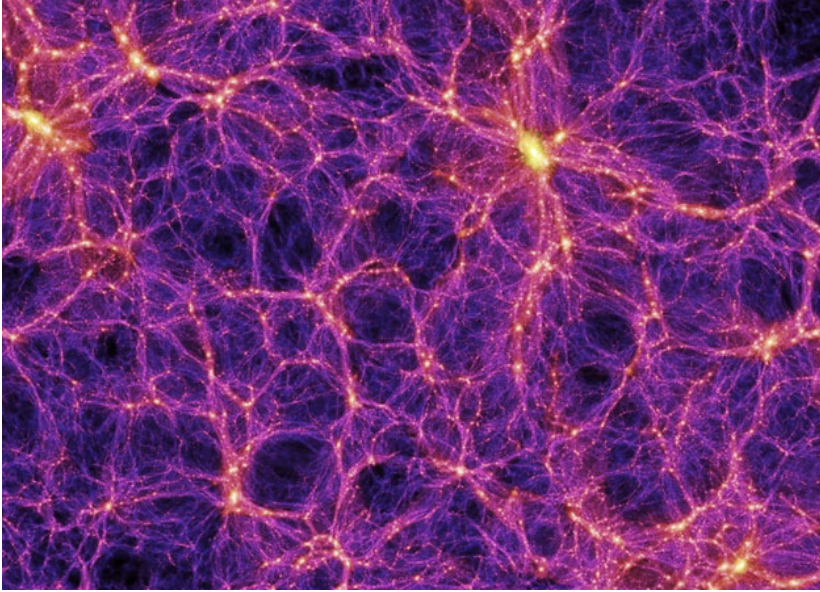
Samenvatting

Sterrenstelsel bestaan niet alleen uit sterren

Voor het observeren en bestuderen van het Universum gebruiken wij (sterrenkundige) voornamelijk de emissie en absorptie van licht, welke met de huidige generatie telescopen gedetecteerd kan worden in veel banden van het elektromagnetische spectrum. Toch blijft het overgrote deel van de materie die zich in de ruimte bevindt onzichtbaar voor ons en interacteert alleen maar met zijn omgeving middels zwaartekracht, deze materie staat bekend als *donkere materie*. Op grote kosmische schalen is donkere materie gedistribueerd langs filamenten die samen komen in knopen, samen vormen zij het Kosmische Web, welke is afgebeeld in Figuur I. De heldere plekken in deze afbeelding komen overeen met de gebieden waar de dichtheid van filamenten en knopen het hoogst is en geven de regionen met de hoogste dichtheid aan materie. In deze gebieden is de accumulatie van donkere materie het hoogst en zij worden ook wel *donkere materie halo's* genoemd. Deze halo's vormen een *zwaartekrachtspuit* en trekken normaal (baryonisch) materiaal aan, welke het vormen van sterrenstelsels in deze halo's mogelijk maakt.

In het universum zijn er ongeveer duizend-miljard sterrenstelsels, welke gedefinieerd kunnen worden als agglomeraten van sterren en gas die samengebonden zijn door zwaartekracht. Het diffuse gas dat zich tussen de sterren bevindt wordt het interstellair medium of ISM genoemd. Een deel van dit medium bestaat uit wolken van zeer koud gas. De ineenstorting van deze wolken leidt tot de creatie van nieuwe sterren en hun planetaire systemen. Sterrenstelsels hebben verschillende vormen en eigenschappen zoals hun massa, hun gasgehalte of de mate waarin zij nieuwe sterren vormen. Ondanks dat sommige sterrenstelsels onregelmatige vormen hebben, zijn de meeste van hen te classificeren als een schijfsterrenstelsel (met de typerende kenmerken zoals spiraalarmen en een centrale uitstulping of staaf) of als een ellipssterrenstelsel. Een algemenere classificatie is ook mogelijk op basis van stervorming. Zo zijn schijfsterrenstelsels de stervormende sterrenstelsels (of het laat-type) en zijn de elliptische sterrenstelsels (of het vroege-type) passiever en vormen geen sterren. In deze context is ons eigen sterrenstelsel, de Melkweg, een schijfsterrenstelsel met een

centrale balk en vormt het elk jaar een paar nieuwe sterren. Onze zon bevindt zich dichtbij een van deze stervormingsgebieden, namelijk dichtbij één van de spiraalarmen van de Melkweg.



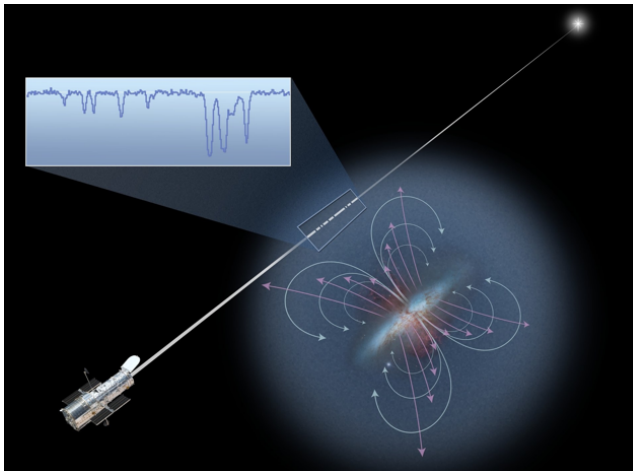
Figuur I: De distributie van donker materie op grote kosmologische schalen bepaald gebruikmakende van de *dark-matter-only* Millennium computer simulatie: hoe lichter de kleur hoe hoger de concentratie aan donkere materie in dat gebied. De donkere materie is verdeeld langs de filamenten die elkaar kruisen in de zo genoemde *knopen* en vormt op deze manier Kosmologisch Web. De heldere gebieden geven de gebieden aan waar de halo's zich vormen. Van Springel et al. (2005).

Dankzij de komst van nieuwe observationele faciliteiten voor de astronomie is het duidelijk geworden dat de regionen rondom sterrenstelsels niet verstoken zijn van materie, maar dat zij in plaats daarvan gevuld zijn met een ongrijpbaar dat het circumgalactische of CGM wordt genoemd. Het CGM wordt gedefinieerd als het medium dat zich buiten de sterrenstelsels, maar binnen de halo's van donkere materie bevindt. Het CGM onderscheidt zich hierin van het intergalactische medium (of IGM), wat het materiaal is dat zich in de ruimte tussen sterrenstelsels bevindt en dus buiten de donkere materie halo's. Het circumgalactische gas staat in direct contact met de centrale sterrenstelsels en het vormt tegelijkertijd een connectie tussen deze sterrenstelsels en het IGM. Het erg belangrijk om deze connectie tussen het sterrenstelsel, het CGM en het IGM te begrijpen wanneer men de evolutie van sterrenstelsels bestudeert. Zo wordt bijvoorbeeld het (koele) interstellair medium in het sterrenstelsel verbruikt voor de vorming van sterren. Dit tekort wordt echter direct aangevuld door de aanvoer van CGM en zorgt ervoor dat de stervorming actief blijft. Bo-

vendien hebben sterren een eindige levensduur en sterven zij aan het einde van hun leven, mits zij massief genoeg zijn, door krachtige explosies die supernova's worden genoemd. Als gevolg van deze explosies ontstaat er gasstromen die door de halo bewegen, welke hieronder in meer detail zullen worden besproken. Door het CGM te bestuderen kunnen wij leren hoe sterrenstelsels hun omgeving beïnvloeden en vice versa, en wij kunnen hiermee we onze kennis over de evolutie van sterrenstelsels verbeteren. De studie van het gas in het CGM vormt de belangrijkste focus van dit proefschrift.

Het circumgalactische medium

Het CGM is een complex systeem dat bestaat uit verschillende fases die co-existeren met elkaar. In dit proefschrift hebben wij de nadruk gelegd op twee hoofdcomponenten van het CGM in het bijzonder: de hete en koude fase. Het hete CGM (ook corona genaamd) heeft een temperatuur van 10^{6-7} graden Kelvin (ofwel tussen één en tien miljoen graden Kelvin). Men gelooft dat deze component de gehele donkere materie halo vult en dat het in evenwicht is met zijn zwaartekrachtspotentiaal. Het bestaan van dit medium was voorspeld in de jaren 50' van de vorige eeuw voor onze Melkweg, en later is het bestaan hiervan bevestigd voor sterrenstelsel van het late- en vroege-type middels X-ray observaties.



Figuur II: Een schets van de observationele techniek die normaliter gebruikt wordt om koud circumgalactische medium te detecteren. De observatie wordt gedaan met een heldere bron in de achtergrond. Het gas wat zich rondom het sterrenstelsel bevindt absorbeert het binnenkomende licht en zorgt voor absorptielijnen (zie de hoek linksboven). Deze lijnen zijn later gebruikt om het koude CGM te analyseren en karakteriseren. Credit: NASA/STScI/Ann Feild.

Het koude CGM heeft daarentegen een temperatuur van ongeveer 10^4 K (ofwel tien duizend graden Kelvin) en bestaat hoogstwaarschijnlijk uit een variëteit aan wolken die ingebed zijn in de hete corona. Deze component werd

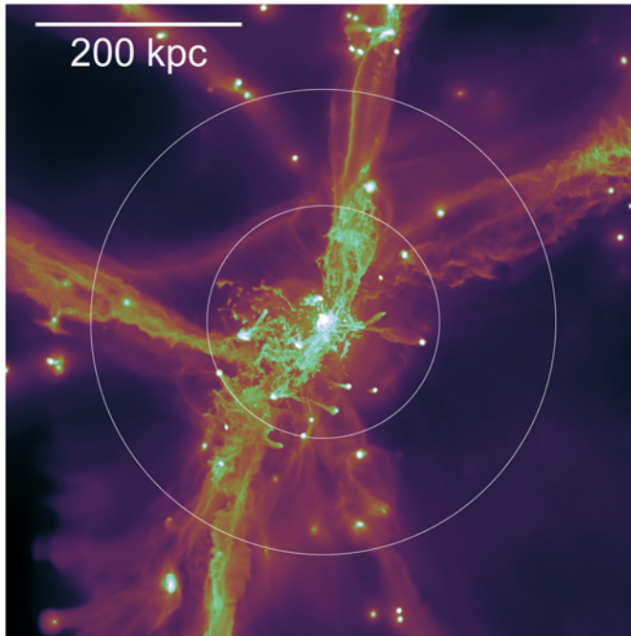
voor het eerst ontdekt eind jaren 70' en is zichtbaar in het ultraviolet band van het elektromagnetische spectrum. Gezien het feit dat de emissie van dit koud gas vrij laag is wordt het normaal gesproken waargenomen in absorptie. Zo wordt het licht een heldere bron die zich gedeeltelijk achter de gaswolk bevindt geabsorbeerd. Dit resulteert in absorptielijnen in het spectrum van de bron, deze lijnen worden vervolgens bestudeerd om de karakteristieken van de wolk te achterhalen. Deze techniek is geïllustreerd in Figuur II. Het koele medium is gebruikmakende van deze observatietechniek waargenomen in verschillende type sterrenstelsels: van dwerg (sterrenstelsels met een lage massa) tot massieve elliptische sterrenstelsel. Deze observaties wijzen erop dat het koele CGM zich bevindt tot op grootte afstanden van het centrale sterrenstelsel, zelfs tot en verder dan de rand van de donkere materie halo. De eigenschappen, maar met name de oorsprong en de dynamica, van deze wolk staan ter discussie, omdat het doorgaans een uitdaging is om de algehele intrinsieke bewegingen van deze wolken te reconstrueren op basis van de enkele gezichtslijn die het sterrenstelsel biedt. Het doel van dit proefschrift was om de dynamiek van deze wolken in de halo's van nabije sterrenstelsels te begrijpen wat en om op deze manier ook hun oorsprong af te leiden.

De aan- en afvoer: de cyclus van het baryonische medium

Wat is de oorsprong van het circumgalactische medium? Zoals eerder besproken stroomt de baryonische materie de donkere materie halo in omdat het aangetrokken wordt door het zwaartekrachtsveld van de halo, daarom verwacht men dat ten minste een fractie van de CGM uit het externe IGM komt. De aanvoer van het IGM zorgt voor schokgolven die het binnenkomende gas opwarmen. Dit proces wordt beschouwd als het belangrijkste vormingsmechanisme voor de hete CGM. Afhankelijk van de eigenschappen van de halo kan het IGM echter ook koel blijven en direct naar het centrale sterrenstelsel stromen. Men veronderstelt dat dit het geval is voor sterrenstelsels met een lage massa en de gene die zich bevonden in eerdere stadia van het heelal (ongeveer 10 miljard jaar geleden, zie Figuur III). Het staat nog steeds ter discussie of deze 'koele stromen' nog steeds plaatsvinden rondom sterrenstelsels die minstens zo massief zijn als de Melkweg. De aanvoer van heet en koud gas kunnen naast elkaar bestaan, waarbij de filamenten van het koud gas de atmosfeer van het hete gas binnendringen en mogelijk het centrale sterrenstelsel kunnen bereiken.

De aanvoer van extern gas is echter niet noodzakelijkerwijs het enige proces dat de gasstromen in halo's van sterrenstelsels bepaalt. Zoals we hebben gezien, kan de aanvoer van koel gas stervorming in het sterrenstel opgang brengen en kan daarmee de vorming van supernova's veroorzaken. Als veel sterren op dezelfde tijd exploderen kunnen er krachtige gasstromen gegenereerd worden die uit het sterrenstelsel kunnen ontsnappen en door de halo kunnen reizen. De combinatie van deze processen staat bekend als stellaire feedback. Deze feedback kan ofwel positief zijn, waarbij de aanvoer van meer koud gas vanuit het

CGM toeneemt en het stervorming versterkt; of negatief, door te voorkomen dat de hoeveelheid gas in de centrale regio's toeneemt, waardoor de vorming van sterren geremd of gestopt wordt. Bovendien kunnen er ook krachtige uitstromingen veroorzaakt worden door het superzware zwarte gat in het centrum van het sterrenstelsel, maar de impact van dit proces op het omliggende CGM valt buiten het bestek van dit proefschrift.



Figuur III: Momentopname van de gasaanvoer die plaatsvindt in een gesimuleerde halo van een sterrenstelsel ongeveer 10 miljard jaar geleden waarbij het sterrenstelsel in het centrum is geplaatst. De omvang van de donkere materie halo wordt weergegeven door de binnenste witte cirkel en de heldere filamenten stellen het koele gas voor. In dit specifieke model stroomt het koele gas rechtstreeks vanuit het intergalactische medium naar het centrale sterrenstelsel toe. Van Nelson et al. (2016).

De evolutie van een sterrenstelsel is dus afhankelijk van het evenwicht tussen stromingen die naar binnen en naar buiten gaan, dit wordt ook wel de baryoncyclus genoemd. Aangezien het CGM het gebied van de halo is waar al deze stromen plaatsvinden is het bestuderen van dit medium van cruciaal belang. Toch zijn er tot op heden verschillende open vragen over dit gas, die wij met dit proefschrift wouden beantwoorden. Wat is het belangrijkste vormingskanaal van het CGM? Wat is de rol van instroom en stellaire feedback in de baryoncyclus? Bereikt het koele gas de centrale sterrenstelsels waardoor het hun stervorming wordt aangewakkerd? Is er een samenhangende verklaring voor alle observaties die er van dit gas zijn gedaan?

Dit proefschrift

Het belangrijkste doel van dit proefschrift was om de hierboven genoemde vragen te beantwoorden en op deze manier een beter begrip te krijgen van hoe

het circumgalactische medium de evolutie van sterrenstelsels beïnvloedt. Wij hebben gezien dat het CGM door zijn stromingen de evolutie van sterrenstelsels in het heelal kan reguleren. Onze benaderingswijze was om theoretische modellen van dit gas (samengesteld uit een hete corona en koele wolken) te ontwikkelen en de voorspellingen die hieruit voort kwamen te vergelijken met observaties. Op deze manier hebben wij de fysische parameters van onze modellen gekalibreerd en de waarnemingen kunnen reproduceren. Deze modellen hebben dus fysische basis en zij zijn tegelijkertijd in overeenstemming met de beschikbare data. Gebruikmakende van deze techniek hebben wij de dynamiek van het CGM en zijn oorsprong in de halo's van verschillende soorten sterrenstelsels onderzocht, dit met als doel om te bestuderen hoe de eigenschappen van sterrenstelsels afhangen van de gaskenmerken.

In hoofdstuk 2 hebben wij vooral het koele gas rondom massieve elliptische sterrenstelsels geanalyseerd. Dit zijn sterrenstelsels van het vroege-type en hun stervorming is extreem laag. Op basis hiervan hadden wij verwacht dat er weinig koel aanwezig zou zijn, omdat de aanvoer van het koele ISM stervorming zou voeden. Recent is echter een grote hoeveelheid koud CGM waargenomen in de halo's van dergelijke sterrenstelsels. Wat is het rol van dit gas? Waarom voedt het de stervorming niet? Met onze modellen hebben wij deze observaties kunnen verklaren. Hierbij gaat het om koele wolken die zijn gegroeid met de aanvoer vanuit het IGM en zij stromen in de richting van de interne regio's van de halo. In plaats van naar het centrale sterrenstelsel toe te stromen (en waar zij de vorming van sterren aan te wakkeren) worden deze wolken echter meestal vernietigd door de interactie met het hete gas. Deze interactie zorgt ervoor dat het koele gas verdampt en dit verklaart waarom de sterrenstelsels in het centrum momenteel passief zijn.

In hoofdstuk 3 hebben wij ons gericht op het CGM dat zich in de halo's van stervormende sterrenstelsels bevindt. Deze sterrenstelsel vormen met een relatief hoge snelheid sterren en de daaropvolgende supernova-explosies kunnen krachtige uitstromen veroorzaken die in het circumgalactische medium waarneembaar zouden kunnen zijn. Het koele gas dat in de halo's van dergelijke sterrenstelsels wordt waargenomen wordt daarom vaak geassocieerd met gasuitstroom die afkomstig is uit de centrale sterrenstelsels. Wij hebben echter bewezen dat het grootste deel van dit koele medium niet kan worden verklaard door dergelijke uitstroming, aangezien er is niet genoeg energie beschikbaar komt vanuit de supernova explosies. Oftewel, de uitstromen zijn niet krachtig genoeg om de observaties te kunnen reproduceren. Wij speculeerden dat het koele medium waarschijnlijk gevormd wordt door de aanvoer van het intergalactisch medium.

In hoofdstuk 4 hebben wij onze modellen toegepast op het voor ons dichtstbijzijnde massieve naburige sterrenstelsel: het Andromeda-sterrenstelsel of M31. Dit is een schijfsterrenstelsel wat stervormend en het heeft een massa vergelijkbaar van de Melkweg. Aangezien het dichtbij ons staat kan dit object, inclusief de CGM, met ongekend detail waargenomen worden. Door onze modellen te vergelijken de observaties, zijn wij instaat geweest om een uitstroombesluit, die

oorsprong van het CGM verklaarde, te verwerpen. In plaats hiervan, ontdekten wij dat het scenario waarbij de aangevoerde gaswolken (die afkomstig uit het IGM) door de hete corona heen vallen alle waarnemingen kunnen reproduceren.

Ten slotte hebben wij in hoofdstuk 5 onderzocht of de koele wolken die zijn waargenomen in de halo van Andromeda, welke zijn aangevoerd vanuit het IGM, daadwerkelijk de centrale schijf kunnen bereiken en of zij de stervorming kunnen voeden. Met behulp van recent ontwikkelde simulaties van dit gas hebben wij ontdekt dat deze wolken relatief snel verdwijnen in de halo van M31 vanwege de interacties met het hete gas, welke plaatsvinden op zeer grote afstanden van het centrale sterrenstelsel.

Het belangrijkste resultaat van dit proefschrift is dat wij hebben laten zien hoe, in het nabije heelal, de overgrote meerderheid van het koele circumgalactische gas kan worden verklaard door de aanvoer van materiaal van buiten de halo van het centrale sterrenstelsel. In dit scenario is de uitstroom veroorzaakt door supernova's veel minder belangrijk dan werd aangenomen. Wij hebben ook ontdekt dat deze naar binnenstromende koele wolken hoogstwaarschijnlijk verdampen in het hete gas en de centrale regio's niet bereiken, dit geldt zowel voor inactieve als voor stervormende sterrenstelsels. De formatie van nieuwe sterren in sterrenstelsels wordt daarom niet gevoed door de directe aanwas van koel gas uit het intergalactische medium, maar is hoogstwaarschijnlijk gekoppeld aan andere processen.

Sommario

Le galassie nell'Universo: non solo stelle

Lo strumento principale che abbiamo per osservare l'Universo è la radiazione elettromagnetica, che, con i telescopi odierni, siamo in grado di rilevare sia in emissione che in assorbimento in diverse bande dello *spettro elettromagnetico*. La stragrande maggioranza della materia che permea il cosmo è tuttavia invisibile in termini di radiazione e interagisce con l'ambiente circostante esclusivamente attraverso l'attrazione gravitazionale: la *materia oscura*. Su grande scala, la materia oscura è distribuita in una struttura filamentare che ricorda una ragnatela ed è per questo nota come *ragnatela cosmica* (visibile in Figura I). I punti più luminosi di tale struttura, collocati lungo i filamenti e i nodi principali di questa ragnatela, sono le zone dell'Universo con la più alta concentrazione di materia e rappresentano accumuli di materia oscura che gli astronomi chiamano *aloni di materia oscura*. Questi aloni agiscono come veri e propri pozzi gravitazionali, attirando al loro interno la materia ordinaria, o *barionica*, che, accumulandosi nel centro di tali aloni, è responsabile della formazione delle *galassie*.

L'Universo ospita all'incirca mille miliardi di galassie, agglomerati di stelle e gas tenuti insieme dall'attrazione di gravità. Il gas diffuso che si trova fra le stelle è in particolare chiamato *mezzo interstellare*, o *ISM* (InterStellar Medium in inglese). Parte di questo materiale è formato da nubi di gas estremamente freddo, il cui collasso porta alla formazione di nuove stelle e dei loro sistemi planetari. Le galassie ad oggi conosciute hanno forme e proprietà diverse, come ad esempio la loro massa, il quantitativo di gas contenuto al loro interno e il tasso con cui formano nuove stelle. Escludendo una frazione di galassie con forme irregolari, nella maggior parte di esse le stelle sono ordinate lungo un disco sottile (che può a sua volta mostrare caratteristiche come dei bracci a spirale, un prominente nucleo e/o una barra centrale) o in una forma più sferica o ellissoidale. Le galassie vengono generalmente suddivise in due classi principali: le galassie a disco, che hanno una formazione stellare attiva, e le galassie ellittiche, che sono invece solitamente passive. In questo contesto, la nostra Galassia, la Via Lattea, è una galassia a disco con una barra centrale, forma qualche nuova

stella ogni anno e il nostro Sole è posizionato vicino a uno dei bracci a spirale.

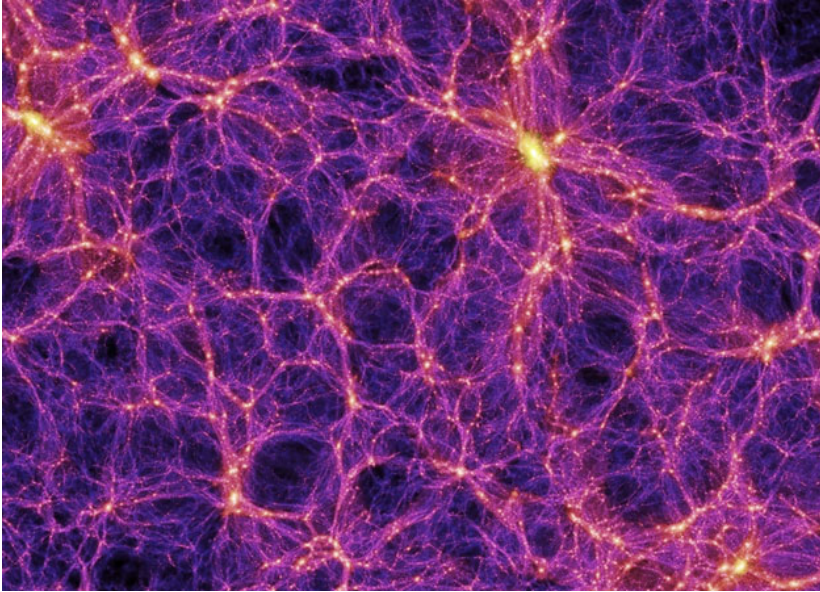


Figura I: Distribuzione su larga scala della materia oscura, come risulta nelle *Millenium simulations*, simulazioni dell'evoluzione nel tempo della sola materia oscura nell'Universo. Si può notare come la materia tenda a distribuirsi lungo filamenti che si intersecano in nodi, formando una distribuzione che ricorda una ragnatela. Le regioni più luminose mostrano le zone con una più alta concentrazione di materia oscura, nelle quali tendono a formarsi gli aloni galattici. Immagine tratta da Springel et al. (2005).

Grazie all'avvento dei moderni telescopi e osservatori, nel corso del tempo è diventato sempre più evidente come le regioni che circondano le galassie non siano formate solo da materia oscura, ma siano invece ricche di un gas chiamato *mezzo circumgalattico*, o *CGM* (dall'inglese CircumGalactic Medium). Il CGM è definito come il materiale che risiede al di fuori delle galassie, ma all'interno dei loro corrispettivi aloni di materia oscura, a differenza del *mezzo intergalattico*, o *IGM* (dall'inglese InterGalactic Medium), che rappresenta invece il gas che si trova nello spazio al di fuori degli aloni. Il mezzo circumgalattico rappresenta perciò la regione di comunicazione tra la galassia e il materiale che si trova al di fuori di essa e la sua caratterizzazione è quindi di fondamentale importanza per capire come le galassie evolvano nel tempo. Ma in che modo il CGM influisce sulla vita di una galassia? L'accrescimento di gas verso l'interno fa sì che il mezzo interstellare freddo venga continuamente rifornito di nuovo materiale, evitando che la formazione di nuove stelle esaurisca la riserva di gas disponibile all'interno della galassia. In più, le stelle hanno un tempo di vita finito e, se sufficientemente massive, sono destinate a morire attraverso delle

esplosioni che sono note come *supernovae*. Tali esplosioni possono a loro volta creare dei fussi di gas verso l'esterno, influenzando il CGM, come vedremo piú avanti. Attraverso lo studio del mezzo circumgalattico possiamo quindi capire come le galassie influiscono sull'ambiente circostante e viceversa, raffinando la nostra conoscenza sulla loro evoluzione. La caratterizzazione di questo materiale rappresenta il fulcro di questa Tesi.

Il mezzo circumgalattico

Il CGM è un sistema complesso, formato da fasi distinte che coesistono l'una con l'altra. In questo lavoro abbiamo trattato in particolare le due componenti principali di questo gas: la fase calda e la fase fredda. Il mezzo circumgalattico caldo, chiamato anche *corona*, ha una temperatura di 10^{6-7} K (tra uno e 10 milioni di gradi) e occupa l'intero volume dell'alone di materia oscura, in equilibrio con il potenziale gravitazionale. Ipotizzato originariamente negli anni '50 per la nostra Galassia, la presenza di questo mezzo in galassie relativamente massive, sia ellittiche che a disco, è stata confermata da numerose osservazioni nella banda a raggi X dello spettro elettromagnetico

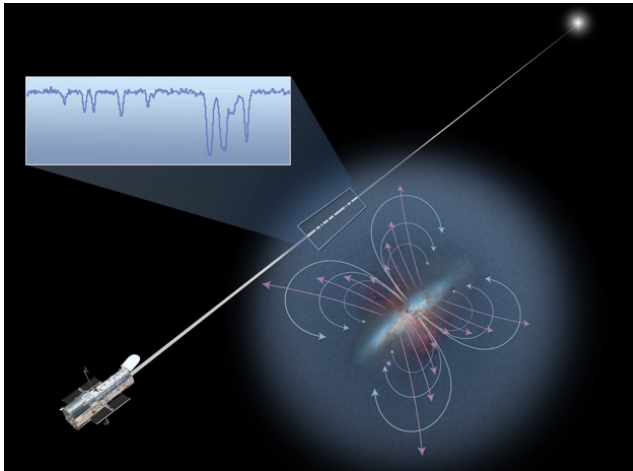


Figura II: Illustrazione che mostra la tecnica di osservazione generalmente utilizzata per rilevare il mezzo circumgalattico freddo. Parte della radiazione emessa da una sorgente luminosa sullo sfondo viene assorbita dal gas presente nell'alone della galassia. Ciò crea delle righe in assorbimento, visibili nello spettro elettromagnetico (mostrato nel pannello in alto a sinistra), che vengono successivamente utilizzate per analizzare e caratterizzare il CGM freddo. Credit: NASA/STScI/Ann Feild.

Il mezzo circumgalattico freddo ha, invece, temperature attorno ai 10^4 K (diecimila gradi) e sembra essere composto da nubi distinte, immerse nella corona di gas caldo. Scoperto per la prima volta negli anni '70, questo materiale si osserva principalmente nella banda ultravioletta (UV) dello spettro elettromagnetico. Dato che la radiazione emessa da questo gas è molto debole, viene solitamente osservato in assorbimento: una sorgente luminosa sullo sfondo

agisce da lampada, la cui luce può essere parzialmente oscurata da materiale (come ad esempio una nube di CGM freddo) che si frappone tra la sorgente e l'osservatore stesso. Questo processo, mostrato in Figura II, crea delle *righe di assorbimento* nello spettro, che vengono utilizzate per analizzare il CGM freddo della galassia centrale. Grazie alla tecnica appena descritta, questo gas è stato rilevato attorno a vari tipi di galassie, dalle *nane* (galassie di piccola massa), alle galassie ellittiche massive, con le nubi che si trovano fino a grandi distanze dalle galassie centrali, estendendosi fino ai limiti (e oltre) degli aloni di materia oscura. Nonostante ciò, le proprietà e specialmente l'origine e la dinamica di questo gas sono ad oggi dibattute: avendo una sola linea di vista per galassia (vedi Figura II), ricostruire il moto complessivo di queste nubi non è banale ed è soggetto a numerose assunzioni e incertezze. Lo scopo principale di questa Tesi è stato quello di comprendere la dinamica delle nubi di CGM freddo attorno a galassie vicine, in modo da dedurne in questo modo anche l'origine.

Il ciclo barionico

Qual è l'origine del mezzo circumgalattico? Come abbiamo visto in precedenza, gli aloni di materia oscura attraggono al loro interno, per mezzo della gravità, flussi di materia barionica. Questo accrescimento rappresenta quindi, molto probabilmente, l'origine di almeno parte del CGM osservato negli aloni delle galassie. Più precisamente, questo processo di accrescimento può creare delle *onde d'urto* che tendono a riscaldare il 'materiale in caduta' (o *inflow*), un meccanismo che si pensa essere all'origine del CGM caldo. A seconda delle caratteristiche dell'alone, il mezzo intergalattico può però anche rimanere freddo e accrescere direttamente nella galassia centrale. Questo secondo scenario sembra essere il mezzo di accrescimento principale in galassie di bassa massa e per galassie che si trovano nei primi stadi evolutivi dell'Universo (circa 10 miliardi di anni fa, vedi ad esempio Figura III). Se questi 'flussi di gas freddo' siano o no presenti anche oggi attorno a galassie con massa simile o maggiore di quella Via Lattea, rimane oggetto di dibattito. I due diversi processi di accrescimento (caldo e freddo) possono anche coesistere tra loro, con filamenti di gas freddo che tendono a penetrare nella corona galattica, raggiungendo in alcuni casi la galassia centrale.

L'accrescimento di gas esterno non è però necessariamente l'unico meccanismo in gioco nel determinare i flussi di gas negli aloni galattici. Come descritto in precedenza, l'accrescimento di gas freddo nella galassia centrale può alimentare la formazione stellare e di conseguenza la creazione di esplosioni di supernovae. Nel caso in cui un gran quantitativo di stelle esploda in un tasso di tempo relativamente breve, queste esplosioni possono causare potenti getti di gas che possono uscire dalla galassia stessa e attraversare l'alone circostante. L'insieme dei processi legati a questi 'flussi in uscita', o *outflows*, è conosciuto come *feedback stellare*. Tale feedback può essere positivo, alimentando l'accrescimento di gas freddo nella galassia e quindi la formazione di nuove stelle; o negativo, impedendo l'accrescimento verso il centro di parte o della totalità del

gas freddo, interrompendo di fatto la formazione stellare. Questi outflows possono essere innescati anche dal *buco nero super massiccio* che risiede al centro della galassia, ma lo studio di questo processo esula dallo scopo di questa tesi.

L'evoluzione di una galassia dipende perciò dall'equilibrio tra questi flussi di gas, la cui combinazione è generalmente chiamata *ciclo barionico*. Dato che questi flussi avvengono principalmente nel mezzo circumgalattico, lo studio di questo gas è fondamentale per la nostra comprensione di come le galassie evolvono nell'Universo. Ciò nonostante, ci sono tuttora molte domande riguardo a questo mezzo che non hanno trovato risposta e che hanno di fatto rappresentato il filo conduttore di questa Tesi. Qual è il principale canale di formazione del CGM? Come contribuiscono accrescimento e feedback al ciclo barionico? Il gas freddo è in grado di accrescere sulle galassie stesse, alimentando la loro formazione stellare? Esiste uno scenario teorico che sia in grado di spiegare tutti i dati osservativi a nostra disposizione?

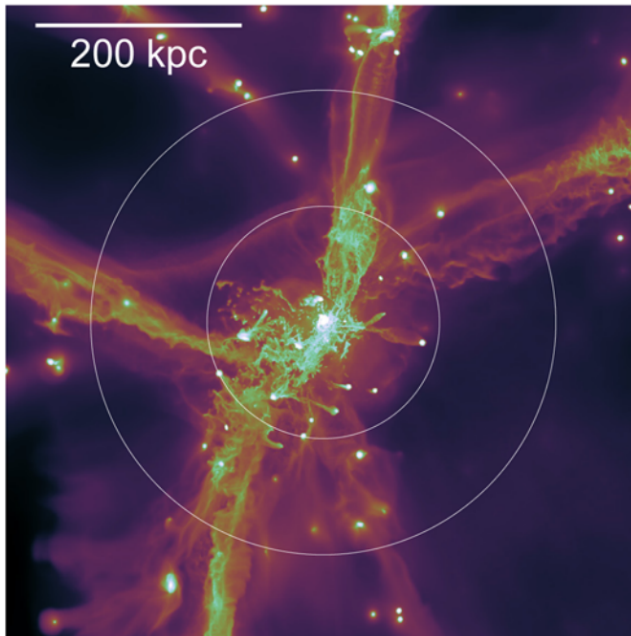


Figura III: Immagine che mostra l'accrescimento di gas, come era 10 miliardi di anni fa, nell'alone di una singola galassia, ottenuta da una simulazione idrodinamica. La galassia si trova al centro dell'immagine, mentre l'estensione dell'alone di materia oscura è rappresentata dalla circonferenza bianca più interna. I filamenti brillanti mostrano il gas freddo che, in questo particolare modello, accresce direttamente nella galassia centrale. Da Nelson et al. (2016).

Questa Tesi

Lo scopo principale di questa Tesi è stato quello di rispondere alle domande elencate nel paragrafo precedente, con l'obiettivo di comprendere quale sia il ruolo del mezzo circumgalattico nell'evoluzione galattica. A questo scopo, abbiamo sviluppato dei modelli teorici che descrivono la composizione (nubi

fredde immerse in una corona di gas caldo) e la dinamica del CGM e abbiamo successivamente confrontato le predizioni di tali modelli con i dati osservativi. Attraverso questo confronto, abbiamo calibrato i vari parametri fisici dei nostri modelli, in modo da riprodurre al meglio le osservazioni. Questi modelli sono perciò motivati fisicamente e allo stesso tempo in accordo coi dati. Con tale tecnica, abbiamo investigato la dinamica e l'origine del CGM presente negli aloni di galassie di vario tipo, con lo scopo di comprendere come le proprietà delle galassie siano legate alle caratteristiche di questo gas.

In particolare, nel Capitolo 2, abbiamo analizzato il gas freddo attorno a galassie ellittiche massive. Queste sono galassie passive, che stanno al momento formando stelle a tassi estremamente bassi. Ci aspettiamo perciò che il gas freddo non abbia la possibilità di cadere dentro tali galassie, dato che in tal modo andrebbe a rifornire la riserva di mezzo interstellare freddo, alimentando la formazione di nuove stelle. Tuttavia, un grande quantitativo di CGM freddo è stato recentemente osservato negli aloni di questo tipo di galassie. Qual è il destino di tale gas? Perché non sta alimentando la formazione stellare? Attraverso l'uso dei nostri modelli, abbiamo trovato che i dati sono ben riprodotti da nubi di gas freddo che cadono dal mezzo intergalattico verso le regioni centrali, attratte dalla gravità. Tuttavia, invece di arrivare fino alla galassia centrale, queste nubi sono distrutte dalle interazioni con il gas caldo circostante e sono destinate ad evaporare in esso, spiegando in tal modo perché le galassie centrali rimangono passive.

Nel Capitolo 3, ci siamo concentrati sul CGM che si trova negli aloni di galassie che formano stelle a dei tassi relativamente elevati. La formazione stellare e le conseguenti esplosioni di supernova possono creare, come abbiamo visto, potenti flussi di gas che dovremmo essere in grado di osservare nel mezzo circungalattico. Per questo motivo, il gas freddo rilevato in tali aloni è spesso associato con questi outflows che si originano nelle galassie centrali. In questo Capitolo, abbiamo dimostrato, invece, come la maggior parte del gas freddo non possa avere questa origine, dato che le esplosioni di supernova non forniscono energia a sufficienza per creare getti abbastanza potenti da poter riprodurre i dati osservativi. L'origine più plausibile del CGM freddo è invece data dall'accrescimento di mezzo intergalattico.

Nel Capitolo 4, abbiamo applicato i nostri modelli alla galassia massiva più vicina a noi, la galassia di Andromeda, chiamata anche M31. Andromeda è una galassia a disco, che forma stelle e che ha una massa simile a quella della nostra Via Lattea. Essendo così vicina, abbiamo su di essa, e sul suo CGM, una vista privilegiata: il gas nell'alone di M31 è stato infatti recentemente osservato in maniera estremamente dettagliata. Tramite il confronto dei nostri modelli con i dati osservativi, siamo stati in grado di escludere uno scenario di outflow come origine del CGM freddo. Abbiamo trovato invece come la caduta di nubi fredde attraverso la corona, accresciute dal mezzo intergalattico, possa riprodurre i dati in maniera autoconsistente.

Infine, nel Capitolo 5, abbiamo cercato di capire se le nubi osservate nell'alone di Andromeda, provenienti dall'IGM, siano in grado di raggiungere il disco

centrale e alimentare la formazione stellare. Grazie all'utilizzo di simulazioni idrodinamiche di questo gas, abbiamo trovato che queste nubi, a causa delle interazioni con la corona calda, vengono assimilate in essa e scompaiono a grandi distanze dalla galassia centrale.

Il risultato principale di questa Tesi è stato quindi quello di mostrare che, nell'Universo locale, la stragrande maggioranza del mezzo circumgalattico può essere spiegata con l'accrescimento di materiale proveniente dall'esterno dell'alone galattico. In tale scenario, i flussi di gas originati dalle esplosioni di supernova hanno invece un effetto relativamente secondario. Abbiamo poi trovato che queste nubi di gas freddo sono molto probabilmente destinate a dissolversi nella corona calda prima di poter raggiungere le galassie centrali. La formazione di nuove stelle non è perciò dovuta all'accrescimento diretto di gas freddo dal mezzo intergalattico, ma è probabilmente legata ad altri tipi di meccanismi.

Acknowledgments

‘...pensando bem, não tenho ideia nenhuma de quem és, mas isso não conta, o que importa é que gostemos um do outro.’
‘...when I think about it, I have no idea who you are, but that’s not important, what matters is that we care about each other.’

As intermitências da Morte, José Saramago

A few years ago, writing essentially a book of more than 200 pages seemed impossible to me and the idea of doing it had never even crossed my mind. And somehow here we are, this ‘book’ has finally seen the light. This Thesis includes basically all the work that I have done in the last four years and it represents the clearest memory of what have been probably the most beautiful years of my life. A lot of people contributed to it, people who I really care about and to whom I would like to express now my most sincere gratitude.

I would like to start by thanking the person who actually made this Thesis possible in the first place. *Filippo*, I don’t think I’ve ever stressed enough how grateful I am. We meet a lot of people along our way, but while most of them just come and go without too much notice, a few really make the difference and change our life. For me, you were one of the latter. You believed in me since the start and you convinced me to leave my safe nest and come to Groningen, which was without a doubt one of the best decisions of my life. Thank you for your constant support throughout the last 6 (!) years and for being not only an advisor but a friend. Thank you for the infinite amount of advice, the dinners, the bottles of wine and the runs in the desert. But mostly thank you for being a continuous source of inspiration, you simply taught me how to love astronomy and science. Looking at you has always made me want to be a better researcher. Collaborating with you was truly a pleasure and I hope that this was just the beginning.

Gabriele, your attention to details and the ease with which you solve problems that to me seem insurmountable will never cease to surprise me. Most of the times you know what I want to do or say before I even formulate clearly the thought in my mind. Discussing with you can be extremely exhausting at times, but it helped me growing up a lot. Thank you for wanting to be part of this project, thank you for caring about it so much and thank you for believing in me. Without you this Thesis would not be even half as accurate or valuable as it is now.

Amina, despite not being directly involved in the day-to-day work, you have always been kind with me and you showed a lot of optimism and interest towards this project, thank you for that. And thank you also for the very useful comments on my propositions.

Thanks to my reading committee, *Crystal*, *Hsiao-Wen* and *Marc*, for taking the time to carefully read this Thesis and for sharing with me your opinions and comments. It was an honour and a pleasure for me, I hope you have enjoyed it.

A warm thank goes to all those that have been part of Filippo's group during the past years, who kept patiently listening to me talking about cold clouds and hot coronae. *Lorenzo* and *Antonino*, your help has been invaluable during my first months in Groningen and has made everything easier since the very beginning. Thank you *Lorenzo* for all the tennis matches and the chats, I missed having you around (and I'm still sorry about your car). *Cecilia*, I am very happy that you came to Groningen, I feel that we got much closer here than during our university years in Bologna. Sharing this part of the road with you was extremely nice. *Asger*, thanks for your patience and the infinite help with the simulations, a very big part of the merit for the 5th chapter of this Thesis goes definitely to you. *Fernanda*, see next page. *Pavel*, thank you for the insightful discussions about my work, you were a good colleague. Thanks also to *Anqi* and *Barbara*, we didn't have time to get to know each other better, maybe there will be more in the future. *Lucia*, even without being here in Groningen, you were always there whenever I needed some help, thank you so much. Finally, one of the most rewarding experiences of the last years has been supervising bachelor and master students, so many thanks to *Thom*, *Lorraine* (thanks for all the cakes), *Thomas* and *Mark*.

If Kapteyn is such a wonderful place, that has become sort of a second family for most of us, it is mostly thanks to *Martine*, *Christa*, *Ramona*, *Maria* and *Lucia*, thank you for caring so much about our well being and for always being there to help with any possible problem. Thanks to the computer group, *Leon*, *Martin* and *Eite*, for being so efficient and for having the patience to keep answering the most stupid questions I could throw at you. Thanks also to all the staff members for making the Institute such a lovely and vibrant place. A special mention for *Inga*, it was a pleasure being your TA, and *Eline*, thank you for hosting us at your place so many times and for your help in translating my propositions into a more proper English.

A big thank to all the people that passed through office 187 during the time of my PhD. *Elaheh* and *Seyda*, your kindness and your authenticity really

made me feel at home at the start of this journey, you made everything easier. *Simon*, I've always wondered how somebody could be at the same time just as quiet, crazy, fun, hard-working and caring as you are. I guess that's what makes you special. Thanks for sharing the office with me and for all the rest. Hope that we'll play tennis again one day and that I'll be able to show you a few more tricks with the go karts. *Dawei*, I would have really liked to get to know you better. I hope you're doing fine. Thanks also to all the others who were there either at the very beginning or at the very end, *Aaron*, *Bohdan*, *Jayatee*, *Simone*, *Aditya*.

I really started enjoying my time here the moment I realized I had a place that I could call home. Plutolaan has been my first love in Groningen, a place that still takes a big part of my heart, thank you *Filippo* for giving me the opportunity to live there. *Teymoor*, I have to admit that the first night we met I was seriously thinking of just running away. Well, I'm glad I didn't. I'm glad I had the chance to spend so much time with you and assimilate so many of your pills of wisdom. It was fun. Laurent, I'll come back to you later. *Giulio*, thank you for being the 'mum' of the house and for taking care of me and Laurent, I enjoyed living with you and it was a pleasure to read your stories. *Fernanda*, thank you for trusting us and deciding to move in with us, even though for a very short time. I hope you had a good time. And thanks for giving me the chance of living with *Capitu* for a while, it was amazing. The 6 months (but effectively quite more) that I lived in Hereweg have been also rather unforgettable. *Marina*, I'll keep a bit more space for you towards the end. *Theo*, thank you for welcoming me since the beginning, for the Gloomhaven and the Magic matches, I'll keep training. *Bilbo* and *Sauron*, thank you for playing with me, it's been truly a lot of fun. You two are without a doubt the most beautiful and sweet creatures that ever existed on this planet.

I've been so lucky to meet in Groningen some of the most amazing people there are out there, who I soon started to call friends. I would like to have the time to write a love letter to each one of you, but my writing skills would not make that very interesting, so I'll just try to be as brief as possible.

Olmo, your eternal chillness makes you one of the people with whom spending time is just as easy as breathing, I'm glad I got to know you. *Nika*, if everybody were just a bit more like you the world would probably be a nicer place where to live and things would get done much quicker. *Enrico*, your way of approaching life and your unlimited curiosity always fascinated me. *Katya*, you are a kind, sweet and fun person and you deserve all the mortadella in the world. Thank you for being so nice with me since day one. *Kristiina* and *Karlis*, I've always admired you guys for your constant search for new adventures, thanks for the days in Istanbul, they have been amazing. *Karu*, I wish everybody was as excited as you are just for being in this world. *Smaran*, you are one of those people that I just like to have around. You are simply the cutest, as you like to say. I'm still waiting for the pictures of the tigers from your old days at the National Geographic. Thanks for illuminating me by telling me the difference between the words bet and bed. *Pavel*, you were not only

a colleague, but also a very good friend, thank you for all the spare ribs and the Friends episodes. *Danielito*, thank you for being such a volcano of energy and for pushing me to go and get things, instead of just waiting for them to happen (sorry for all the times I ditched you at circuit-training). *Valentina*, I'm so happy that we went together to that school in Annecy, knowing you better was the best thing that happened during that trip. You are my favourite gossiper in the world and I will miss your super-powerful laugh. I hope I'll see you soon in the motherland. *Peter*, I still haven't decided whether I like more normal Peter or party/drunken Peter, they are both great. *Pier* and *Martyna*, one of the sad things of living in a place for a limited amount of time is that sometimes you have to leave just at the moment when you are starting to get closer to somebody that you really like. You guys are amazing, hope we can see more weird movies together in the future. *Henrique*, in you I finally found somebody that loves rackets as much as I do, probably even more. Thank you for being my squash/tennis/padel buddy during these years. But also thank you for the cheese, the pepernoten, the rum, the crew, the pizzas, the more or less profound conversations. I will be waiting for you in Santiago, I know you won't disappoint me. *Alessandro*, thanks for teaching me a lot of things that I will probably never need in my life, I miss your random and absolutely useless facts. *Pranav*, your excitement for life is contagious. The fact that you threw the best party that Groningen has ever seen does not surprise me. Sorry I missed that. *Jonas*, the world needs more kind people like you. The best part about training for running the marathon (it never happened, in case anybody was wondering) was sharing it with you. I love our conversations, you have an amazing soul. Thanks for the electric piano and for trying to teach me how to play, you have no idea how much it helped. *Vaggelis*, you were probably the first non-astronomer person that I properly met here, thank you for showing me that there are other great people outside of this bubble. *Alex*, thank you for your professional advice on cat-mouth-related injuries. The same accident never happened again after that, it cannot be a coincidence. *Daniele*, I'm glad I found in you a person that can be more late than I am and is not ashamed of admitting it. Your other half has a lot to learn from you. *Bram*, thank you so much for translating the summary of the Thesis for me, my knowledge of Dutch is not there yet. *Umit*, your wedding in Istanbul has shown me that I actually don't need alcohol to dance, I didn't think that was possible. Thank you for inviting us, it was a lot of fun. *Willeke*, if I was half as active as you are, this Thesis would have at least three more chapters. Thanks for the amazing food, the socks and the Friday nights during the quarantine, I hope we'll manage to finally come and see you in Leiden one day.

And thanks also to *Anastasia*, *Ioana*, *Tadeja*, *Alka*, *Raph*, *Stefano*, *Pedro*, *Christoph*, *Claire*, *Renate*, *Slavyana*, *Hyoyin*, *Georg*, *Avanti*, *Emma*, *Julia*, *Anne*, *Laura*, *Crescenzo*, *Davide P.*, *Davide M.*, *Cristiana*. Each one of you meant something to me in the past years and has made this experience unforgettable.

Laurent, thank you for standing my presence in Plutolaan till the end, you were the only one that survived and did not run away. Thanks for the pop

corn on fire, the grey omelettes, the parties, the police, the brunches, the runs, the pepernoten, the bike rides, the tv series, the board games, the badminton matches (best sport ever). Just thinking about all the things that we have lived together makes me want to go back and live them all over again. Thank you for being patient and waiting for me even in the rare occasions when I happened to be late and for counteracting my laziness with your never ending energy. Thanks for making fun of me during my most stressful days, that actually helped a lot. You were the best flatmate I could ever ask for, I miss you already.

Pavel, this is the real one, sorry for making you wait. I think you know how much you mean to me and I think that the fact that we have visited together 3 continents and 10 different countries, that you are one of the few people in the world with whom I can be completely myself, that I had more stupid fights with you than with anybody else I know (taken all together) and that everybody at the Institute has been thinking for years that we are boyfriends, just makes it even more evident. You are not just a friend for me, you are Pavel, you are simply there. I will miss so much spending my daily time with you, thank you for these years, it was fantastic (unless it wasn't, but I think it really was). I know that you think we already had our last dance, but I promise you that many more will come. Peace.

Marina, I am not good enough with words to express what I want to tell you. I did not think it would be possible to care about someone as much as I care about you, to have fun with someone as much as I have fun with you, to feel just right in any single moment I spend with you. Thank you for being there, for sharing my same dreams, thank you for coming to Laurent's party that night, for wanting to cut my hair around a year later and for asking me to try the Greek duolingo. Thank you for wanting to live with me and for taking care of me, for being always able to say the right thing, for being the shoulder on which I can lean, for deciding to embark on this crazy journey around the world with me. This Thesis is so much yours, your help with the cover, the template and the design of all the details was invaluable. You essentially made it, then I just had to fill it up with a couple of things about astronomy. Can't wait to see what we are going to accomplish together next. Σ'αγαπώ πάρα πολύ.

Vorrei per concludere ringraziare quelle persone che in qualche modo mi sono state vicine in questi anni anche da lontano. Gli amici di Bologna, coi quali abbiamo cominciato insieme questa pazza avventura che è l'astronomia, in particolare *Carlo*, *Federica*, *Matilde* e *Cristiano*. Carlo, compare, grazie di aver condiviso così tanto con me, grazie per le chiamate, le giornate a Bologna e quelle a Santa Cruz. Alla fine non sono mai riuscito a farti vedere la mia bella Groningen, ti aspetto in Cile però. Grazie agli amici di Forlì, che mi hanno visto crescere e che credo in qualche modo resteranno sempre con me, per quanto le nostre strade possano prendere direzioni diverse: *Balda*, *Barbi*, *Beppe*, *Cipri*, *Fede*, *Lillo*, *Orso*, *Paolo*, *Pico*, *Pier*, *Simo* (rigorosamente in ordine alfabetico, nessuna preferenza). Il grazie più grande va infine a quelle persone che non ringrazio mai abbastanza, che mi hanno reso la persona che

sono oggi e che darebbero tutto per me, senza che io abbia davvero dato loro niente in cambio. *Nonna*, sto bene, mangio e sono in salute, quelle sono le cose importanti come dici te. Ci vediamo presto. *Marco*, lo so che forse non te lo faccio mai vedere abbastanza, ma sei una delle persone più importanti della mia vita e sono felice che tu abbia avuto modo di vedere Groningen e di avere un assaggio della mia vita qua. Ti auguro tutta la felicità del mondo. *Babbo e mamma*, semplicemente grazie, senza di voi tutto questo di certo non sarebbe stato possibile. Vi voglio un bene infinito e ve ne vorrò sempre. Non importa in quale parte del mondo io sia, voi siete sempre con me.

*'And there never was an apple, in Adam's opinion, that wasn't worth the trouble
you got into for eating it.'*

Good Omens, Neil Gaiman & Terry Pratchett